TECHNISCHE UNIVERSITÄT MÜNCHEN

Fakultät für Physik
Lehrstuhl für Funktionelle Materialien

Influence of solvent additives on the morphological degradation in polymer-fullerene solar cells

Dan Yang

Vollständiger Abdruck der von der Fakultät für Physik der Technischen Universität München zur Erlangung des akademischen Grades eines

Doktors der Naturwissenschaften (Dr. rer. nat.)

genehmigten Dissertation.

Vorsitzende:	Prof. Dr. David Egger
Prüfer der Dissertation:	1. Prof. Dr. Peter Müller-Buschbaum
	2. Prof. Dr. Friedrich C. Simmel

Die Dissertation wurde am 15.06.2020 bei der Technischen Universität München eingereicht und durch die Fakultät für Physik am 13.07.2020 angenommen.

Abstract

In this thesis, two approaches, namely inserting an interfacial layer and doping a third component are examined for optimizing the morphology of bulk heterojunction (BHJ) films in organic solar cells (OSCs). Besides, the effects of solvent additives on the device stability are investigated on the lower bandgap polymer blends of PTB7-Th:PC$_{71}$BM and PffBT4T-2OD:PC$_{71}$BM based solar cells. The studies are based on combining grazing incidence X-ray scattering measurements and current-voltage tracking simultaneously. The results suggest that the escaping of residual solvent additives from the device leads to a BHJ morphological degradation, causing a decay of the fill factor (FF). Moreover, solvent additives can affect the interpenetrating network of BHJ film and the polymer crystallinity, which have profound effects on the device stability. Thus, this thesis provides fundamental information for choosing a proper solvent additive for more stable organic solar cells.

Zusammenfassung

In dieser Arbeit wird sowohl das Einbringen einer Grenzflächenschicht als auch das Dotieren mit einer dritten Komponente untersucht, um die Morphologie eines Bulk Heterojunction (BHJ) Films in organischen Solarzellen (OSCs) zu optimieren. Darüber hinaus werden die Auswirkungen von Lösungsmitteladditiven auf die Stabilität des Bauelements an Polymermischungen mit niedriger Bandlücke auf PTB7-Th:PC$_{71}$BM- und PffBT4T-2OD:PC$_{71}$BM basierten organischen Solarzellen untersucht. Die Untersuchung beruht auf einer gleichzeitigen Kombination von Röntgenstreumessungen mit streifendem Einfall und Strom-Spannungs-Messungen. Die Ergebnisse legen nahe, dass das Austreten von Lösungsmittelresten aus dem Bauteil zu einer morphologischen BHJ-Degradierung führt, was in einem Abfall des Füllfaktors (FF) resultiert. Darüber hinaus können die Lösungsmitteladditive das interpenetrierende Netzwerk des BHJ-Films als auch die Polymerkristallinität beeinflussen, was wesentliche Auswirkungen auf die Stabilität des Bauteils hat. Somit liefert diese Arbeit fundamentale Informationen zur Auswahl eines geeigneten Lösungsmittelzusatzes für stabilere organische Solarzellen.

Contents

List of abbreviations

BHJ: bulk heterojunction

CBA: *o*-chlorobenzaldehyde

DOS: density of states

DWBA: distorted wave born approximation

DIO: 1,8-diiodooctane

FF: fill factor

FTO: fluorine doped tin oxide

FWHM: full width at half maximum

GISAXS: grazing incidence small angle X-ray scattering

GIWAXS: grazing incidence wide angle X-ray scattering

HOMO: highest occupied molecular orbital

ITO: indium-doped tin oxide

I-V: current-voltage characteristics

J_{sc}: short circuit current

LMA: local monodisperse approximation

LUMO: lowest unoccupied molecular orbital

M_n: number average molecular weight

M_w: weight average molecular weight

OSCs: organic solar cells

PCE: power conversion efficiency

PEDOT:PSS: poly(3,4-ethylenedioxythiophene):poly(styrenesulfonate)

PSD: power spectral density

P3HT: poly(3-hexylthiophene-2,5-diyl)

PBDTTPD-COOH: poly[(4,8-bis((2-ethylhexyl)oxy)benzo[1,2-b:4,5-b']dithiophen-2-yl)[4,
6-dioxo-4H-thieno[3,4-c]pyrrol-5(6H)-yl) undecanoic acid]]

PTB7-Th: poly[4,8-bis(5-(2-ethylhexyl)thiophen-2-yl)benzo[1,2-b;4,5-b']dithiophene-2,6-
diyl-alt-(4-(2-ethylhexyl)-3-fluorothieno[3,4-b]thiophene-)-2-carboxylate-2-6-diyl)]

PffBT4T-2OD: poly[(5,6-difluoro-2,1,3-benzothiadiazol-4,7-diyl)-alt-(3,3'''-di(2-octyldode
cyl)-2,2';5',2'';5'',2-quaterthiophen-5,5'''-diy)]

$PC_{71}BM$: [6,6]-Phenyl-C71-butyric acid methyl ester

RMS: root mean squared (roughness)

SDD: sample detector distance

SLD: scattering length density

TOF-SIMS: time-of-flight secondary ion mass spectrometry

UV/Vis: ultraviolet/visible spectroscopy

V_{oc}: open circuit voltage

1 Introduction

Energy resources are highly demanded for the development of industries and human activities. To date, fossil fuels, including gas, coal and oil, are the main energy sources, which are nonrenewable and account for more than 80% of the global primary energy demand [1] and it is not expected to change significantly until 2030. Also, the combustion of these fossil fuels contribute a tremendous amount of CO_2 emission into the atmosphere. In 1900, the Inter-governmental Panel on Climate Change (IPCC) has announced that human activities result in the production of four gases, namely carbon dioxide, methane, chlorofluorocarbon and nitrous oxide, significantly contributing to global warming. Whereas, CO_2 has the greatest adverse impact on the greenhouse effect [2]. To meet the rapid increase of global energy consumption and environmental issues, sustainable and green resources are expected. Wind, sun, and biomass are considered as the main renewable energy sources. It has been reported the solar energy that strikes the surface of the earth in one hour can provide enough energy to power the entire world for a whole year [3]. Thus, it has the capability to meet the world's large and growing energy demand and much attention is focused on converting solar power into electricity. Solar cells, or photovoltaic cells, are developed to harvest solar energy directly from sunlight and convert it into electrical power.

The history of photovoltaic devices can be traced back to 1839 when Alexandre-Edmond Becquerel reported the first observation of the photovoltaic effect from an electrolytic cell [4]. In 1954, the first practical solar cell based on silicon was announced in the Bell Laboratories, which yields a power conversion efficiency (PCE) of 6 % [5]. According to the development of photovoltaic devices, the wafer-based crystalline silicon devices are called first generation solar cells, which reach a PCE of above 25 % [6, 7]. Silicon solar cells currently dominate the photovoltaic market, as they have good performance and high stability. However, manufacturing single crystal silicon and obtaining a desired thickness level (200-300 μm) of the wafer causes a high production cost and intensive energy consumption. The second generation of solar cells, also called thin film solar cells, is development based on amorphous silicon and III–VI semiconductors, such as GaAs, CdTe, and Cu(In, Ga)(Se, S)$_2$ (CIGS) [8]. This type of solar cells can harvest a large range of the solar spectrum and the PCEs above 20 % were achieved [6, 9]. However,

the materials employed in the thin film solar cells are unstable, scarce and toxic, which seriously hinder the further progress of this thin film solar cell.

The discovery of conductive polymers in 1977 [10] provides a chance to realize lower-cost and flexible solar cells by using inexpensive, environmentally friendly, and robust materials. The emerging organic thin-film devices are called third generation solar cells, including organic solar cells (OSCs) [11], dye-sensitized solar cells (DSSCs) [12], and quantum dot solar cells (QDSCs) [13]. Among them, solution processable OSCs have distinct advantages: low weight, the potential for low cost production, transparency, flexibility, and large scale fabrication. Over the last decade, perovskite solar cells, which are considered as the fourth generation of solar cells, have attracted a lot of researchers' attention. The mixed organic-inorganic halide perovskites ABX_3 (A = CH_3NH_3 or NH_2CHNH_2, B = Pb or Sn, X = Cl, Br, I or mixed halides) is applied to work as the photovoltaic layer, and the solar cells based on perovskites have achieved PCEs of beyond 25 % [7, 14, 15]. The long charge diffusion length, high absorption coefficient, tunable bandgap and solution processability make perovskite solar cells capable of competing with their counterparts. However, avoiding toxic Pb and improving long term stability are still the challenges of perovskite devices.

In this thesis, the environmental friendly OSCs are in the focus. As mentioned before, the outstanding advantages, such as solution processability, low cost and short energy payback time [16, 17] make OSCs potentially usable in the real world, which may not be achievable by other solar cells that even have much higher efficiencies. According to the working principle of OSCs, the exciton generation, exciton diffusion and dissociation, as well as charge transport occur in the bulk heterojunction (BHJ) film, which is made by a blend of the donor (D) and acceptor (A) materials. Therefore, the BHJ morphology plays a critical role in device performance [18,19]. In general, a typical morphology should contain sufficient interpenetrating networks between donor and acceptor materials for exciton dissociation and continuous pathways for charge transport [20]. Recently, the PCEs of OSCs have been improved to over 17.3 % in tandem devices [21], while the champion device efficiency for single-junction OSCs is around 16 % [22]. To further improve the efficiency of OSCs, many efforts are done to optimize the BHJ morphology, such as tuning the D/A ratio [23–25], film post-treatments (thermal and solvent annealing) [26–29], doping solvent additives [30–32] and inserting interfacial layers [33–35]. Aside from high PCEs, another big challenge for the organic photovoltaic community is to have sufficient long-term stability ($\geq$ 10 years) combined with high performance [36, 37]. The instability of OSCs originates mainly from chemical and morphological degradation pathways [38–41]. To overcome chemical degradation, suggested solutions are the production of inherently chemically stable materials and encapsulation of devices [42,43]. In contrast, an approach,

which can slow down the morphological degradation, is to lock the initially installed BHJ structure by increasing the crosslinking of the D/A morphology [44]. However, the mechanisms behind the morphological degradation are still not clear. What drives the morphology changes in the BHJ layer still needs to be explored further.

The main target of the present thesis is to address the effects of solvent additives on the stability of OSCs. Doping with solvent additive in the D/A blend solution is considered as the simplest and fastest method to optimize the BHJ morphology, especially in comparison with solvent annealing and thermal annealing, which are undesirable for a large scale fabrication. Here, 1,8-diiodooctane(DIO) and o-chlorobenzaldehyde (CBA) are used as solvent additives in poly[4,8-bis(5-(2-ethylhexyl) thiophen-2-yl)benzo[1,2-b;4,5-b']dithiophene-2,6-diyl-alt-(4-(2-ethylhexyl)-3-fluorothieno[3,4-b]thiophene-)-2-carboxylate-2-6-diyl)] (PTB7-Th):[6,6]-phenyl-C71-butyric acid methyl ester ($PC_{71}BM$) and poly[(5,6-difluoro-2,1,3-benzothiadiazol-4,7-diyl)-alt-(3,3"'-di(2-octyldodecyl)-2,2';5',2";5",2"'-quaterthiophen-5,5"'-diyl)](PffBT4T-2OD): $PC_{71}BM$ based solar cells. The morphology changes during the device degradation are simultaneously investigated via in-operando grazing incident X-ray scattering techniques. This thesis starts with the theoretical background (Chapter 2), which contains the basic theory of polymer phase separation and conductive polymers, working principles of solar cells, and fundamental theory of the applied scattering technique. In Chapter 3, the instruments used in this thesis are described, including theoretical background and operating parameters. Thereafter, the sample preparation process, as well as the deposition methods, are presented in Chapter 4. The research results and corresponding discussions are address from Chapter 5 to Chapter 8. An overview of these research projects is schematically depicted in Figure 1.1.

A hydrophilic PEDOT:PSS film is usually used as a blocking layer in the conventional structure of OSCs, which can lead to a PCBM-rich interface in the BHJ film. One effective way to tailor the polymer or PCBM molecule distribution is to introduce a hydrophobic interfacial layer on the top of PEDOT:PSS layer [33, 45]. However, the interfaces in contact with the multicomponent BHJ can be beneficial, disadvantageous, or neutral, concerning the performance of the OPV device. In Chapter 5, a guideline for choosing an effective interface is discussed and verified. Five interface molecules, with different surface energies, are introduced as examples. Contact angle measurements with 4 probe liquids enable calculation of the surface energies, and the results are compared with the performance of forward-biased OPV devices. Thus, a simple algorithm based upon surface energy considerations is discussed, when an interfacial layer is for a given BHJ in an OPV device.

As pointed out above, the crystallinity and morphology of both polymer and fullerene have a profound influence on the performance of BHJ organic photovoltaic devices. To
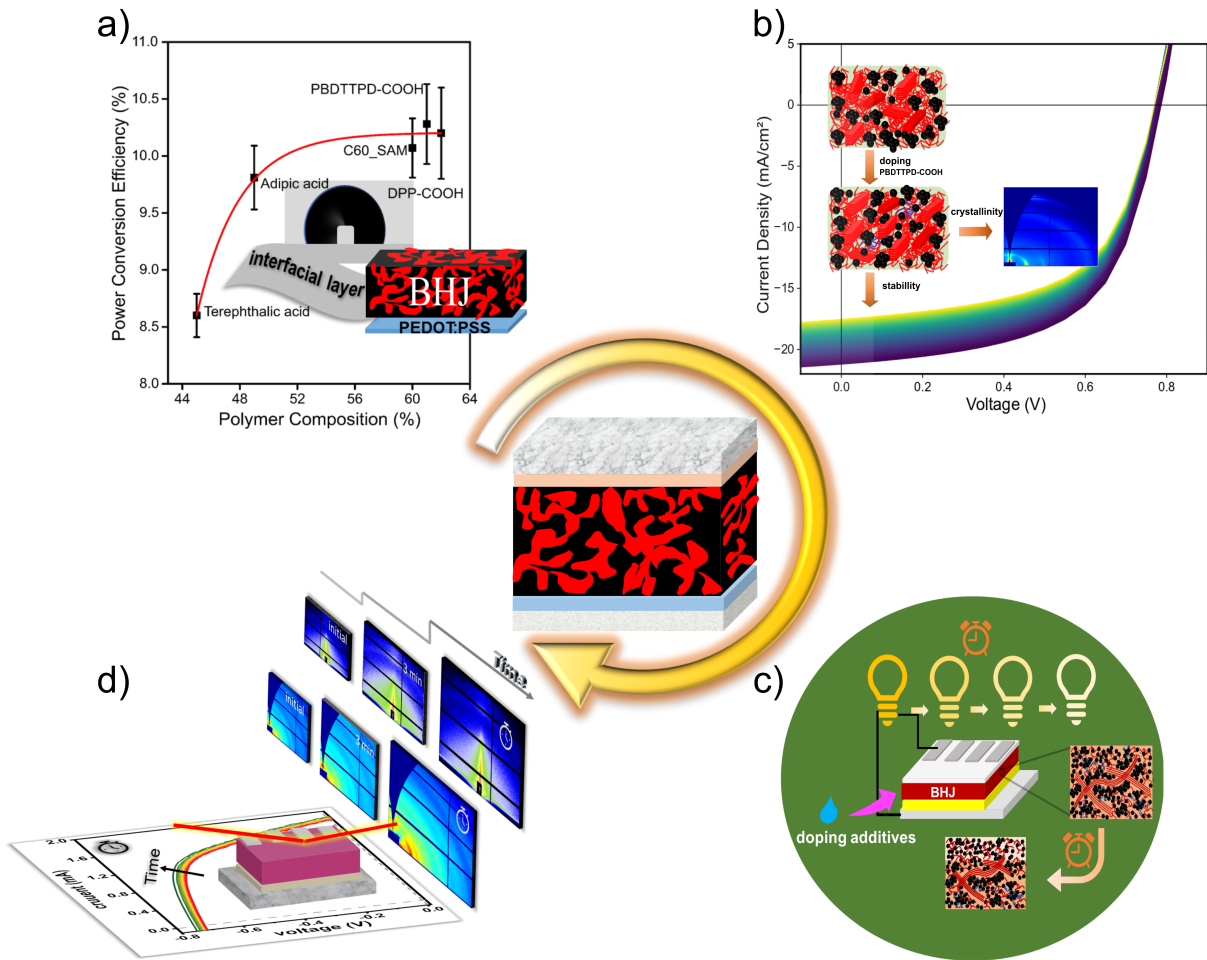
Figure 1.1: *Schematic overview of research topics in the present thesis. a) How to properly choose an interfacial layer for organic solar cells. b) Tailoring polymer crystallinity by doping PBDTTBT-COOH as a third component in PTB7-Th:$PC_{71}BM$ and PffBT4T-2OD: $PC_{71}BM$ based solar cells. c) Investigating on the effects of solvent additives on the stability of PTB7-Th:$PC_{71}BM$ solar cells. d) Studying the effects of solvent additives on the stability of PffBT4T-2OD:$PC_{71}BM$ solar cells via in-operando GIXS measurements.*

improve the light absorption range, crystallization and the compatibility of the D/A materials, a third component is introduced into the photoactive layer [46, 47]. In Chapter 6, the conjugated polymer PBDTTPD-COOH is employed as a third component in BHJ films of PTB7-Th:$PC_{71}BM$ and PffBT4T-2OD:$PC_{71}BM$. Subsequently, the domain sizes, crystallite sizes and crystalline orientations of donor polymers are investigated. The correlation of crystallinity and morphology of BHJ films and the performance of assembled devices are discussed. Besides this, the stability of ternary solar cells is compared with the corresponding binary devices.

To anticipate one outcome, the device performance can be significantly improved by

introduction of solvent additives, which facilitate to obtain an interpenetrating network and proper domain sizes in the BHJ layer for charge dissociation and charge transport [48, 49]. However, due to the high boiling point of additive solvents, the influence of residual solvents in the device on the device stability needs to be figured out. In Chapter 7, PTB7-Th:PC$_{71}$BM based solar cells are fabricated without solvent additive and with DIO or CBA. Morphology degradation during device aging is investigated. The correlations of the morphology changes during the evaporation of solvent additive and the response of photovoltaic parameters are discussed.

As the residual solvents in the solar cells can induce morphology degradation, performance of the resulting device will be deteriorated, which is presented in Chapter 7. However, if the solvents can be removed in the fabrication process, it is also investigated whether the solvent additives still affect the stability of solar cells. Therefore, in Chapter 8, PffBT4T-2OD:PC$_{71}$BM based solar cells, including without solvent additive and with DIO and CBA, are investigated via in-operando GISAXS/GIWAXS measurements. Due to high temperature spin-coating and thermal annealing, no detectable solvents are left in the assembled device. The morphology and crystallinity of donor polymer are discussed in view of device performances.

At last, the research findings of the present thesis are systematically summarized in Chapter 9. These results provide more approaches and mechanism understanding for further promoting the development of solar cells. Besides, a brief outlook based on these results is given for further studies as well.

2 Theoretical aspects

In this chapter, the theoretical background of polymers, organic solar cells and X-ray scattering are briefly introduced. The basic concepts of polymers, phase separation behavior and polymer conductivity are discussed in section 2.1. The working principles and the architectures of organic solar cells, as well as degradation mechanisms, are presented in section 2.2. The chapter ends with an introduction of X-ray scattering techniques in 2.3, especially on the grazing incidence small/wide angle X-ray scattering.

2.1 Polymer

Polymers are large molecules made up of repeating chemical units known as monomers. These monomer are linked together via covalent bonds to form a new molecule. The monomers combining process is called polymerization. The number of monomers in apolymer is defined as the degree of polymerization. If the molecular weight M is larger than 10 kg/mol, we call it a polymer. Otherwise, it is an oligomer ($M<10$ kg/mol) [50].

In general, polymers present a distribution of the degree of polymerization, rather than a unique molar mass or a unique chain length. Hereby, polymers are usually described by statistical mean values, e.g. the number average molar mass M_n and the average molecular weight M_w.

$$M_n = \frac{\sum_i n_i M_i}{\sum_i n_i} \tag{2.1}$$

$$M_w = \sum w_i M_i = \frac{\sum_i n_i M_i^2}{\sum_i n_i M_i} \tag{2.2}$$

where n_i and M_i represent the macromolecule number and molar mass of component i, respectively. Moreover, the ratio of M_w to M_n is named as polydispersity index (PDI), which describes the width of distribution. PDI is given by

$$PDI = \frac{M_w}{M_n} = U + 1 \tag{2.3}$$

where U is the inconsistency, indicating the distribution width of the molar masses. Where U = 0 means a monodisperse polymer.

2.1.1 Phase separation in polymer blends

For BHJ organic solar cells, donor polymers are directly dissolved with small molecule acceptors to increase the interface areas between donor and acceptor for exciton dissociation. Due to the low miscibility between donor and acceptor on the molecular level, phase separation occurs during the BHJ film formation processing, resulting in a specific morphology for BHJ films. Device performance has a strong correlation with the BHJ morphology. Thereby, many approaches are proposed to control and optimize the BHJ morphology to obtain more effective solar cells. Thereby, understanding the phase separation of the polymer mixture is essential before modifying the BHJ morphology.

Based on a mean field approach, the Flory-Huggins (FH) theory, a thermodynamic model that describes the phase separation behavior of polymer blends, is developed [51,52]. In case of a polymer blend consisting of two different components, the mixing Gibbs free energy (ΔG_{mix}) is applied to describe the phase separation of the mixed polymer components by

$$\Delta G_{mix} = \Delta G_{AB} - (\Delta G_A + \Delta G_B) \tag{2.4}$$

Where ΔG_{AB} the Gibbs free energy of the mixture, and ΔG_A and ΔG_B the Gibbs free energy of the pure components A and B. In a case $\Delta G_{mix} < 0$, the blend state has lower Gibbs free energy, which indicates that the molecules prefer the mixed state. While in case $\Delta G_{mix} > 0$, the blend system possesses a higher Gibbs free energy, suggesting an unstable state in the mixed system. Therefore, phase separation is favored in this blend system. Moreover, ΔG_{mix} can be also expressed by the change of entropy ΔS_{mix} and enthalpy ΔH_{mix} at the given temperature during the mixing

$$\Delta G_{mix} = \Delta H_{mix} - T\Delta S_{mix} \tag{2.5}$$

In two components blend system, ΔS_{mix} and ΔH_{mix} are correlated with the degree of polymerization of the two components (N_A, N_B), the volume ratio of the two components (ϕ_A, ϕ_B) and the FH interaction parameter χ_{AB}. Hence, the mixing entropy (ΔS_{mix}) is described by $-k_B \cdot n \cdot (\frac{\phi_A}{N_A}ln\phi_A + \frac{\phi_B}{N_B}ln\phi_B)$. While the mixing enthalpy is addressed by $k_B n T \phi_A \phi_B \chi_{AB}$. Then the ΔG_{mix} can be written as

$$\Delta G_{mix} = k_B NT(\frac{\phi_A \ln \phi_A}{N_A} + \frac{\phi_B \ln \phi_B}{N_B} + \chi_{AB}\phi_A\phi_B) \tag{2.6}$$

Where k_B is the Boltzmann constant, n the number of molecules on the lattice model of the mean field approach, N the Avogadro number and T the temperature. It can be seen that χ_{AB} is the key relevant parameter to ΔG_{mix}. As $\phi_{A,B} \leq 1$, if $\chi_{AB} < 0$, mixing would always occur in the blend components. Otherwise, it needs to evaluate the degree of polymerization, temperature (T) and χ_{AB} to determine the demixing or mixing state in the solution.

2.1.2 Conductivity in polymers

Polymers are often applied as electrical insulation of cables for electrical devices, as they are usually insulating materials with high resistivities. However, in 1977, it was reported that polyacetylene (PAc) shows significant electric conductivity when dopants are applied (Nobel prize in chemistry in 2000) [10]. It has been found that conjugated polymers possess a wide range of conductivities, which can be tuned by doping from a typical insulator ($<10^{-7}$ S/cm) to a semi-conductor ($<10^{4}$ S/cm) [53, 54]. The electrical conductivity of these polymers usually has a conjugated π-electron system with alternating single and double bonds. The p-orbitals which form the double bonds can overlap to form a delocalized π-system, where the mobility of electrons can be enhanced through the doping process. Electrons move through the delocalized system and so the polymer can conduct.

Band structure and charge carriers
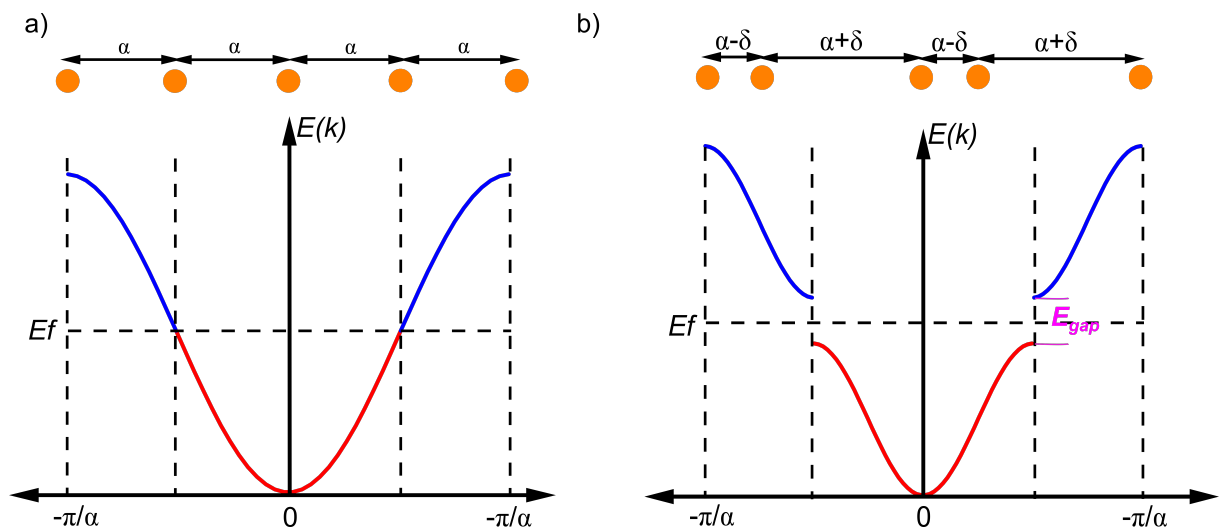

Figure 2.1: *Illustrations of Peierl's instability theorem: band structures and sketches of the 1D chain with (a) all atoms located with a periodic distance of α, and (b) the periodic distance slightly distorted by δ.*
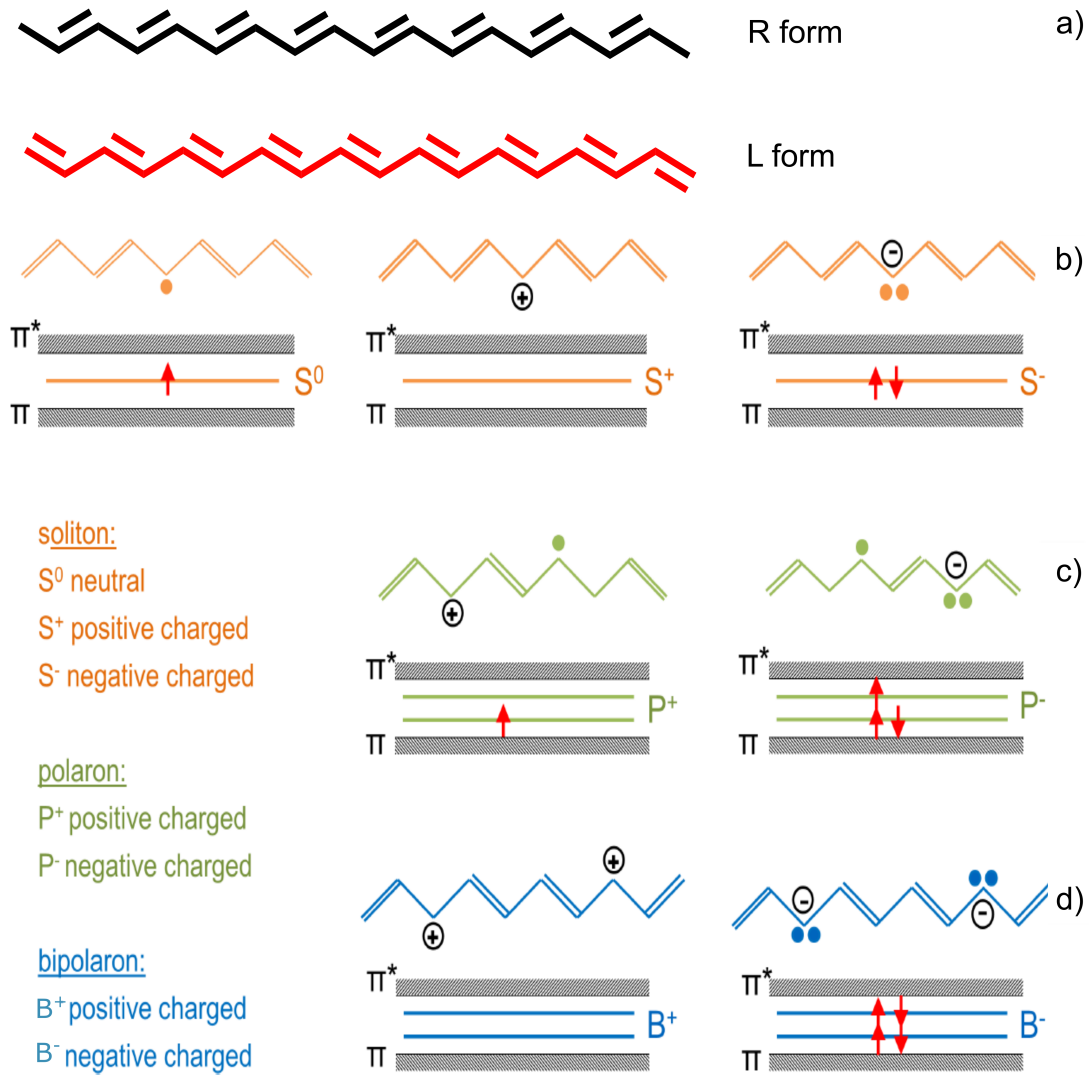
Figure 2.2: *Energetic states of the three quasiparticles for the example of polyacetylene. a) The two mesomeric groundstates of PAc. b) Solitons are shown in their neutral state S^0, positively charged S^+, and negatively charged S^-. c) Polarons are only observed with either a positive P^+ or negative charge P^-. d) Bipolarons are observed with either two positive B^+ or two negative charges B^+. This image is adapted from Ref [55].*

Peierls instability theorem is applied to describe the band structure of polymers with alternative single and double bonds. In this model, one dimension (1D) metal chain has a constant periodic distance a, and the band is half-filled up to Fermi level E_f as illustrated in Figure 2.1a. However, it is not stable that the one-dimensional chain has equally spaced along with one electron per ion in case of conjugation or dimerization. Therefore, the periodic distance is distorted and a bandgap (E_g) is formed to reduce the total energy of the system as depicted in Figure 2.1b. Generally, the E_g of conductive polymers is in

the range from 1.5 eV to 3 eV, which are impacted by many factors, such as the degree of polymerization, crystallinity, or dopants.

To illustrate the principles of conduction mechanisms in conducting polymers, PAc is taken as an example. The chemical structure of PAc is shown in Figure 2.2a. Two corresponding polyene chains R and L (Figure 2.2a) in ground state are interconverted through the involvement of a mobile charge carrier, a soliton. As most conducting polymers lack intrinsic charge carriers, partial oxidation with electron acceptors (i.e. anions) or partial reduction with electron donors (i.e. cations) is required. Therefore, three charged defects, namely solitons, polarons and bipolarons (2.2a), are introduced into the polymer structures as a result of the doping process [56]. At first, solitons are a special type of charged defect that is unique to CPs with a degenerate ground state (e.g. trans-polyacetylene). Solitons can be neutral, positive and negative charged (Figure 2.2b), namely S^0, S^+ and S^-. A neutral soliton (S^0) is created when two degenerate ground states meet. When an electron is removed from the polymer chain, a positive charge is left behind, a positive soliton (S^+) is generated. In contrast, a negative soliton (S^-) is produced by donating an electron to the polymer chain. Polarons are achieved by making the conduction/valence band partially filled. The injection of states into the band gap from the bottom of the conduction band or the top of the valance band results from the creation of negative polarons (P^-) and position polarons (P^+) (as shown in Figure 2.2c). Bipolarons are generated by further addition/removal of another electron resulting in the formation of dianion/dication (as shown in Figure 2.2d).

2.2 Organic photovoltaics (OPV)

Organic photovoltaic (OPV) devices are composed of conductive organic polymers or small organic molecules, for light absorption and charge transport to produce electricity from sunlight by the photovoltaic effect. Compared with silicon-based devices, OPV devices are lightweight, potentially portable and inexpensive to fabricate (roll-to-roll fabrication), flexible, customizable on the molecular level. Additionally, bulk heterojunction (BHJ) solar cells, in which a blend of electron donor and acceptor materials is cast as a mixture, open a field of ultrafast charge transfer. The BHJ of organic solar cells in the present thesis is a blend of a donor polymer and a small molecule. The working principles of organic solar cells are depicted in section 2.2.1. The solar cells are fabricated with forward structure and inverted structure (details in section 2.2.2).
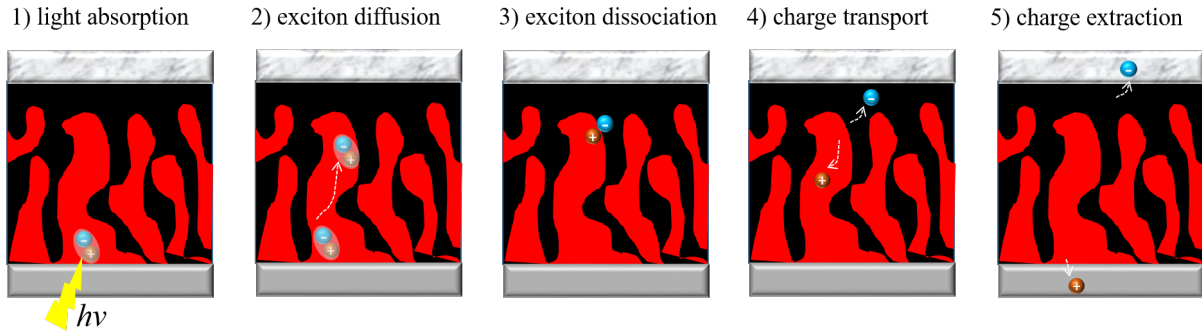
1) light absorption   2) exciton diffusion   3) exciton dissociation   4) charge transport   5) charge extraction

Figure 2.3: *Schematic illustration of the light-electricity conversion process. The red and blue colors indicate the donor and acceptor materials, respectively.*

2.2.1 Working principle of OPVs

In organic solar cells, the BHJ film is the main functional layer, in which the conversion from light to electricity is carried out. Generally, the conversion mechanisms can be described by five steps (as shown in Figure 2.3): 1) light absorption and excitons formation, 2) exciton diffusion and 3) dissociation, 4) charge carriers transport in the corresponding materials and finally (5) collecting free charge carriers at the electrodes.

Light absorption and exciton formation

The presence of a conjugated π electron system in a donor polymer leads to interesting optical and electrical properties. The absorption of light by conductive polymers follows the Lambert-Beer law. When a photon impinges on the donor polymer and the energy of this photo is larger than the band gap of the polymer, resulting in absorption of the photon, then an electron will be excited from the HOMO level to the LUMO level. Simultaneously, a quasiparticle, so-called hole, with equivalent charge exists in the HOMO. The electron and the hole are bound by the Coulomb interaction, which is called "electron-hole pair" or "exciton". The exciton in conductive polymers is considered as Frenkel exciton, having a strong binding of 0.35 eV-0.5 eV.

Exciton diffusion

Upon light absorption, due to the small permittivity ($\varepsilon_r \approx$ 3-4) of materials, singlet excitons are promptly generated in organic polymers instead of free charge carriers. The generated excitons need to diffuse to the interface of donor and acceptor materials to convert to charge carries before recombination. The exciton diffusion length L_D is given

by $L_D = (D_\tau)^{0.5}$, where D is the diffusion coefficient and τ is the exciton lifetime. As the lifetime of excitons in most conjugated polymer films is short (typically less than 1 ns), the diffusion length of the excitons is limited to less than 20 nm [57].

The exciton diffusion in semiconductive polymers is described by two energy transfer processes, namely the trivial energy transfer and the Förster resonant energy transfer. The trivial energy transfer process is prominent in the relative long diffusion distance. A photon is emitted by the donor and then absorbed by the acceptor. Hereby, an exciton is formed in the acceptor. In short, the exciton lifetime is extended through this process [58]. It has been estimated that the rate of trivial energy transfer ($K_{D \to A}^{ET}$) is inversely proportional to the squared distance (R^2) between the acceptor and donor domains:

$$K_{D \to A}^{ET} \propto R^{-2} \tag{2.7}$$

In contrast, Förster resonant energy transfer is dominant in the short diffusion distance. This process is also called as the fluorescence resonant energy transfer (FRET). The energy transfer is resulted by the dipole-dipole coupling between donor and acceptor. The transfer rate $K_{D \to A}^{FRET}$ is given by:

$$K_{D \to A}^{FRET} = \frac{1}{\tau_D} \left(\frac{R_0}{R} \right)^6 \tag{2.8}$$

Exciton dissociation

To generate a photocurrent, the bound electron-hole pairs have to be dissociated to get charge carriers. The excitons can be separated at the interfaces of donor and acceptor, when the energy offset in the lowest unoccupied molecular orbital (LUMO) between donor and acceptor materials that is larger than the Coulomb binding energy of electron and hole. Once the exciton reaches the interface, the dissociation can occur very fast around 10 fs, which is faster than the decay time of an exciton. Two types of exciton dissociation can take place at the interface: (1) electrons are directly transferred from donor to acceptor, or (2) energy is firstly transferred from donor to acceptor, followed by holes are transferred from acceptor back to the donor. However, the exciton dissociation is referred to as polaron pair dissociation, the charge carriers are also called polarons in the molecules. The polaron pairs are still Coulomb bound rather than free. Therefore, to get free charge carriers, further dissociation is needed in the polaron pairs.

Based on two oppositely charged ions with the help of an electric field, the dissociation of polaron pairs is described by the Braun-Onsager model [59,60]. In this model, the field dependent polaron pair separation yield $P(F)$ is given by

$$P(F) = \frac{k_d(F)}{k_d(F) + k_r} \tag{2.9}$$

where $k_d(F)$ is the the possibility of polaron dissociation, k_r is the rate of polaron pair recombination. $k_d(F)$ can be expressed with the mobility: $k_d(F) = \mu\kappa_d$. While k_r is proportional to the life time of polaron pair τ^{-1}. Therefore, the $P(F)$ can be addressed by

$$\mathrm{P}(F) = \frac{\kappa_d(F)}{\kappa_d(F) + (\mu\tau_r)^{-1}} \tag{2.10}$$

Thereby, the polaron separation yield is colsely related to the charge carrier mobility and polaron pair lifetime [61].

Charge transport

The charge carriers can be transported in the ordered crystals freely along the conjugated backbone, which is described by the Su-Schrieffer-Heeger (SSH) theory. The charge transport along the backbone is the most efficient, but it can only produce a microscopic scale of current, as the conducting polymer is not highly ordered. Therefore, it requires that charge carriers must be transported between chains to generate a macroscopic current flow. The transport mechanism between chains is referred to as hopping transport, which typically occurs in the amorphous regions or for crystalline regions with defects and impurities.

The hopping process is also described as electron tunneling and thermal activation. The hopping rate is parametrized by Miller and Abrahams [62]

$$\nu_{ij} = \nu_0 exp(-2\gamma\Delta R_{ij}) \begin{cases} exp\left(-\dfrac{\varepsilon_j - \varepsilon_i}{\kappa T}\right); \varepsilon_j > \varepsilon_i \\ \\ 1; \varepsilon_j \leq \varepsilon_i \end{cases} \tag{2.11}$$

where ν_0 is model prefactor, γ is the inverse localization radius, R_{ij} is the distance between j and i sites. In this model, when the energy of site j is larger than that of the starting site i (upward hopping), the hopping rate is described as Boltzmann-like hopping probability. In contrast, the site j has lower energy, the hopping rate is 1. Furthermore, Miller-Abrahams mode is extended by Bässler via Monte-Carlo simulation to predict the macroscopic hopping transport. In the Bässler model, the mobility μ of macroscopic hopping transport is given by [63]

$$\mu = \mu_\infty exp\left(-\left(\frac{2\sigma}{3\kappa T}\right)^2 + C_{bas}\left(\left(\frac{\sigma}{\kappa T}\right)^2 - \Omega\right)\sqrt{E}\right) \propto exp\sqrt{E} \tag{2.12}$$

The μ_∞ and C_{bas} are model parameters. σ and Ω at the energetic distribution width and a measure of spatial disorder, respectively.

A Gaussian distribution is used to describe the energetic disorder of density of state as shown in Figure 2.4. In this model, the energetic disorder of hopping sites is assumed to be Gaussian distributed with a width of σ. The center of the Gaussian distribution is the so-called transport energy. The center of charge density is below the center of the density of state by $-\sigma^2/\kappa_B T$, which is referred to as an effect of the thermalization of charge carriers. The energy of charge carriers in that gap can be potentially thermalized.
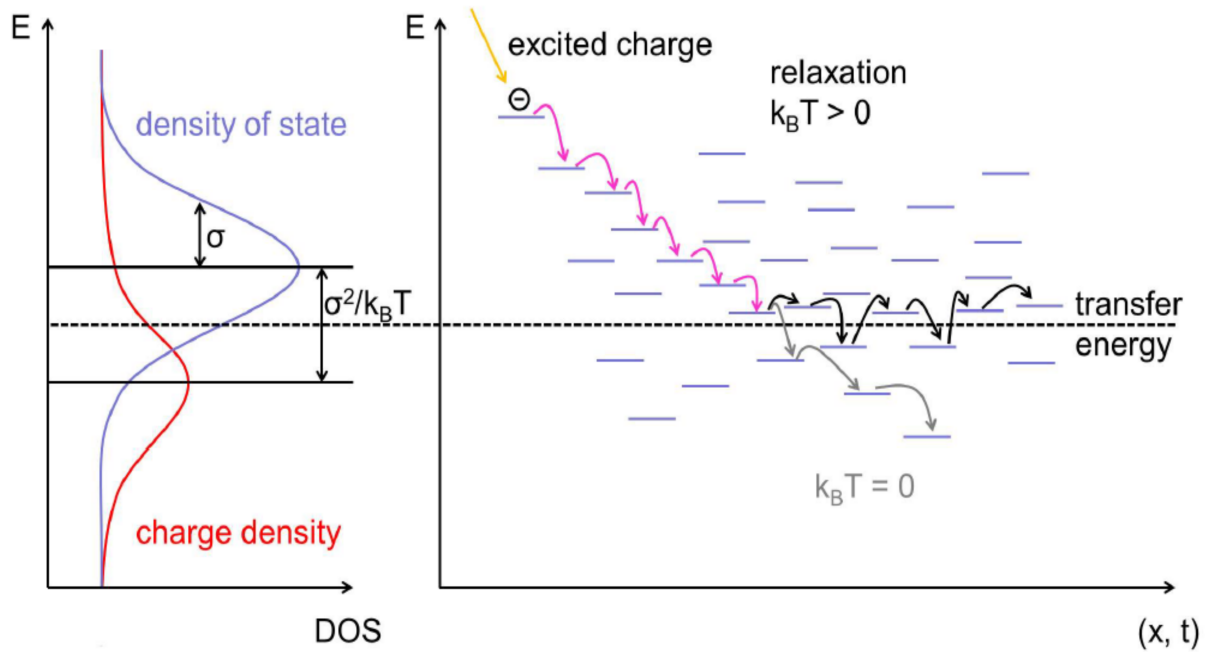

Figure 2.4: *Schematic depiction of hopping transport in a polymer. The total density of states is descibed as a Gaussian distribution in the left image. The red line is the charge density. The transport mechanism is present in the right image. The ecited charge relaxes to a quasi-equilibrium (magenta arrows), and then either hops along the transfer energy with thermal activation (black arrows) or continuously relaxes down to a trap state (grey arrows). Extracted from [34].*

Charge extraction

At last, the charge carriers are needed to be extracted at the corresponding electrodes. In general, it highly depends on accumulation at the interface, the device architecture, the mobility of charge carriers and the energy levels of the device. However, the mechanism behind the charge carrier extraction at electrodes is still under debate. A model, which

combines the the Braun-Onsager model [60] and the Sokel and Huges model [61], is usually applied to describe the extracted photocurrent J_{ph}, expressed by

$$J_{ph} = qP(F)G_{pp}L \left(\frac{exp(\frac{qV}{\kappa T} + 1)}{exp(\frac{qV}{\kappa T} - 1)} - \frac{2\kappa T}{q} \right) \tag{2.13}$$

Where q is the elementary charge, P(F) is the polaron dissociation yield, G_{pp} is the generation rate of polaron pairs, L is the thickness, V is the internal voltage.
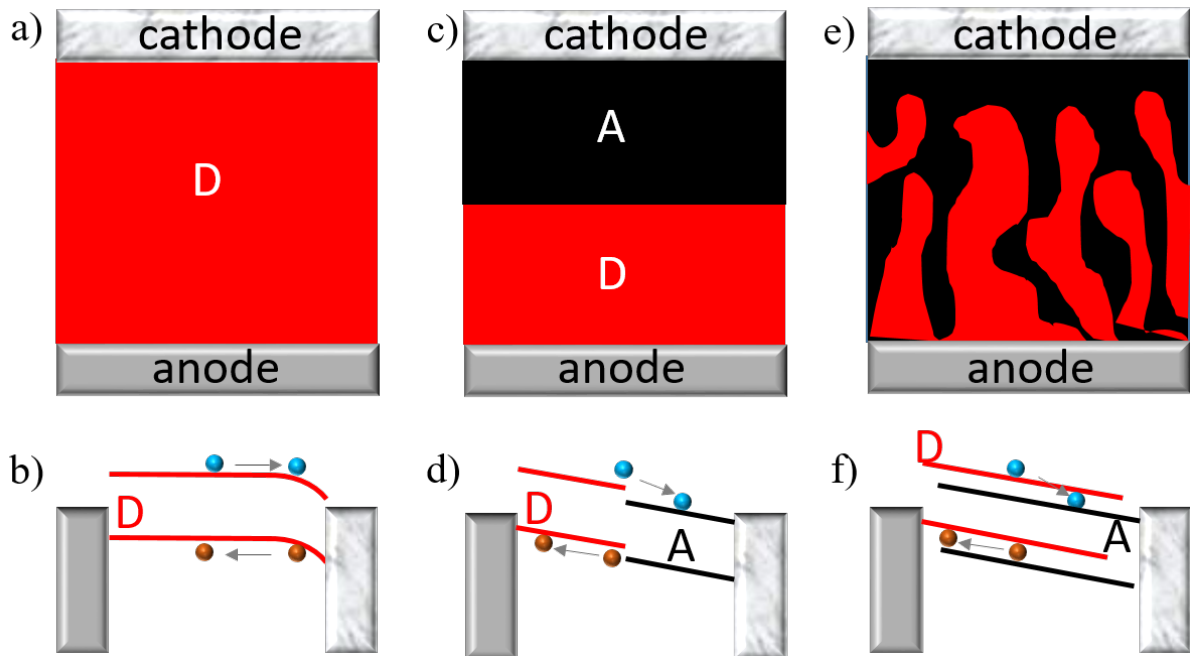
2.2.2 Architecture of organic solar cells

Figure 2.5: *Illustration of OSC archtectures and corresponding schematic band structures. a) and b) single layer cell. c) and d) bilayer solar cell. e) and f) bulk heterojunction solar cells.*

The earliest architecture of OSCs is a sandwich structure, in which the organic molecules layer is placed between two electrodes of different workfunctions (as shown in Figure 2.5 a), also known as single layer solar cells. The difference of work function in the anode and cathode facilitates the movement of charge carriers. A Schottky barrier can be formed between the polymer and the lower work function electrode (see in Figure 2.5 b) [64]. The excitons are separated at the interfaces of the organic layer and the electrodes. However, in such single layer solar cells, charge recombination can easily occur, leading to

a very poor efficiency [65]. Afterwards, the bilayer concept was introduced in the device architecture to reduce the charge transport distance and recombination. It is depicted in Figure 2.5 c, an electron donor layer and an electron acceptor layer, which is sandwiched between the electrodes. In general, the workfunctions of electrodes should match the highest occupied molecular orbital of donor and lowest unoccupied molecular orbital of acceptor [66]. In 1986, the efficiency of a device with bilayer structure had the first breakthrough, which presented the power conversion efficiency (PCE) of approximately 1 % [67]. Due to the limited exciton diffusion length (10 nm - 20 nm), the thickness of the polymer layer is limited. Therefore, the thin polymer film will lead to poor light absorption. Moreover, the interface area between donor and acceptor is very small for the exciton splitting. Thus, a concept of bulk heterojunction (BHJ) was proposed (as shown in Figure 2.5 e), which is aimed to overcome the issue of limited exciton diffusion lengths and limited interfaces between donor and acceptor in organic solar cells. The BHJ layer, an interpenetrating network of donor and acceptor domains, is obtained via demixing of the two components during the fabrication process. Nowadays, BHJ architecture is the most efficient concept and the PCE of BHJ solar cells has been exceeding 15 % [22,68]. The photovoltaic performance of the BHJ solar cells highly depends on the morphology of the BHJ layer. Adequate D/A interfaces and connected charge transport pathways are expected in the BHJ films. The morphology of the BHJ layer can be modified by many methods, such as thermal annealing [69], solvent annealing [70], suitable solvents and solvent additives [71], or molecule modification [72]. To achieve an optimal morphology, a trade-off between forming D/A interfaces and connecting charge pathways exists in the BHJ layer. The exciton dissociation requires fine domains, in which excitons can effectively arrive the D/A interfaces within their lifetime to be separated. However, rather coarse and connected domains are desired for smooth charge transport. Thus, to get a high performance photovoltaic device, it needs to compromise between efficient exciton splitting and charge transport.

Conventional and Inverted Geometries

The organic solar cells can be fabricated in either conventional or inverted geometry. Figure 2.6a presents the conventional structure of photovoltaic devices. The transparent conductive layer (TCL) of indium tin oxide (ITO) or fluorine doped tin oxide (FTO), deposited on the top of the glass, acts as the anode in these solar cells. Then an electron blocking layer (EBL), such as PEDOT:PSS, tungsten oxide (WO_3), molybdenum oxide (M_OO_3), is applied to help the charge extraction and reduce the charge recombination. Thus, the work function of the EBL needs to be located between the one of the TCL and the HOMO level of donor. Afterwards, a BHJ layer is followed, where the light is
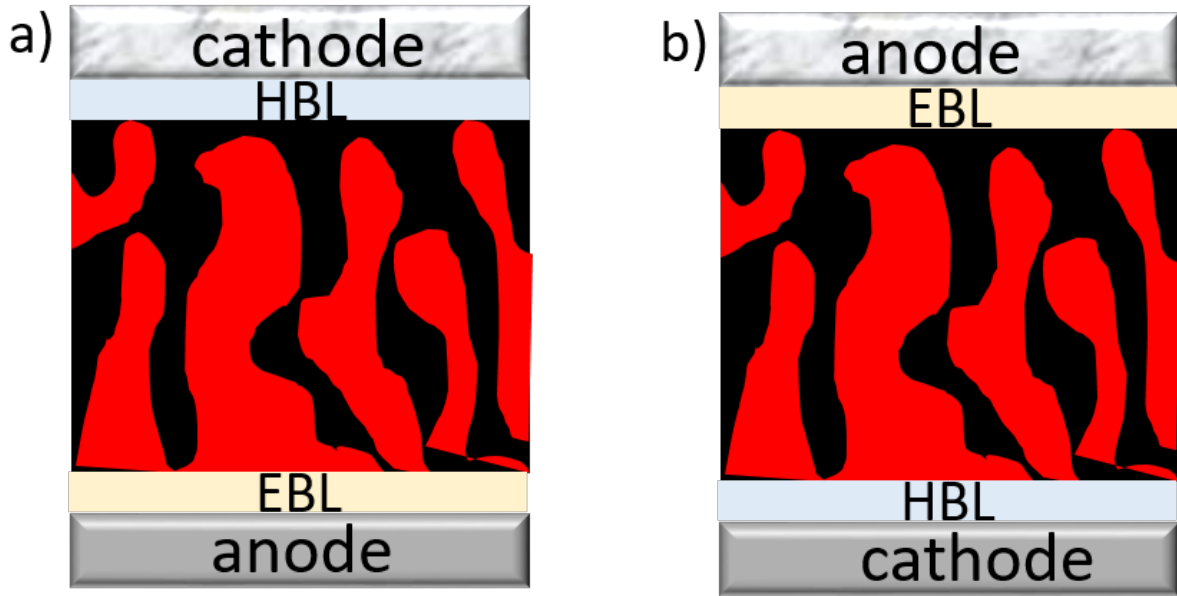
Figure 2.6: *Schematic architecture of an organic solar cell in a) conventional and b) inverted geometry. Layer stack with anode/cathode, electron blocking layer (EBL)/hole blocking layer(HBL), bulk heterojunction layer (BHJ), HBL/EBL, and metal cathode/anode.*

absorbed and the charge carriers are generated. The working principles are introduced in detail in section 2.2.1. On the top of the BHJ layer, the hole blocking layer (HBL), e.g. LiF, is optionally chosen to improve the charge extraction and transport. At last, the metal electrode with low work function, such as Al, is evaporated on the top, acting as the cathode. In the inverted geometry, the TCL and metal electrode layer now act (Au, Ag or Al) as cathode and anode, respectively. A ZnO or TiO_2 layer is applied on the TCL to act as the HBL. A EBL is deposited on the BHJ layer. It has been found that the devices with inverted architecture present a longer lifetime. [49]

2.2.3 Degradation mechanisms of organic solar cells

Low stability strongly limits the further development of organic solar cells. Without encapsulation devices could fully degrade in 24 hours. In general, the various degradation processes occurring in OSCs can be roughly divided into two types, namely chemical and physical degradation [38, 73]. The chemical degradation is mainly attributed to the reaction between water and oxygen with the materials in the device. If devices are in oxygen and moisture atmosphere, oxidation of the low work function metal by oxygen or oxidation by water could occur in the device, which will lead to contact delamination and reduce the

effective contact area of the metal electrode. Thus, the TCL and metal electrode can be corroded via the chemical/electrochemical reactions, resulting in impurity diffusion into the BHJ layer. Moreover, oxygen and water can diffuse through the device via pinholes in the metal electrode or the porous substrates [73, 74]. Besides, photochemical reaction in the BHJ is a big issue inducing the device degradation. If the device is exposed to oxygen and water during the illumination, the oxidation of donor polymer can be triggered by light [75–77]. Furthermore, the light may induce the rearrangement/break of C-H or C-O-C bands, leading to more defects in BHJ film, especially at the interfaces of donor and acceptor [78–80]. Typically some defects cause a decrease of V_{OC}.

In contrast, physical degradation is considered to arise mainly from the morphology deterioration of bulk heterojunction (BHJ) films. It has been reported by Schaffer et al. that the polymer domains (P3HT) are getting coarse during the long-term photovoltaic characterizations, resulting in the loss of short circuit current [39]. For another BHJ system, the evaporation of residual solvent additive during the operation time induces a shrinkage of polymer domains (PCPDTBT), resulting in more traps in the BHJ layer and a decay of fill factor [40]. However, what drives the morphology changes in the BHJ layer still needs to be further explored, which is the main topic of the present work.

2.3 Scattering techniques

As discussed in section 2.2.1, the BHJ morphology plays a critical role in the photovoltaic device performance. In general, real-space imaging techniques, like SEM and AFM, can only provide the surface morphology, which is not sufficient to represent the whole morphology of the BHJ film. Therefore, X-ray scattering techniques are applied to investigate the inner morphology of thin films with a resolution up to a few to hundreds of nanometers. The scattering measurements are non-destructive and of high statistical relevance. Moreover, the high brilliant X-ray source of a synchrotron makes it possible to follow changes with time with high time resolution via scattering methods, such as in-operando experiments in chapter 7 and 8. The scattering principles are discussed in section 2.3.1. Next, grazing incidence small and wide angle x-ray scattering (GISAXS/GIWAXS) are introduced in section 2.3.2 and 2.3.3, respectively.

2.3.1 Scattering basics

X-rays are electromagnetic waves with a wavelength ranging from 0.01 nm to 10 nm. The electric field $\vec{E}(\vec{r})$ can be expressed as a plane electromagnetic wave

$$\vec{E}(\vec{r}) = \vec{E}_0 \exp(i\vec{k}_i\vec{r}) \tag{2.14}$$

where $\vec{E}_0$ describes the polarization and amplitude of the electric field, $\vec{k}_i$ is the wave vector and $\vec{r}$ is the position vector. The propagation of such an electromagnetic wave through a medium with position dependent refractive index $n(\vec{r})$ can be described by the Helmholtz equation [81]

$$\Delta\vec{E}(\vec{r}) + k^2 n^2(\vec{r})\vec{E}(\vec{r}) = 0 \tag{2.15}$$

In the present thesis, exclusively elastic scattering phenomena are considered, in which the kinetic energy is conserved, but its direction of propagation is modified. The modulus of the scattering wave vector $k_i = |\vec{k}_i| = |\vec{k}_f| = \dfrac{2\pi}{\lambda}$ keeps constant, where λ is the wavelength of the radiation. As in equation 2.16, the refractive index is described with a real and an imaginary part, corresponding to the dispersion ($\delta(\vec{r})$) and absorption($\beta(\vec{r})$) of the material, respectively

$$n(\vec{r}) = 1 - \delta(\vec{r}) + i\beta(\vec{r}) \tag{2.16}$$

where the dispersion and absorption parts can be respectively written as

$$\delta(\vec{r}) = \frac{\lambda^2}{2\pi}\rho(\vec{r}) = r_e\frac{\lambda^2}{2\pi}\rho_e(\vec{r}) \tag{2.17}$$

$$\beta(\vec{r}) = \frac{\lambda^2}{2\pi}\mu(\vec{r}) \tag{2.18}$$

whereby $\rho = r_e\rho_e$ is the scattering length density (SLD) of the penetrated medium, and $r_e = 2.814 \times 10^{-5}$ $\mathring{A}$ is the classical electron radius, ρ_e is the electron density of the investigated materials, and μ is the mass absorption coefficient of the studied material. The contrast between two phases within the same film is addressed by

$$\Delta\delta^2 + \Delta\beta^2 = (\delta_1 - \delta_2)^2 + (\beta_1 - \beta_2)^2 \tag{2.19}$$

where the subscripts 1 and 2 indicate the two phases. According to equation 2.16, 2.17 and 2.18, the scattering contrast in X-ray scattering experiments depends on the difference in electron density.

The scattering geometry is schematically depicted in Figure 2.7. The X-ray beam impinges on a sample with an incident angle α_i, then the reflected beam exits the sample with an angle α_f. If $\alpha_f = \alpha_i$ and the beam stays in the xz-plane, it is called specular reflection (2.7a). If the reflected beam with an additional angle ψ_f presents in the xy-plane, as shown in 2.7b, it is known as diffuse scattering. The momentum transfer of the scattered beam is described by the scattering vector $\vec{q}$:

$$\vec{q} = \vec{k_f} - \vec{k_i} \tag{2.20}$$

The X-ray beam can be also transmitted after interacted with the material with an angle α_f, shown in Figure 2.7a. The angle of the transmitted beam depends on the incident angle and the refractive indices (n) of the studied material, expressed by Snell's law:

$$n_0 \cos(\alpha_i) = n \cos(\alpha_t) \tag{2.21}$$

where $n_0 = 1$ is the refractive index of air. if $\alpha_t = 0$, indicating that the beam is totally reflected. In this case, the incident angle is taken as the critical angle (α_c) of the material. With the small angle approximation, the critical angle is written as:

$$\alpha_c \approx \cos(\alpha_c) = n \cos(\alpha_i) \approx \sqrt{2\delta} = \lambda\sqrt{\rho/\pi} \tag{2.22}$$

Therefore, the incident angle determines the X-ray scattering depth during the scattering measurements. If $\alpha_i < \alpha_c$, the X-ray beam is completely reflected and the scattering depth is around several nanometers. In case $\alpha_i > \alpha_c$, the beam can penetrate the whole film, thus the diffuse scattering signal originates from a relatively large sample volume.
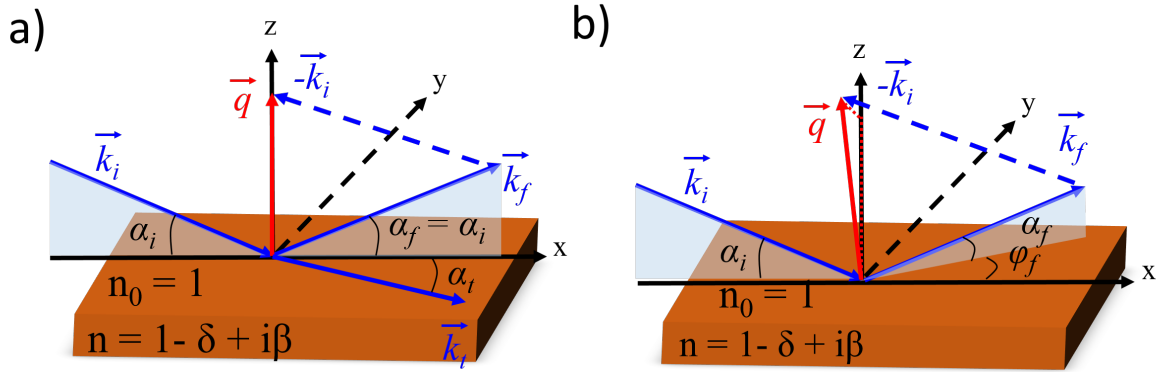

Figure 2.7: *Basic definitions of angles and directions in the geometry of a) specular scattering and b) diffuse scattering.*

2.3.2 Grazing incidence small angle X-ray scattering (GISAXS)

GISAXS is a powerful technique to probe thin film structures on a length scale ranging from several nanometers up to micrometers. The X-ray beam impinges on the sample with a shallow angle to ensure large footprints on the sample. Thus, good statistics data and high-intensity signals can be obtained over large sample areas despite the low film

thickness. In the present work, the X-ray scattering is considered as elastic scattering, which means the absolute value of the incoming and exiting photon momenta is conserved. In GISAXS experiments, the diffuse scattering of X-rays after interaction with investigated films is collected. The scattering geometry is shown in Figure 2.7b. The scattering vector $\vec{q}$ is given by [82]

$$\vec{q} = \frac{2\pi}{\lambda} \begin{pmatrix} q_x \\ q_y \\ q_z \end{pmatrix} = \frac{2\pi}{\lambda} \begin{pmatrix} \cos(\alpha_f)\cos(\psi) - \cos(\alpha_i) \\ \cos(\alpha_f)\sin(\psi) \\ \sin(\alpha_f) + \sin(\alpha_i) \end{pmatrix} \tag{2.23}$$

The diffuse scattering is commonly described in the distorted wave Born approximation (DWBA) [83, 84], in which the scattering is considered as the perturbation of an ideal system. In the ideal system, the interfaces are perfectly smooth, the perturbations are the film roughness and the lateral structures. Therefore, within the DWBA, the scattering cross-section can be expressed as

$$\frac{d\sigma}{d\Omega} = \frac{S\pi^2}{\lambda^4}\left(1 - n^2\right)^2 \mid T_i \mid^2 \mid T_f \mid^2 P_{diff}(\vec{q}) \propto P_{diff}(\vec{q}) \tag{2.24}$$

being S the illuminated area, and $P_{diff}(\vec{q})$ the diffuse scattering factor [85]. T_i and T_f are the Fresnel transmission coefficients of the incoming and scattered beam respectively, which can reach a maximum at the critical angle of the investigated material. Thus, the maximum intensity at α_c is called material sensitive Yoneda peak [86]. Therefore, in the present thesis, horizontal line cuts of GISAXS are performed at the Yoneda peak of study materials. Thereby, $T_{i,f}$ is an overall scaling factor of the scattering intensity and the intensity of the scattered wavevector is proportional to the diffuse scattering factor $P_{diff}(\vec{q})$.

$P_{diff}(\vec{q})$ is described with two terms, namely the form factor of each object $F(\vec{q})$ and the structure factor $S(\vec{q})$:

$$P_{diff}(\vec{q}) \propto N|F(\vec{q})|^2 S(\vec{q}) \tag{2.25}$$

where N is the number of scattering objects with random orientation. The form factor $F(\vec{q})$ is the Fourier transform of the electron distribution of the objects, and the structure factor $S(\vec{q})$ refers to the distance of objects, which is approximated by a one-dimensional paracrystalline lattice (1DDL) [87].

Within the framework of DWBA, four different types of scattering events can occur [55]. As shown in Figure 2.8, radiation can be directly scattered at the object(2.8a), and first reflected on the substrate, then scattered on the object (2.8b), and first scattered on the objects, then reflected on the substrate (2.8c), and reflected on the substrate, followed by scattering on the object, and then reflected on the substrate (2.8d). The local

monodisperse approximation (LMA) is applied to describe the distribution of sizes, which is considered as a Gaussian distribution. In the approximation, it is assumed that the objects of the same sizes are spatially grouped together, hereby coherent scattering is only allowed for the same objects, which indicates that different objects are independent and therefore the final scattering intensity is contributed by a sum of that of each objects [88].
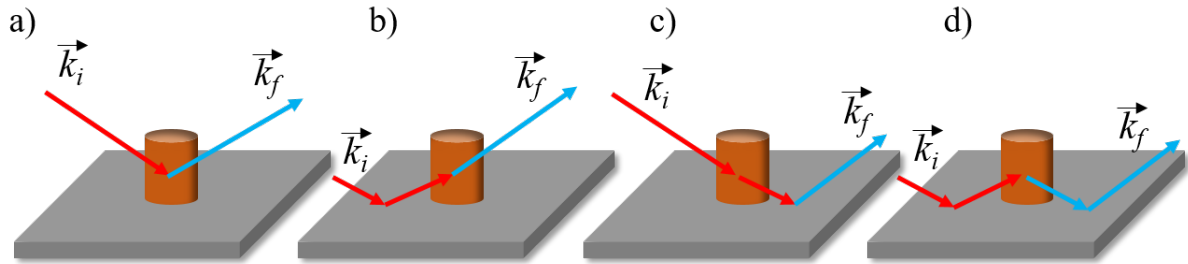

Figure 2.8: *Schematic description of four type scattering contributions in the DWBA. a) directly scattered beam, b) first reflected, then scattered beam, c) first scattered, then reflected beam, d) reflected - scattered - reflected beam.*

2.3.3 Grazing incidence wide angle X-ray scattering (GIWAXS)

Grazing incidence wide angle X-ray scattering (GIWAXS) is quite similar to GISAXS but with a much shorter sample-detector distance. Thus, the scattering signal at large q-values can be observed, which is corresponding to the structures with sub-nanometer scales. In GIWAXS measurements, the incident angle is fixed with a small angle, which is larger than the critical angle of the investigated material but smaller than that of the substrate to avoid the scattering from the substrate. In the present thesis, GIWAXS is applied to investigate the crystallinity of donor polymers in organic photovoltaic films.

The origin of the scattering intensity in GIWAXS is the same as the typical diffraction. As shown in Figure 2.9a, the atoms in a crystal lattice provide the scattering center and are considered as periodic gratings for X-rays. The incoming X-ray beams with an incident angle of Θ scatter at the periodic lattice plane. Then the exiting beam is deflected by an angle of 2Θ versus the incoming beam. If the optical path difference $\Delta\lambda$ between two waves is a multiple of the full wavelength, a diffraction maximum appears, which is called constructive interference. The lattice plane distance (d) can be obtained via Bragg's equation:

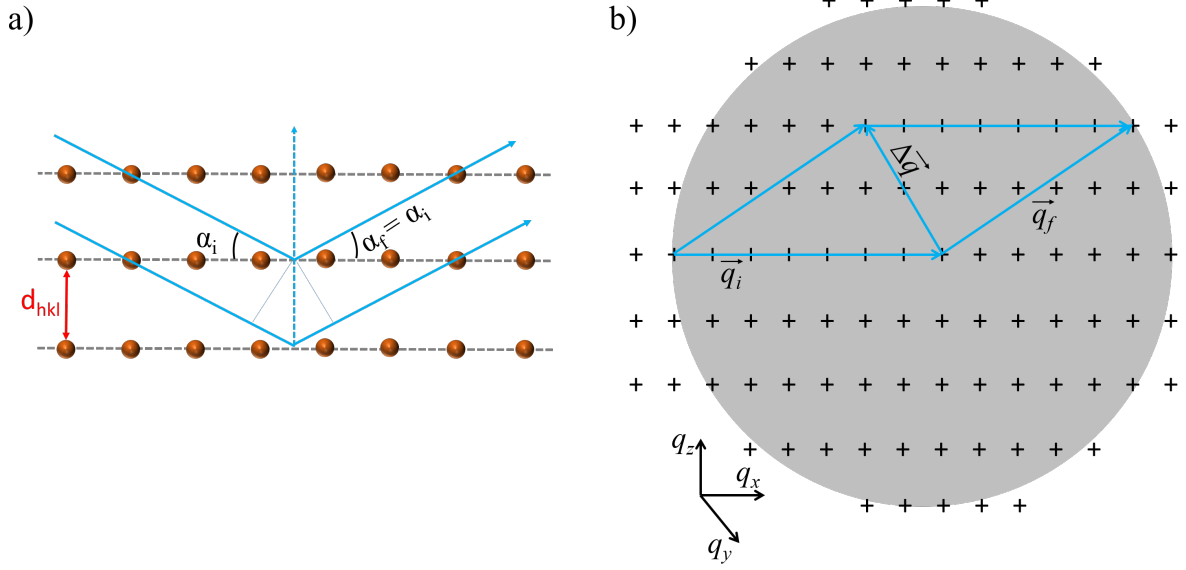$$d = n\frac{2\pi}{q} = \frac{n\lambda}{2sin(\theta)} \tag{2.26}$$

Figure 2.9: *Sketch of X-ray diffraction and Ewald's sphere. a) a description of Bragg's law: the incoming beam scatters at a hkl-plane. b) Construction of the Ewald's sphere: Diffraction patterns occur when the momentum transfer vectors fulfill the Laue condition.*

Figure 2.9b shows that the diffuse scattering signal comes at a fixed incident beam k_i, the scattered wavevector k_f describes a sphere in reciprocal space, the so-called Ewald sphere, and the reciprocal lattice points are described as +-signs. to get the observable scattering, the momentum transfer vectors must fulfill two conditions: 1) starting and ending on the surface of the Ewald's sphere; 2) satisfying the Laue condition $\vec{q} = \vec{G}$. In GIWAXS, the small-angle approximation is no longer valid, which means that the outgoing radiations are no longer decoupled from each other. The momentum transfer $\vec{q}$ is projected onto a flat detector in two dimensions, which is depicted by q_y and q_z directions. However, both of them contain a non-negligible contribution of q_x direction. Therefore, the raw GIWAXS images contain a distortion, which is induced by the conflict between the spherical and flat hypersurfaces of the Ewald's sphere and the flat crystalline planes. To properly present GIWAXS data, the $\vec{q}$ map is displayed with q_z versus q_r, where $q_r = \sqrt{q_x^2 + q_y^2}$. This is the so-called χ-correction, and more details can be found in the literature [89, 90].

In the present thesis, GIWAXS measurements are applied to detect the crystallinity of donor polymers. It can be found in Chapters 5, 6 and 8 that the out-of-plane (100) Bragg peak is prominent for the studied polymer. Therefore, the evaluation of the polymer crystalline state is based on this peak. The correlated cuts are performed on the GIWAXS images, then the peaks are fitted by Gaussian functions to extract the peak position, the

peak full width at half maximum value (Δ_{FWHM}) and peak intensity. The crystalline size L is calculated via the Scherrer equation

$$L = \frac{K\lambda}{\Delta_{FWHM}cos(\theta)} \tag{2.27}$$

where $K \approx 0.9$ is the Scherrer form factor, varying with the shape of the crystallites [91].

3 Characterization methods

In the present chapter, all characterization techniques, adopted to probe BHJ films, solar cells and interfaical layers, are described with instrument specifications, working principles and the principles of data analysis. The absorption characteristics of thin films are probed by spectroscopic methods. The surface and inner structures of BHJ films are detected via real–space and reciprocal–space techniques, respectively. The film's surface energies are determined by measuring contact angles.

3.1 Optical microscopy (OM)

Optical microscopy (OM) is utilized to evaluate the device area out of solar cells and the surface morphology of BHJ films. The measurements are carried on an Axiolab A microscope from Carl Zeiss, which is equipped with objectives for 1.25, 10, 50 and 100–fold magnifications. A PixeLink PL-S621CU CCD sensor (1280 × 1024 pixels, 8.52 mm sensor diagonal) is mounted to record digital micrographs. The real–space distance can be calculated based on the resolutions per pixel, provided in Table 3.1. In this thesis, the samples are imaged at the magnifications of 1.25. The images are analyzed by using ImageJ [92].

magnification	resolution [μm/pixel]
1.25	6.26
2.5	3.11
10	0.82
50	0.17
100	0.082

Table 3.1: *Resolution of the optical microscope for various magnifications.*

3.2 Contact angle

The most common method for the calculation of the surface free energy (SFE) of solids is utilizing the results of contact angle measurements, which is first described by Thomas Young in 1805. It is a common method for determining the interaction energy between a liquid (L) and a solid (S) [93]. The equilibrium contact angle of a droplet placed on a smooth surface is determined by the interfacial tensions through Young's relation (Figure 3.1):

$$\gamma_{SV} = \gamma_{SL} + \gamma_{LV} \cos(\theta) \tag{3.1}$$

where γ_{SV} (mN/m), γ_{SL} (mN/m) and γ_{LV} (mN/m) are the solid-vapor, solid-liquid and liquid-vapor solid-liquid interfacial tensions respectively. θ is the contact angle.
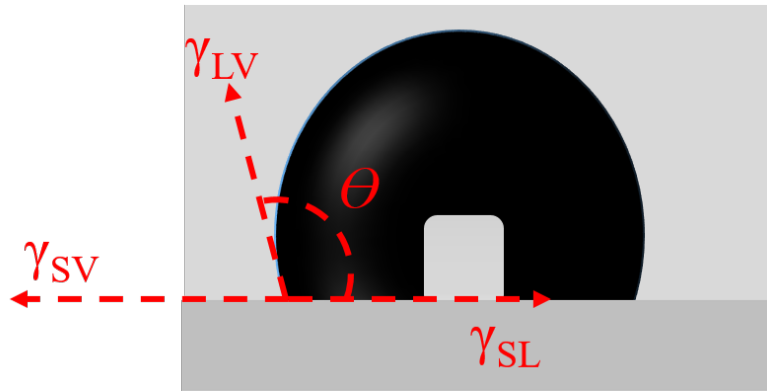

Figure 3.1: *Schematic representation of the Young's equation*

For the static case, Dupre later expressed the work of adhesion (W_{adh}) between a solid and a liquid, which is in terms of the surface tension and equals the change in free energy of the system [93, 94]. The equation for work of adhesion can be written as

$$W_{adh} = \gamma_{SV} + \gamma_{LV} - \gamma_{SL} \tag{3.2}$$

when combined with Young's relation, gives the Young-Dupre equation [95]:

$$W_{adh} = \gamma_{LV}(1 + \cos(\theta)) \tag{3.3}$$

In this present work, the acid-base model is applied to do surface energy calculation. The solid-liquid interfacial tension is represented by the expression

$$\gamma_{SV} = (\sqrt{\gamma_{SV}^{LW}} - \sqrt{\gamma_{LV}^{LW}})^2 + 2(\sqrt{\gamma_{SV}^{+}} - \sqrt{\gamma_{LV}^{+}})(\sqrt{\gamma_{SV}^{-}} - \sqrt{\gamma_{LV}^{-}}) \tag{3.4}$$

where γ^{LW} stands for the Lifshitz-van der Waals interaction. γ^{+} and γ^{-} are Lewis acid and base components, respectively.

Contact angle measurements are carried out using a First Ten Angstroms FTA200 goniometer, which is equipped with a 360 frames per second camera, a focused microscope, a dispense pump and a tip Z control. For each different surface, contact angles were collected using four different probe liquids: diiodomethane, water, ethylene glycol and formamide. The volume of solvent drops is controlled at 0.4 μL and contact angles of a minimum of 8 droplets are recorded. Each drop was allowed to equilibrate for 15 s until a stable contact angle was reached.

3.3 UV-Vis Spectroscopy

Ultraviolet-Visible (UV-Vis) spectroscopy is applied to probe the absorption of light of solid BHJ films in the ultraviolet-visible spectral region, providing the information about the energetic levels of materials. The measurements presented in this work were carried out on a Lambda 35 spectrometer by PerkinElmer. The spectrometer is equipped with a deuterium lamp and a tungsten halogen lamp, which generate UV light in a wavelength range of 190 nm - 326 nm and light in the visible and near infrared spectrum (326 nm - 1100 nm), respectively. The lamps are automatically switched at the wavelength of 326 nm. The generated light is monochromatized by an optical grating. Subsequently, the monochromatic beam is equally split into two beams of which one probes the sample and the other one detects a reference sample. At last, the transmission intensity of both beams is detected by two photodiodes. To obtain the absorbance (A) from transmission spectrum, the Lambert-Beer law is applied

$$A(\lambda) = -log_{10}\Big(\frac{I_t(\lambda)}{I_0(\lambda)}\Big) = a(\lambda)Llog_{10}e \tag{3.5}$$

$I_t(\lambda)$ is the transmitted intensity of probed the sample and $I_0(\lambda)$ is the transmitted intensity of reference sample.$\alpha(\lambda)$ is the specific absorption coefficient, L is the light path length through the sample, and e is the Euler's number.

ITO-coated glass substrates are used to support the measured films in the present work. Scanning speed of 120 nm/min is applied with a wavelength resolution of 1 nm.

3.4 Time-of-Flight secondary ion mass spectrometry (TOF-SIMS)

TOF-SIMS depth profiles are used to probe the polymer gradient in BHJ films in Chapter 6. The experiments were performed using an ION-TOF TOF.SIMS 5-100 (ION-TOF

GmbH, Münster, Germany) equipped with two ion sources, having a base pressure better than 5×10^{-9} mbar. During depth profiling, both beams hit the target at an angle of 45°. Bi$^+$ ions were used as the analytical source, operated at 25 kV; Cs$^+$ ions were used as the sputtering source, operated at 500 V, with an ion current of 20 nA. By alternating these two ion beams on samples, depth profiles were generated. The craters sputtered were about 300×300 μm^2, while acquisition areas of profiles were 40×40 μm^2 in the centers of the craters.

3.5 IV characterization

Organic photovoltaics are generally characterized by current-voltage analysis. Solar cells are measured under dark and illumination conditions, respectively. For dark measurements, an external bias is applied on the device to exam the diode properties of respective devices. However, for illumination tests, external bias and simulated sunlight (AM 1.5, 100 mW/cm^2) are both applied to solar cells. The generated electric current is recorded by a computer-controlled Keithley 2400 source meter.

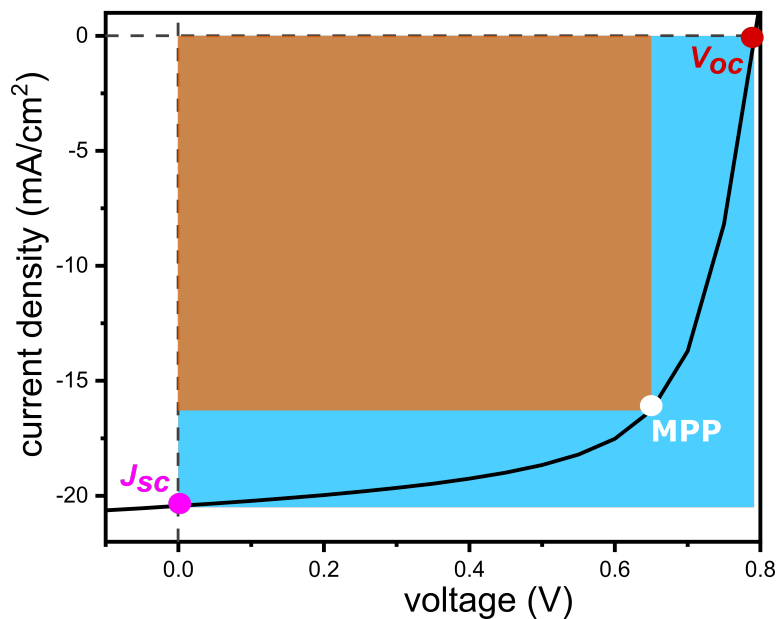**Figure 3.2:** *An exemplary J-V curve of an organic solar cell. The V_{OC}, J_{SC} and maximal power point (MPP) are indicated by a red dot, a purple dot and a white dot, respectively. The orange and blue rectangles indicate the maximal output power and the theoretical maximal output power, respectively. The FF corresponds to the ratio between the grey and blue areas.*

Photovoltaic performance of solar cells is quantified by the parameter called power conversion efficiency (PCE). The PCE is impacted by the device characteristic photovoltaic

parameters, namely the short-circuit current density at $V = 0$ V (J_{sc}) (see Figure 3.2), the open-circuit voltage at $I = 0$ A (V_{oc}) (see Figure 3.2), the fill factor (FF), the serial resistance at $I = 0$ A (R_s) and the shunt resistance at $V = 0$ V (R_{sh}). The FF is the ratio of the power at the maximum power point (MPP) (indicated by violet rectangle) and the theoretically maximum possible power of $P_{max} = V_{oc}J_{sc}$ (indicated by blue rectangle), is given by

$$FF = \frac{P_{MPP}}{P_{max}} = \frac{V_{MPP}J_{MPP}}{V_{oc}J_{sc}} \tag{3.6}$$

The PCE is defined as the ratio of the device output power (P_{MPP}) and the irradiation input power (P_{in}). Thus, PCE can be given by

$$PCE = \frac{P_{MPP}}{P_{in}} = \frac{V_{oc}J_{sc}FF}{P_{AM1.5}} \tag{3.7}$$

with P_{in}(AM 1.5) $= 100$ mW/cm^2.

In the present work, the light intensity is calibrated by measuring the light power via a thermopile (XLP12–3S–H2) or by a silicon-based calibration solar cell (WPVS Reference Solar Cell Typ RS-ID-3 by Fraunhofer ISE) before *J-V* measurements. The bias voltage *V* is swept from -1.5 V to 1 V with a 0.05 V increment. Each device is performed in sequence with one dark and several light measurements to sort out the best device performance. For an in-operando measurements in Chapters 7 and 8, the devices are tested in a loop to track the evolution of photovoltaic parameters along with time.

3.6 Atomic force microscopy (AFM)

Atomic force microscopy (AFM) is a high-resolution scanning probe microscopy with three major abilities, namely force measurement, imaging, and manipulation. In Figure 3.3, a schematic overview of the AFM instrument is shown which consists of a cantilever with a sharp tip at its end that is used to scan the sample surface. When the tip is scanning the sample, forces between the tip and the atoms, molecules and crystals on the sample surface will lead to a deflection of the cantilever according to Hooke's law [96]. According to the different interactions between tip and sample, three main scanning modes, which are contact mode, tapping mode and non–contact mode, are developed. In the present thesis, AFM is used to investigate the surface morphology of BHJ films. The measurements are performed in tapping mode using a Digital Instruments/Veeco multimode tapping atomic force microscope. The tip positioned on the cantilever has a curvature radius of 7 nm. The spring constant of the cantilever (OMCL–AC240TS–R3, Asylum Research) is 2
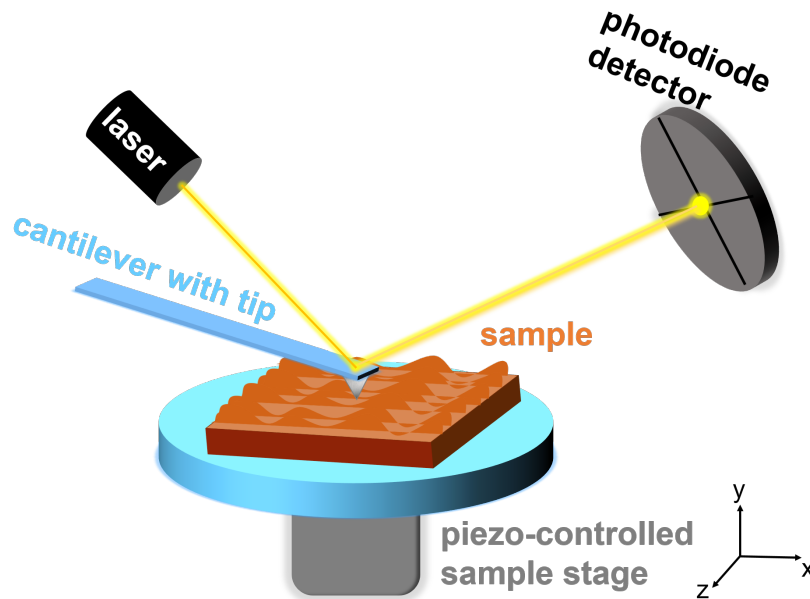
Figure 3.3: *A simplified sketch of the AFM set–up. The cantilever with a tip performs scan over the sample surface, which is placed on a piezoelectric sample's stage. The deflection of the cantilever is measured by a laser beam and the reflected beam is detected by a photodiode detector.*

Nm^{-1} with a resonance frequency of 70 kHz. The cantilever is firstly driven to oscillate close to its resonance frequency. Then the cantilever is brought downwards till the tip is very close to the film surface. Afterwards, the tip touches the film surface repeatedly during the taping mode operation. Due to the film's surface structure and roughness, the interaction between molecules on the film surface and the tip changes with scanning time. Therefore the amplitude of the oscillating cantilever changes, which can be detected by the reflected laser beam shown in Figure 3.3. The laser beam gets reflected a second time at a mirror and then detected by a position–sensitive photodiode detector which consists of four segments. In this way, the height and phase images are recorded based on the stage's motion. The collected data are analyzed using the open source software Gwyddion [97].

3.7 X-ray reflectivity (XRR)

X-ray reflectivity (XRR) is a scattering technique based on the specular reflection of X-rays to obtain the vertical structure and composition of thin film samples in reflection geometry. The working principle of this technique is to reflect a beam of x-rays from a flat

surface and to measure the intensity of x-rays reflected in the specular direction (reflected angle equal to incident angle). More details related to the theoretical aspects of XRR are provided in section 2.3.

In this present work, XRR measurements are performed to obtain film thickness and polymer density with a Bruker D8 ADVANCE X-ray Reflectometer. Figure 3.4 illustrates that the XRR instrument consists of three main parts, namely X-ray source, sample stage and detector. The X-ray beam, generated by a copper Kα- source operated at 40 kV and 40 mA, has a wavelength of 0.1541 nm. To avoid over illumination on the samples, a knife-edge cutter is applied over the sample with a short edge–to–surface distance. The incoming beam is collimated with a 0.2 mm slit and the exiting beam is collimated with a 0.2 mm and a 0.05 mm slit. Measurements are done with a Θ-2Θ mode by moving both source and detector. The obtained XRR data is analyzed with the aid of the MOTOFIT package for IGOR [98].
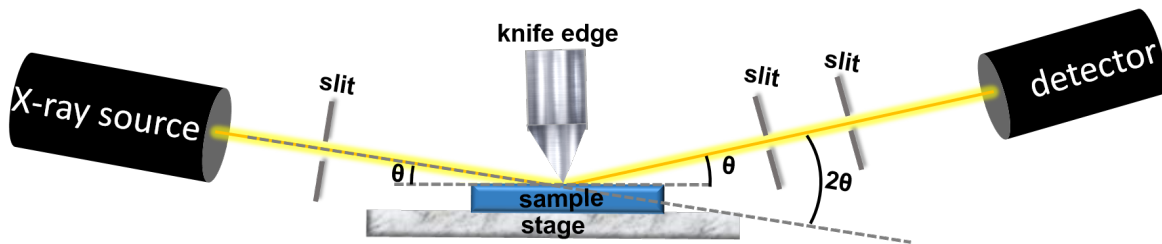

Figure 3.4: *Schematic overview of XRR set–up. The generated X-ray beam guided by a slit before impinging onto the film surface at certain angle θ. The reflected X-ray beam is collected by a point detector at an exit angle of 2θ. A knife edge is placed close to the sample surface to avoid overillumination at small angle.*

3.8 Grazing-incidence small-angle X-ray scattering

Grazing incidence small angle X-ray scattering (GISAXS) is a non-destructive measurement technique that provides lateral structure information from the film on a large range of length scales approximately between 1 nm and 1 μm. In contrast to AFM and OM, it is possible to probe the inter structures of the film volume. A schematic view of the grazing-incidence geometry is shown in Figure 3.5, where the X-ray beam impinges the film under a shallow angle. The incident angle is set to be above the critical angles of target materials in the probed film, but normally below 1°. The photons are scattered elastically by the film volume. The GISAXS measurements need a long sample-detector distance (SDD) to zoom in the small angle scattering signals which correspond to the
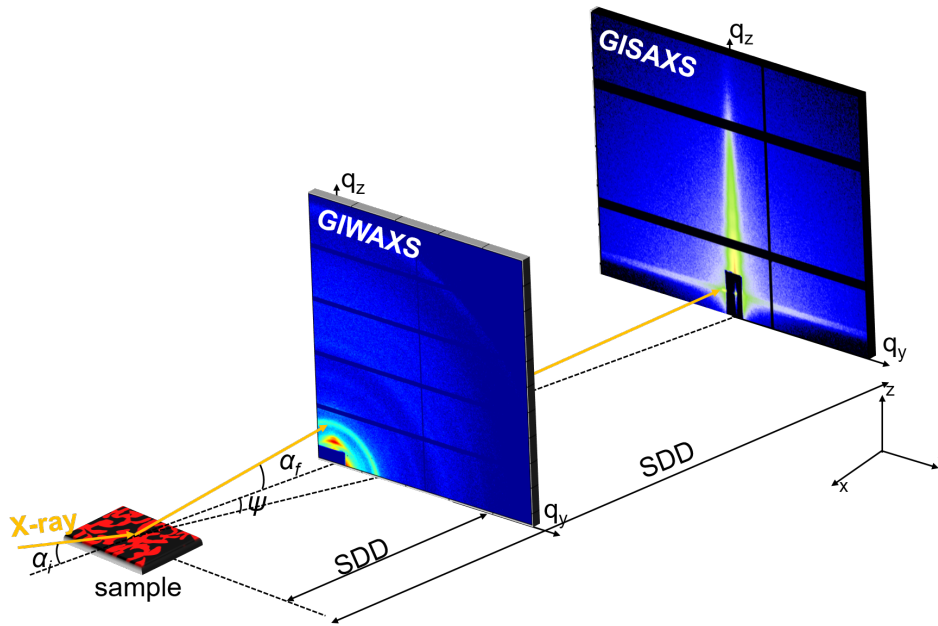
Figure 3.5: *Schematic view of grazing incidence X-ray scattering setups. The X-ray beam impinges on the sample with the incident angle α_i and is scattered under an angle α_f. The wide and small angle scattering signals are recorded by setting the detector at short and long sample-detector distance, respectively.*

large structure sizes. The GISAXS measurements discussed in this thesis are performed at the AUSTRIAN SAXS beamline of the Elettra Sincrotrone in Trieste, Italy. The beam energy is 8 keV and the incident angle is 0.4° which is larger than the critical angle of polymers (0.16°) and $PC_{71}BM$ (0.19°). The SDD is set to 1.4 m and a vacuum fly tub is mounted along the path of the scattered X-ray routine to minimize air scattering. Finally, the scattering signals are collected by a noise-free Pilatus 1M Detector by Dectris, with a 981×1043 pixel array and a pixel size of 172×172 μm^2. Moreover, the high brilliant X-ray source and fast readout time of the detector (3.6 ms) make kinetic measurements (in Chapter 7 and 8) with high temporal resolution possible.

The GISAXS data analysis is carried out by doing vertical line cuts and horizontal line cuts, which provide information about the vertical film structure relative to the sample plane and the lateral structures that occur parallel to the substrate, respectively. The cuts are extracted with the aid of the software DPDAK [99]. Afterwards, the horizontal line cuts are modeled based on the effective interface approximation and local monodisperse approximation (LMA), in which it is considered that the height of the scattering objects is allowed to be decoupled with their radii [85, 100], and the geometry and mean radii of the scattering objects by a form factor of cylindrical or spherical geometry following a

Gaussian distribution. Besides, the mean distance of neighboring objects is taken as the structure factor. More details can be found in Chapter 2.

3.9 Grazing-incidence wide-angle X-ray scattering

In contrast to GISAXS, grazing-incidence wide-angle X-ray scattering (GIWAXS) has a shorter SDD (see Figure 3.5), where it is possible to collect the scattered beam at wide angles. Therefore, GIWAXS measurements can access the crystalline lattice distances and crystallite grain sizes of materials on a sub-nanometer scale. The GIWAXS measurements in this thesis are conducted at the Elettra beamline as well. The Pilatus 1M detector is moved close to the sample with a distance of 291 mm. It has been demonstrated that the corrections of 2D GIWAXS data, e.g. solid angle correction, q-reshaping and conversion, efficiency correction (air path and pixel sensitivity under oblique angles) and polarization correction, are required to retrieve the corrected reciprocal space patterns from the raw data [55]. The correction can be done with the aid of the software Grazing Incidence X-ray Scattering Graphical User Interface (GIXSGUI) [101]. Afterwards, sector integrals are used to extract sample crystallite characteristics. To avoid the impact of the background, the sector cuts are subjected to a background subtraction of a reference sample, resulting in a flat-background profile (Figure 3.6b). At last, the Bragg peaks are fitted with Gaussian function to obtain peak position, full width at half maximum (FWHM) and peak intensity.
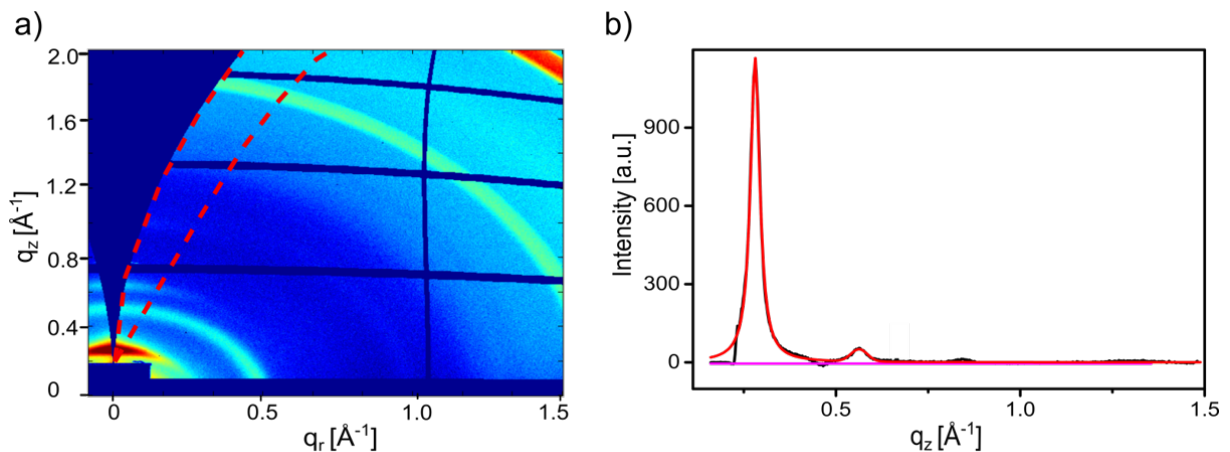

Figure 3.6: *a) Example of a GIWAXS image of a BHJ film with highlight sector integrals between the dashed lines. b) A sector cut after background-subtraction and fitted by Gaussian functions.*

In addition, the polymer crystal orientations can be figured out by GIWAXS measure-

ment. In Figure 3.7, face-on and edge-on orientated poly[(5,6-difluoro-2,1,3-benzothiadiazol-4,7-diyl)-alt-(3,3"'-di(2-octyldodecyl)-2,2';5',2";5", 2-quaterthiophen-5, 5"'-diy)] (PffBT4T-2OD) crystals and corresponding GIWAXS images are exemplary shown. The (100) peak is attributed to the chain stacking (a) and the (010) peak is contributed by the π–π stacking (b).
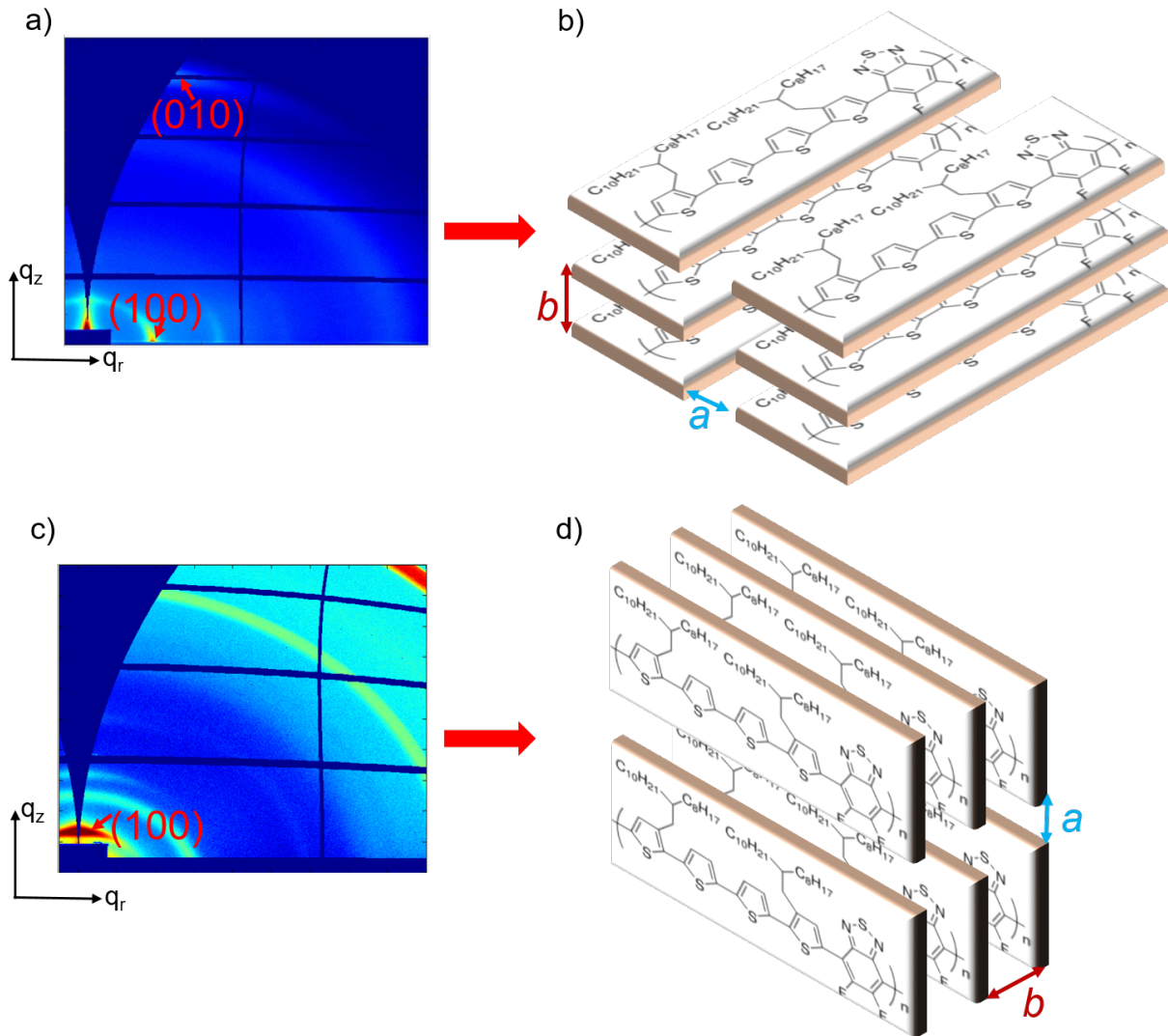

Figure 3.7: *Schematic representation of PffBT4T-2OD crystals orientation in PffBT4T-2OD:PC$_{71}$BM film. a) and c) 2D GIWAXS images of PffBT4T-2OD:PC$_{71}$BM (1:1.2) films. c) face-on and d) edge-on orientation of PffBT4T-2OD crystallites. The lattice constants a and b are depicted as well.*

3.10 In-operando grazing-incidence x-ray scattering

In Chapter 7 and 8, the solar cells are characterized by in-operando GIXS measurements. Hereby, the device performance and BHJ morphology can be tracked simultaneously, providing insights in the origins of device degradation. To fulfill the measurement requirements, a custom-made chamber was designed and built by M. Ruderer, J. Schlipf and B. Kalis. As shown in Figure 3.8a, two Kapton windows allows the X-ray beam to enter and exit the chamber. A quartz glass window at the bottom enabled the simultaneous illumination of the sample. On the left side of the chamber, a PerkinElmer PX5 150 W xenon arc lamp is mounted to simulate the sun's radiation spectrum. The distance between the lamp and the device is adjusted by screws. An illumination control shutter and a reflective mirror are placed under the chamber. On the other side, a vacuum pump is connected to keep the chamber at vacuum conditions (6×10^{-2} mbar) during the device characterization to rule out the decay factors of oxygen and water. Inside the chamber (Figure 3.8b), the sample is connected by five gold-capped pins for the IV characterization, which was tracked by a source meter (Keithley 2400). A pattern mask is placed under the device, which effectively reduced the degradation induced by the illumination and prevented increased temperatures. Before the in-operando measurements, each device is aligned so that the beam was positioned on the active layer close to the aluminum top electrodes.

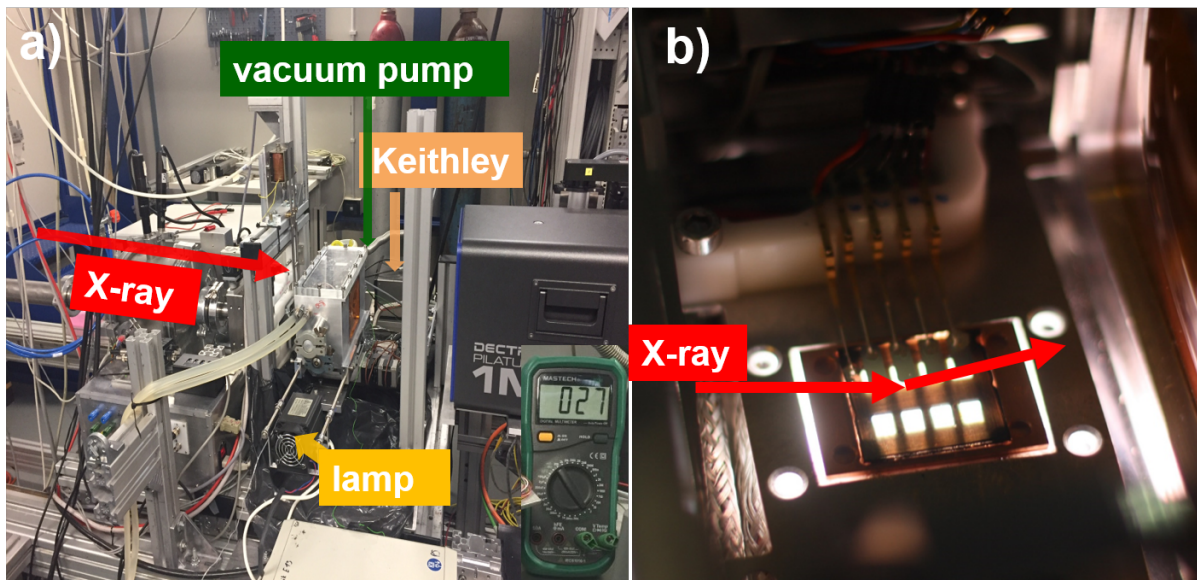**Figure 3.8:** *a) Photograph of the experimental setup with the custom-made chamber for in-operando measurements mounted in the synchrotron beamline. Characteristic parts are highlighted. b) Inside view of the chamber with a mounted solar cell.*

Each OSC is fixed in a petri dish, then sealed in a aluminum bag under nitrogen atmosphere to minimize the device aging, induced by water and oxygen in ambient. The samples are stored in the sealed bags until the in-operando measurement and exposed to air less than 10 min before being transfered into the measurement chamber. The device performances are continuously tracked for 2-4 h. The IV curves are recorded constantly every 16 s. The GIXS measurements are taken every 1 min for the first 10 min. Later, the GIXS measurements were recorded every 5 min for 5 s.

4 Sample preparation

This chapter gives information about the main materials, sample preparation procedures and thin deposition techniques applied in Chapter 5-8. In section 4.1, the main materials used are introduced with chemical structures and their main properties. The subsequent section is about the thin film fabrication process, which contains the substrate cleaning process, solution preparation and thin film deposition methods. Finally, the assembly routines of a solar cell with conventional and inverted architecture are described in section 4.3.

4.1 Materials

The chemical structure and basic properties of main materials related to this thesis are briefly introduced in this section.

Poly[4,8-bis(5-(2-ethylhexyl)thiophen-2-yl)benzo[1,2-b;4,5-b']dithiophene-2,6-diyl-alt-(4-(2-ethylhexyl)-3-fluorothieno[3,4-b]thiophene-)-2-carboxylate-2-6-diyl)] (PTB7-Th)

PTB7-Th is a benzodithiophene-based conjugated photovoltaic polymer with HOMO and LUMO levels of -5.3 eV and -3.52 eV, respectively. PTB7-Th:PC$_{71}$BM-based solar cells present power conversion efficiencies (PCEs) over 9 % without any post-treatment during the device fabrication [102]. The polymer used in the present work is purchased from ONE-Material (Chapter 6) Inc or Cal-os Inc (Chapter 7). The molecular weight (Mw) of the PTB7-Th is around 57 kDa. The chemical structure is shown in Figure 4.1.

Poly[(5,6-difluoro-2,1,3-benzothiadiazol-4,7-diyl)-alt-(3,3"'-di(2-octyldodecyl)-2,2';5',2";5",2-quaterthiophen-5,5"'-diy)](PffBT4T-2OD)

PffBT4T-2OD is a novel semiconducting donor polymer with a low band-gap of 1.65 eV for organic photovoltaics, which has yielded PCEs approaching 11 % [103]. PffBT4T-2OD

has high crystallinity and a wide range of light absorption. The holes show high mobility on the order of $10^{-2} \mathrm{cm}^2 \mathrm{V}^{-1} \mathrm{s}^{-1}$ in the PffBT4T-2OD film [104]. The polymer used in the present work is purchased from ONE-Material Inc (Chapter 5) or Cal-os Inc (Chapter 8). The molecular weight (Mw) of the PffBT4T-2OD is around 112 kDa. The chemical structure of PffBT4T-2OD is shown in Figure 4.1.
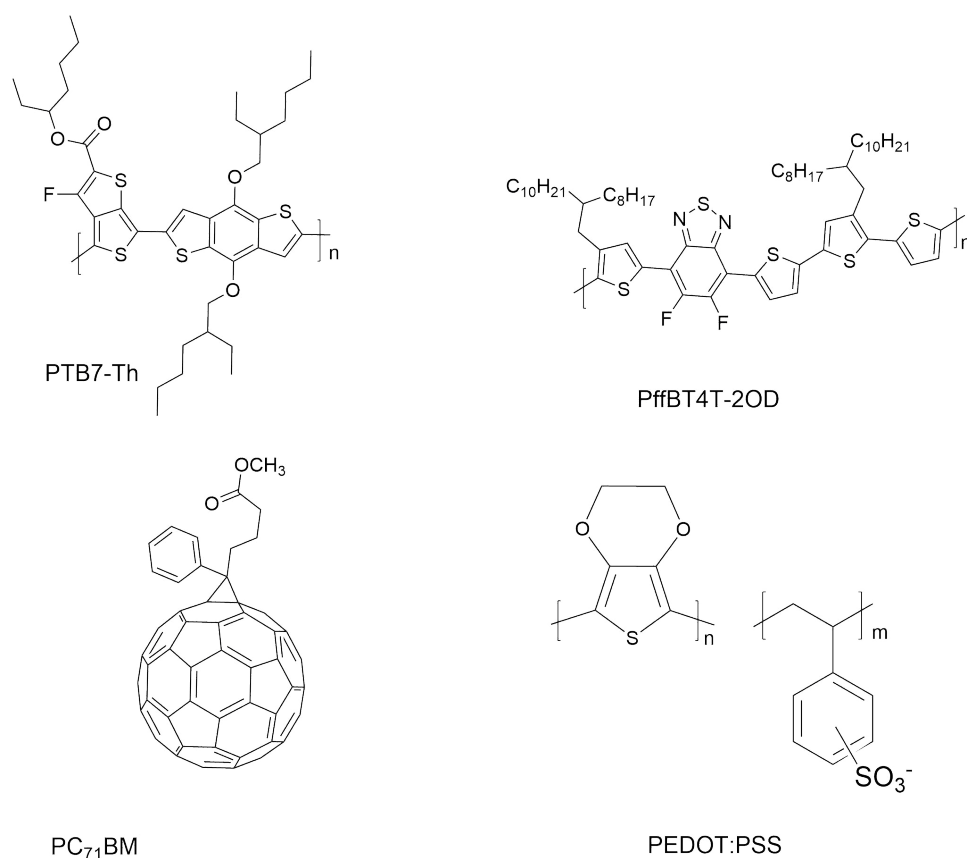

Figure 4.1: *Chemical structures of polymer PTB7-Th and PffBT4T-2OD, fullerene PC_{71BM} and PEDOT:PSS.*

[6,6]-Phenyl-C71-butyric acid methyl ester (PC$_{71}$BM)

PC$_{71}$BM (Figure 4.1) is a fullerene electron acceptor commonly used in efficient organic photovoltaic devices. Compared with PC$_{61}$BM, the non-symmetrical C70 cage of PC$_{71}$BM enables energetic transitions, which are forbidden in PC$_{61}$BM. Besides, there is an improvement of the absorption characteristics of PC$_{71}$BM over PC$_{61}$BM in the visible range of the solar spectrum [105]. The HOMO and LUMO levels of PC$_{71}$BM are at -6.1 eV and -3.7 eV, respectively. PC$_{71}$BM used in this work is purchased from ONE-Material Inc (Chapter 7 and 8) or American Dye Sources Inc (Chapter 5 and 6).

Poly(3,4-ethylenedioxythiophene):poly(styrenesulfonate) (PEDOT:PSS)

PEDOT:PSS is available as a water-based solution (1.3 ∼ 1.7 wt %), which contains a blend of semiconducting PEDOT and nonconducting PSS (shown in Figure 4.1). Due to the high conductivity, transparency and proper work function (5 eV) [106], PEDOT:PSS films are commonly applied as electron blocking layers in organic photovoltaic devices. PEDOT:PSS solution is purchased from Heraeus (Clevios P VP AI4083). Before film casting, the solution is filtered through a 0.2 μm cellulose acetate filter.

2,5-bis(11-(1-carboxyl acid))-3,6-bis-(2-thienyl)-1,4-dioxopyrrolo[3,4-c]pyrrole (DPP-COOH)

DPP-COOH is synthesized describable in a the previous paper [101]. ^{1}HNMR (500 MHz, deuterated DMSO) d [ppm]: 11.90 (s, 2H), 8.78 (dd, J = 3.9 Hz, 1.2 Hz, 2H), 8.07 (dd, J = 5.0 Hz, 1.2 Hz, 2H), 7.38 (dd, J = 5.0 Hz, 3.9 Hz, 2H), 3.98 (t, J = 7.4 Hz, 4H), 2.14 (t, J = 7.4 Hz, 4H), 1.63–1.57 (m, 4H), 1.45–1.42 (m, 4H), 1.30–1.20 (m, 24H). ^{13}CNMR (500 MHz, deuterated DMSO) d [ppm]: 24.44, 26.06 28,43, 28.48, 28.64, 28.71, 28.74, 29.16, 33.62, 41.36, 106.53, 128.60, 129.03, 132.86, 134.59, 139.26, 160.32, 174.42 ppm. HRMS (ESI, m/z): calculated for $C_{36}H_{48}N_2O_6S_2$ [M+Na]: 668.91, found 667.2871.

Zinc oxide (ZnO) precursor

The ZnO precursor solution is made by dissolving zinc acetate dihydrate (1 g) and ethanolamine (0.28 g) in 2-methoxyethanol (10 mL) and stirring overnight for a hydrolysis reaction [107]. All related reagents are purchased from Sigma-Aldrich.

Host solvent

Chlorobenzene (CB) and 1,2-dichlorobenzene (DCB) (shown in Figure 4.2) are used as host solvents for the polymer-fullerene blend solution. Both of them are purchased from Sigma-Aldrich with a purity ⩾ 99.5 %. The boiling temperature of CB is 132 °C, while for DCB it is 184 °C.

Additive solvent

1,8-diiodooctane (DIO) and o-chlorobenzaldehyde (CBA) (Figure 4.2) are doped in the BHJ blend solution to modify the morphology of the photoactive layer with a ratio of 3 % and 5 % by volume to all solvents, respectively. DIO and CBA are purchased from Sigma-Aldrich. The boiling temperature of DIO is 332.5 °C, while for CBA it is 212 °C.
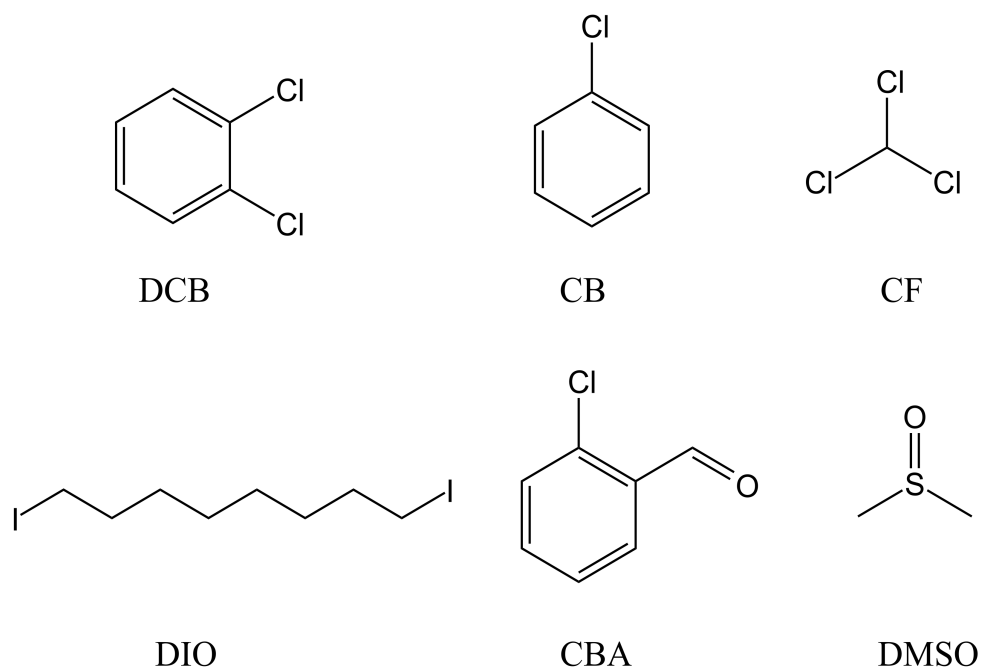
Figure 4.2: *Chemical structures of host solvents and solvent additives.*

Silicon wafer

P-doped silicon Si(100) wafers are used as substrates of static film deposition for the X-ray scattering and X-ray reflectivity measurements. The native oxide layer is important for proper coverage of film deposition.The wafers are purchased from SiMat (Kaufering, Germany) with a diameter of 10 cm and a thickness of 525 μm. The silicon substrates are cut into small pieces (e.g. 10×10 mm^2) for film application and then cleaned as introduced in section 4.2.1.

Indium-doped tin oxide-coated glass substrate

Solar cells are fabricated on indium-doped tin oxide (ITO) coated glass substrates, which are purchased from Delta Technologies Ltd. A 100 nm thick ITO layer is deposited on the substrate with a typical resistance of 8-12 Ω/sq. The work function of the ITO layer is around -4.7 eV. Before the film deposition, ITO substrates are cleaned as introduced in section 4.2.1.

4.2 Thin film fabrication process

The thin film fabrication process of organic solar cells has a profound impact on device performance. The soluble materials, e.g. the BHJ blend, PEDOT:PSS and ZnO precursor, are deposited via spin-coating from solution onto the clean substrates in this work. Next, thermal evaporation is applied to the insoluble materials to obtain a thin film. More details are presented in the following section.

4.2.1 Substrate preparation

Cleaning of silicon substrates

Silicon substrates are treated with an acidic cleaning to remove surface impurities before their utilization. The acid bath is a dilute piranha solution, which consists of 200 mL of H_2SO_4 (purity 95.0 %), 70 mL of H_2O_2 (purity 30.0 %) and 130 mL of deionized water (DI, purity 99.9 %) [108]. The acid bath is heated to 80 °C by a water bath. Afterwards, substrates are mounted in a PTFE holder and then immersed in the acid bath for 15 min. Subsequently, silicon substrates are rinsed thoroughly with deionized water and dried in a nitrogen flow. After drying, the substrates are carefully restored and ready for use. To avoid oxidation and other contamination on the surface, the film preparation is performed on the same day of cleaning.

Cleaning of ITO substrates

To clean ITO substrates, they are put into a PTFE holder, then soaked in four organic solvents, namely Alconox® detergent solution (16 mg mL^{-1}), ethanol (99.8 %), acetone (99.9 %) and 2-propanol (99.8 %), in sequence for 10 min each in an ultrasonic bath. Before film deposition, the ITO substrates are exposed to a plasma oven to further remove the organic particles and improve the hydrophilic properties of the surface. The plasma is applied with a power of 200 W and a pressure of 0.4 mbar for 10 min under an oxygen atmosphere or 5 min air plasma in a Harrick plasma cleaner (0.1 mTorr, PDC 32 G, 18 W).

As present in Chapter 7 and 8, a special solar cell layout is needed for in-operando measurements to avoid the metallic pins penetrating through the whole layer stack of a device. As shown in Figure 4.3, ITO substrates are patterned to etch away some parts of ITO. The remaining ITO part is covered with a scotch tape. The exposed ITO is etched via a catalytic reaction of zinc powder with HCl (12 M). After etching, the substrates are
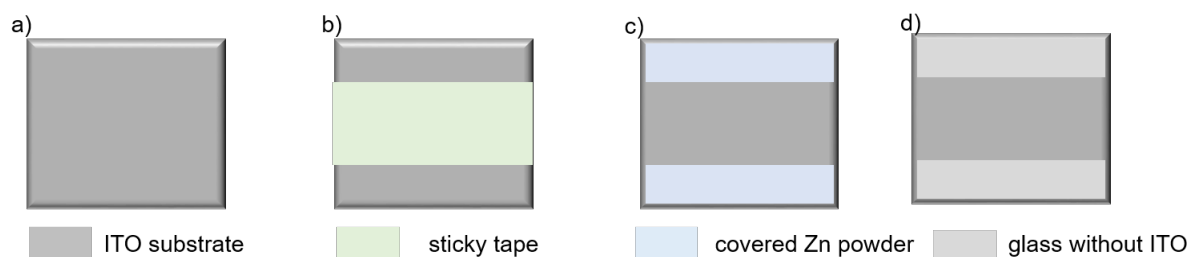
Figure 4.3: *ITO Etching. a) Plain ITO-coated glass substrate. b) Central area is covered by a 15 mm wide sticky tape. c) Edge parts are covered with Zn powder to do etching. d) The final pattern of ITO substrates.*

washed with DI water and dried by a nitrogen flow. Etched ITO substrates undergo the same cleaning procedure as the substrates without etching.

4.2.2 Solution preparation

Due to the light-sensitive properties of photovoltaic materials and the heating requirement, brown screw-top vials with PTFE-faced lids supplied by Fisher Scientific, are chosen as solution containers. Vials are cleaned with CB to avoid contamination.

PTB7-Th:PC$_{71}$BM

PTB7-Th:PC$_{71}$BM blends with an overall concentration of 25 mg/mL and a weight ratio of 1:1.5 are used within this work. In Chapter 6, 3 vol % of DIO is added and different amounts of PBDTTPD-COOH are doped as the third component in the blend solution, respectively. PBDTTPD-COOH is dissolved in a mixture of chloroform (CF)/dimethyl sulfoxide (DMSO) (10:1) with a concentration of 25 mg/mL. Different weight ratios of PBDTTPD-COOH are achieved by varying the doping volume of the PBDTTPD-COOH solution. Afterwards, mixed CF/DMSO is added to ensure the concentrations of PTB7-Th:PC$_{71}$BM are the same in all solutions. In Chapter 7, the solutions are prepared without and with solvent additives, namely 3 vol % of DIO and 5 vol % CBA. The final solutions are stirred and heated at 70 °C overnight. Notably, the solution needs to return back to room temperature before film deposition. Typically, 100 μL of PTB7-Th:PC$_{71}$BM solution are taken to fabricate each sample (20×20 mm^2).

PffBT4T-2OD:PC$_{71}$BM

The blend of PffBT4T-2OD:PC$_{71}$BM (volume ratio = 1:1.2, 20 mg/mL in total) is dissolved in mixed DCB/CB (volume ratio = 1:1). In Chapters 5 and 6, DIO is used as the solvent additive for all solar cells with 3 vol %. In Chapter 8, solar cells are prepared without and with solvent additives. The samples with solvent additives are made by doping 3 vol % of DIO and 5 vol % CBA, respectively. In Chapter 6, PBDTTPD-COOH is doped in the PffBT4T-2OD:PC$_{71}$BM solution as PTB7-Th:PC$_{71}$BM based ternary solar cells introduced in section 4.2.2 . All solutions are stirred and heated at 100 °C overnight.

Interfacial layer solution

In Chapter 5, the interfacial layers of adipic acid and terephthalic acid are individually dissolved in DMSO with a concentration of 0.05 mg/mL. 2,5-bis(11-(1-carboxyl acid))3,6-bis(2-thienyl)-1,4-dioxopyrrolo[3,4-c]pyrrole (DPP–COOH), C$_{60}$-SAM and PBDTTPD–COOH are dissolved in CF/DMSO (10:1) with a concentration of 0.05 mg/mL, respectively.

4.2.3 Deposition methods

Spin-coating

In this thesis, all BHJ films, interfacial layers and PEDOT:PSS films are made by spin-coating, which is a widely-used technique for preparing homogeneous thin films, especially for lab-scale thin film fabrication. The spin-coated films are fabricated with a WS-650-23 device by Laurell Technologies or a Delta 6 RC TT device by Süss MicroTec Lithography GmbH. In general, a rotary plate is set in the center of a spin coater, where the sample is attached by applying a vacuum (as shown in Figure 4.4a). The solution is dropped and spread over the whole surface of the mounted sample. Afterwards, the substrate is rotated at a preset angular speed and consequently the excess solution is expelled from the substrate by centrifugal forces. Finally, a homogeneous thin film is achieved.

The thickness of thin films by spin-coating is below 1 μm. It is determined by the solvent, the viscosity, and the concentration of the related solution. It can be roughly evaluated via the Schubert equation [109]:

$$d = C\omega^{-\frac{1}{2}}c_0 M_W^{\frac{1}{4}}$$ (4.1)

where C is an experimental parameter empirically determined by the sample system, ω is the angular velocity, c_0 is the solution concentration and M_W is the molecular weight of the polymer.

Thermal annealing

It has been demonstrated that thermal annealing is available to modify the film morphology and crystallinity, as annealing provides molecules sufficient energy to an equilibrium state [110–112]. Moreover, annealing is key for removing the residual solvents in the film after spin-coating, while it can impact on the performance of a final device. In this thesis, PEDOT:PSS films, ZnO films, interfacial layers and PffBT4T-2OD:PC$_{71}$BM films are treated with thermal annealing at a defined elevated temperature for a certain time. All annealing treatments are carried out at a RCT basic heat plate by IKA Werke GmbH. A copper plate is equipped to ensure homogeneous temperature distribution. PffBT4T-2OD:PC$_{71}$BM films are annealed under a nitrogen atmosphere to avoid the degradation caused by H_2 and O_2.

Thermal evaporation

In Chapter 5 and 6, solar cells are made in the conventional forward structure, in which 0.8 nm of LiF, 20 nm of aluminum and 60 nm of magnesium are deposited via thermal
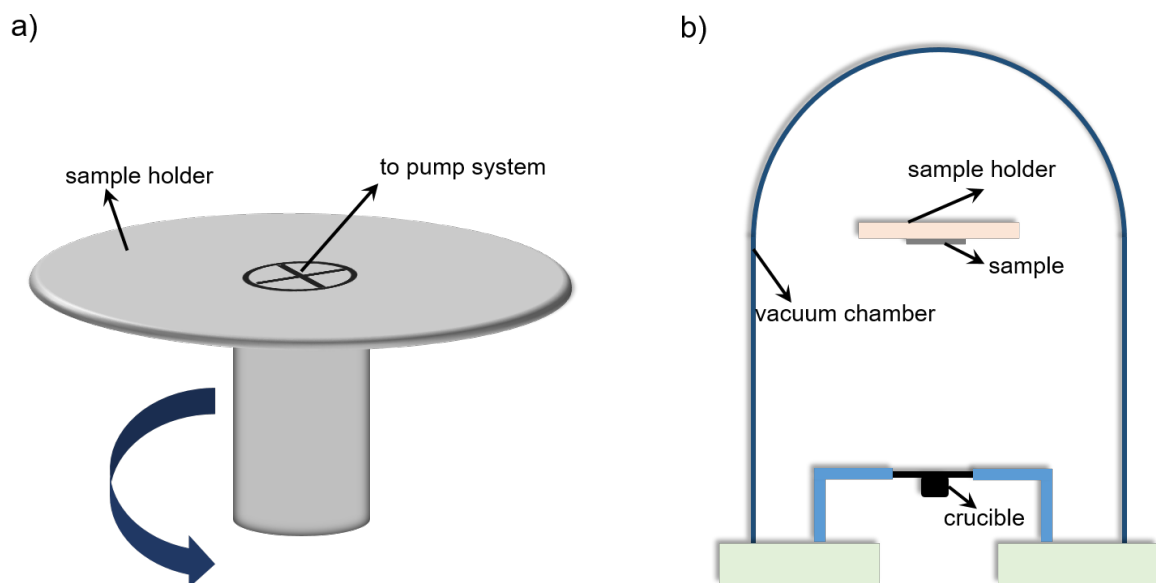

Figure 4.4: *Illustration of spin coating (a) and thermal evaporation (b) as deposition techniques for thin film fabrication.*

evaporation. In Chapters 7 and 8, the solar cells are prepared in an inverted structure, which contains 8 nm of MoO_3 as blocking layer and 60 nm of the aluminum film as back electrode fabricated by thermal evaporation. A schematic of a thermal evaporation setup is shown in Figure 4.4b. A crucible with the target material is fixed at the bottom of the chamber. Once the substrates are placed, the chamber is closed and evacuate to 3×10^{-6} Pa. Afterwards, an electrical current is forced to flow through the crucible to induce evaporation. The evaporation rate of LiF, MoO_3, Al and Mg are controlled at around 0.1 Å/s, 2 Å/s, 2 Å/s and 2.5 Å/s, respectively.

4.3 Assembly of solar cells

A graphical representation of the most general solar cell preparation routine is shown in Figure 4.5. The solar cells are fabricated with two architectures, namely forward and inverted structure. In a forward architecture, a PEDOT:PSS layer is firstly spin-cast on the top of clean ITO substrates (section 4.2.1) and then is annealed at 150 °C for 10 min. Afterwards, the BHJ solution is deposited via spin-coating on the PEDOT:PSS surface. At last, LiF, Al and Mg are evaporated in sequence on the samples to achieve the final device. In an inverted architecture, a ZnO film replaces the film of PEDOT:PSS to be a blocking layer and annealed at 150 °C for 30 min. BHJ films are made according to the procedure in a conventional structure. A MoO_3 film is evaporated on the top of the BHJ layer as a hole transport layer, then the back electrode of Al and Mg is deposited to finish the device fabrication.

Notably, the polymer PffBT4T-2OD cannot be dissolved in the mixed solvents of DCB and CB at room temperature. Therefore, PffBT4T-2OD:PC_{71}BM films are spin-cast from a warm solution. The BHJ solution is stirred and heated at 100 °C overnight. Before spin coating, ITO substrates are preheated on a hot plate at 120 °C for 1 min. The time gap from taking a substrate to a spin-coater to starting spin-coating is limited to 10 s.
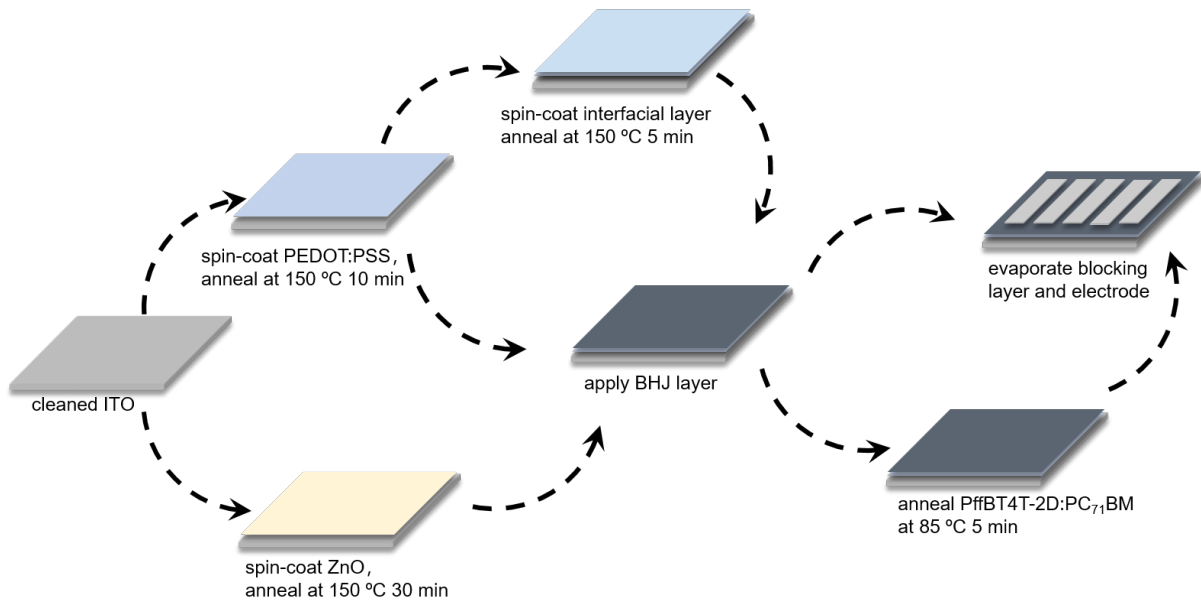
spin-coat interfacial layer
anneal at 150 ºC 5 min

spin-coat PEDOT:PSS,
anneal at 150 ºC 10 min

cleaned ITO

apply BHJ layer

evaporate blocking
layer and electrode

spin-coat ZnO,
anneal at 150 ºC 30 min

anneal PffBT4T-2D:PC$_{71}$BM
at 85 ºC 5 min

Figure 4.5: *Schematic illustration of the fabrication process of solar cells in the present work.*

5 Tuning device performance by an interface modifier

Parts of this chapter have been prepared as a manuscript: How to choose an interfacial modifier for organic photovoltaics using simple surface energy considerations (D. Yang et al. *in preparation*, 2020).

Organic photovoltaics (OPV) continue to attract attention due to the possibility of low-cost manufacturing, and the seemingly endless number of combinations of materials with which new device architectures can be assembled [21, 66, 113–115]. A typical OPV device comprises a layered structure in which a blend of donor and acceptor materials, the bulk heterojunction (BHJ), is sandwiched between the anode and cathode. Interfacial layers are employed in various locations within the sandwich architecture, notably between the BHJ and the electrodes to facilitate the charge carrier collection [116, 117]. Recently, the power conversion efficiency (PCE) of organic solar cells (OSCs) has been improved to over 17.3 % in tandem devices, [21] while champion device efficiencies for single-junction OSCs are around 16 % [22, 118–120]. In the conventional forward structure, the widely adopted configuration is ITO/PEDOT:PSS/donor:acceptor BHJ/LiF/Al [46, 121, 122], which relies upon PEDOT:PSS and LiF as the key interfacial layers on either side of the BHJ. PE-DOT:PSS has many known advantages, including high-conductivity, transparency, water-processability and smoothing the roughness of the underlying ITO [123, 124]. However, PEDOT:PSS has also disadvantages, such as acidic nature, the presence of ions (sodium ions in particular), and its intrinsic hydrophilicity.

In general, polymers are more hydrophobic than fullerene. When the BHJ solution is deposited on the top of hydrophilic PEDOT:PSS film, $PC_{71}BM$ molecules tend to accumulate close to the hydrophilic layer. Thus, a fullerene-rich layer can form near the PEDOT:PSS film, whic is an unfavorable position. In the conventional architecture of OSCs, electrons are transported in the acceptor materials, namely fullerene in our work, and collected at the top metal electrode. In contrast, holes are transported in the donor materials (here polymers) and extracted at the bottom anode. Thus, in such a BHJ film,
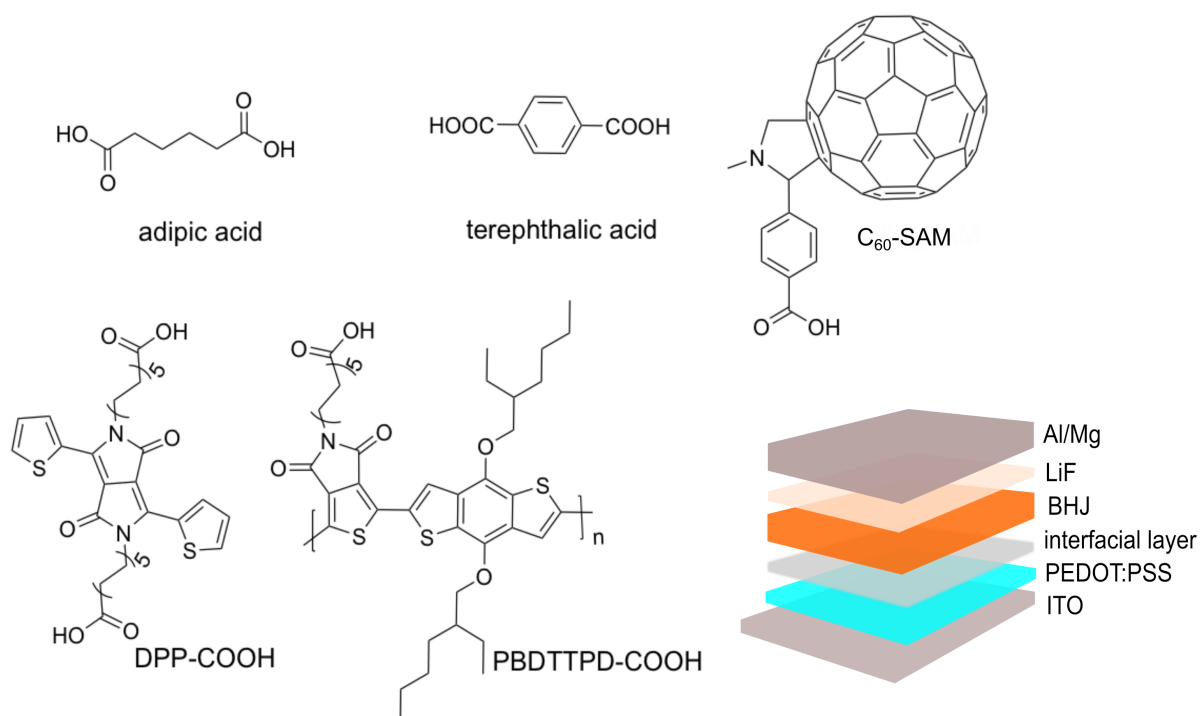
Figure 5.1: *Chemical structures of interfacial molecules and schematic of solar cell architecture.*

the charges will experience a long transport distance, which brings more chances for charge recombination, resulting in poor photovoltaic performances. Therefore, it is necessary to modify the gradient of BHJ materials to short the charge transport distance and further improve the device performance by . Because PEDOT:PSS is typically in direct contact with the BHJ, efforts have been directed towards the development of PEDOT:PSS modifiers that modulate its surface chemistry [125–127].

When designing interfacial modifiers, the molecular structure and resulting electronics tend to be the focus to enable tuning of interfacial energy levels. Recently, however, some attention has been paid to the surface energy of the interfacial modifiers and their role in inducing changes in the local composition, which in a BHJ layer that is less than 200 nm or even 100 nm thick could have profound effects on the performance of the solar cell [33, 128]. For example, in previous work, we found that modification of PEDOT:PSS with a thin layer of a conducting polymer (PBDTTPD–COOH) would lead to improved efficiencies with certain BHJ combinations, but decreased the performance with others [33]. We determined that the observed behaviour was related to the relative surface energies of the interfacial layer, and that of the two components within the BHJ. Depending upon these relative surface energies, donor or acceptor would accumulate at that interface, thus affecting charge transport in either a positive or negative manner.

Here, we generalize this observation and show how one can predict the effects of the interfacial layer on the efficiencies of a given solar cell with a simple determination of the surface energies. Comparing solar cell device performance is highly labour intensive due to the time and resources need to synthesize and test full devices, and thus a shortcut to choosing an ideal interfacial modifier is useful.

In the present work, we introduce 5 interfacial materials (see Figure 5.1) with different surface energy into solar cells individually. Contact angles determined using 4 probe liquids are determined for each of the ITO/PEDOT:PSS/interfacial layers and the calculated surface energies are used to predict accumulation of the BHJ donor and acceptor components, and correlated with the resulting effects on device performance. This work provides guidelines to enable the selection of an interfacial layer for a given BHJ.

5.1 Surface energy of interfacial layers

In order to calculate the effect on surface energies of these 5 components on a PEDOT:PSS layer, contact angle measurements are carried out on ITO/PEDOT:PSS/interfacial layers, glass/PC$_{71}$BM, and glass/donor polymers, respectively. Four different probe solvents, diiodomethane, water, ethylene glycol and formamide, are used to perform contact angle

Sample	Water [°]	Diiodomethane [°]	Ethylene Glycol [°]	Formamide [°]
PffBT4T–2OD	101.2 ± 1.7	90.5 ± 1.7	88.4 ± 1.0	59.7 ± 2.8
P3HT	102.5 ± 0.6	56.1 ± 0.7	76.7 ± 0.4	84.7 ± 0.8
PC$_{71}$BM	76.7 ± 2.1	14.7 ± 2.5	49.8 ± 2.4	60.5 ± 3.1
ITO/PEDOT:PSS /adipic acid	29.7 ± 3.5	27.1 ± 2.0	4.0 ± 0.8	3.9 ± 1.2
ITO/PEDOT:PSS /terephthalic acid	30.1 ± 3.5	21.2 ± 2.1	8.9 ± 1.5	4.4 ± 1.1
ITO/PEDOT:PSS /DPP–COOH	78.9 ± 3.8	39.6 ± 1.8	28.4 ± 3.1	34.6 ± 7.6
ITO/PEDOT:PSS /C$_{60}$–SAM	88.9 ± 3.0	39.3 ± 0.6	34.8 ± 2.8	48.1 ± 5.0
ITO/PEDOT:PSS /PBDTTPD–COOH	101.0 ± 2.6	42.0 ± 2.6	55.2 ± 3.0	48.5 ± 1.2

Table 5.1: *Measured contact angles for the molecules/surfaces used in this study.*

measurements for each surface (as introduced in section 3.2). The mean of the contact angles and the related standard deviation of each probe liquid and each surface are calculated and reported in Table 5.1. The surface energy parameters used for the probe liquids are taken from the literature [33].

The water contact angle of ITO/PEDOT:PSS cannot be measured properly due to the extreme hydrophilicity of this interface, and is thus near 0°. As shown in Table 5.1, the minimum water contact angle for the ITO/PEDOT:PSS/ interfacial layers combinations is 29.7° for adipic acid, and the maximum value of 101.0° is noted for the PBDTTPD–COOH interlayer, as summarized in Table 5.1. An acid-base model (see section 3.2) [93], widely applied for macromolecules [129, 130] and fullerenes [45, 131], is used to calculate the surface energy components of these ITO/PEDOT:PSS/interfacial layers. The calculated surface energies of the ITO/PEDOT:PSS/interfacial layers samples fall between 38.9 mJ/m^2 and 52.9 mJ/m^2 (Table 5.2), providing a useful range of surface energies. The degree of interfacial phase segregation is predicted to vary an appreciable amount in order to see difference in the PCE of these devices. Table 5.2 also shows the total surface energy of films of the representative donor polymers used (23.5 mJ/m^2 and 28.2 mJ/m^2), as well as that of PC$_{71}$BM (45.8 mJ/m^2) [45].

5.2 Modeling evaluation of polymer composition

Using the surface energies of the donor polymers, PC$_{71}$BM, and interfacial materials, it is possible to predict the relative component concentration of a BHJ at a given interface. Here, we calculate the relative concentration of donor polymer near the ITO/PEDOT:PSS /interfacial layer interface. When a species from solution is depositing on an interface, the energy barrier ΔG of deposition, at the interface can be quantified according to the following equation [93]:

$$
\begin{aligned}
\Delta G/2 = &- \left(\sqrt{\gamma_1^{\mathrm{LW}}} - \sqrt{\gamma_3^{\mathrm{LW}}} \right) \left(\sqrt{\gamma_2^{\mathrm{LW}}} - \sqrt{\gamma_3^{\mathrm{LW}}} \right) \\
&+ \left(\sqrt{\gamma_1^{+}} - \sqrt{\gamma_2^{+}} \right) \left(\sqrt{\gamma_1^{-}} - \sqrt{\gamma_2^{-}} \right) \\
&- \left(\sqrt{\gamma_1^{+}} - \sqrt{\gamma_3^{+}} \right) \left(\sqrt{\gamma_1^{-}} - \sqrt{\gamma_3^{-}} \right) \\
&- \left(\sqrt{\gamma_2^{+}} - \sqrt{\gamma_3^{+}} \right) \left(\sqrt{\gamma_2^{-}} - \sqrt{\gamma_3^{-}} \right)
\end{aligned}
\tag{5.1}
$$

With the calculated barrier ΔG and equation 5.2, where γ_i is the respective surface energy, the relative composition of polymers near that interface can be calculated. The details of these calculations are found in the previous work [33].

	γ^T [mJ/m^2]	γ^{LW} [mJ/m^2]	γ^+ [mJ/m^2]	γ^- [mJ/m^2]
PffBT4T–2OD	23.5 ± 0.9	23.5 ± 0.9	0	0.94 ± 0.2
P3HT	28.2 ± 0.4	28.2 ± 0.4	0	0.35 ± 0.1
PC$_{71}$BM	45.8 ± 1.7	45.8 ± 1.7	0	0.88 ± 0.7
ITO/PEDOT:PSS /adipic acid	52.9 ± 1.2	45.4 ± 0.8	0.4 ± 0.1	43.2 ± 6.6
ITO/PEDOT:PSS /terephthalic acid	52.7 ± 0.8	47.4 ± 0.7	0.2 ± 0.08	43.6 ± 3.9
ITO/PEDOT:PSS /DPP–COOH	43.3 ± 1.8	39.6 ± 0.9	2.7 ± 1.2	2.2 ± 0.2
ITO/PEDOT:PSS /C$_{60}$-SAM	40.5 ± 0.8	40.0 ± 0.3	2.1 ± 0.6	0.2 ± 0.04
ITO/PEDOT:PSS /PBDTTPD–COOH	38.9 ± 1.4	38.9 ± 1.4	0.8 ± 0.3	0

Table 5.2: *Calculated surface energy components of polymers and interfaces. Values derived using data from Table 5.1 and the acid-base model of surface energies [93]. γ^T, γ^{LW}, γ^+ and γ^- are the total, Lifshitz-van der Waals (dispersive), Lewis acid and base surface energy components.*

$$c_i^{\text{inter}} = \frac{c_i \exp(-N_A^{1/3} V_i^{2/3} \Delta G_i / RT)}{\sum_{n=1}^{N} c_n \exp(-N_A^{1/3} V_n^{2/3} \Delta G_n / RT)} \tag{5.2}$$

where N_A is the Avogadro constant, c_i^{inter} is the interfacial composition of the $i-th$ component, and V_i is the molar volume of the i component. Using these two equations and the data in Table 5.2, predictions of relative concentrations of donor polymer

Interfacial layer	PffBT4T–2OD [%]	P3HT [%]
Adipic acid	49	42
Terephthalic acid	45	40
DPP–COOH	61	47
C$_{60}$-SAM	60	47
PBDTTPD–COOH	62	51

Table 5.3: *Predicted polymer compositions at the ITO/PEDOT:PSS buried interface for PffBT4T–2OD:PC$_{71}$BM and P3HT:PC$_{71}$BM.*

within a given BHJ at the ITO/PEDOT:PSS/interfacial layer are calculated. Table 5.3 summarizes the results of these calculations. In general, the polymer concentration at the ITO/PEDOT:PSS/interfacial layer interface has a negative correlation with the total surface energy of the interfacial layer, i.e. the higher the surface energy of the interfacial layer, the lower the relative polymer concentration at the interface. In a forward-biased solar cell device, a polymer-rich ITO anode is desired since holes are transported through the polymer phase to be collected at the ITO anode [132–134]. According to the results in Table 5.3, BHJs composed of PffBT4T–2OD:PC$_{71}$BM see the widest range of polymer concentrations deviation at the ITO/PEDOT:PSS/interfacial layer, from 45 % to 62 %, while the change is smaller in P3HT:PCBM-based BHJs. For cells containing PffBT4T–2OD, the donor polymer concentration is lowest (45:55) when terephthalic acid is used as the interfacial layer, but is enriched with C$_{60}$-SAM (60:40), DPP–COOH (61:39) and PBDTTPD–COOH (62:38). Therefore, for an OPV assembled with conventional forward polarity, the ITO/PEDOT:PSS surfaces modified with terephthalic acid have a lower concentration of donor polymer at this interface, which would theoretically lower the efficiency of the corresponding devices. In other words, those ITO/PEDOT:PSS electrodes functionalized by more hydrophobic compounds such as C$_{60}$-SAM, DPP–COOH and PBDTTPD–COOH, are predicted to have higher efficiencies.

5.3 Device performances

To test this hypothesis, the work functions of the interfacial layers on ITO/PEDOT:PSS films are measured by ultraviolet photoelectron spectroscopy (UPS). As shown in Fig-
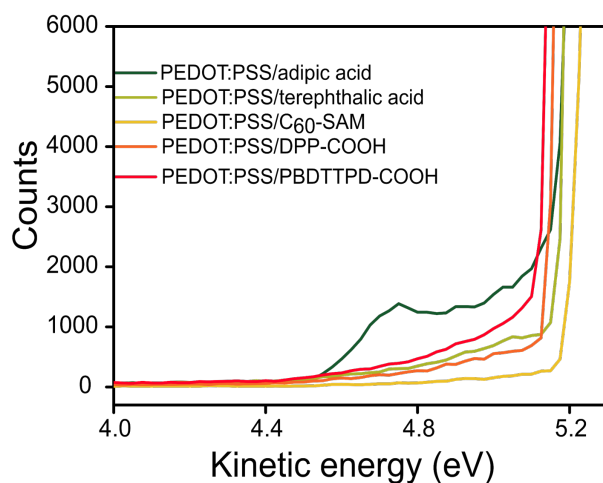

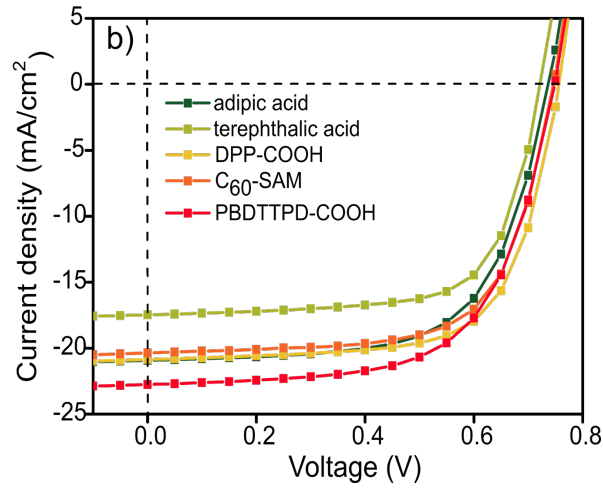**Figure 5.2:** *UPS spectra of the surfaces with interfacial layers on the ITO/PEDOT:PSS anode.*

Figure 5.3: *Champion J-V curves of PffBT4T–2OD: PC$_{71}$BM based device with different interfacial layers on the ITO/PEDOT:PSS anode.*

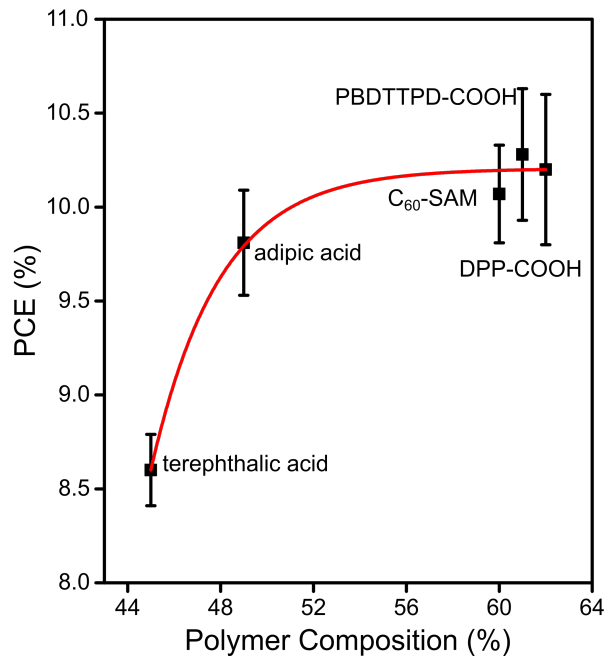**Figure 5.4:** *Calculated polymer composition at the buried ITO/PEDOT:PSS/interfacial layer interface vs PCE of the corresponding PffBT4T–2OD:PC$_{71}$BM devices. PCE values represent the mean of at least 8 different devices, and the error is taken as the standard deviation in these values. The solid line is a guide to the eye.*

ure 5.3a, the values of the work function are in the range of 5.14 eV to 5.22 eV, which are comparable to that of ITO/PEDOT:PSS (5.1 eV) [33]. Since the HOMO level of PffBT4T–2OD is 5.34 eV [135], there is no obvious energy barrier for hole collection. Organic solar cells, consisting of ITO/PEDOT: PSS/interfacial layer/PffBT4T–2OD:PC$_{71}$BM

/LiF/Al/Mg are fabricated, where the champion $J - V$ curves of these devices with each interfacial layer are shown in Figure 5.3b and the average PCEs with minimum 8 devices are displayed in Table 5.4. To further evaluate and compare the performances of PffBT4T–2OD:PC$_{71}$BM solar cells, average shifted histograms [136] are calculated to distinguish the changes of distributions of photovoltaic parameters with respect to interfacial layers (Figure 5.5). These results show, that in all cases the improvement in efficiency is dominated by an increases in J_{sc}. Figure 5.5 shows a plot of the efficiencies of the devices against the calculated ratio of donor polymer:PC$_{71}$BM at the ITO/PEDOT:PSS/interfacial layer. The highest efficiencies are observed for those interfacial layers that are predicted to result in the highest accumulation of donor polymer at the anode.
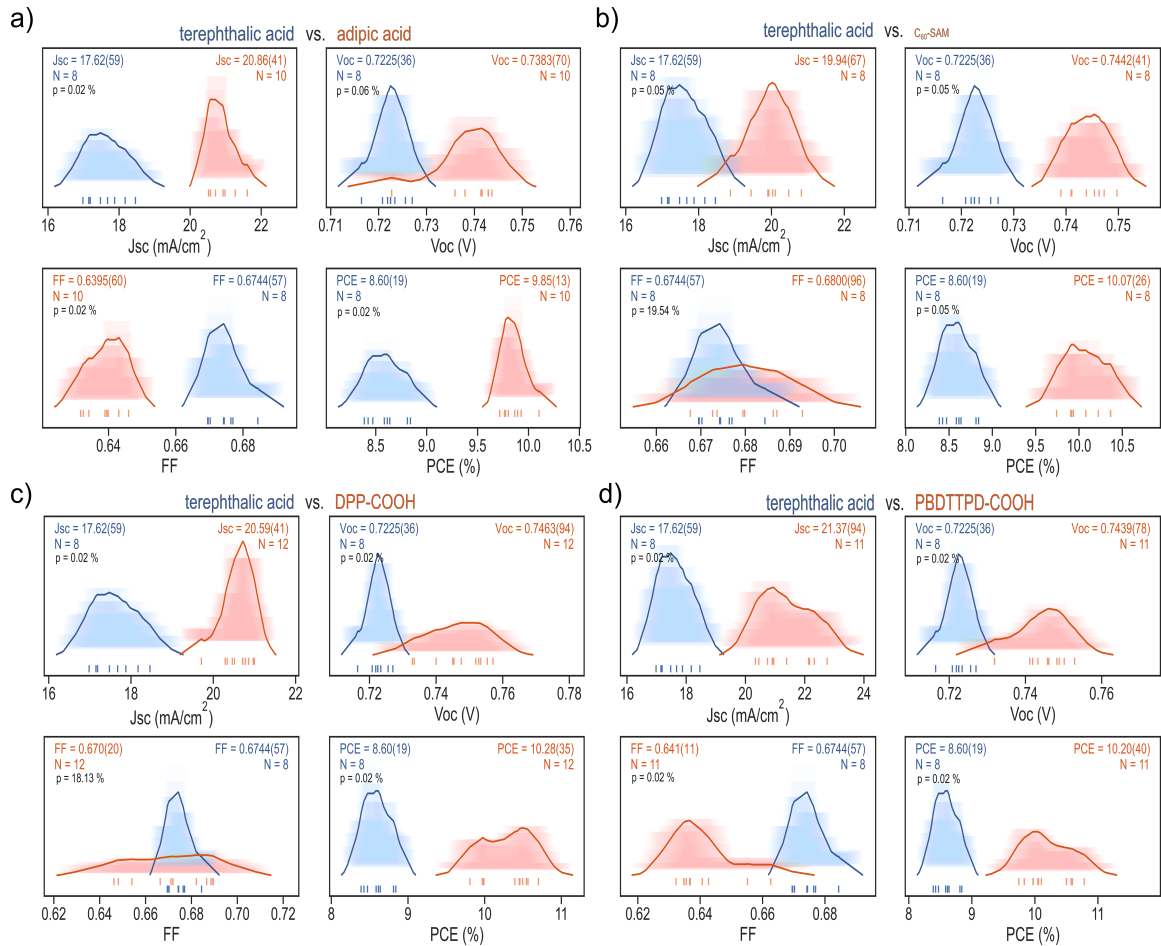

Figure 5.5: *Comparison of the performance of devices with different interfacial layers with the following architecture, ITO/PEDOT:PSS/interfacial layer/PffBT4T–2OD:PC$_{71}$BM/LiF/Al, using average shifted histograms (ASHs).*

The use of terephthalic acid as the interfacial layer results in the lowest PCE of 8.6 ± 0.2 % owing to a lower J$_{SC}$ (17.6 ± 0.6 mA/cm$^{2)}$) and V_{oc} (0.72 ± 0.04 V). Adipic acid, with

a predicted ratio of donor polymer:PC$_{71}$BM of 49:51 shows an improved performance to 9.9 ± 0.1 %, with a J_{sc} and V_{oc} of 19.4± 0.7 mA/cm^2 and V_{oc} 0.75 ± 0.06 V, respectively. Finally, with DPP–COOH, C$_{60}$-SAM and PBDTTPD–COOH as interfacial layers, the predictions suggest an increase of donor polymer at the ITO:PEDOT:PSS electrode to 60 % from 45 % for the terephthalic acid, and the corresponding efficiencies increased to 10.3 ± 0.4 %, 10.1 ± 0.3 %, and 10.2 ± 0.4 %, respectively.

The apparent connection between the calculated ratio of donor polymer:PC$_{71}$BM at the ITO/PEDOT:PSS/interfacial layer surface is further tested with P3HT:PC$_{71}$BM solar cells. As seen in Table 5.3, the predicted interfacial composition of P3HT ranges from 40 % to 51 %, which is slightly less than the range for PffBT4T–2OD (45 % to 62 %). However, in this case, the results are rather different, where the PCE ranges from 4.8 % to 4.9 % (Figure 5.6) with no statistically significant difference in their values. [137] These results suggest that increasing the donor concentration at the buried anode interface of a forward biased BHJ solar does not necessarily improve the PCE.

5.4 Morphology investigation

In this section, the influence of interfacial layers on the BHJ morphology is investigated. Thus, Time-of-Flight Secondary Ion Mass Spectrometry (TOF-SIMS) is applied to probe the polymer distribution in the BHJ film. Grazing-incidence wide-angle X-ray scattering (GIWAXS) is used to reveal the influences of interfacial modifiers on the polymer crystallinity.

5.4.1 Polymer gradient

Interfacial layer	Polymer composition [%]	[RB-IR]*100%/RB [%]
Adipic acid	49	17
Terephthalic acid	45	20
DPP–COOH	61	11
C$_{60}$-SAM	60	10
PBDTTPD–COOH	62	12

Table 5.4: *Predicted polymer compositions at the ITO/PEDOT:PSS buried interface for PffBT4T–2OD:PC$_{71}$BM and P3HT:PC$_{71}$BM.*
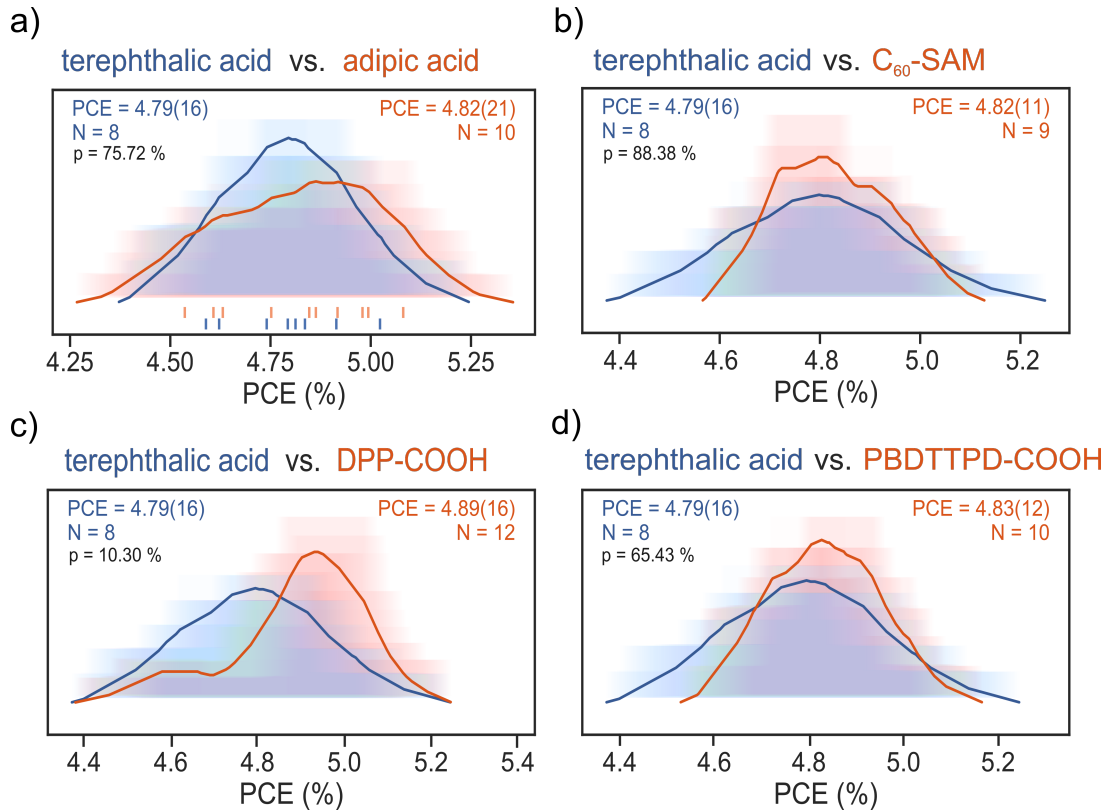
Figure 5.6: *Comparison of the performance of ITO/PEDOT:PSS/interfacial layer/P3HT:PC$_{71}$BM/LiF/Al devices with different interfacial layers, using average shifted histograms. All the p-values are larger than 5 %, suggesting no distinct variation of device performance with respect to applying these different interfacial layers. This result is consistent with our prediction that these interfacial layers would be predicted to have no effect on P3HT:PC$_{71}$BM devices based on the composition calculation.*

Interfacial layer	IR	RB
Adipic acid	0.089 ± 0.003	0.107 ± 0.002
Terephthalic acid	0.079 ± 0.004	0.098 ± 0.002
DPP–COOH	0.132 ± 0.005	0.149 ± 0.004
C$_{60}$-SAM	0.128 ± 0.003	0.142 ± 0.004
PBDTTPD–COOH	0.120 ± 0.004	0.135 ± 0.004

Table 5.5: *The F:C rato segment at each interface (IR) and the central point of the BHJ film (RB).*

To investigate whether there is indeed a change in the distribution of the donor and acceptor within the BHJ due to modification of the interfacial layer, depth profile analysis using ToF-SIMS is a useful analytical tool [138,139]. The fluorine (F)-containing segment,

only found in the PffBT4T–2OD donor polymer constituent, is used to track the gradient of the donor polymer in the BHJ layer. The carbon (C)-segment indicates the total carbon content of blend of donor and acceptor. To work out the changes of the polymer gradient within a BHJ, we calculate the ratio of the intensity of the fluorine-containing segment to that of carbon. The results are plotted as the black lines in Figure 5.7. To determine the location of the interface between the BHJ and interfacial layers, the signal of the sulfur (S)-containing segment (blue curves in Figure 5.7) are collected. It can be seen that the intensity of the sulfur-segment in all samples presents a peak at around 4000 s sputter time. This peak is due to the high concentration of sulfur in the PEDOT:PSS layer. Therefore, we mark the position of the onset of the sulfur peak as the interface between the BHJ and the interfacial layers (IR, represented by grey lines in Figure 5.7). The onset spot is estimated by the intersection of the tangents from before the sulfur peak, and the beginning of the the sulfur peak (dark red lines in Figure 5.7).

To be more precise, we took a 100 pixel-wide stripe to locate this interface. The IR values are the average F:C ratio in that 100 pixels. The average F:C ratio of BHJ films, at the central position of the BHJ layer is represented by the teal stripes and label RB in Figure 5.8. It is noted that the F:C ratio from the central spot of the BHJ (the
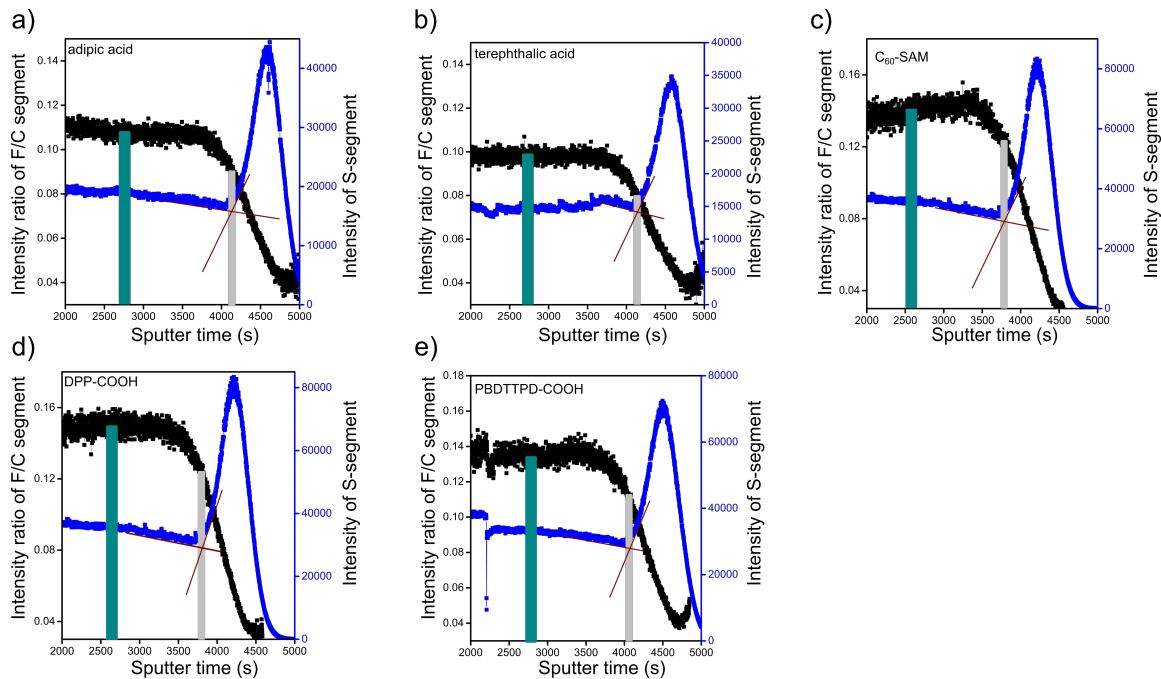

Figure 5.7: *ToF-SIMS depth profiles of ITO/PEDOT:PSS/interfacial layer/PffBT4T–2OD: $PC_{71}BM$ BHJ films with different interfacial layer components. The black line is the intensity ratio of F:C over the sputtering time. The blue line represents the intensity of the S-segment with sputter time.*
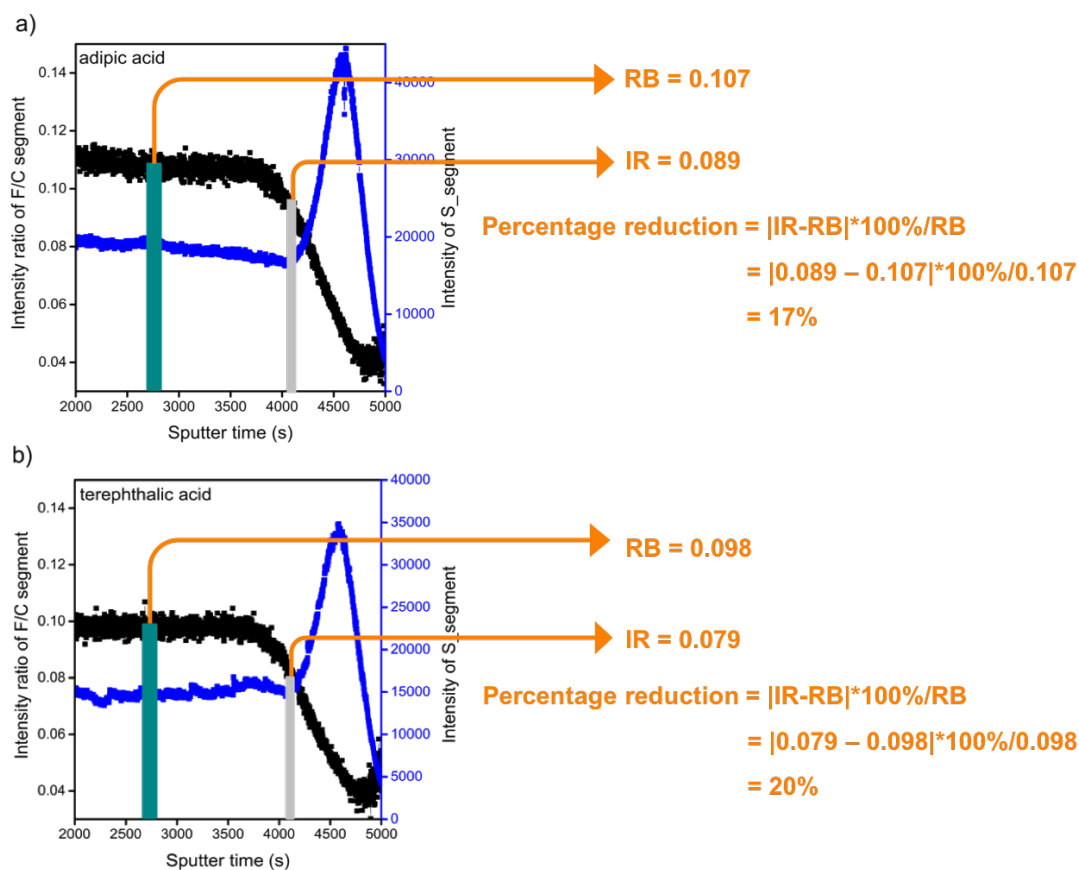
Figure 5.8: *Description of how the RB and IR values are determined and the calculation of the F:C ratios.*

point labelled RB) to the intersection with the interfacial layer (labelled IR), calculated by [RB-IR]*100%/RB, is different depending upon the choice of interfacial layer. For instance, as shown in Table 5.4, with the high surface energy interfaces of adipic acid and terephthalic acid, the F:C ratios are higher, 17 % and 20 %, compared to 10-12 % with DPP–COOH, C_{60}-SAM, and PBDTTPD–COOH. The calculation process are shown in Figure 5.8 and Table 5.5 . These results suggest a higher concentration of donor polymer at the ITO/PEDOT:PSS/interfacial layer surface with DPP–COOH, C_{60}-SAM, and PBDTTPD–COOH as the interfacial layer.

5.4.2 Surface morphology

Atomic force microscopy (AFM) measurements are performed to study surface morphology of those BHJ films with different interfacial layers. The details about AFM measurements have been introduced in section 3.6. To avoid the influence of the evaporation process on the film morphology, the measurements are performed on the fabricated de-
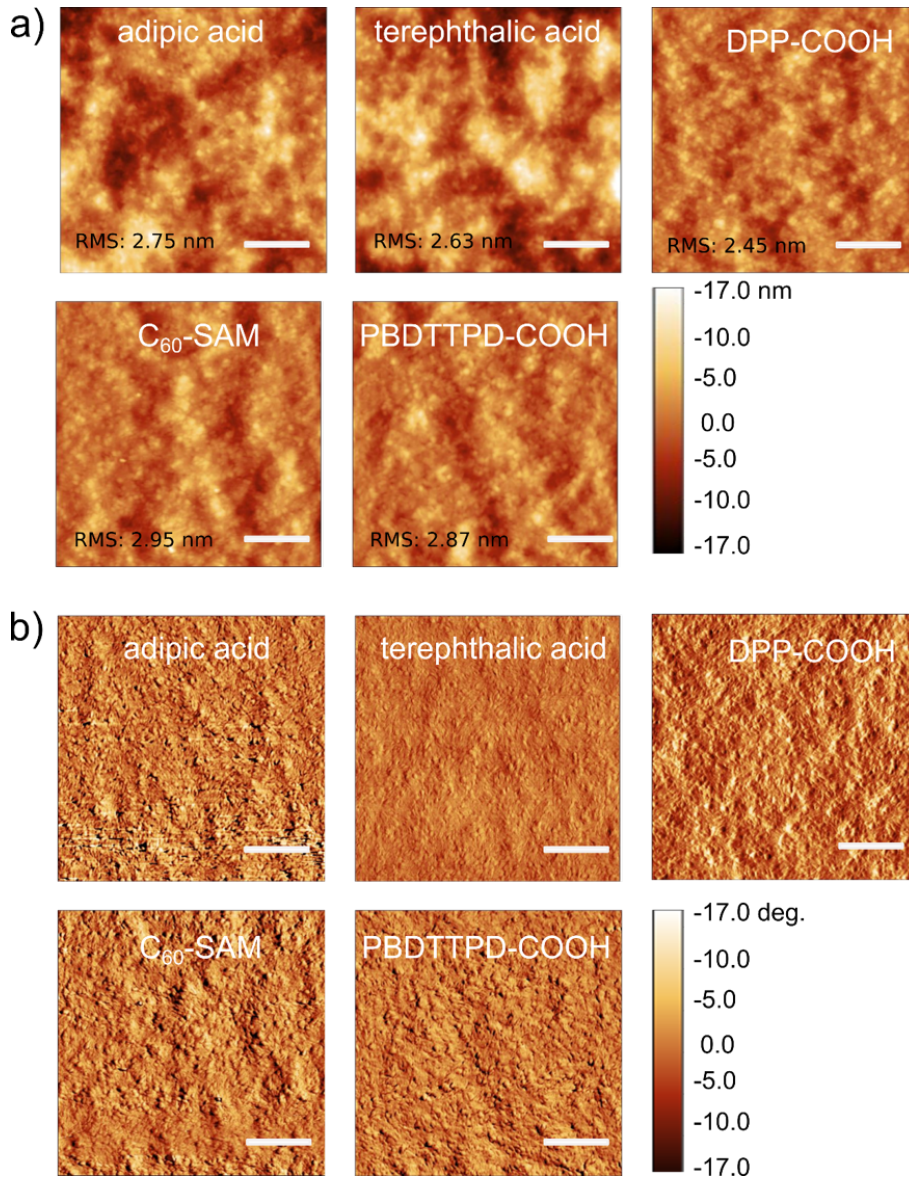
Figure 5.9: *AFM micrographs of ITO/PEDOT:PSS/interfacial layer/PffBT4T–2OD: $PC_{71}BM$ films. The scale bar is 500 nm. The interfacial layer is indicated. a) topograph and b) phase data are shown.*

vices on the areas without top bolcking layer and top contact. The exposed BHJ film (ITO/PEDOT:PSS/interfacial layer/PffBT4T–2OD:$PC_{71}BM$ films) on the device is chosen to probe. The corresponding height and phase images are shown in in Figure 5.9. Moreover, the film roughness, obtained via software Gwyddion, is presented on the height images. There is no significant difference of the morphology and roughness of the these BHJ films. As such, we conclude that the interface has no influence on the surface morphology of the BHJ films.
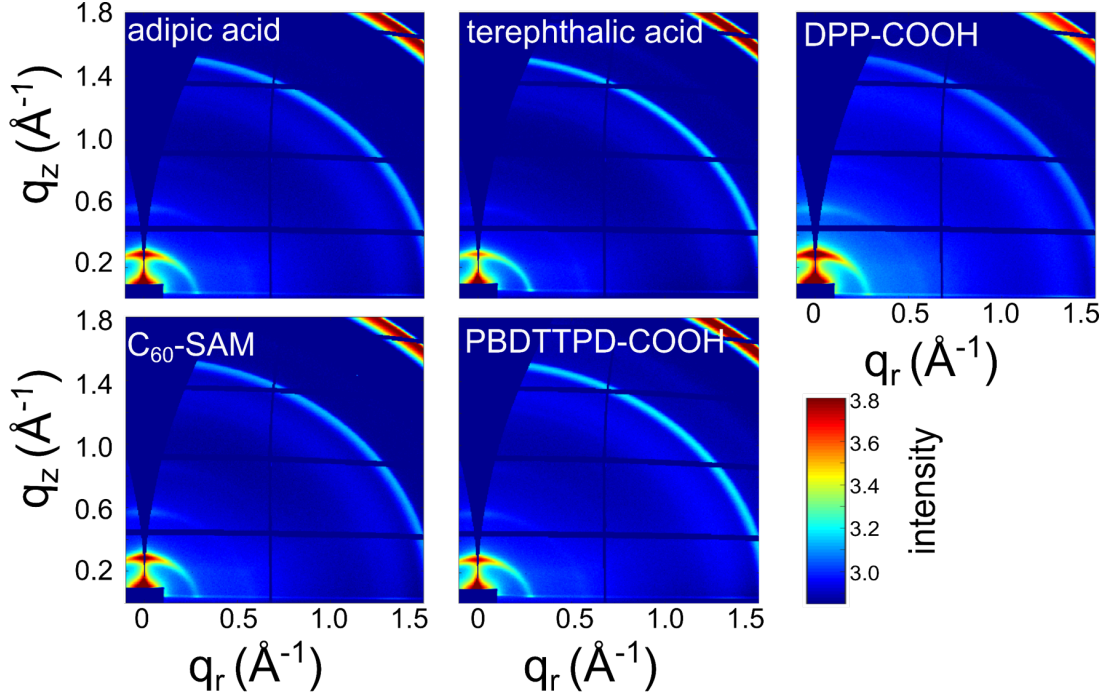
5.4.3 Crystallinity of BHJ films

Figure 5.10: *2D GIWAXS data of ITO/PEDOT:PSS/interfacial layer/PffBT4T–2OD: PC$_{71}$BM films with different interfaces. Comparison of devices with different interfacial layers.*

Interfacial layer	q [nm^{-1}]	crystal size [nm]	intensity
adipic acid	2.85	13.9	2981
terephthalic acid	2.84	14.6	1456
DPP–COOH	2.85	13.9	6832
C$_{60}$-SAM	2.85	14.6	3322
PBDTTPD–COOH	2.85	13.9	2167

Table 5.6: *PffBT4T-2OD (100) Bragg peak position, crystal size and peak intensity for the samples with different interfacial layers.*

GIWAXS measurements are carried on the samples of ITO/PEDOT:PSS/interfacial layer/ PffBT4T–2OD:PC$_{71}$BM to investigate a possible morphological link between the interfacial layers and the BHJ. The 2D GIWAXS data are illustrated in Figure 5.10. To quantify the crystallinity of the materials, vertical sector integrals are taken from the 2D GIWAXS data and the related cuts are presented in Figure 5.11. It is noted that the (100), (200), (300) and (010) Bragg peaks of PffBT4T–2OD are visible in the vertical
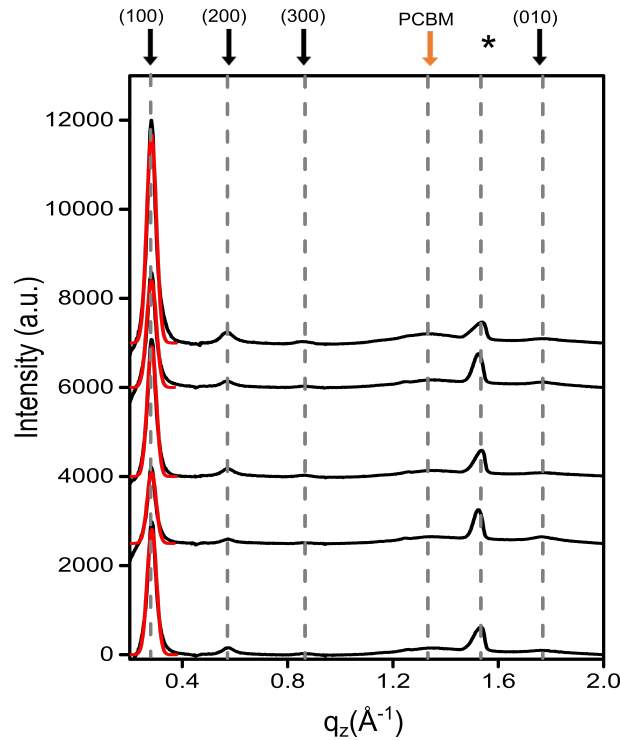
Figure 5.11: *Vertical sector integrals of 2D GIWAXS data of ITO/PEDOT:PSS/interfacial layer/PffBT4T–2OD:PC$_{71}$BM films with different interfacial components (adipic acid, terephthalic acid, C$_{60}$-SAM, PBDTTPD–COOH and DPP–COOH, from bottom to top). The black and orange arrows denote the scattering signal from PffBT4T–2OD and PC$_{71}$BM crystallites, respectively. The peak marked with a star is due to the ITO substrate. The red curves represent Gaussian fits of the (100) Bragg peak. All curves are shifted along the y-axis for clarity.*

cuts. The out-of-plane (100) Bragg peak is found with the highest intensity at $q_z \approx$ 2.84 nm^{-1} in each sample, which means that an edge-on orientation of the polymer is dominant in these films. The corresponding out-of-plane (010) Bragg peaks at $q_z \approx$ 17.6 nm^{-1}, which correspond to crystallites with a face-on orientation, are relatively weak. The Bragg peaks are fitted with Gaussian functions to extract the full width at half-maximum (FWHM) for the determination of crystallites sizes [140]. The calculated (100) crystal dimensions are summarized in Table 5.6. It can be seen that the (100) crystal sizes within the PffBT4T–2OD:PC$_{71}$BM blend films are about 14 nm, which is larger than the reported value of about 7 nm for similarly prepared films [141]. Moreover, the scattering intensities of PffBT4T–2OD (100) Bragg peak in the samples with different interfacial layers are listed in Table 5.6 as well. We can see the lowest scattering intensity present in the sample with terephthalic acid interfacial layer, which indicates the poorest polymer crystallinity in this sample. In general, a high crystallinity in the BHJ layer is critical for

a high device current, as the charge mobility and even the exciton diffusion length are enhanced in crystallites. [156] Thus, we conclude that the interface of terephthalic acid leads to poor the polymer crystallnity in the BHJ layer, resulting in the low J_{sc} value in the photovoltaic performance of corresponding device.

5.5 Discussions

We learn from the presented data, that the PCE of BHJ solar cells can be modified by inducing vertical phase segregation in the BHJ. It is typically assumed that a segregation profile where the BHJ is donor-rich at the hole-collecting anode and acceptor-rich at the electron collecting cathode will result in an improvement of the PCE [33, 142]. The improvement in PCE from such a morphology is believed to be due to improved charge collection/reduced recombination at the electrode interfaces. If this vertical phase segregation does indeed reduce non-geminate recombination, it would be expected that the fill factor improves with the degree of favourable phase segregation. However, from our data (Figure 5.4 and Figure 5.5) it is found that the increase in PCE (with respect to a terephthalic acid interfacial layer) is primarily the result of an increase in J_{sc}. These results are consistent with those found by Huang et al [128], where a donor enriched buried anode interface also resulted in a larger J_{sc}. Moreover, the results for P3HT:PC$_{71}$BM cells (Figure 5.6) did not show any improvement in PCE, despite similar differences in predicted interfacial composition as the PffBT4T–2OD:PC$_{71}$BM cells. As such, these data suggest that improvement of PCE by inducing a favourable phase segregation in the BHJ is more nuanced than simply a reduction in non-geminate recombination.

Several possibilities exist for the improvements in J_{sc} observed in the PffBT4T–2OD: PC$_{71}$BM cells. As proposed by Huang et al [128], improvements in J_{sc} of BHJ cells with preferential phase segregation can be attributed to changes in the polymer crystallinity resulting in increased exciton generation rate. This is certainly a plausible mechanism for the data presented in this work and is consistent with the P3HT:PC$_{71}$BM results, which have a much larger active layer thickness (250 nm), as such the composition gradient located near the buried anode interface is expected to have much smaller impact on the total absorption. Another possible mechanism to consider is that the rate of geminate recombination is lower due to phase segregation resulting in a more percolated morphology, e.g. there could be fewer isolated donor/acceptor domains that are not connected to the anode/cathode interfaces. The relative impact of these two mechanisms could be quantified by measurement of the internal quantum efficiency.

5.6 Summary

In general, to find a proper interfacial layer, OPV device assembly and testing requires statistically significant numbers, up to 500 solar cells per new material. Thus it is a highly laborious process. In our work, we provide a model to precheck if an interfacial layer is suitable for the device. We start with the wetting properties of all related materials, then the polymer composition can be calculated based on the materials surface energies. According to the polymer composition, we can have a good preview of the effect of the interfacial modifier.

To test our model, 5 molecules are employed as interfacial layer materials, which show a wide range of surface energy. Firstly, contact angle measurements are performed on the sample of ITO/PEDOT:PSS/interfacial layer film, pure polymer film and pure fullerene film to determine the surface energy via the acid-base model. Afterward, we can get the polymer composition at the interface by our model. Based on the polymer composition values, we know that PffBT4T-2OD-based system is more sensitive on these interfacial layers. Therefore, we predict that the performance of the devices based on PffBT4T-2OD:$PC_{71}BM$ can be modified by inserting an interfacial layer.

To verify our prediction, we assemble the PffBT4T-2OD:$PC_{71}BM$ and P3HT:$PC_{71}BM$ devices. We found the *PCE*s of PffBT4T-2OD:$PC_{71}BM$ based devices are improved, when the interfacial layer becomes hydrophobic. However, these interfaical layers have no significant effects on the P3HT:$PC_{71}BM$ based devices. Furthermore, to track the change caused by interfacial layers, morphology investigation are carried on the ITO/PEDOT:PSS/interfacial layer/BHJ films. According to TOF-SIMS characterization, we found the polymer gradient at the interface is reduced on the hydrophobic interfaces, indicating that a more homogeneous BHJ film forms. Besides, the interfacial layer doesn't affect the crystallnity and surface morphology of BHJ film.

In conclusion, based on the relative surface energies of interfacial modifiers and the components of the BHJ, a relative accumulation or depletion of the donor or acceptor at an electrode interface can be predicted. A gradient of donor and acceptor through the BHJ film could have a beneficial or deleterious effect on device performance. The approach described here provides a set of simple guidelines to rationally predict, ahead of time, the role of an interfacial modifier or interface before undergoing laborious device synthesis and testing. The extension to other BHJ compositions, including small molecule-based BHJs, is of great interest to further probe the generality of this algorithm.

6 The third component of PPDTBT-COOH in organic solar cells

In the previous chapter, a guideline about how to choose a proper interfacial layer is presented. The effective interfacial layer provides a promising approach to tailor the composition of the BHJ film at the interface, which can enhance the photovoltaic performance of respective solar cells. However, further enhancement of the performance of BHJ organic solar cells is limited by an approach based on binary components due to the problems in balancing the absorption range, the crystallization and the compatibility of the D/A materials [145, 146]. Irrespective of the improvements by newly synthesized conjugated polymers, it has been found that for a single homopolymer it is almost impossible to absorb the entire visible range of the solar spectrum. An ideal strategy, which copolymerizes two or more different monomers to get complementary absorptions, however, has been proven to be hardly realizable because of difficulties in the copolymerization [147–150]. Another possible way to capture a wider band of the solar spectrum is realized in a tandem or multi-junction solar cell by using several BHJ layers with different bandgaps [151]. However, the manufacturing process becomes significantly more complex by going from a single junction cell to tandem or multi-junction solar cells. Although such type of devices is record setting today, a real-world application will be rather limited due to a significantly more costly and demanding large-scale fabrication. Alternatively, ternary OSCs formed by a blend of donor1/donor2/acceptor (D1/D2/A) or donor1/acceptor1/acceptor2 (D1/A1/A2) have attracted considerable attention, because
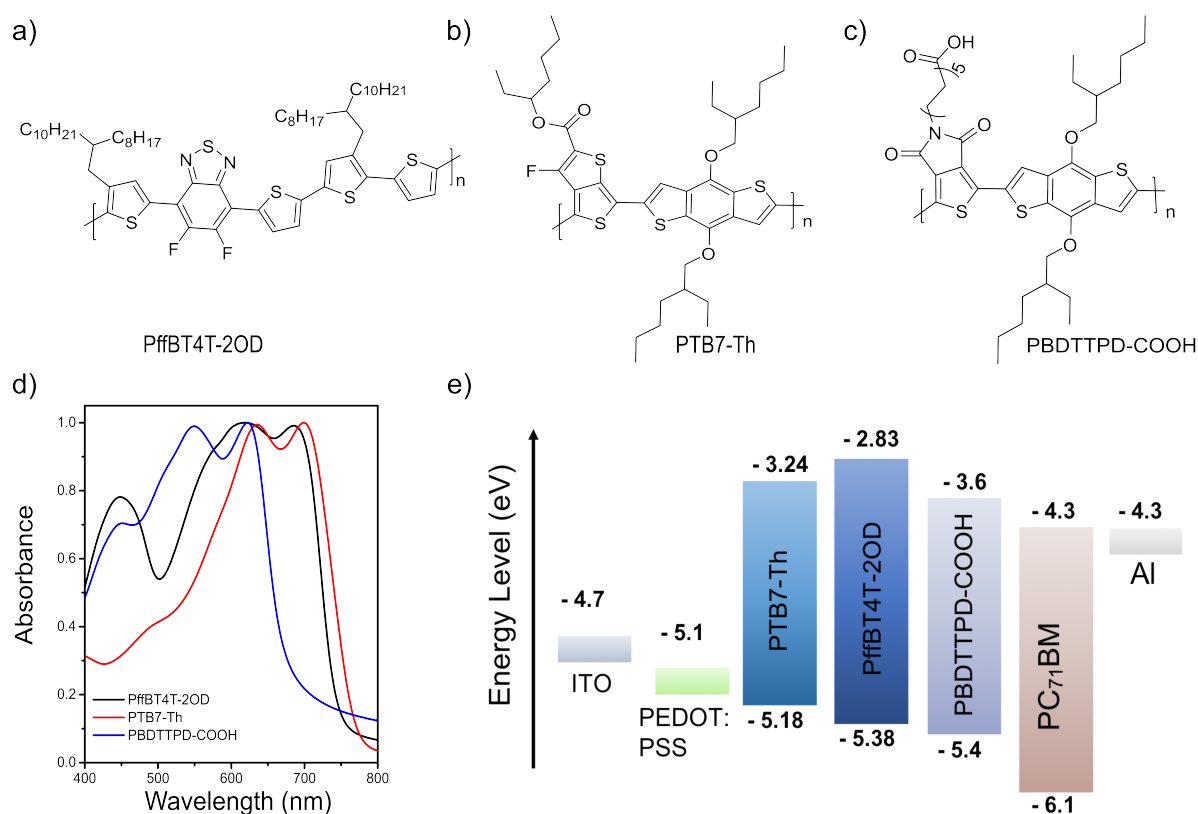
Figure 6.1: *a)-c) Chemical structures of donor materials PffBT4T-2OD, PTB7-Th and of the added third component PBDTTPD-COOH. d) UV/Vis absorption spectra of donor polymers and PBDTTPD-COOH. e) Corresponding energy levels of all materials used in the OPV stacks of these BHJ devices are obtained from references [33, 43, 143]. Reprinted with permission from Ref. [144]. Copyright 2020 American Chemical Society.*

they allow to maintain the simple craftsmanship used in binary OSCs, and simultaneously expand the absorption range [146, 152, 153]. By moving from 2 to 3 components in the active layer, the complexity is further increased by the larger number of possible D/A partners. Fundamental knowledge from binary systems cannot be easily transferred to the ternary devices [152, 154, 155]. For example, the problems of controlled crystallization and tailored compatibility of D/A materials in BHJ need to be investigated in more details. In general, it has been widely reported that a high crystallinity in the BHJ layer is critical for a high device current, as the charge mobility and even the exciton diffusion length are enhanced in extended crystallites [156, 157]. Moreover, the control of the orientation of the crystallites with respect to the electrodes is essential, since charge transport is commonly anisotropic for the crystallites [48, 158]. Another big challenge for the organic photovoltaics community is to have sufficient long-term stability combined with high performance, with a generally accepted target being a 10 years lifetime [36, 37].

The instability of OSCs originates mainly from chemical and morphological degradation pathways [40, 41, 71]. To overcome these challenges, suggested solutions are the production of inherently chemically stable materials, encapsulation and crosslinking of the D/A morphology to lock the initially installed BHJ structure [42–44].

Recently, non-fullerene acceptor materials have been largely used in OSCs [159–163]. Despite the limitations in PCE caused by the use of fullerene acceptors, OSCs based on fullerene acceptors are still of high interest because many fabrication pathways have been established for such class of D/A blends and cannot be easily changed. Moreover, non-fullerene acceptors today are still rather expensive, which renders them presently less interesting for real world applications.

In this work, poly[(5,6-dihydro-5-octyl-4,6-dioxo-4H-thieno[3,4-c]pyrrole-1,3-diyl)[4,8-bis[(2-ethylhexyl)oxy]benzo[1,2-b:4,5-b]dithiophene-2,6-diyl]] (PBDTTPD) with a carboxylic acid-based side chain, PBDTTPD-COOH, is introduced as a third component in two types of fullerene based BHJ layers. We compare OSCs of poly[4,8-bis(5-(2-ethylhexyl) thiophen-2-yl)benzo[1,2-b;4,5-b']dithiophene-2,6-diyl-alt-(4-(2-ethylhexyl)-3-fluorothieno-thiophene-)-2-carboxylate-2-6-diyl)] (PTB7-Th):[6,6]-phenyl-C71-butyric acid methyl ester (PC$_{71}$BM) and poly[(5,6-difluoro-2,1,3-benzothiadiazol-4,7-diyl)-alt-(3,3"'-di(2-octyld odecyl)-2,2';5',2";5",2"'-quaterthiophen-5,5"'-diyl)] (PffBT4T-2OD):PC$_{71}$BM in the present study (Figure 6.1a-c). As shown in the UV-visible absorption spectrum of PBDTTPD-COOH and both donor materials in films (Figure 6.1d), the main absorption range of PBDTTPD-COOH is around 500 - 650 nm, while the absorption of PTB7-Th and PffBT4T-2OD is strong around 600 - 750 nm and 500 - 720 nm, respectively. which is assigned to intramolecular charge transfer in the conjugated thiophene copolymers. Thus, the third component PBDTTBT-COOH can slightly broaden the BHJ absorption spectrum of active layers consisting of PTB7-Th or PffBT4T-2OD. Moreover, the highest occupied molecular orbital (HOMO) and the lowest unoccupied molecular orbital (LUMO) energy levels of PBDTTPD-COOH (Figure 6.1e) are located between the corresponding energy levels of the donors (PTB7-Th and PffBT4T-2OD) and acceptor to form the cascade energy level alignment [33, 143, 164]. Therefore, as shown in Figure 1e, the third component could work as a charge transport bridge in the BHJs. The excitons generated in donors can be dissociated into charge carriers at the interfaces of donors and the third component, respectively [165, 166]. Then the electrons can be effectively transported to the cathode through the channels formed by the third component, and the holes are collected at the anode [152, 167, 168]. Moreover, hydrogen bonds are likely to form among the PBDTTPD-COOH molecules [169], which means that the network between D and A can be tailored by the presence of the third component in a BHJ film. A direct proof of the presence of H-bonds remained difficult due to the low concentration of the third component

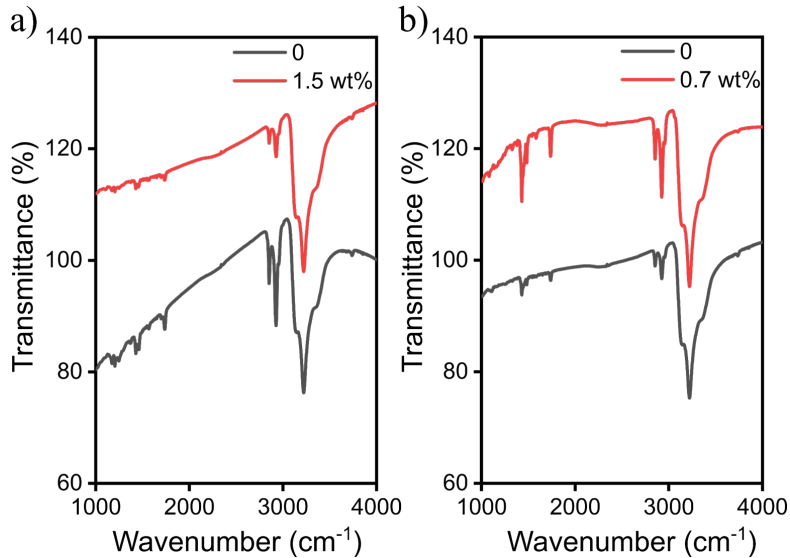(see Figure 6.3). In BHJ solar cells, the film morphology plays a key role for the device

Figure 6.2: *FTIR spectra of a) PTB7-Th:PC$_{71}$BM binary film and PTB7-Th:PC$_{71}$BM ternary film, b) PffBT4T-2OD:PC$_{71}$BM binary film and PffBT4T-2OD:PC$_{71}$BM ternary film. Reprinted with permission from Ref. [144]. Copyright 2020 American Chemical Society.*

performance [170]. In the present work, we focus on morphology changes introduced by doping PTB7-Th:PC$_{71}$BM and PffBT4T-2OD:PC$_{71}$BM blends with PBDTTPD-COOH. Grazing-incidence small/wide-angle X-ray scattering (GISAXS/GIWAXS) measurements are applied to evaluate the inner domain sizes and crystallinity of the active layers. The surface morphology is probed with atomic force microscopy (AFM). The structure information is correlated with device data and the long-term stability of the OSCs is analyzed with respect to the T80 times. The addition of PBDTTPD-COOH turns out to be beneficial for the crystallinity as well as for the device stability.

6.1 Morphologies of BHJ films with the third component

To probe the morphology of BHJ films, the blend solution of polymer and fullerene was deposited on the PEDOT:PSS/Si substrates for GISAXS (section 6.1.1) and GIWAXS (section 6.1.2) measurements. Both measurements are performed at the Austrian SAXS beamline of the ELETTRA-Sincrotrone Trieste synchrotron radiation facility, at an X-ray energy of 8 keV. For GISAXS measurement, the incidence angle was set to 0.4° and the sample-detector distance was 1160 mm. For GIWAXS measurement, the grazing incidence angle was below 0.4° and the sample-detector distance was 296 mm. The exposure time is

5 s for each sample in the GISAXS and GIWAXS measurements. The surface morphology observations by AFM and OM are performed on the spare part of the final devices (section 6.1.1).
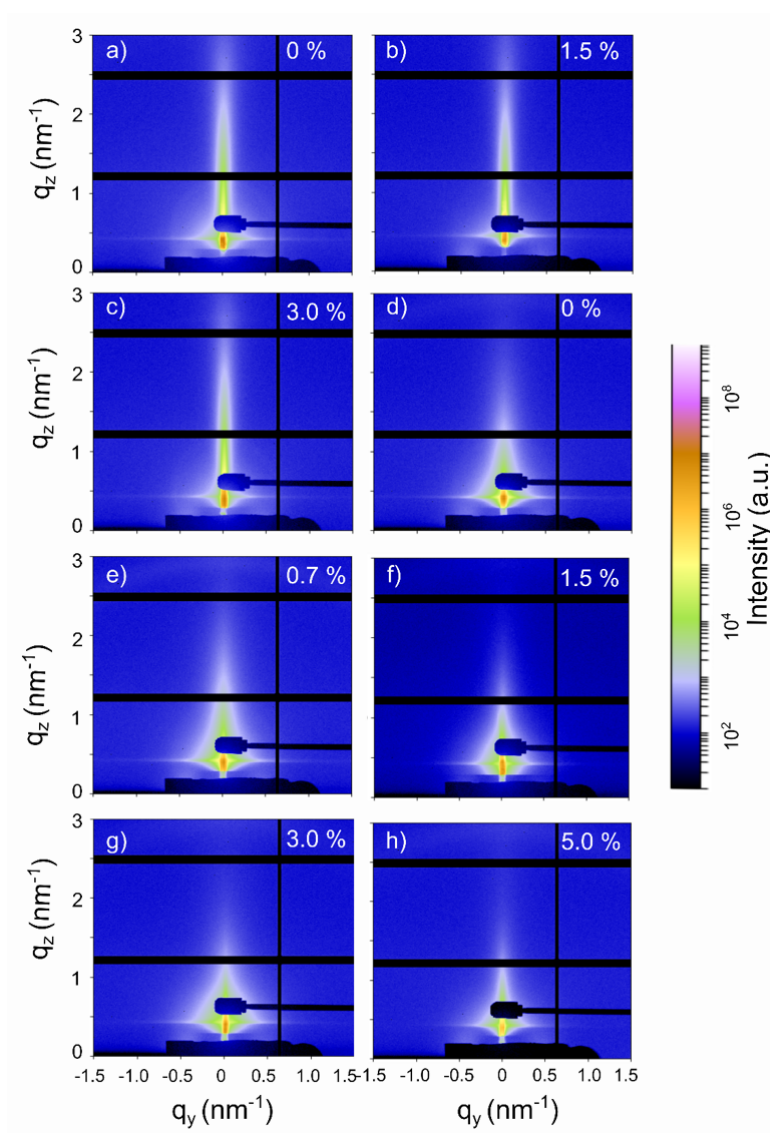
6.1.1 Inner and surface morphology

Figure 6.3: *2D GISAXS data of BHJ films: a)-c) PTB7-Th:PC$_{71}$BM and d)-h) PffBT4T-2OD:PC$_{71}$BM films with different blend ratio of PBDTTPD-COOH. The specular peak is shielded with a rectangular beamstop. The black vertical and horizontal stripes are intermodal gaps of the detector. Reprinted with permission from Ref. [144]. Copyright 2020 American Chemical Society.*

The inner film morphology of BHJ films has an important impact on the device perfor-

mance. The morphology with small scale interpenetrating domains will allow for an efficient exciton splitting, but could also enhance nongeminate recombination, which would cause a lower fill factor (FF) [25, 40, 71]. Large domains induced by a strong phase separation will reduce nongeminate recombination, but cause a less efficient charge carrier generation, which would lower the J_{sc} [40]. Here, GISAXS is applied to probe the inner
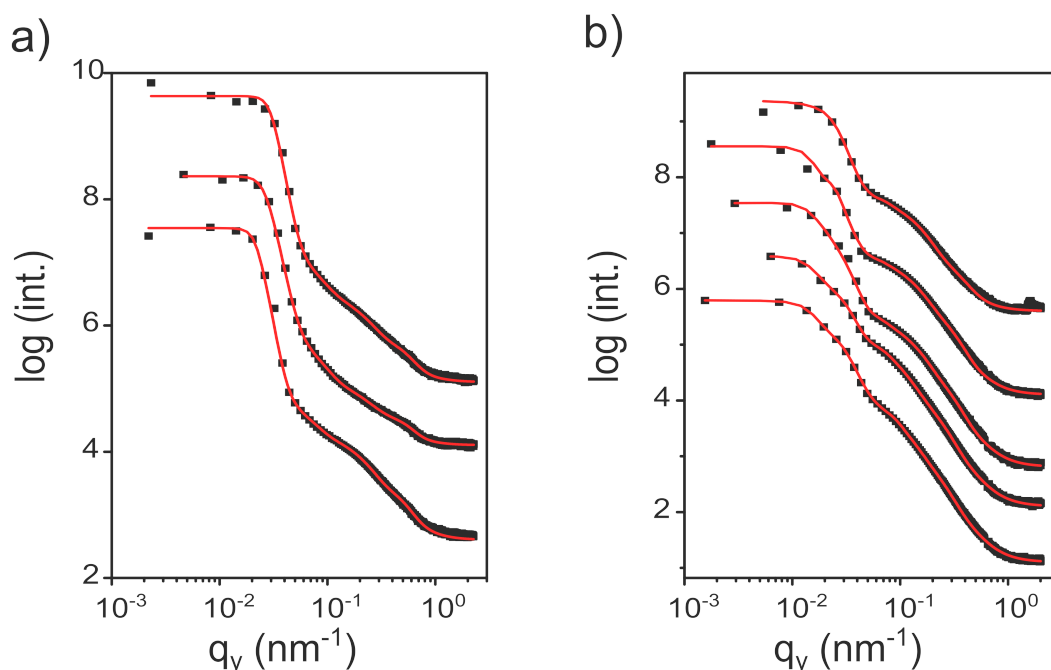

Figure 6.4: *Horizontal line cuts (black solid squares) and fits (red curves) of 2D GISAXS data: a) PTB7-Th:PC$_{71}$BM films with different ratios of the third component (0 wt%, 1.5 wt%, and 3.0 wt% from bottom to top); b) PffBT4T-2OD:PC$_{71}$BM films with different ratios of the third component (0 wt%, 0.7 wt%, 1.5 wt%, 3.0 wt% and 5.0 wt% from bottom to top). All curves are shifted along the y axis for clarity of the presentation. Reprinted with permission from Ref. [144]. Copyright 2020 American Chemical Society.*

morphology of the BHJ films. Figure 6.3 displays the two-dimensional (2D) GISAXS data of the BHJ films with different weight ratio of PBDTTPD-COOH as additive. To extract the scattering information of the polymer domains, horizontal line cuts are performed at the critical angle of the respective polymers (PTB7-Th and PffBT4T-2OD). These line cuts are displayed in Figure 6.4. To estimate the characteristic length scales of the polymer domains, the horizontal line cuts are modeled within the framework of the distorted wave born approximation (DWBA) [88]. Best fits (red curves in Figure 2) are achieved by assuming three independent cylindrically-shaped structures within the local monodisperse approximation (LMA) [100, 171]. The resulting fit parameters are shown in Figure 6.5. In the reference PTB7-Th:PC$_{71}$BM film (without third component) the three structures
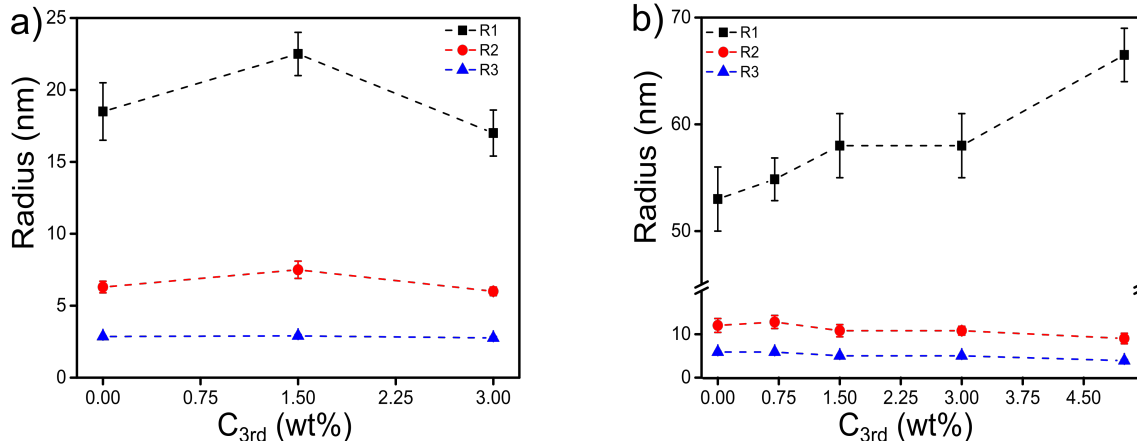
Figure 6.5: *Extracted characteristic length scales: a) polymer domain radius in BHJ films of PTB7-Th:PC$_{71}$BM with different PBDTTPD-COOH content and b) polymer domain radius in BHJ films of PffBT4T-2OD: PC$_{71}$BM with PBDTTPD-COOH content. Blue, red and black colors represent three substructures in the samples, respectively. Reprinted with permission from Ref. [144]. Copyright 2020 American Chemical Society.*

have radii of 19 ± 2 nm, 6.3 ± 0.4 nm and 2.9 ± 0.2 nm, respectively. When 1.5 wt% of PBDTTPD-COOH is added to the PTB7-Th:PC$_{71}$BM film, the polymer domain radii increase to 23 ± 2 nm, 7.5 ± 0.6 nm, and 2.9 ± 0.1 nm, respectively. A further increase of the PBDTTPD-COOH content to 3.0 wt% reduces the domain radii to 17 ± 2 nm, 6.0 ± 0.3 nm and 2.8 ± 0.1 nm, respectively.

In case of the PffBT4T-2OD:PC$_{71}$BM series the behavior is different. The largest polymer structure becomes successively bigger from 53 ± 3 nm to 67 ± 3 nm, when the amount of PBDTTPD-COOH is increased from 0 wt% to 5 wt%. The middle size polymer structure has its largest value of 13 ± 1 nm at 0.7 wt% of PBDTTPD-COOH. The small sized polymer structure is almost not affected by the addition of the third component. Considering characteristic exciton diffusion lengths in OPV (10 to 20 nm) [172]. We conclude that the third component does not drastically change the domain sizes to an extend which would be easily attributed to an improved exciton splitting. However, all films have domains, which are well within the favorable range (10-20 nm) [173] for exciton splitting so that high currents can be expected. Moreover, the morphology with the largest domains (PTB7-Th:PC$_{71}$BM at 1.5 wt% and PffBT4T-2OD:PC$_{71}$BM at 0.7 wt% of PBDTTPD-COOH) can be expected to show the largest *FF* values, which can contribute to higher *PCE* values.

The surface morphology of the BHJ films is studied by atomic force microscopy (AFM) measurements. The height images are shown in Figure 6.6a-i and the surface roughness is extracted from the AFM images and displayed in Figure 6.6j-k. The reference films,
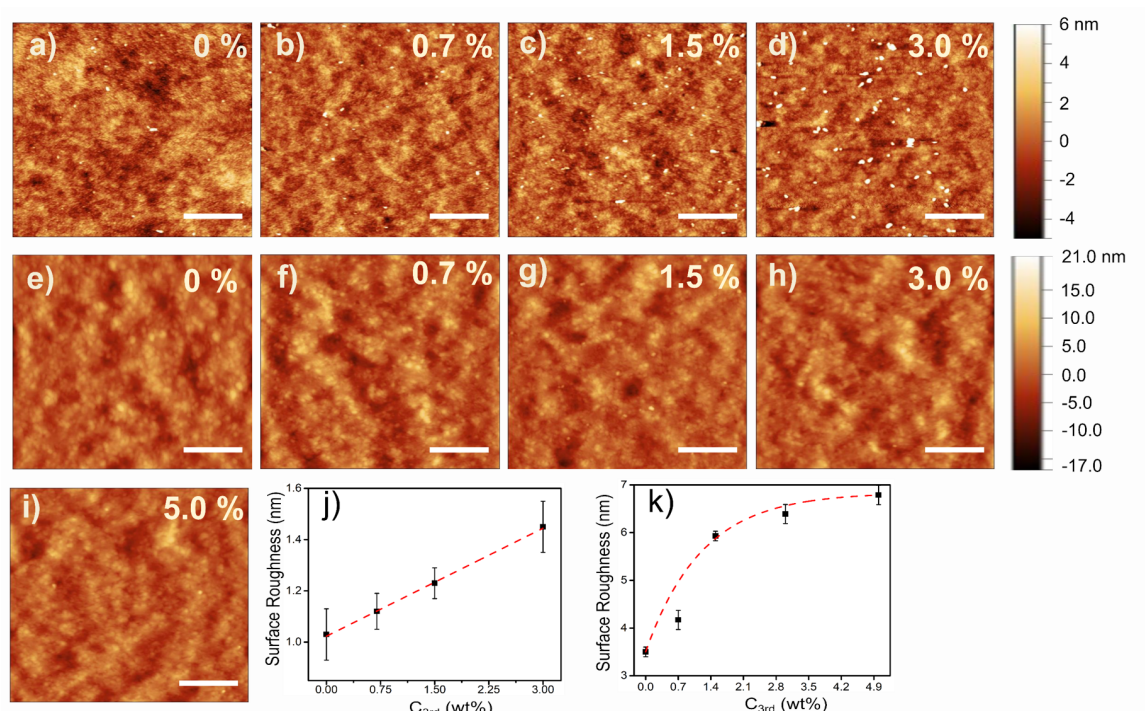
Figure 6.6: *AFM height images of BHJ films: a-d) PTB7-Th:PC$_{71}$BM and e-i) PffBT4T-2OD:PC$_{71}$BM films with different ratios of PBDTTPD-COOH. The scale bar is 500 nm. j-k) Corresponding root mean square (RMS) surface roughness. Reprinted with permission from Ref. [144]. Copyright 2020 American Chemical Society.*

namely pure PTB7-Th:PC$_{71}$BM and PffBT4T-2OD:PC$_{71}$BM films, are slightly smoother than the films with the added third component. Moreover, the films are getting rougher when the amount of PBDTTPD-COOH is increased. We consider that the roughness increase is possibly induced by molecule aggregations in the BHJ films, such as PBDTTPD-COOH aggregations via hydrogen bonds, or D and A phase separation in the presence of high content of the third component. However, from the AFM images it is difficult to precisely figure out which component are located there. On a large scale, the surface morphology is investigated with optical microscopy (OM) and the images are shown in Figure 6.7. It can be seen that more black dots appear on the surface of the BHJ films when increasing the PBDTTPD-COOH content, which indicate molecule aggregations in the films.

6.1.2 Polymer crystallinity

To investigate the influence of the third component on the crystalline structures of the BHJ films, GIWAXS measurements are performed. The 2D GIWAXS data are shown in Figure 6.8 and corresponding sector integrals are displayed in Figure 6.9. For a quantitative
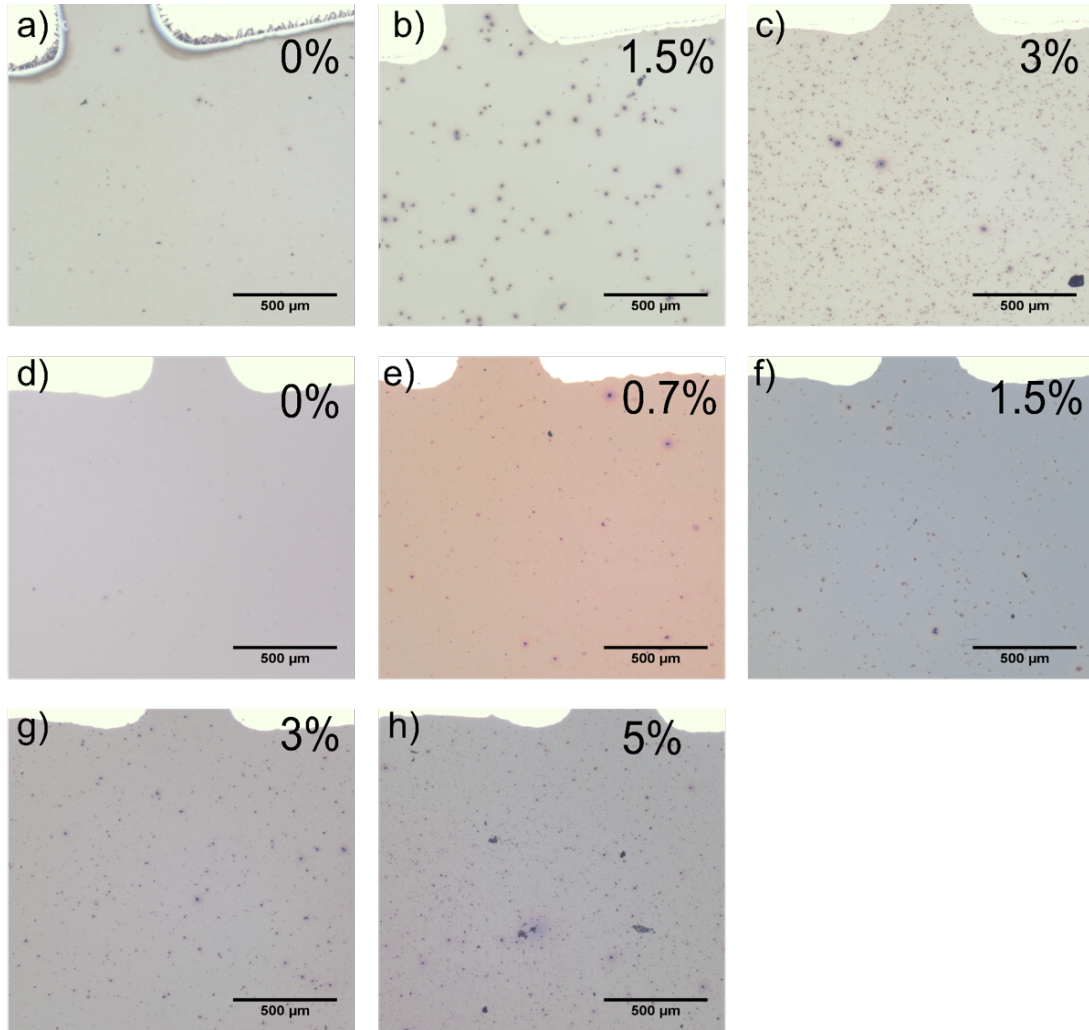
Figure 6.7: *Optical images of BHJ films with different blend ratios of PBDTTPD-COOH. a)-c) PTB7-Th:PC$_{71}$BM samples containing 0 wt%, 1.5% and 3.0 wt% PBDTTPD-COOH. d)-h) PffBT4T-2OD:PC$_{71}$BM samples containing 0 wt%, 0.7 wt%, 1.5 wt%, 3.0 wt% and 5.0 wt% PBDTTPD-COOH. The top bright part is the metal electrode of devices.*

analysis, the cuts are fitted with Gaussian functions. The extracted mean q-positions and full width at half-maximum (FWHM) values are summarized in Table 6.1. In Table 1, we can see that the binary PTB7-Th:PC

In organic solar cells, the polymer crystal orientation must be taken into account, as it is strongly related to the charge mobility in the devices [174]. Hole mobilities are known to be higher along the polymer backbones and in the direction of the π-π stacking than along the side chains [158, 175]. Therefore, a face-on orientation is more favorable to obtain higher charge mobility than an edge-on orientation in the solar cells, where the charge carriers are collected at the front and back electrodes [176, 177]. In this work, the thicknesses of PTB7-Th based BHJ films are 100 ± 5 nm, while PffBT4T-2OD
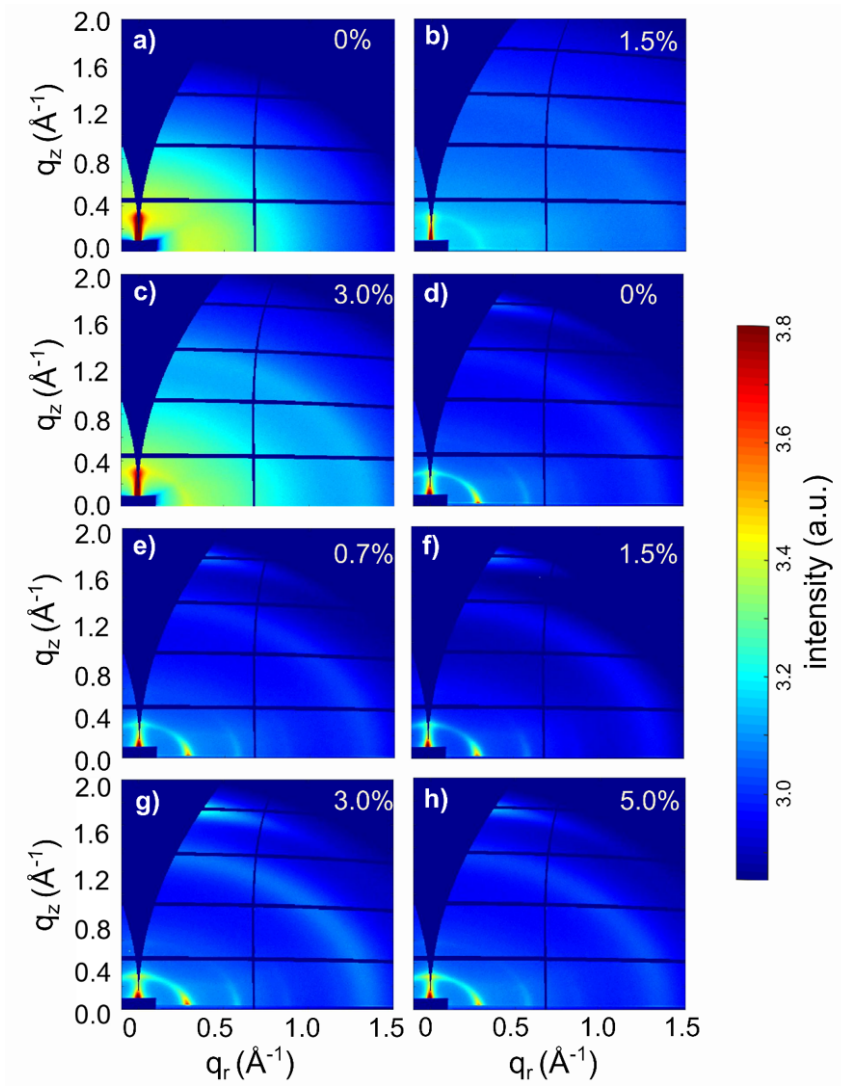
Figure 6.8: *2D GIWAXS data of BHJ films: a)-c) PTB7-Th:PC$_{71}$BM and d)-h) PffBT4T-2OD:PC$_{71}$BM films with different ratios of PBDTTPD-COOH as indicated. The vertical and horizontal black stripes are due to the inter-module gaps of the detector. Reprinted with permission from Ref. [144]. Copyright 2020 American Chemical Society.*

based films are 200 $\pm$ 7 nm thick. Thus, we consider that doping PBDTTPD-COOH doesn't affect the film thickness. The detected film volume via GIWAXS measurements should be the same in each series. Here, we take the intensity ratio of in-plane (100) Bragg peak and out-of-plane (100) Bragg peak as an index to quantify the ratio between face-on and edge-on oriented crystallites in the films. As seen in Table 6.1, the PTB7-Th:PC$_{71}$BM film with 1.5 wt% PBDTTPD-COOH and the PffBT4T-2OD:PC$_{71}$BM film with 0.7 wt% PBDTTPD-COOH exhibit the highest values of this ratio (0.37 and 5.61) in the corresponding series. Thus, the third component influences the crystal orientation and face-on oriented crystallites are enhanced by the addition of the third component.
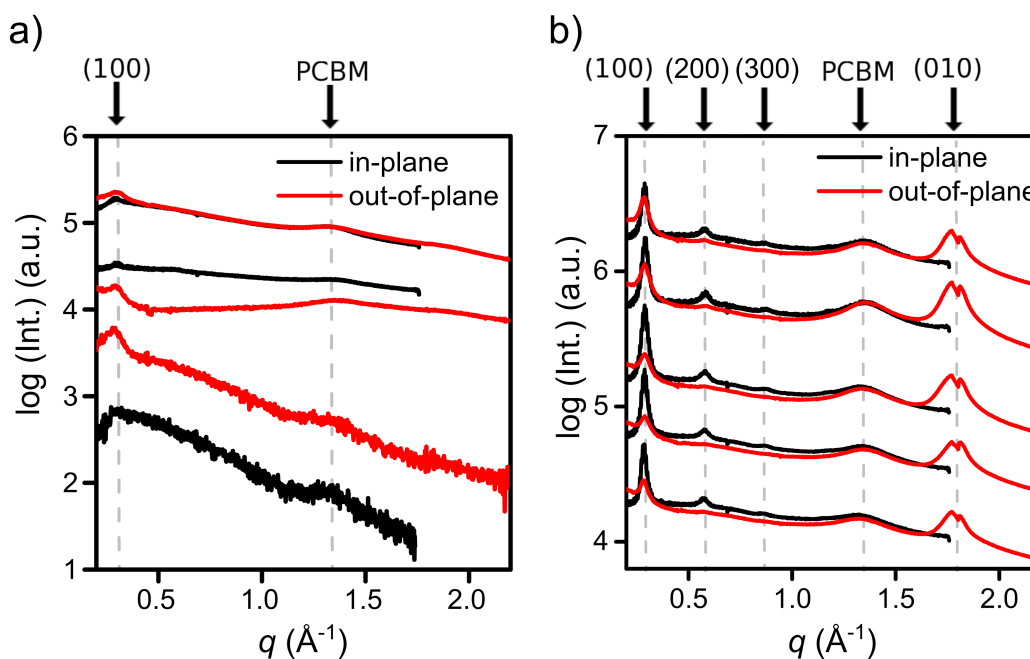
Figure 6.9: *Horizontal (black curves) and vertical (red curves) sector integrals of 2D GI-WAXS data for BHJ films with different blend ratios of PBDTTPD-COOH. From bottom to top in the a) PTB7-Th:PC$_{71}$BM samples containing 0 wt%, 1.5% and 3.0 wt% PBDTTPD-COOH from bottom to top. b) PffBT4T-2OD:PC$_{71}$BM samples containing 0 wt%, 0.7 wt%, 1.5 wt%, 3.0 wt% and 5.0 wt% PBDTTPD-COOH from bottom to top. Reprinted with permission from Ref. [144]. Copyright 2020 American Chemical Society.*

Correspondingly, the best performing solar cells could be expected in case of adding 1.5 wt% PBDTTPD-COOH to PTB7-Th:PC$_{71}$BM film and 0.7 wt% PBDTTPD-COOH to PffBT4T-2OD:PC$_{71}$BM films.

6.2 Solar cell performances

For investigating the solar cell performance, devices with an architecture of glass/ITO/PE-DOT:PSS/BHJ (with or without the third component)/LiF/Al/Mg are fabricated and characterized. The representative $J-V$ curves of all devices are shown in Figure 6.10. The external quantum efficiency (EQE) spectra of reference cells and optimal devices are recorded over a wide range of 300-800 nm (Figure 6.11), corresponding well to the absorption of the relevant materials. The average performance values of each device type are summarized in Table 6.2. It can be seen that the PCEs of the reference samples are slightly lower than the previous reports [103, 178], which is attributed to using the

	$C_{3rd}{}^a$	Out-of-plane (100)			Out-of-plane (010)			In-plane(100)			R^b
		q-value	FWHM	Int.	q-value	FWHM	Int.	q-value	FWHM	Int.	
	[%]	[Å^{-1}]	[Å^{-1}]	[a.u.]	[Å^{-1}]	[Å^{-1}]	[a.u.]	[Å^{-1}]	[Å^{-1}]	[a.u.]	[a.u.]
a)	0	0.28	0.10	673	–	–	–	–	–	–	–
	1.5	0.30	0.07	222	–	–	–	0.30	0.09	82	0.37
	3.0	0.30	0.09	697	–	–	–	0.30	0.08	245	0.35
b)	0	0.28	0.04	749	1.78	0.12	649	0.29	0.03	2871	3.83
	0.7	0.29	0.05	561	1.79	0.14	728	0.29	0.03	3150	5.61
	1.5	0.29	0.05	631	1.78	0.14	835	0.29	0.04	3131	4.96
	3.0	0.29	0.05	1239	1.78	0.13	1434	0.29	0.04	3037	2.45
	5.0	0.29	0.05	1302	1.78	0.12	851	0.30	0.04	2101	1.61

Table 6.1: *Extracted quantities from GIWAXS data analysis of a) PTB7-Th:PC$_{71}$BM series and b) PffBT4T-2OD:PC$_{71}$BM series. ^{a}the concentration of the third component; ^{b}the scattering intensity ratio of in-plane (100) to out-of-plane (100). Reprinted with permission from Ref. [144]. Copyright 2020 American Chemical Society.*

equivalent solvent of CB and DMSO (10:1) to keep the concentration of donor and acceptor constant. As to be expected, the V_{oc} values in each series are hardly affected by the third component. In the PTB7-Th:PC$_{71}$BM series, optimal devices are obtained from a BHJ with 1.5 wt% of PBDTTPD-COOH, which show a *PCE* of 10 %. Compared to other devices of the PTB7-Th:PC$_{71}$BM series the photovoltaic parameters J_{sc} and *FF* are improved by 10 % and 7 %, respectively. The increasing trend of J_{sc} is consistent with the calculated result from EQE (Figure 6.11a).In the PffBT4T-2OD: PC$_{71}$BM series, the best performance is achieved by adding 0.7 wt % PBDTTPD-COOH. It causes a *PCE* increase from 7.8 % to 8.9 % due to an increase in J_{sc} (17.6 to 18.3 mA/cm^2) and *FF* (59 to 64 %). A similar trend of JSC was observed in the case of the EQE spectra and the respective calculated values of J_{sc} (Figure 6.11b) as well. Thus, in both types of low band gap BHJ series the device performance can be enhanced by adding a suitable amount of the third component, and the improvement mainly originates from the photovoltaic parameter of J_{sc} and *FF*. Samples with higher amount of PBDTTPD-COOH result in a decrease in all photovoltaic parameters.

Based on the GISAXS and GIWAXS results, the optimal conditions for J_{sc} and *FF* can be identified. The proper amount of added PBDTTPD-COOH results in more face-on oriented crystallizes in the films, which promote a better charge mobility and charge transport, causing an improved current density. A higher FF is closely related to a better D/A network in the BHJ films [179]. Hereby, the present of the third component leads to a better morphology for exciton dissociation and charge transport in the devices.
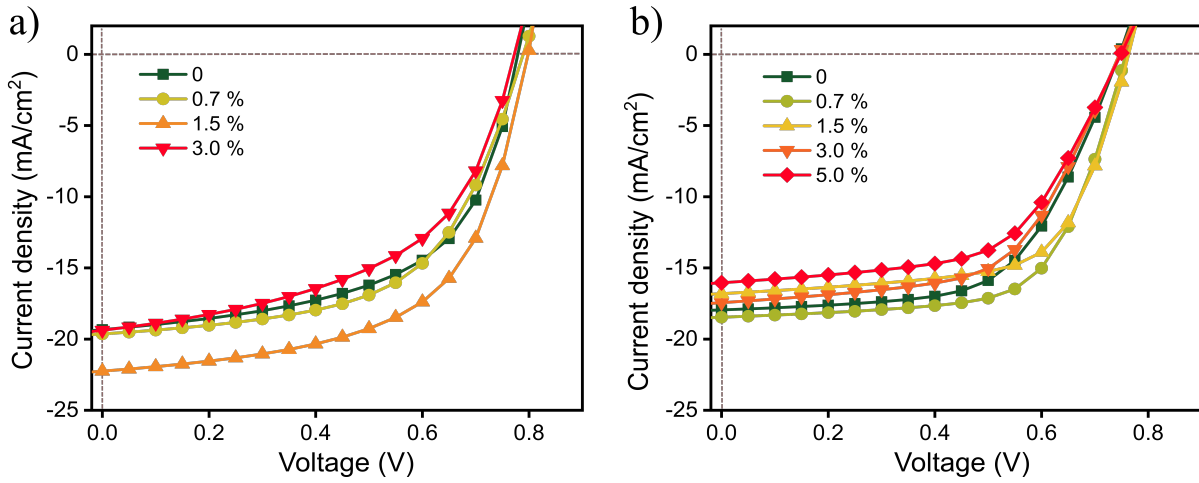
Figure 6.10: *Representative $J-V$ curves of a) PTB7-Th:PC$_{71}$BM devices and b) PffBT4T-2OD:PC$_{71}$BM devices with different ratios of PBDTTPD-COOH as indicated. Reprinted with permission from Ref. [144]. Copyright 2020 American Chemical Society.*

	C$_{3rd}$[a]	J_{sc}	V_{oc}	FF	PCE
	[%]	[mA/cm^2]	[V]	[%]	[%]
a)	0	18.8 ± 0.5	0.781 ± 0.001	55 ± 1	8.3 ± 0.1
	0.7	19.7 ± 0.3	0.783 ± 0.001	56 ± 1	8.8 ± 0.1
	1.5	20.1 ± 0.5	0.790 ± 0.001	59 ± 1	10.1 ± 0.1
	3.0	19.1 ± 0.4	0.783 ± 0.001	50 ± 1	7.5 ± 0.2
b)	0	17.6 ± 0.8	0.754 ± 0.003	59 ± 1	7.8 ± 0.2
	0.7	18.3 ± 0.4	0.765 ± 0.004	64 ± 1	8.9 ± 0.1
	1.5	16.7 ± 0.4	0.766 ± 0.004	65 ± 1	8.3 ± 0.1
	3.0	16.3 ± 0.4	0.754 ± 0.009	60 ± 1	7.3 ± 0.1
	5.0	16.0 ± 0.4	0.753 ± 0.005	57 ± 1	6.8 ± 0.1

Table 6.2: *Mean photovoltaic parameters of devices with different amount of PBDTTPD-COOH. a) PTB7-Th:PC$_{71}$BM series and b) PffBT4T-2OD:PC$_{71}$BM series. [a] the concentration of the third component. Reprinted with permission from Ref. [144]. Copyright 2020 American Chemical Society.*

6.3 Device stability

To investigate the impact of the third component on the device stability, accelerated long-term stability tests are carried out for the reference devices and for the optimized devices of each series [180, 181]. The I-V measurements are performed periodically on the device for around 4 h under illumination in ambient conditions. The temporal evolution of the
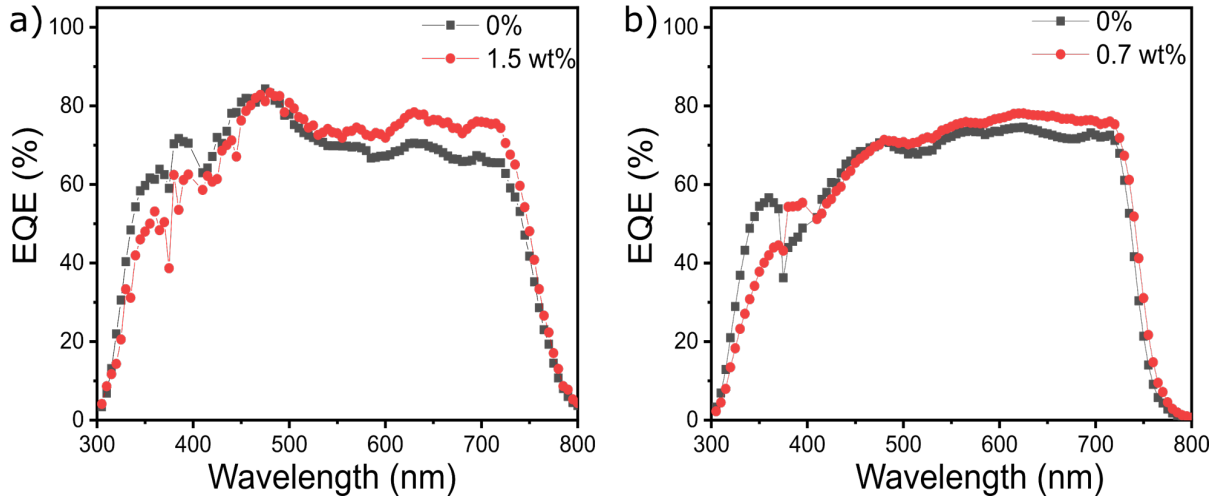
Figure 6.11: *EQE spectra of a) PTB7-Th:PC$_{71}$BM reference cell (black) and optimal ternary device (red) and of b) PffBT4T-2OD:PC$_{71}$BM reference cell (black) and optimal ternary device (red). Reprinted with permission from Ref. [144]. Copyright 2020 American Chemical Society.*

photovoltaic parameters J_{sc}, V_{oc}, FF and PCE is extracted from the I-V measurements and plotted in Figure 6.12. To realize accelerated degradation, the devices are not encapsulated. Thus, J_{sc}, V_{oc} and FF decay and cause a degradation of PCE over time. The addition of the third component increases the stability of a PTB7-Th:PC$_{71}$BM device significantly. A value of 80 % of PCE (T80 lifetime)[68] is maintained after 3.7 h in the devices with added third component, whereas the reference devices show only 35 % of the initial PCE at that time. Thus, the T80 lifetime is increased to about 3.7 h by adding PBDTTPD-COOH as compared to 0.35 h in the original binary device. The increase in stability originates from a more stable J_{sc} and FF. In ternary PffBT4T-2OD:PC$_{71}$BM devices, the PCE decreases to 78 % of its original PCE after 4.5 h as compared with 72 % in case of the reference sample. Also in this series, the more stable PCE is mainly caused by an improved stability in J_{sc} and V_{oc}. Also in the ternary devices the T80 value of 4.3 h is significantly improved as compared to the binary reference devices (T80 ~2.6 h). Thus, PBDTTPD-COOH works as a morphological stabilizer, which is beneficial to maintain the interpenetrating network of donor and acceptor materials in the BHJ films to prevent morphological degradation commonly causing aging in solar cells with BHJ morphology [38].
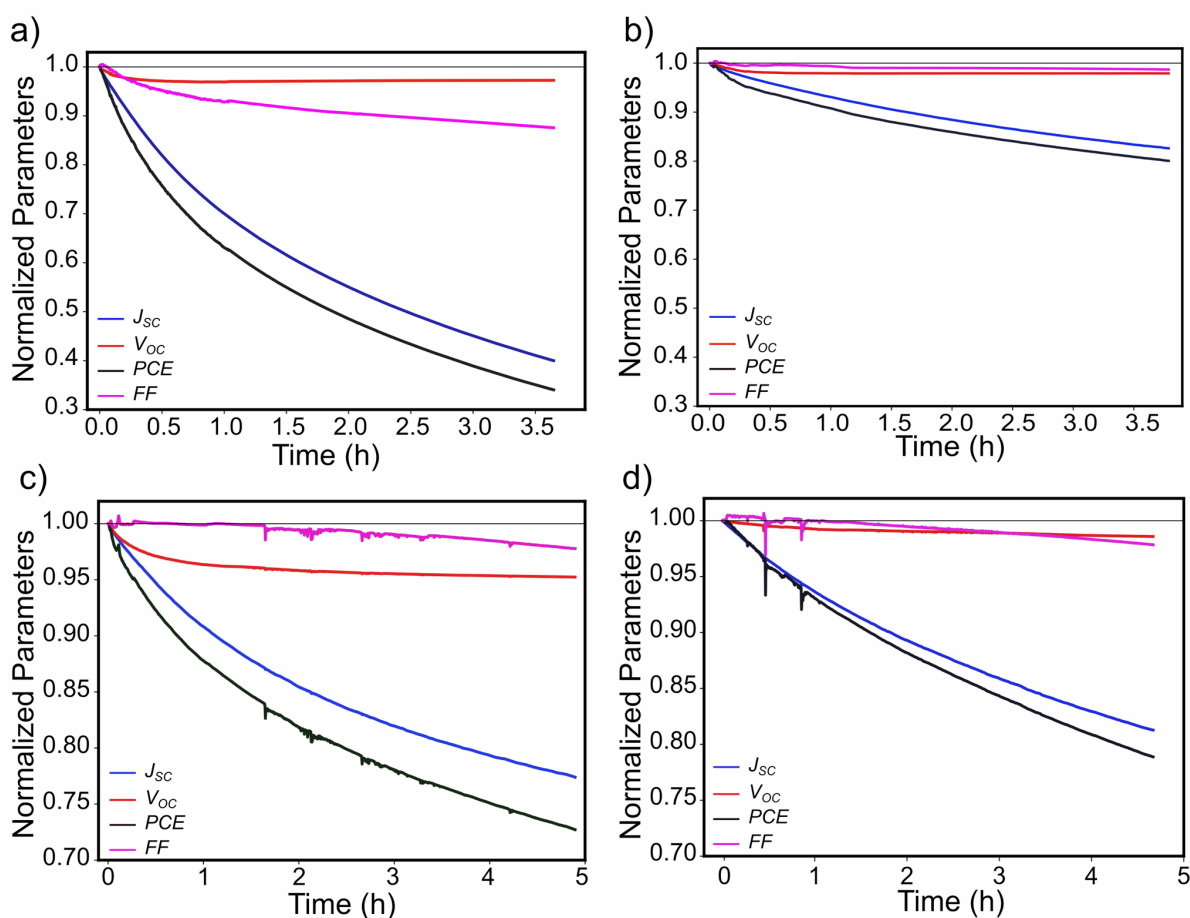
Figure 6.12: *Time evolution of the normalized photovoltaic parameters (J_{sc}, V_{oc}, FF and PCE) probed under illumination in ambient conditions. a) PTB7-Th:PC$_{71}$BM reference cell, b) PTB7-Th:PC$_{71}$BM with PBDTTPD-COOH, c) PffBT4T-2OD:PC$_{71}$BM reference cell, d) PffBT4T-2OD:PC$_{71}$BM with PBDTTPD-COOH. J_{sc}, V_{oc}, FF and PCE are normalized to their maximum values. Reprinted with permission from Ref. [144]. Copyright 2020 American Chemical Society.*

6.4 Summary

To improve the compatibility of donor and acceptor materials in the photovoltaic layer, a conjugated polymer PBDTTPD-COOH is applied as a third component into two series of low band gap binary organic solar cells, namely PTB7-Th:PC$_{71}$BM and PffBT4T-2OD:PC$_{71}$BM. To figure out the effects of the third component on the BHJ films, inner and surface film morphology of binary and ternary films are probed by GISAXS and AFM measurements, respectively. The results present that properly doping PBDTTPD-COOH does not significantly affect the polymer domain sizes, especially for domains in the size of charge diffusion length. However, further adding the dopant will lead

to an aggregation in the film, which shows high roughness in the AFM measurements. Besides, GIWAXS characterization is employed to track the polymer crystallinity with the addition. It has been found that the size of polymer crystallites and crystal orientation are modified by doping PBDTTPD-COOH. More face-on oriented crystallites are formed in the ternary films, which is favorable for charge transport. When the corresponding devices are assembled, we observe that J_{sc} and FF are improved by an adding optimal content PBDTTPD-COOH, which is caused by the optimized polymer crystallinity and morphology. Furthermore, the stability tests show that PBDTTPD-COOH significantly improves the device stability. The T80 lifetime values of the optimized devices (3.7 and 4.3 h) enlarge by the addition of PBDTTPD-COOH as compared to the corresponding references (0.35 and 2.6 h). Therefore, our study presents a new and efficient strategy to optimize crystallinity and compatibility of BHJ materials as well as device stability, and could thereby contribute to further development of OSCs towards real world applications.

7 Influence of additives on the stability of PTB7-Th:PC$_{71}$BM based devices

Our previous work shows approaches to optimize the BHJ morphology to achieve high efficiency. The polymer composition at the interface can be modified by inserting a hydrophobic interfacial layer in the device architecture (chapter 5). The modified polymer gradient at the interface makes the charge transport more effective, resulting in an increase of J_{sc}. In chapter 6, doping PBDTTPD-COOH in the binary BHJs of PTB7-TH:PC$_{71}$BM and PffBT4T-2OD:PC$_{71}$BM improves both the device efficiency and stability. The morphology, crystallite orientation and size are optimized for better device performance by the proper amount of the third component. Aside from optimizing the initial PCE of solar cells, their long-term stability is considered as a key factor for successful commercial use of OSCs [38, 182, 183]. Therefore, more and more attention is paid to understand the degradation mechanism of OSCs [184–186]. In general, the various degradation processes occurring in OSCs can be roughly divided into two types, namely chemical and physical degradation [38, 187]. The chemical degradation is mainly attributed to the reaction between water and oxygen with the materials in the device [37, 188]. Hence, encapsulation techniques and more stable materials are being developed to avoid these problems. In contrast, physical degradation is considered to arise mainly from the morphology deterioration of bulk heterojunction (BHJ) films [38]. However, the mechanism behind the morphological change in the BHJ layer is not fully understood and therefore, needs to be further explored.

Solvent additives are widely used to modify the morphology of BHJ films to achieve an optimal interpenetrating network of donor and acceptor materials, which is beneficial for the exciton dissociation and charge transport [48, 189–191]. In previous studies, the additives were classified as either non-aromatic or aromatic. [192] Both types of solvent additives need to fulfil two features: 1) their boiling point (bp.) has to be much higher than the one of the host solvent and 2) one component of the blend has to be more soluble in the additive than the other one [103, 193]. A famous example of non-aromatic additives is 1,8-diiodooctane (DIO), which has been applied in various devices using low-band gap polymers to obtain high efficiencies [103, 193, 194]. Due to its high bp. of 332.5 °C and selective solubility for fullerenes, a highly phase-separated morphology can be developed to balance charge carrier mobility and reduce charge recombination in bulk heterojunction (BHJ) solar cells [192, 195]. Recently, o-chlorobenzaldehyde (CBA) with a bp. of 212 °C has been used as an aromatic additive, which is beneficial for 200 up to 300 nm thick active layers to form nanoscale morphologies [47]. It has been reported in a previous work, that the residual solvent additive in the final device leads to an obvious decay of the fill factor (FF) during operation when the leftover solvent is escaping from the device under vacuum [40]. Therefore, the effect of different solvent additives on the stability of an optimized active layer morphology of OSCs should be identified.

In the present chapter, we explore the BHJ morphology changes induced by solvent additives during the device degradation process. Three kinds of devices based on the high-efficiency low-band gap benzodithiophene copolymer mixed with a fullerene derivative (PTB7-Th:PC$_{71}$BM) are fabricated, namely without any solvent additives, with 3 vol% DIO and with 5 vol% CBA.

7.1 In-operando GISAXS measurement

GISAXS measurement can provide lateral structure information from the film on a large range of length scales approximately between 1 nm and 1 μm. Furthermore, kinetic investigations of the film morphology are enabled by a high brilliance X-ray source, such as synchrotron. When the morphology change is monitored with GISAXS, while the solar cell is under illumination, the measurement is called in-operando. In the experiment, *J-V* and GISAXS measurements are performed simultaneously at the same sample. The details are explained in section 3.10.
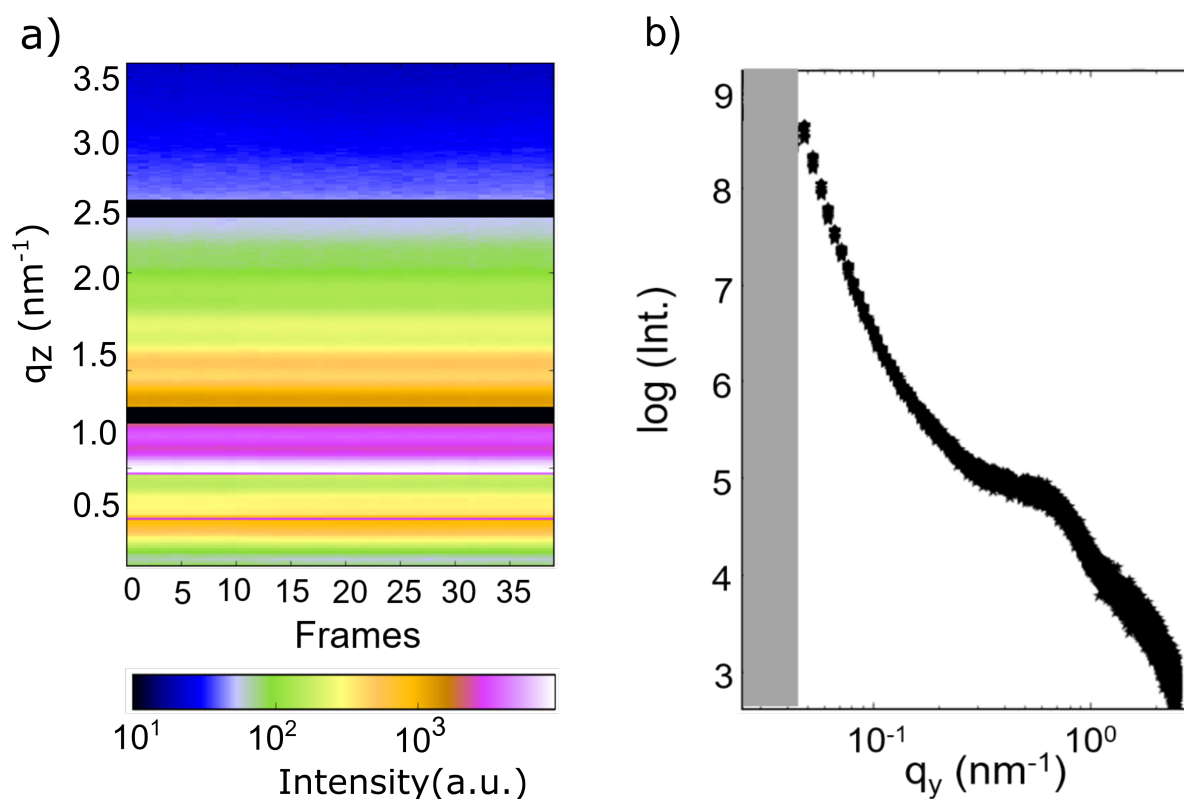
a)

b)

Figure 7.1: *a) Color mapping of vertical line cuts of all 40 GISAXS measurements and b) horizontal line cuts of the 2D GISAXS data stacked, measured during the radiation damage test experiment. The beamstop shielding the detector is indicated by the gray area. (Reprinted with permission from Ref. [71]. Copyright 2019 American Chemical Society.)*

7.1.1 Setup and protocol

In-operando GISAXS is used to investigate the morphology changes during the device aging. All in-operando measurements are performed in a custom-made measurement chamber, which is mounted into the Austrian SAXS beamline of the ELETTRA synchrotron source in Trieste, as described in section 3.10. A pattern mask with 8 illumination holes for the individual solar cell pixels is positioned below the sample to reduce the device temperature as well as the photodegradation. Vacuum conditions are applied to avoid degradation from oxygen and moisture. It should be noted, that with special encapsulation in general organic solar cells can be improved in their lifetimes, however, to match the accessible time scale of a synchrotron radiation experiment, no encapsulation is used. The in-operando GISAXS measurements start with device illumination. The incident X-ray beam with a wavelength of 1.5 Å impinges on the sample at a shallow angle of 0.4°. The sample-detector distance is 1160 mm.

Radiation damage caused by the high-brilliance X-ray beam needs to be taken into

consideration during the measurements with synchrotron radiation. Therefore, a radiation damage test is essential before the real in-operando measurements can be performed. In our test, 40 GISAXS measurements were continuously done at one fixed spot (around 5 mm away from the electrode) of a solar cell with 5 s exposure time for a single measurement. Figure 7.1a shows the corresponding mapping of these 40 measurements by showing the vertical line cuts of all measurements. No changes in the intensity during this exposure time are visible. Furthermore, horizontal line cuts are performed at the Yoneda peak position of PTB7-Th and plotted together in Figure 7.1b. All horizontal line cuts overlap very well. Hence, we conclude that radiation damage do not occur within the total exposure time of 200 s. In the entire in-operando measurement the total exposure time was set to 110 s, so that radiation damage is excluded.

To avoid scattering signals from the metal contacts of the probed solar cells, the devices are aligned in such a way that the X-ray beam impinges on the active layer close to the electrodes. Before illuminating the solar cells, an initial two-dimensional (2D) GISAXS data set is measured (denoted as 0 min). After starting the illumination, current-voltage curves are periodically recorded every 26 s via a source meter for 120 minutes. In parallel, 2D GISAXS data are taken with an exposure time of 5 s after 3, 10, 20, 40, 60, 90 and 120 min of illumination.

7.1.2 BHJ morphology tracking during device aging

The BHJ morphology is closely related with the device performance. To figure out the morphology changes during the device degradation, in-situ GISAXS measurements are performed on the solar cells during the operation process. Figure 7.2 shows the 2D data from the device without additive, with DIO and with CBA. Since the morphological degradation stems mainly from the photoactive layer, horizontal line cuts are performed at the strongest scattering signal (Yoneda region) [196] of PTB7-Th. In order to experimentally determine this Yoneda position, X-ray reflectivity (XRR) measurements were performed on a pure PTB7-Th film with a Siemens D5000 diffractometer at a wavelength of 0.154 nm (Cu-Kα radiation). The XRR curve was fitted using the IGOR Pro program combined with its Motofit plugin. From the XRR fit (Figure 7.3), the scattering length density (SLD) of PTB7-Th was found to be 10.50$\times$10^{-6} Å^{-2}, which corresponded to a density of PTB7-Th of 1.15 g/cm^3 and a critical angle of 0.16°. The respective horizontal line cuts for each device are plotted in Figure 7.4. The horizontal line cuts from the 2D GISAXS data look very similar on the first view, which indicates small changes in the film morphology during aging. To extract the changes, a rigorous data analysis via model fitting is needed. Here, the data are modelled based on the effective interface approximate
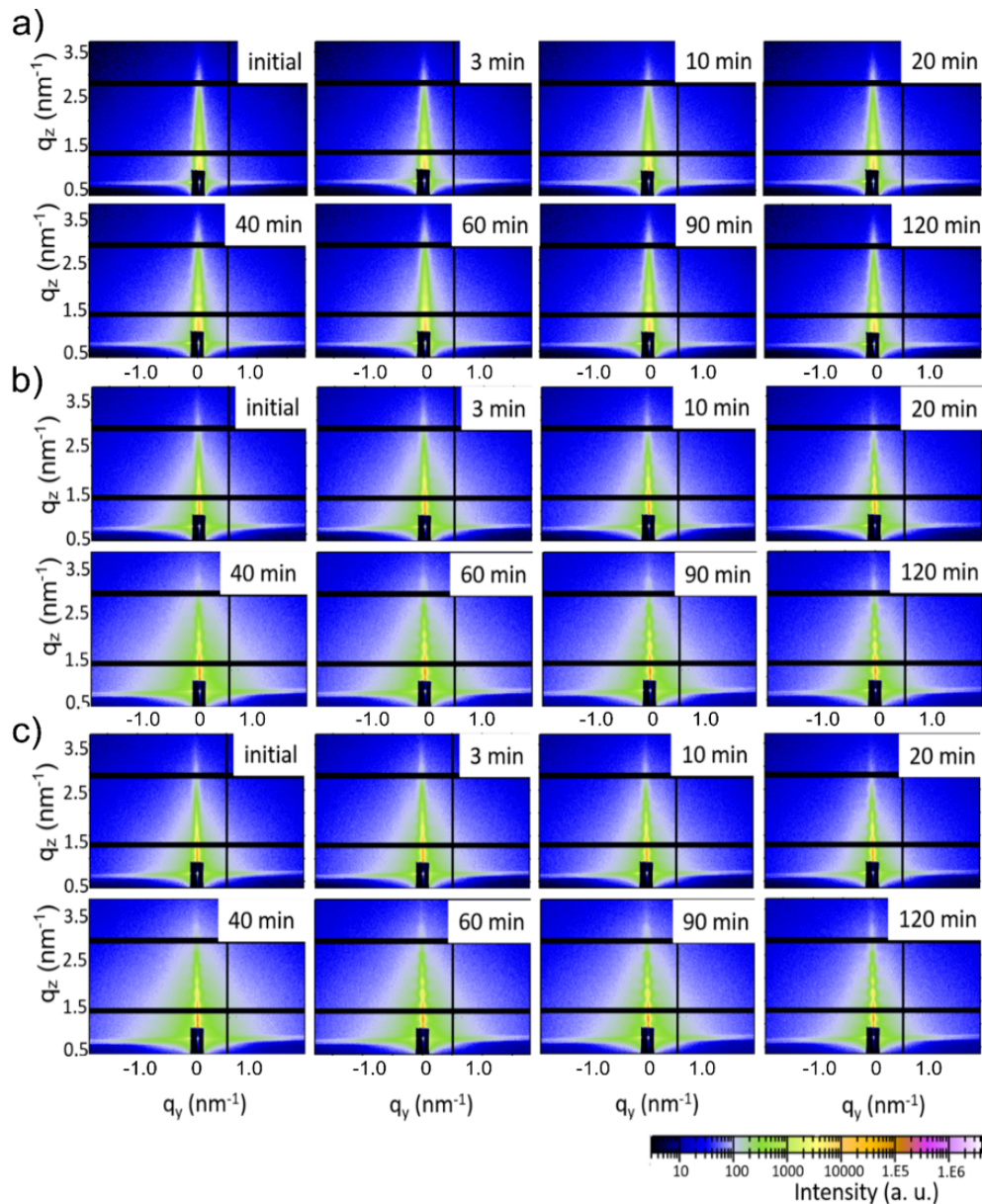
Figure 7.2: *2D GISAXS data of solar cells after different illumination times as indicated: (a) device without additive, (b) device with DIO additive, and (c) device with CBA additive.(Reprinted with permission from Ref. [71]. Copyright 2019 American Chemical Society.)*

and local monodisperse approximation (details are introduced in section 2.3.2). The average structure sizes of polymer domains in the active layer are extracted from the fitting of the horizontal line cuts.

Figure 7.5 shows the size evolution of different structures present in the active layer of the studied device. To fit the horizontal line cuts, we need two characteristic structures for the films prepared with and without solvent additive. Thus, the morphology of active
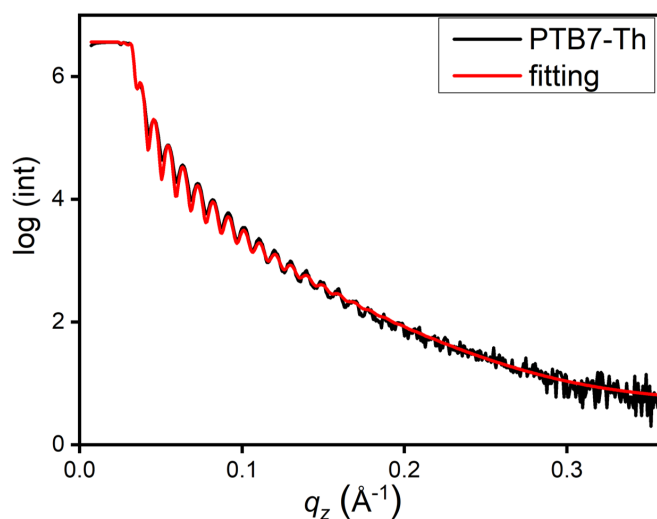
Figure 7.3: *X-ray reflectivity data (black) and the model fit (red) of a pure PTB7-Th film on a silicon substrate.*
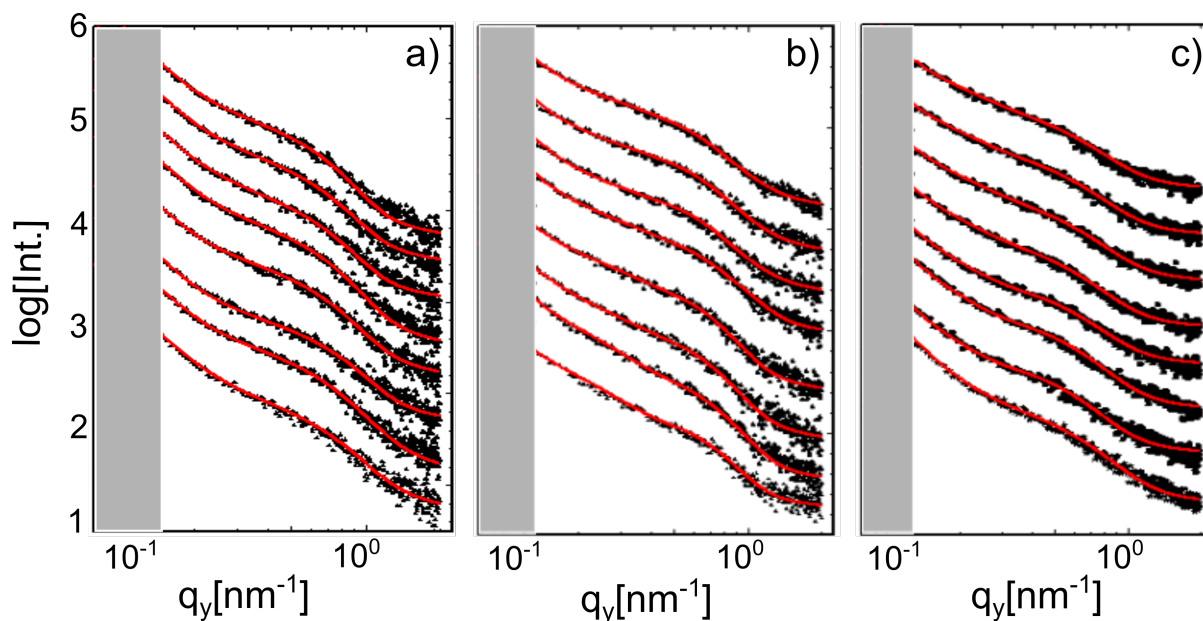

Figure 7.4: *Horizontal line cuts (black dots) and modelling results (red lines) measured for devices without solvent additive (a), with addition of DIO (b) and with CBA (c). From bottom to top: In-operando measurement after 0, 3, 10, 20, 40, 60, 90 and 120 minutes of device operation. The curves are shifted for clarity along the y axis. The area shielded by the beamstop is marked in grey.(Reprinted with permission from Ref. [71]. Copyright 2019 American Chemical Society.)*

layers is modified by the use of a solvent additive as known from literature [197, 198]. For the device fabricated without solvent additive (Figure 2a), the polymer domain sizes grow
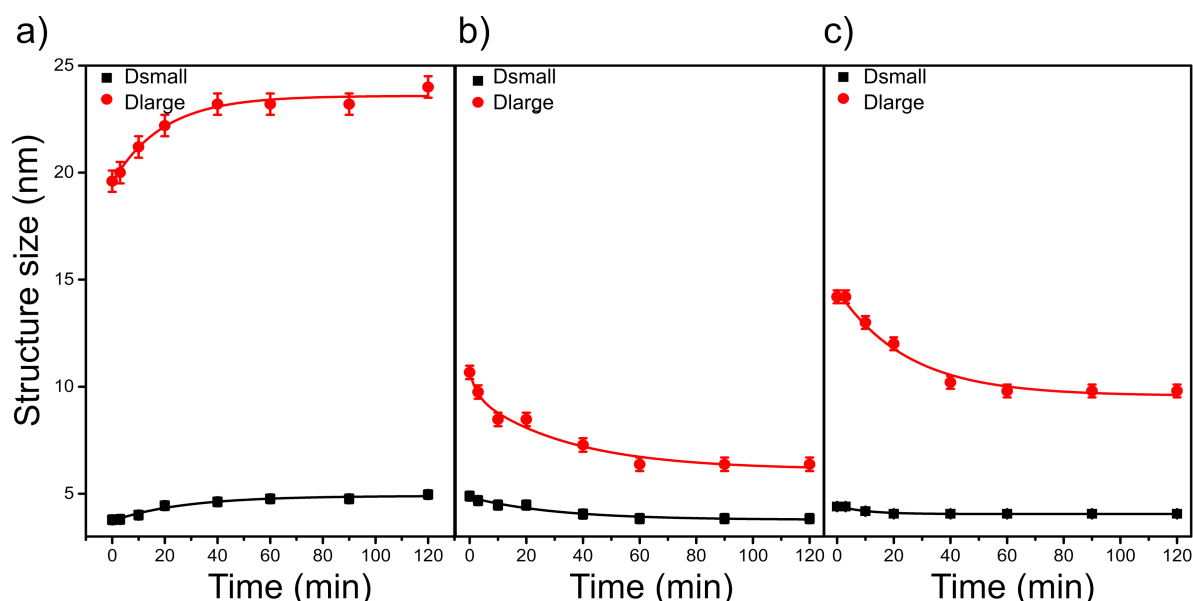
Figure 7.5: *Temporal evolution of diameters of small (black) and large (red) polymer structures present in the devices without additive solvent (a), with DIO (b) and with CBA (c). (Reprinted with permission from Ref. [71]. Copyright 2019 American Chemical Society.)*

with increasing operation time, whereas the devices with solvent additive show the inverse trend of domain shrinkage. According to this, we conclude that solvent additives cause different morphology changes, which could result in different degradation mechanisms, as discussed in the following.

7.2 Photovoltaic performances

The solar cells based on PTB7-Th:PC$_{71}$BM are fabricated as the introductions in the section 4.2.2 and 4.3. The respective photovoltaic parameters of PTB7-Th:PC$_{71}$BM devices are list in Table 7.1 and the J-V curve of the champion device is presented in Figure 7.6. Notably, the mean performance of solar cells are is concluded from 8 or more devices. It can be seen that devices without additive have PCEs of 3.8 %, which is very close to published results [199, 200]. The PCEs of devices with solvent additive are around 8.0 %, which match also with reported results of PTB7-Th:PC$_{71}$BM solar cells [197, 201, 202].

Figure 7.7 shows the temporal evolution of the photovoltaic parameters of the solar cell without solvent additive. In the beginning, the open-circuit voltage (V_{oc}) shows the most pronounced decrease, but stabilizes quickly and does not fall below 90 % of its original value. In contrast, the decay of the fill factor (FF) and J_{sc} become the main factors of the degradation only after around 20 minutes of operation. Especially, the decay rate

	J_{sc} [mA/cm^2]	V_{oc} [V]	PCE [%]	FF	PCE_{max} [%]
without	13.91 ± 0.25	0.73 ± 0.01	3.8 ± 0.1	0.38 ± 0.01	3.9
DIO	20.72 ± 0.12	0.71 ± 0.01	7.8 ± 0.1	0.53 ± 0.01	7.9
CBA	20.22 ± 0.07	0.75 ± 0.01	8.3 ± 0.2	0.54 ± 0.01	8.5

Table 7.1: *Mean photovoltaic parameters of devices with different solvent additives. (Reprinted with permission from Ref. [71]. Copyright 2019 American Chemical Society.)*

of the FF is quickly overpassed by that of the J_{sc}, which then dominates the entire device degradation (see Figure 7.12). Such a decrease in the J_{sc} can be attributed to the increasing polymer domain sizes, which reduces the chances of charge carrier separation and thereby reached J_{sc}. A similar behavior was already reported by Schaffer et al. for organic solar cells based on P3HT:PC$_{61}$BM [39].

Figure 7.5b and 7.5c reveal the temporal evolution of characteristic structure sizes in devices with solvent additive DIO and CBA. Irrespective of the type of additive, the polymer domain sizes decrease during device operation. It was proposed by Schaffer et al. that such a decrease is caused by the evaporation of the solvent additive [40]. As a result, the connection of neighboring polymer domains in the interpenetrating network is
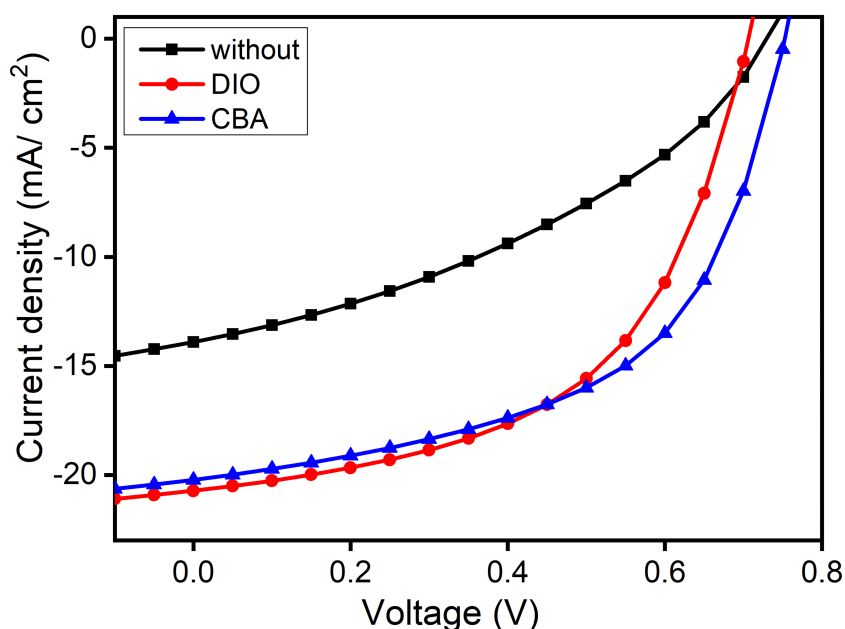

Figure 7.6: *Representative J-V curves of PTB7-Th: PC$_{71}$BM devices without and with additives solvent, as indicated. (Reprinted with permission from Ref. [71]. Copyright 2019 American Chemical Society.)*

lost [40]. Such disconnected domains, which are like isolated islands in the active layer, will act as traps for free charge carriers. Therefore, smaller domain sizes result in higher chances of charge carrier recombination, thereby reducing the FF. However, a decrease in the domain sizes can also cause a more efficient exciton splitting, which results in more free charge carriers to be transported and collected. Consequently, a trade-off between J_{sc} and FF would occur in shrinking domains [40]. We find this trend also in the present J-V characteristics. Figure 7.7b and 7.7c show the time-resolved photovoltaic parameters of the devices with solvent additive DIO and CBA. The FF decays the strongest in case of CBA solvent additive similar to what was reported earlier for OSCs based on PCPDTBT:PC$_{71}$BM with 1,8-octanedithiol (ODT: bp. 270 °C) [40]. Meanwhile, a slight increase of J_{sc} can be observed from 80 min to 120 min (Figure 7.7c), which is due to more collected free charge carriers from the smaller domains. In contrast, for DIO the FF does not play the key role in the degradation process for the full period under observation. For the first 2400 s, the FF decay dominates the performance of this solar cell. At longer time scales, the FF decrease is less pronounced, while the J_{sc} exhibits a strong decrease, which dominates degradation. Thus, the J_{sc} decay dominates the degradation of the device without solvent additive, while the main decay factor is the decay of the FF in the sample with solvent additives.
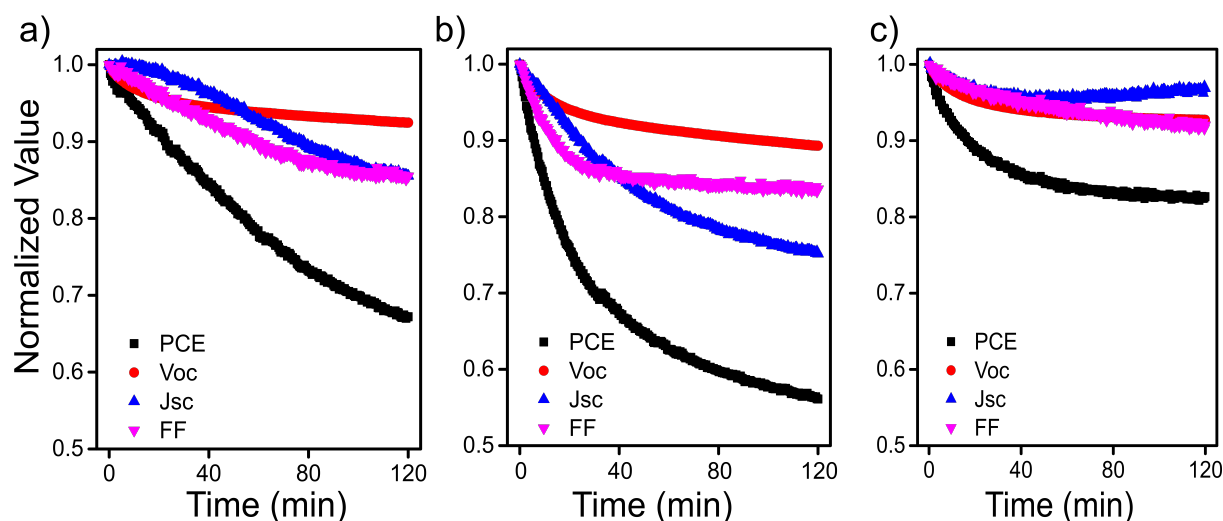

Figure 7.7: *Time evolution of the photovoltaic characteristics of devices without solvent additive (a), with DIO (b) and with CBA (c) solvent additive. PCE (black), V_{oc} (red), J_{sc} (blue) and FF (purple) are normalized to their initial values for clarity of the presentation. (Reprinted with permission from Ref. [71]. Copyright 2019 American Chemical Society.)*

7.3 Evidences of solvent additives evaporation

Figure 7.8 shows the appearance of the active layers with different additives after spin-coating. The film produced without solvent additive is dark brown (Figure 7.8a), the film with DIO is dark green (Figure 7.8b) and the film with CBA is brown (Figure 7.8c). The film colors indicate that partial DIO or CBA is left in the active layer and that the residual amount of DIO is larger as compared with CBA. Although the concentrations of DIO and CBA are 3 vol % and 5 vol %, respectively, there is more DIO left in the active layer after the fabrication process since DIO has a higher bp. than CBA. To prove the escaping of solvent additives during the measurements, we analysis the in-operando GISAXS data according.
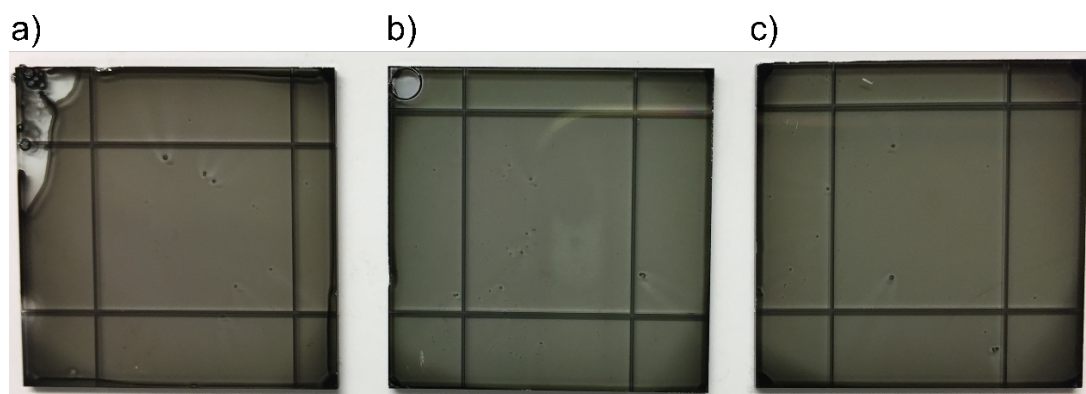

Figure 7.8: *Photographs of PTB7-Th:PC$_{71}$BM films a) without solvent additive, b) with DIO additive and c) with CBA additive after spin-coating. The lines are the precut lines on the back side of ITO substrates. The chip size is 2.5 * 2.5 cm.*

7.3.1 In-operando GISAXS data

To determine the content of the residual additive solvent, we calculate the ratio of the intensity around the critical angle of an additive solvent to that of PTB7-Th in the vertical line cuts. The temporal evolution of the scattering intensity ratio ($I_{add-sol}/I_{pol}$) is summarized in Figure 7.9 during the in-operando study. It can be observed that both scattering intensity ratios decrease with time, which indicates a loss of residual DIO or CBA during the device operation. Moreover, the stronger decay in the intensity ratio in the case of DIO doping indicates a larger loss of residual DIO as compared to CBA.
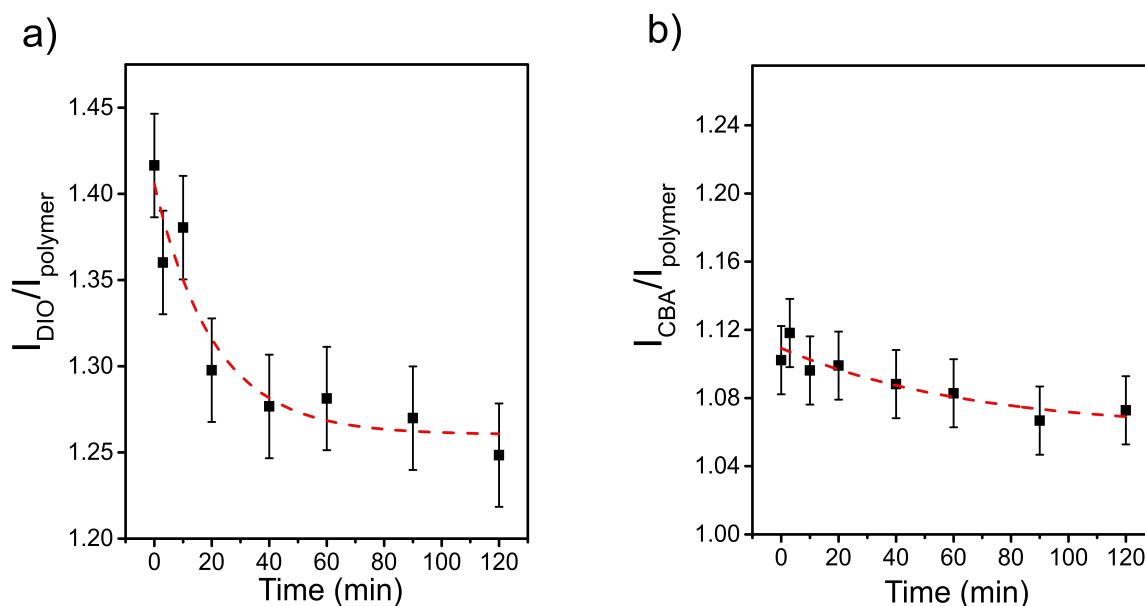
Figure 7.9: *Temporal evolution of the scattering intensity ratio $I_{add-sol}/I_{pol}$ during the in-operando study determined for DIO (a) and CBA (b). The scattering intensities are taken around the Yoneda peak of additive (DIO or CBA) and PTB7-Th. (Reprinted with permission from Ref. [71]. Copyright 2019 American Chemical Society.)*

7.3.2 Optical images before and after in-operando measurements

Optical microscopy (OM) images confirm these observations (Figure 7.10), which extend the morphology information towards more macroscopic surface structures. The few black dots in the OM images appear on the surface of a device with DIO only after the in-operando experiment. It has been widely reported, that DIO selectively dissolves PCBM aggregates in the BHJ solution [49, 179, 203]. Figure 7.10c shows that the dots are originally blurry in the film, but after 2h of operation in the vacuum chamber, the dots become clear and obvious. This phenomenon is only observed in the devices with DIO, as DIO has the highest boiling point among the applied solvents and it was verified that some residual DIO existed in the film after device fabrication [48, 204, 205]. Moreover, the top surface should contain $PC_{71}BM$ domains due to the kinetics of film formation and processing [33]. Therefore, we conclude that the few black dots are ascribed to domains of $PC_{71}BM$. DIO evaporation causes $PC_{71}BM$ to phase separate and form domains. Without additive DIO and CBA the surfaces do not undergo changes on length scales resolved in the OM images.
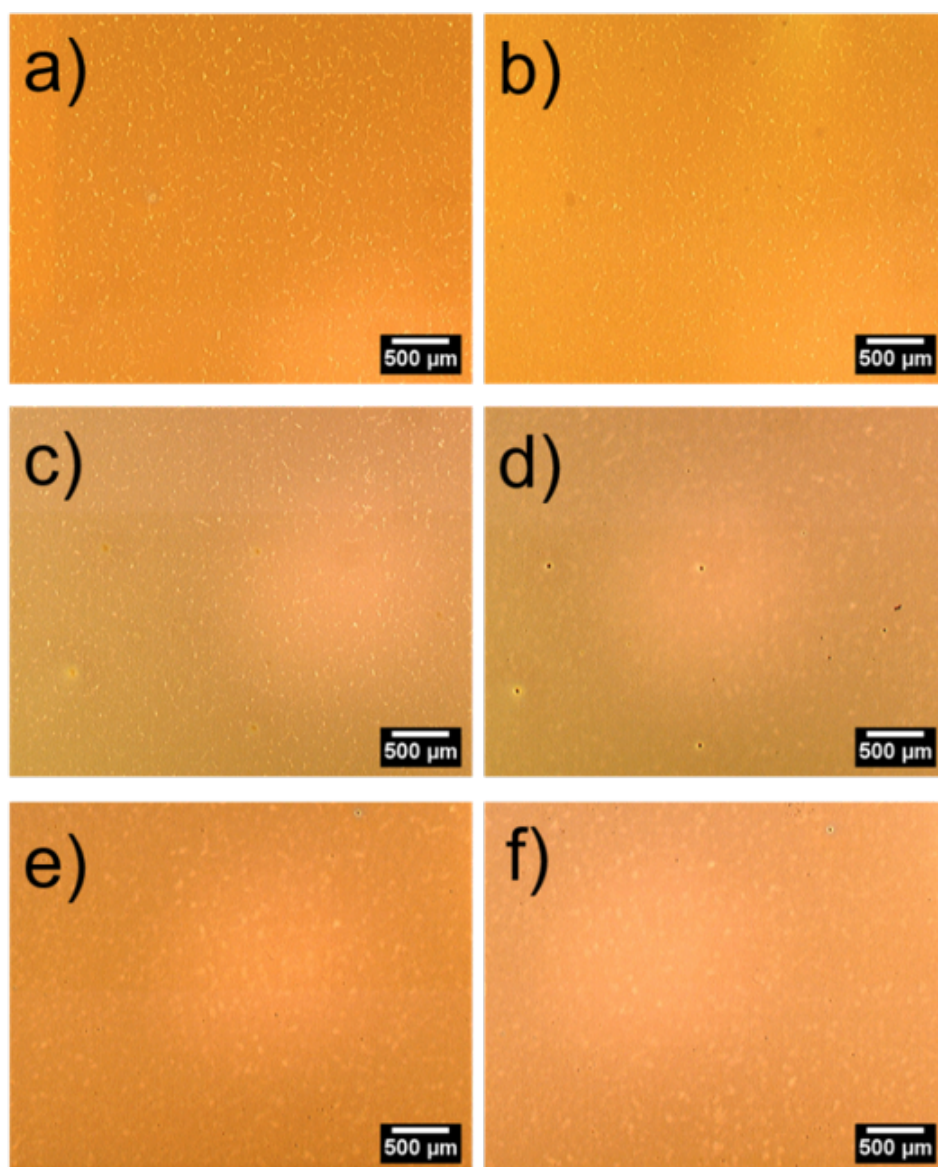
Figure 7.10: *Optical microscopy images of the devices a,b) without solvent additive, c,d) with DIO additive, and e,f) with CBA additive before the exposure to illumination (a,c,e) and after 2h of illumination (b,d,f), respectively. (Reprinted with permission from Ref. [71]. Copyright 2019 American Chemical Society.)*

7.3.3 Vertical film structure

To further understand the more complex behavior of the devices with DIO additive (FF decay at the beginning of the device operation), we analyze the vertical film structure. Vertical line cuts of 2D GISAXS data at $q_y = 0$ are shown in Figure 7.11. The amplitude of the resonant diffuse scattering along the q_z direction increases significantly with time (Figure 7.11b) for the device with DIO. The increase of these interference fringes with
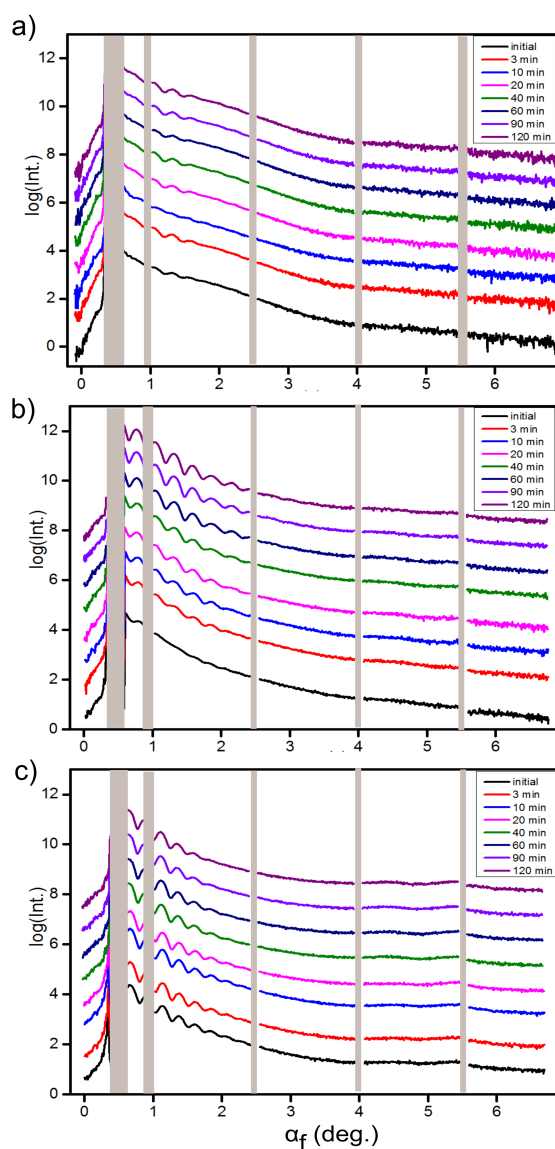
Figure 7.11: *Vertical line cuts of the 2D GISAXS data measured after different operation times: a) device without additive, b) device with DIO additive, and c) device with CBA additive. The curves are shifted along the y axis for clarity. The beamstop shielding the detector and detector gaps are indicated by the gray area. (Reprinted with permission from Ref. [71]. Copyright 2019 American Chemical Society.)*

increasing time indicates the formation of a strongly correlated interface during device operation [206, 207]. The thickness of this correlated layer (d) can be determined by the distance between adjacent minima in the intensity via $d = 2\pi/\Delta q_z$ [208, 209], as the resonant diffuse scattering fulfills the one dimensional Bragg condition [83, 210]. In this approach, the significantly smaller q_x component is neglected [207]. Thus, we conclude that a distinguished top layer is formed based on the GISAXS observation, which has a

thickness of 35 nm and might be hardly detectable by other characterization methods. Assuming that DIO is more likely evaporated from the top part of the active layer, we can identify a 35 nm thick layer forming at the film surface by DIO evaporation in the in-operando measurement. After 60 min, the intensity of the resonant diffuse scattering almost remains constant, meaning that this formed layer does not change during the further operation of the device for the probed times.

When analyzing the amplitude of the resonant diffuse scattering for the devices with CBA a different behavior is observed. Already right after preparation the intensity oscillations are present, meaning that the initial film has a layered structure in the vertical direction. Likely, this is induced by CBA evaporation during film preparation. During device operation, slight changes in the diffuse scattering are visible in terms of decreasing the amplitudes of the intensity oscillations at larger q_z values. This indicates that the interlayer is disappearing, which can be explained by the evaporation of a small amount of residual CBA from the active layer. During device operation, the active layer is becoming more homogenous. Hereby, we conclude that the residual CBA in the active layer can be almost fully evaporated, which causes the changes in the lateral film structure discussed earlier accompanied with a continuous degradation of the FF.

7.4   Discussions

To further investigate the influence of the particular types of solvent additive on the device degradation, we separately compare the decay rates of PCE, V_{oc}, J_{sc} and FF of the devices (Figure 7.12). Figure 7.12a tells us that the PCE in the device with DIO has higher decay rate than that of other two samples. From Figure 7.12b, 7.12c and 7.12d it becomes obvious that the degradation of V_{oc}, J_{sc} and FF of the device with DIO additive are more significant than for the other devices. From the IV curves we know that the device with DIO additive has the lowest V_{oc} value (0.71 V) as compared with solar cells fabricated with additive (0.73 V) or with CBA (0.75 V) (Table 7.1). The lower V_{oc} value can be explained with defect states at the interface between the polymer and PC$_{71}$BM being dissolved in the residual DIO and thus additive dependent [211]. In Figure 7.12d, we can see that the FF undergoes a big change during the first 2400 s, in which DIO is evaporating. However, the temporal evolution of J_{sc} is more complex when the device is made with DIO. Since the changes in the vertical and horizontal direction inside the active layer all will impact the actual value of J_{sc}, no easy correlation is found. In general, we conclude that the presence and type of residual solvent additive has a considerable influence on the stability of solar cells.
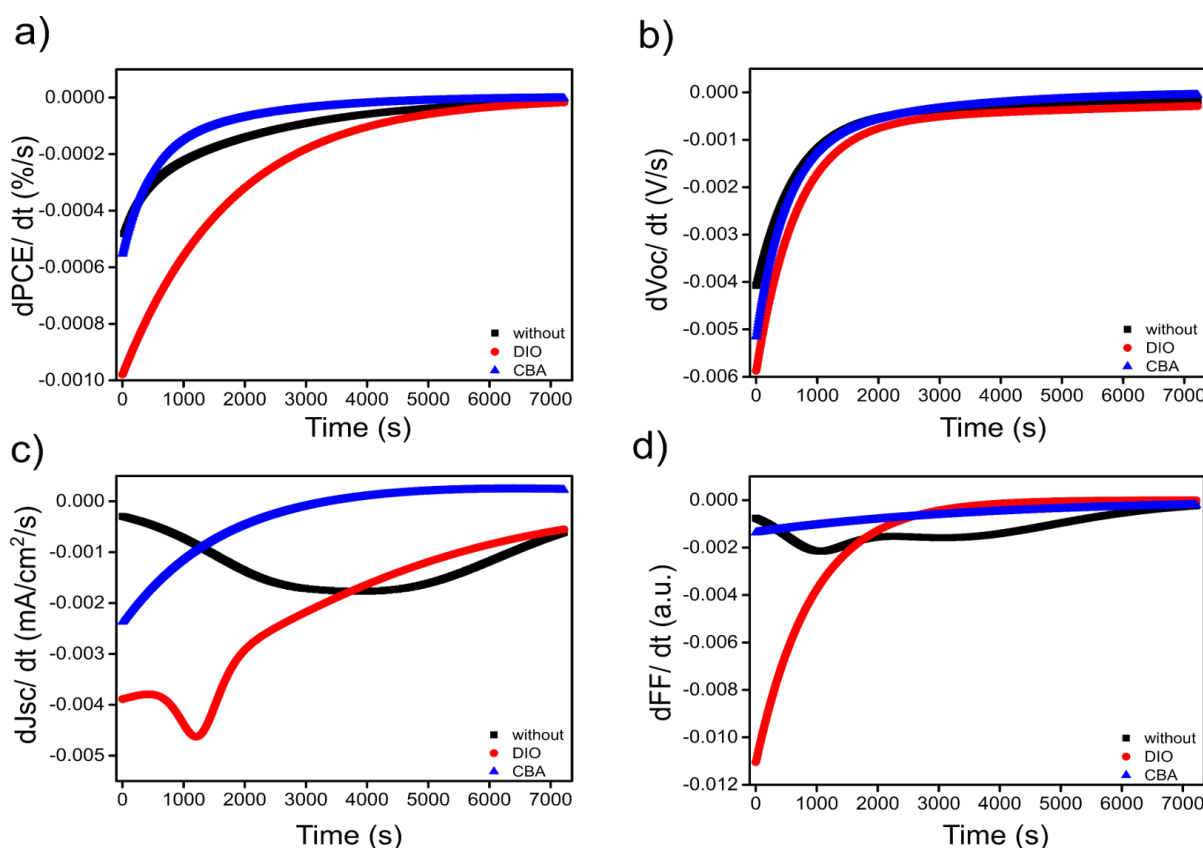
Figure 7.12: *Temporal evolution of the degradation rates of the photovoltaic parameters a) PCE, b) V_{oc}, c) J_{sc} and d) FF for the studied devices without additive (black), with DIO additive (red) and with CBA additive (blue). (Reprinted with permission from Ref. [71]. Copyright 2019 American Chemical Society.)*

In conclusion, we investigate and compare the degradation of PTB7-Th: $PC_{71}BM$ based solar cells fabricated without and with different types of solvent additives by in-operando measurements. The solar cell performance is probed simultaneously to a structure characterization via GISAXS measurements. Figure 7.13 schematically summarizes the morphological changes found in the active layers in the solar cells without solvent additive, with DIO and with CBA during operation. Without solvent additive (Figure 7.13a), the polymer domain sizes increase. With solvent additives DIO (Figure 7.13b) or CBA (Figure 7.13c), the polymer domains become smaller and more isolated after the residual solvent additives are evaporated during the in-operando process. Since DIO has a higher boiling point, more of it is left in the film compared to CBA. The final film still contains some DIO.
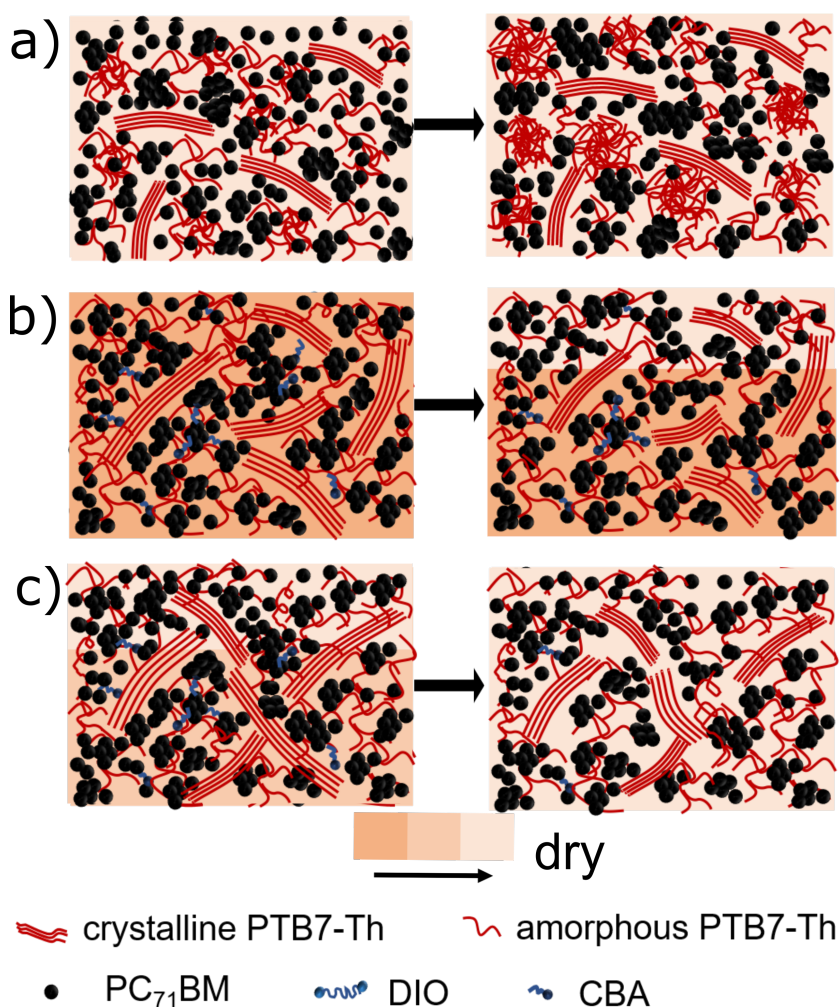
Figure 7.13: *Schematic illustration of changes of the morphology of PTB7-Th:PC$_{71}$BM solar cells without solvent additive (a), with DIO (b) and with CBA (c) from the initial state (left) to an operated state (right). The different components are indicated. Residual solvent is shown by the color bar. (Reprinted with permission from Ref. [71]. Copyright 2019 American Chemical Society.)*

7.5 Summary

In the present chapter, the effects of solvent additives on the stability of PTB7-Th: PC$_{71}$BM based solar cells without and with solvent additives (DIO and CBA) are investigated via in-operando GISAXS measurements. In detail, the degradation of the device without solvent additive is dominated by the decay of J_{sc}. Accoding to the in-operando GISAXS measurements, the polymer domains in this solar cells become larger during operation. The increase domain sizes lead to an extended charge transport distance, and provide more chances for charge recombination, resulting in a lower J_{sc}. In

contrast, PTB7-Th domains in the device with solvent additives (DIO and CBA) decrease in size since the residual solvent additives are evaporated from the active layer during the operation process. Initially, connected domains loose connection when polymer domains shrink and charge carriers get trapped in such not well-connected structures. Consequently, charge recombination increases and causes degradation driven by a decrease in the FF. Moreover, the presence and temporal change of vertical structures further complicate the morphological degradation process. As DIO has a high boiling point, only a part of residual DIO in the active layer can be evaporated during the in-operando experiment from PTB7-Th:PC$_{71}$BM. It can be found that a vertical film structure is induced in the PTB7-Th:PC$_{71}$BM films by fabrication (CBA) or established during operation (DIO).

The results give us a better understanding of the complex degradation processes in organic solar cells when using low-band gap polymers and solvent additives. Two major types of morphological degradation processes, namely domain growth or domain shrinkage, are confirmed for the high efficiency system PTB7-Th:PC$_{71}$BM depending on the presence of solvent additives. Such general knowledge will be important to improve the stability of organic solar cells and thereby contribute to successful real-world use of this class of next generation solar cells.

8 Stability study of PffBT4T-2OD: PC$_{71}$BM based devices

Parts of this chapter have been published in the article: In-operando GISAXS and GIWAXS stability study of organic solar cells based on PffBT4T-2OD: PC$_{71}$BM with and without solvent additive (D. Yang et al., *Advanced science*, accepted, 2020, DOI: 10.1002/advs.202001117).

In Chapter 7, we investigate the effects of solvent additives on the stability of PTB7-Th:PC$_{71}$BM based solar cells via in-operando GISAXS measurements. The experiments are carried out on three kinds of solar cells, namely without solvent additives, with DIO and with CBA additive. According to the results of the in-operando GISAXS measurements, we find that the polymer domain sizes become larger in the device without solvent additives during the device aging, which leads to a decay of the J_{sc}, as the excitons are getting harder to reach the D/A interfaces to separate. However, the solvent additives (DIO and CBA) with high boiling points cannot be entirely removed from the devices during the fabrication process, which is confirmed by the optical microscopy and GISAXS measurements. Thus, the residual solvent additives are evaporated during the in-operando measurements, resulting in a shrinkage of polymer domain sizes, and a top interface layer formed in the BHJ film with DIO additive. In contrast, since CBA has a lower boiling point than that of DIO, the interface layer in the BHJ film with CBA additive is formed in the fabrication process, and is disappearing during the in-operando measurements. The structure domains in the BHJ layers make BHJ morphology more disconnected and cause more traps for charge carriers, which results in the degradation of the FF.

In general, a solvent additive should have a higher boiling point than that of host solvents [103, 193]. Thus, it can extend the film drying process and bring more chooses for the morphology self-assembly. Therefore, doping with solvent additives is beneficial for achieving a good interpenetrating network of the D/A materials, which is expected to have a benficial impact on the device performance [48, 189–191, 212, 213]. Moreover, based on the previous study, we know that the evaporation of residual solvents causes a shrinkage of

the domain sizes, resulting in a decay of the FF. Therefore, avoiding the residual solvents in the final device should be taken into consideration. Here, poly[(5,6-difluoro-2,1,3-benzothiadiazol-4,7-diyl) -alt-(3,3"'-di(2-octyldodecyl)-2,2',5',2",5",2"'-quaterthiophen-5, 5"'-diyl)] (PffBT4T-2OD) and [6,6]-phenyl-C71-butyric acid methyl ester (PC$_{71}$BM) are chosen as the donor and acceptor materials, respectively. PffBT4T-2OD:PC$_{71}$BM films are spun-cast at 110 °C and thermal annealing followed at 85 °C for 5 min under nitrogen atmosphere, which is considered that solvent additives can be removed as much as possible during the device fabrication process. Moreover, PffBT4T-2OD is a highly crystalline polymer [29, 142, 214], which is expected for high charge mobility [215–217] and provides a possibility to do a crystallinity investigation via GIWAXS measurements. The solar cells are fabricated as well without a solvent additive, with DIO (boiling point at 332 °C) and with CBA (boiling point at 212 °C) additive, respectively. We intend to detect further effects of solvent additives on the device degradation behavior, even though almost all solvent additives are assumed to be removed during the device fabrication process.

8.1 Photovoltaic performances

Firstly, we do the photovoltaic performance investigation of related solar cells. Three kinds of devices based on PffBT4T-2OD:PC$_{71}$BM are fabricated, namely without any solvent additives, with 3 vol% DIO and with 5 vol% CBA additive, which are the optimal volume ratios for solar cells according to the literature [47, 191]. During the in-situ GI-
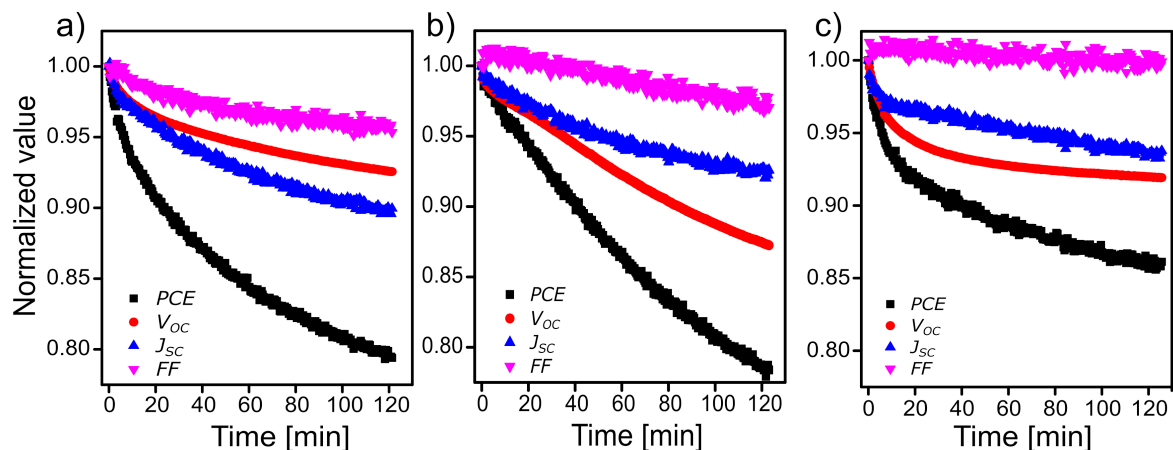

Figure 8.1: *Time evolution of PCE (black), FF (purple), J$_{sc}$ (blue) and V$_{oc}$ (red) of the devices without solvent additive (a), with DIO additive(b) and with CBA additive(c) additive, respectively.*

	J_{sc} [mA/cm^2]	V_{oc} [V]	PCE [%]	FF
without	9.3±0.3	0.76±0.01	3.4±0.1	0.48±0.01
DIO	18.1±0.2	0.72±0.01	7.7±0.1	0.58±0.01
CBA	10.0±0.1	0.76±0.01	3.8±0.2	0.48±0.01

Table 8.1: *The average photovoltaic performances of PffBT4T-2OD: PC71BM devices without and with solvent additives. The average values are taken from 8 or more devices.*

WAXS measurements, the photovoltaic performances of the different devices are recorded periodically and the temporal evolution of the normalized photovoltaic parameters of the devices are displayed in Figure 8.1. As the device performances are tracked during in-situ GISAXS and in-situ GIWAXS measurement individually, two sets of long-term photovoltaic performances are obtained. Figure 8.2 shows the time resolved normalized photovoltaic parameters of all devices, tracked during the in-situ GISAXS experiments. Small individual differences in the decrease of the parameters are see in particular in the initial burn-in phase. At later stages of the device degradation, the overall temporal characteristics agree well for the in-operando GISAXS and GIWAXS experiments. The individual differences arise from the well-known spread in the photovoltaic parameters among different devices of the same type. The average photovoltaic performance of all devices is shown in Table 8.1, as measured in the lablaboratory. The PffBT4T-2OD:PC$_{71}$BM solar cells fabricated with DIO additive have higher PCE values than the other devices, and
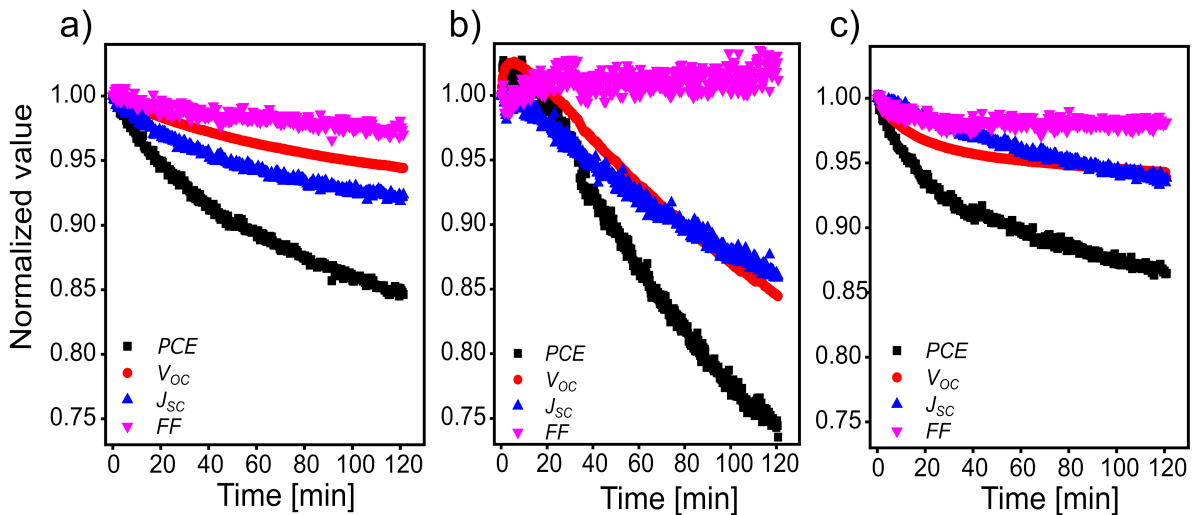

Figure 8.2: *Temporal evolution of PCE (black), FF (purple), J_{sc} (blue) and V_{oc} (red) of the devices without solvent additive (a), with DIO additive (b) and with CBA additive(c) during in-operando GISAXS measurements, respectively.*
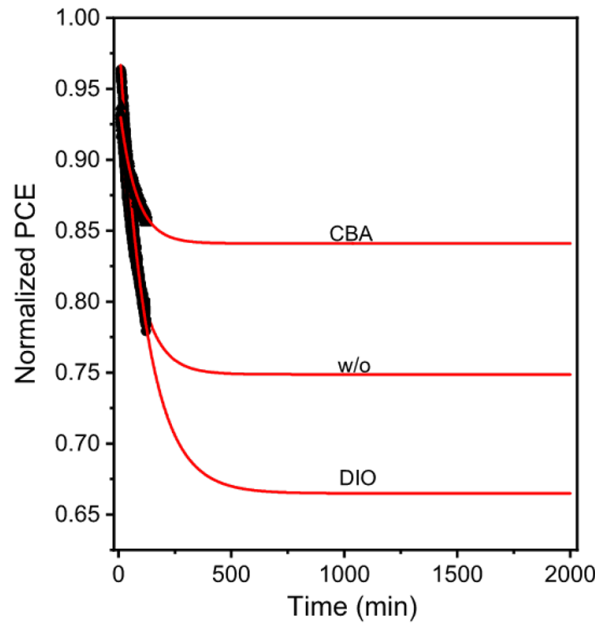
Figure 8.3: *Extending the temporal evolution of the PCE decay curves (black symbols) from the measurements towards times t $\gg$ 120 min with modelling via exponential functions (red lines). The corresponding devices are indicated.*

doping with CBA additive cannot further enhance the device performance, which is attributed to the small difference of the boiling points between 1,2-dichlorobenzene (DCB, 180 °C) and CBA (212 °C). However, comparing the temporal evolution of the normalized *PCE* values of all devices (Figure 8.1), it can be seen that the devices with CBA additive are the most stable and the devices with DIO additive show the strongest decay of thr device performance, To make the comparison clearer, we model the PCE decay curves via exponential functions (Figure 8.3) and find that the 85 % of the PCE maintain even after 2000 min in the device with CBA treatment, but only 66 % of the PCE preserves in the device with DIO additive, which directly indicates that solvent additives can affect the device stability. The 10 % loss of the short circuit current (J_{sc}) is the main degradation factor in the device fabricated without a solvent additive. However, for the samples with solvent additives, the FF now is the most stable parameter whereas the device aging is mainly from the decay of the V_{oc}. Above all, we can know that the solvent additives have a different effect on the degradation of PffBT4T-2OD:PC$_{71}$BM based solar cells compared to the solar cells in Chapter 7.

8.2 BHJ morphology tracking during device aging

In-operando GISAXS/GIWAXS characterizations are successfully used to determine to determine the correlation between the evolution of BHJ morphology and the photovoltaic device performances [39–41, 218]. Here, GISAXS/GIWAXS are sequentially performed on a series of PffBT4T-2OD based devices, namely with and without a solvent additive, to reveal the structure changes of nanostructures and crystallinity in the BHJ layer during the aging process. The measurement chamber, the experimental protocol and other experimental details are described in section 3.10. As a general remark, the devices are measured without any kind of cell encapsulation. Owing to compensation to this the cells are held under vacuum atmosphere during the data acquisition.

8.2.1 Setup and protocol

In Chapter 7, the used measurement setup has already been introduced in detail. To collect the morphology evolution, GISAXS/GIWAXS and current-voltage measurements are simultaneously performed on the devices. The chamber is maintained at vacuum conditions (p $\approx$ 6×10^{-2} mbar) during the operation process to avoid degradation via oxygen and water. A PerkinElmer PX5 150 W xenon arc lamp is applied to simulate a sun radiation spectrum illuminating the solar cells, and the photovoltaic performance is recorded by a source meter (Keithley 2400). Two Kapton windows were equipped on the front and backside of the chamber to allow the X-ray beam to enter and exit the chamber. To avoid the strong scattering signals from the metal electrode, the beam is aligned to probe the active layer film close to the electrode (1 mm distance from metal contact). Before the in-operando experiments, two-dimensional (2D) GISAXS/GIWAXS data are measured to characterize the initial device state (denoted as 0 min). Afterwards, the devices are illuminated, and current-voltage curves are recorded periodically every 26 s for 120 minutes in total. In parallel, 2D GISAXS/GIWAXS data are taken after 3, 10, 20, 40, 60, 90 and 120 min of illumination with an exposure time of 5 s each.

8.2.2 Inner morphology evolution

Changes of the morphology of the BHJ layer is tracked on a nanometer scale during the device degradation process via in-operando GISAXS. Figure 8.4 displays the 2-dimensional (2D) GISAXS data of each device at selected times in the operation process. Detailed observations of morphological changes are determined via extracting the scattering signals of PffBT4T-2OD at the Yoneda [196] region via horizontal line cuts of the 2D GISAXS
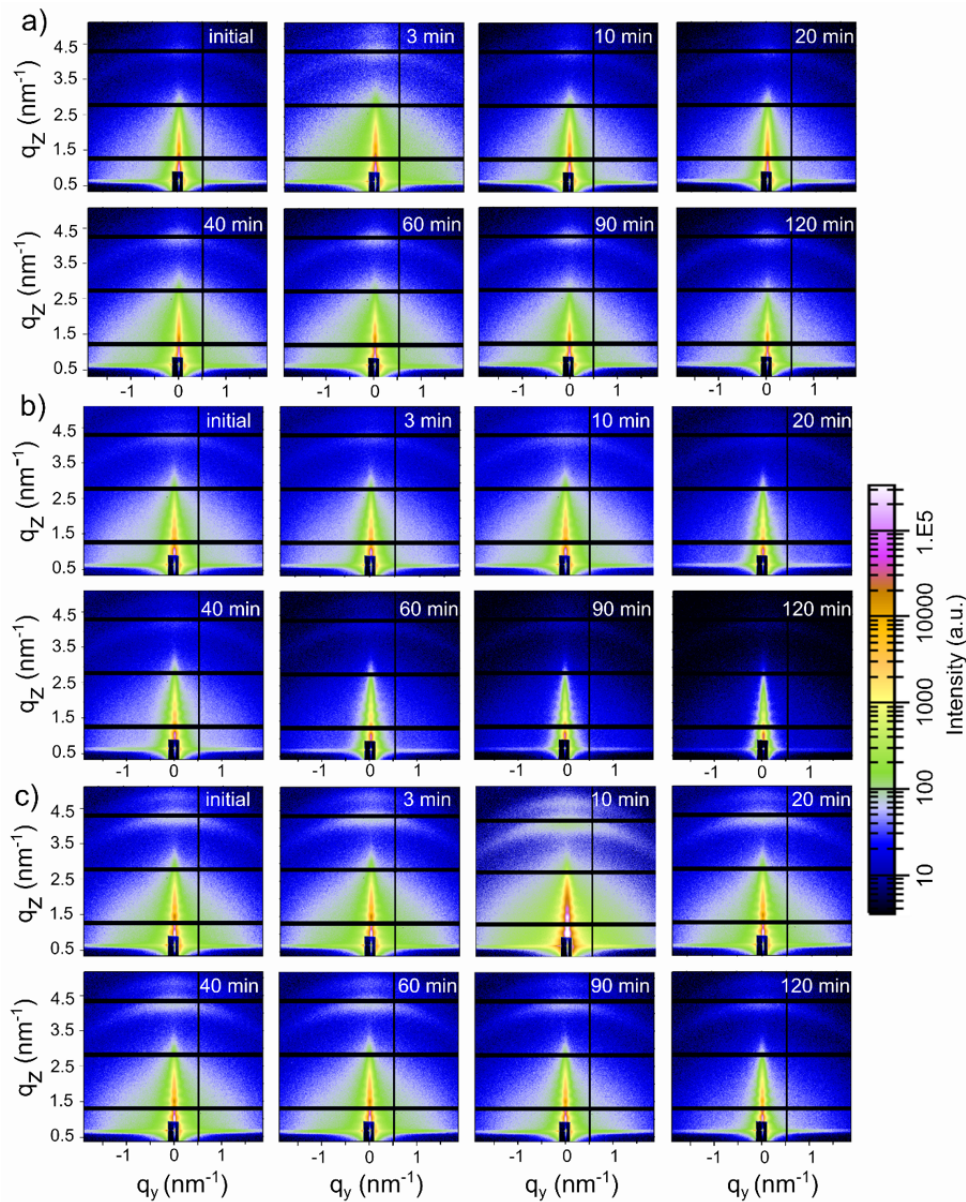
Figure 8.4: *2D GISAXS data of solar cells after different illumination times as indicated: a) device without additive, b) device with DIO additive, and c) device with CBA additive.*

data. The horizontal line cuts are shown in Figure 8.5. To evaluate the nanostructures of the polymer, these horizontal line cuts are modeled based on the effective interface approximation and the local monodisperse approximation (LMA) [219,220]. The effective interface approximation of the distorted wave Born approximation (DWBA), which works well for modeling GISAXS data of polymer films, is chosen to model scattering data in the small angle regime. In addition, to deal with data containing several average sizes of objects, the LMA is applied [219,220], which is based on the assumption that local domains have the size of the coherence length of the beam, only monodisperse objects. In this

model, the total scattering signal can be approximated by the incoherent superposition of the scattering intensities of the individual substructures that appear within the film, if the length scales of the distinct substructures are sufficiently separated [221].
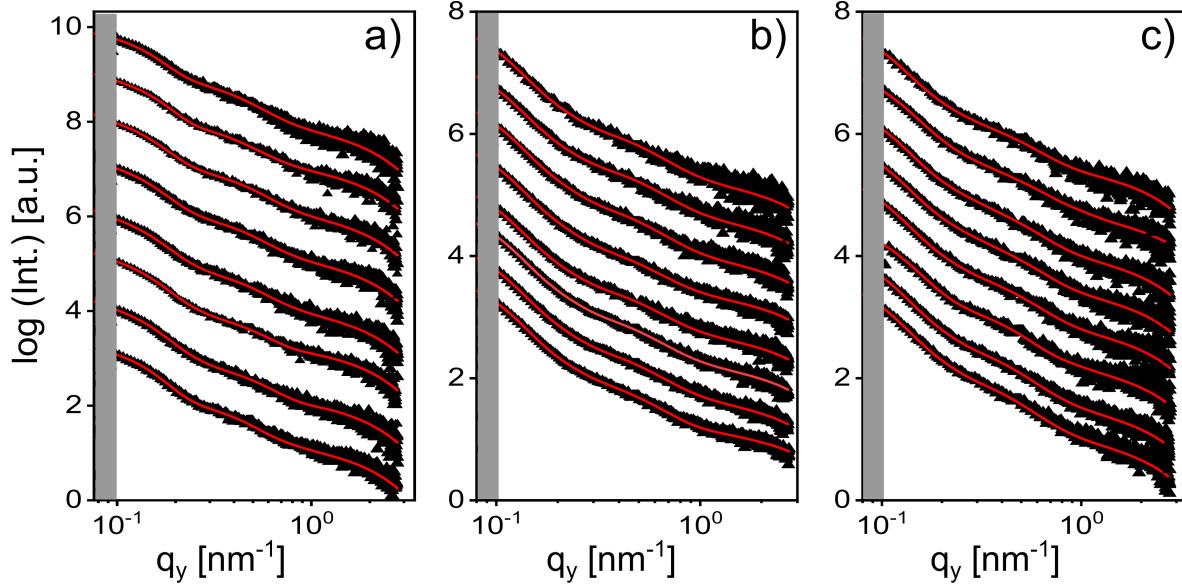

Figure 8.5: *Horizontal line cuts of the 2D GISAXS data measured after different operation times: a) device without additive, b) device with DIO additive, and c) device with CBA additive. From bottom to top: the GISAXS measurement after 0, 3, 10, 20, 40, 60, 90 and 120 minutes of device operation. The curves are shifted along the y axis for clarity. The q-range shielded by the beamstop is indicated by the gray area. The fitting model can be found in the previous publications [40, 71].*

In our model (red curves in Figure 8.5), three characteristic cylinder nanostructures are applied to for the samples with and without solvent additive. The average radii of the polymer domains at the respective times are plotted for each device in Figure 8.6. It can be seen that the initial radii of the largest polymer domains in the sample without solvent additive is around 11.5 ± 0.3 nm, which is smaller than in the devices with DIO (15.5 ± 0.3 nm) and CBA (15 nm ± 0.4) additive. The slight increase in the polymer domain sizes in the devices with solvent additives is due to polymer aggregation in solution. Thus, the addition of DIO and CBA leads to a morphology modification in the active layers, which agrees well previous reports [48, 179, 222]. During operation, the average radii of the largest polymer domains increase with time in the device fabricated without solvent additive (Figure 8.1a). Contrary no obvious changes of the polymer domain radii are visible in the devices with DIO (Figure 8.1b) and CBA (Figure 8.1c) additive. Solvent additives, having a high boiling point and selectively dissolving $PC_{71}BM$, provides a better integration of the $PC_{71}BM$ molecules into donor polymer aggregates [179, 223]. The more
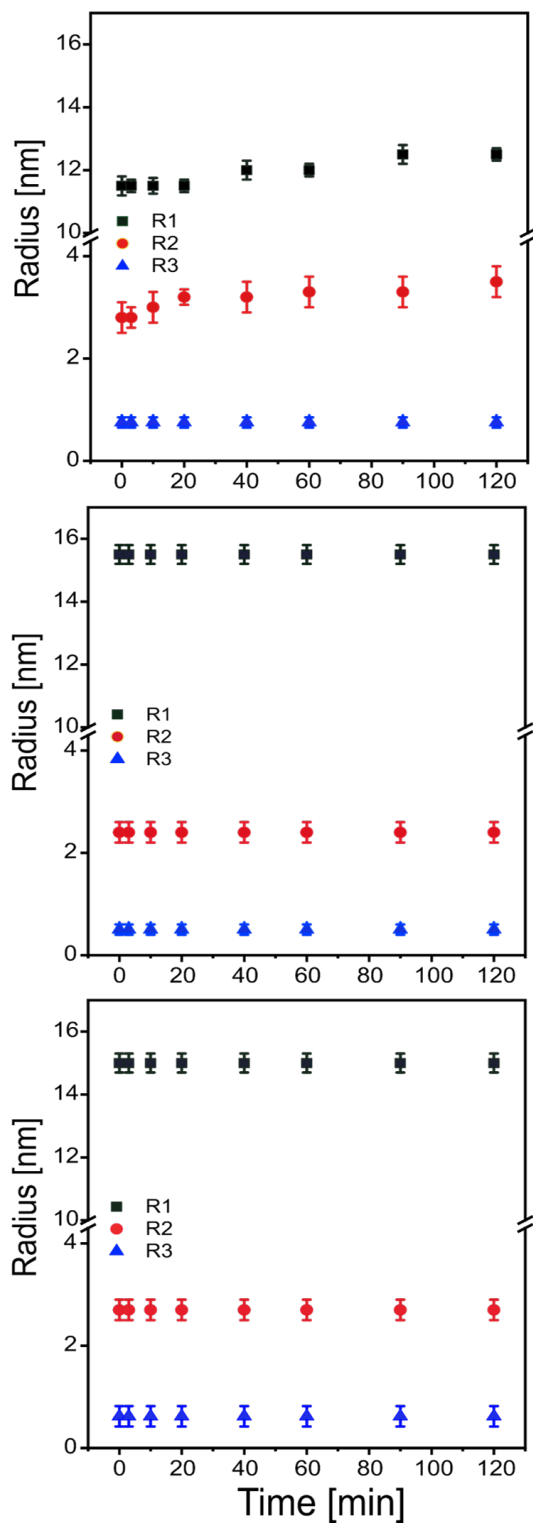
Figure 8.6: *Temporal evolution of the average radii of three polymer structures in the device without a solvent additive (a), with DIO (b) and with CBA (c).*
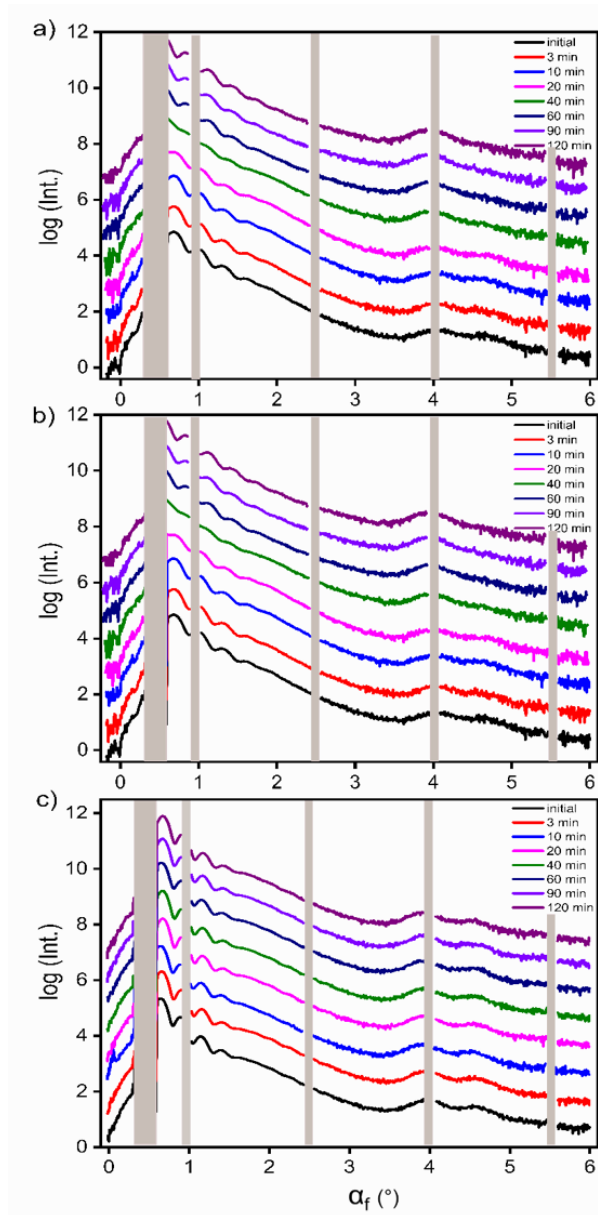
Figure 8.7: *Vertical line cuts of the 2D GISAXS data measured after different operation times: a) device without additive, b) device with DIO additive, and c) device with CBA additive. The curves are shifted along the y axis for clarity. The non-accessible q-regions due to the beamstop shielding the detector and detector gaps are indicated by grayed-out areas.*

pronounced interpenetration between donor and acceptor molecules in the system with an additive is, the smaller is the gives less opportunity for the migration of molecules, which can explain the more stable BHJ morphology for devices with DIO and CBA additive. An efficient charge carrier separation and transport highly depends on the sizes of the nano-structured domains in the BHJ layer [224, 225]. As the exciton diffusion length is

typical in the range of 10 to 20 nm for conjugated polymers, the domain sizes determine if excitons can reach the D/A interface to get dissociated. Thus, the inner nanostructure of the active layer directly impacts on the device performance [226, 227]. We conclude that the continuous decay of J_{sc} (Figure 8.1a) in the device without an additive is induced by the increase of polymer domains with time, probed in the GISAXS measurement, which leads to a decrease of the chances for charge carrier separation. The differences in the decay of Jsc between the devices with DIO and CBA solvent additive illustrate the complexity of the morphology impact on individual device parameters. Besides the simple size of the polymer domains also other morphology parameters such as their connectivity and crystallinity are of importance.

The loss of residual solvent additives from the BHJ layer was identified to cause a shrinkage of the polymer domains, which reduced the connectivity of domains and caused a decrease of the FF [40, 71]. In contrast in the present work, the FF is observed to be the most stable photovoltaic parameter in the devices fabricated with solvent additive (DIO or CBA Figure 8.1b and c), which we attribute to having no more additive left inside the active layers to be removed during the device operation. Actually, we detect no solvent additive losses from the vertical line cuts of the 2D GISAXS data (Figure 8.7), because the distance and amplitude of the resonant diffuse scattering along the q_z direction are almost stable during the entire measurement time. The in-operando GISAXS measurements provide polymer morphology changes during the device aging process. An increase of polymer domain sizes is found in the device without a solvent additive, while the polymer domain sizes are quite stable with time in the device with solvent additives (DIO and CBA).

8.2.3 Crystallinity evolution

As shown in Figure 8.1b and c, the decrease of the V_{oc} dominates the device degradation in the devices with solvent additive (DIO or CBA). V_{oc} is impacted by many factors, such as recombination rates, density-of-state (DOS) shape, charge carrier and exciton mobility in the organic photovoltaics [228, 229]. All these impact factors are closely related with the crystalline state of the materials in the BHJ layer [211, 225, 230]. Thus, in-operando GIWAXS measurements are sequentially applied to reveal changes of crystalline parts of the active layer during the in-operado measurements. Figure 8.8 shows the collected 2D GIWAXS data of each device at selected times during operation. Cake cuts of the 2D GIWAXS data are performed to extract the respective crystalline information. The pronounced (100) Bragg peak located at $q_z = 0.27$ Å^{-1} is ascribed to the PffBT4T-2OD crystallites, whereas the polymer (010) Bragg peak and the fullerene peak are both
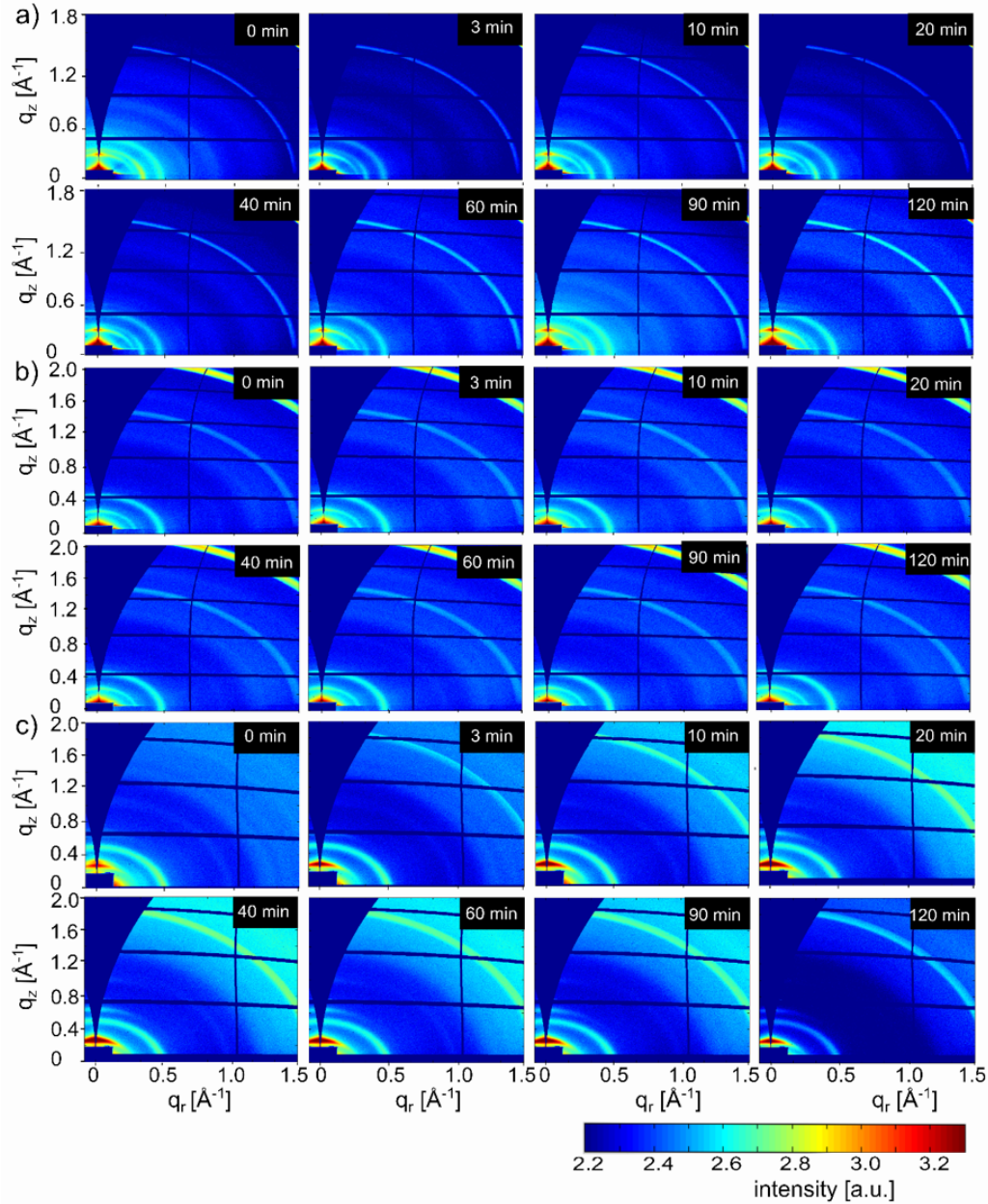
Figure 8.8: *2D GIWAXS data of solar cells after different illumination times as indicated: a) device without additive, b) device with DIO additive, and c) device with CBA additive.*

weak in intensity and broad (Figure 8.12). Thus, an edge-on orientation of the polymer crystallites is dominant in these films while the face-on orientation is strongly suppressed. The fullerene peak is located at q = 1.3 A-1. Changes in crystallinity caused by device operation are seen from a comparison of the initial and the final vertical cake cuts of the device with DIO as example, since the polymer (010) Bragg peak is only observed for this device (Figure 8.13). We find that the PC71BM peak and the polymer (010) Bragg peak are almost constant during the measurements, whereas the polymer (100)
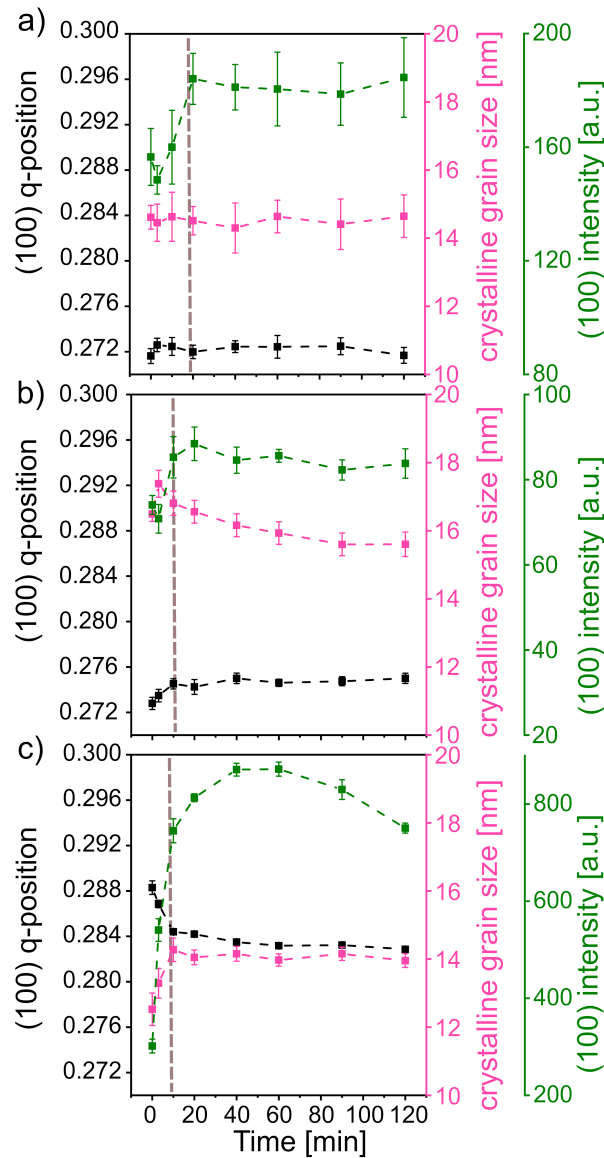
Figure 8.9: *Time resolved of the (100) PffBT4T-2OD Bragg peak. As a function of time, the peak intensity (blue), peak center position (black), and peak FWHM (pink) are displayed for the samples without a solvent additive (a), with DIO (b) and with CBA (c), respectively. The error bars are obtain from the fitting model.*

Bragg peak changes. Consequently, we determine changes of the polymer crystalline state during the operation process by tracking the PffBT4T-2OD (100) Bragg peak. By fitting with Gaussian functions, we obtain the q-position, the crystalline grain size (estimated via Scherrer equation) and the peak intensity for all devices. The respective results are summarized in Figure 8.9. Prior to the GIWAXS analysis, efficiency-, solid-angle- and χ-correction were performed on the raw GIWAXS data to obtain correct q_z vs. q_r images, because a distortion originating from by the conflict between the spherical and

flat hypersurfaces of the Ewald's sphere and the flat crystalline planes and q_x needs to be accounted for in GIWAXS measurements, especially for large exit angles [90]. In this work, the corrections are done by the aid of the GIXSGUI 1.6.1 software [101]. Subsequently, the reference GIWAXS data of the pure ITO substrate is subtracted from the 2D GIWAXS data to remove the contribution from the substrate and background (section 3.9). Afterwards, cake cuts were extracted from the background-corrected data across the (100) Bragg peak along q across in the perpendicular direction, as introduced in section 3.9. At last, the cake cuts were fitted by the Gaussian distributions to obtain the intensity, q-position and FWHM value of the (100) PffBT4T-2OD Bragg peak. The crystalline grain sizes were evaluated via the Scherrer equation along the crystal direction [hkl] = [100]. Due to the intensity fluctuation of X-ray beam, the peak intensity was corrected based on the intensity of Kapton window ($q = 0.46$ Å^{-1}).
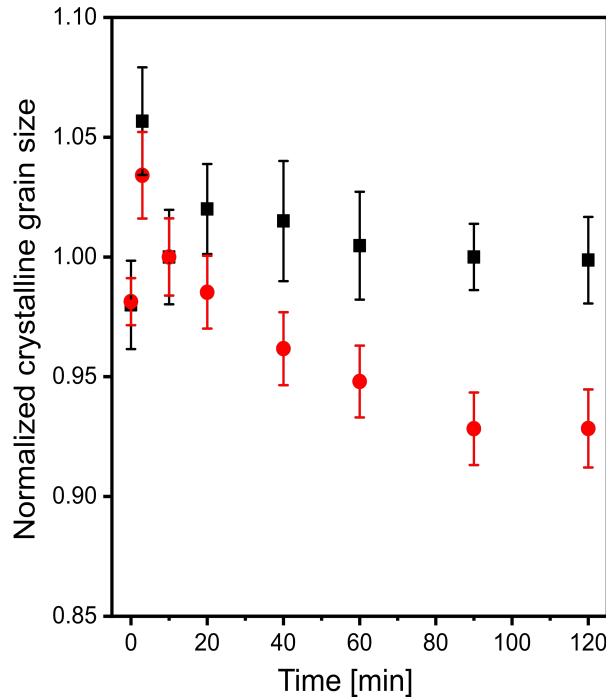

Figure 8.10: *Time evolution of the polymer crystalline grain size of devices with DIO. Red data points correspond to the GIWAXS measurements under solar illumination, whereas black data points correspond to a control measurement in the dark. The data are normalized to the value at 10 min.*

It should be noted that the initial stage, marked in Figure 8.9 with grey dashed lines, is considered as a "burn-in" phase, since the peak intensity shows a fast increase in the beginning of the operation for samples [231]. A 'burn-in' stage was reported in the literature before, while its origin is still debated. Oxygen trapped within the films, the broad polydispersity of the polymers, and organic or inorganic impurities in the polymers
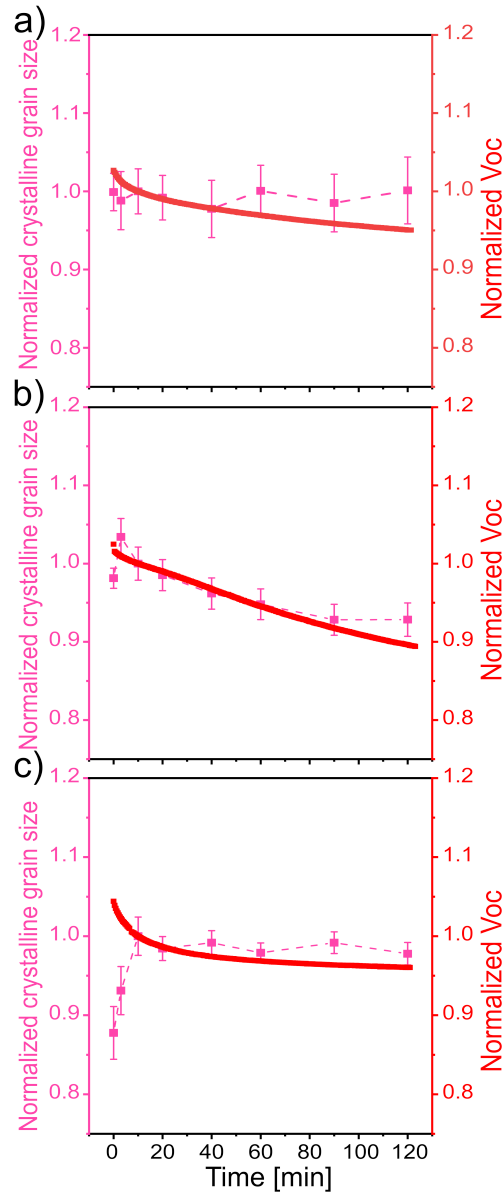
Figure 8.11: *Time comparison of estimated crystalline grain size (pink) along the crystal direction (100) vs V_{oc} (red) for the samples of without a solvent additive (a), with DIO (b) and with CBA (c), respectively. The data are normalized to the value at 10 min.*

(such as palladium catalysts) were suggested as possible origin of the "burn-in" phenomena [232–235]. Since the "burn-in" is followed by the device degradation, we will restrict to the aging in the present work. In Figure 8.9, it can be observed that the q-position of the (100) Bragg peak stays almost unchanged during the operation process in all devices after the initial "burn-in" stage. Thus, the polymer crystallizes undergo no changes of the crystal lattice during operation. The crystalline grain sizes of PffBT4T-2OD remain constant in the devices without an additive and with CBA additive, whereas they de-
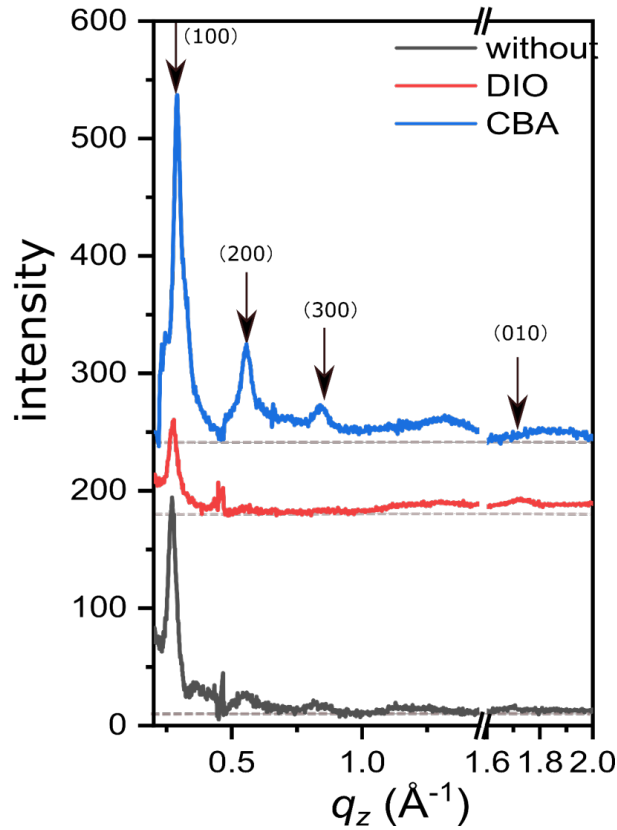
Figure 8.12: *Vertical cuts of the initial GIWAXS data of all samples without any correction treatment: without additives (black line), with DIO (red line) and with CBA (blue line).*

crease in the device with DIO additive. To further determine the influence of the applied bias voltage and the used vacuum conditions on the crystallinity of the BHJ film, a dark in-operando measurement is carried on another fresh DIO device. The bias voltage is periodically applied on the device without illumination and an in-situ GIWAXS measurement is performed like for the illuminated device. The results of the dark in-operando measurements are shown in Figure 8.10. The crystalline grain sizes almost stay constant within the error bars after the burn-in stage in the dark control experiment, indicating the morphological changes observed in the illuminated sample require the presence of voltage and illumination. It was reported in a previous study that a codependence exists between crystalline states of the BHJ layer and the V_{oc} value probed during the aging process [41]. In Figure 8.11, the crystalline grain sizes and V_{oc} values are plotted together for all three devices. We can see that the change of V_{oc} shows a close correlation with the evolution of the crystalline grain sizes after the burn-in stage. The crystal grain sizes and V_{oc} value in the device without an additive and with CBA additive are almost stable after the burn-in stage, while the crystalline grain sizes and V_{oc} value show a correlated decrease in the device with DIO additive. Thus, the shrinkage of the crystalline grain sizes causes the ob-
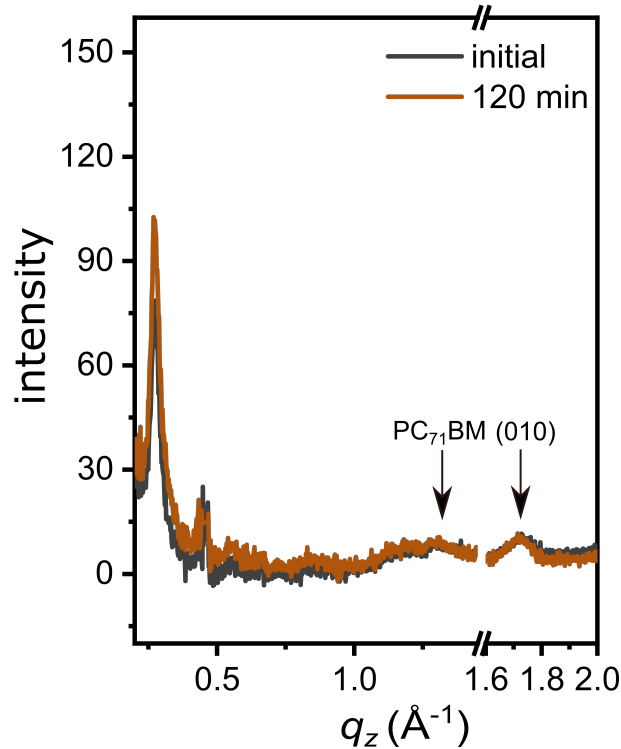
Figure 8.13: *Vertical cake cuts of the initial (black) and the final (brown) GIWAXS data of the device with DIO additive after correction. The fullerene peak (q = 1.3 A^{-1}) and the polymer (010) Bragg peak are labelled.*

served decrease of the V_{oc} values in the device with DIO additive, as seen before in case of P3HT based devices [41]. Moreover, the initial V_{oc} value of the device with DIO additive is 0.72 V, which is lower than that of the devices without an additive and with CBA additive (0.76 V, as shown in Table 8.1). Based on the GIWAXS observations, we know that the crystallite sizes in the device with DIO additive are slightly larger than those present in the samples with CBA additive and without any additive. It was demonstrated that the donor crystallites with extended π-conjugation could cause a slight increase of the highest occupied molecular orbital (HOMO) level of the donors and therefore result in a decrease of the Voc value [185, 236]. Furthermore, the lower degree of polymer crystallinity in the device with DIO additive, obtained by comparing the initial Bragg peak intensities of all devices (Figure 8.9), might lead to a lower V_{oc} value as well [237]. In detail, we can also observe that the Bragg peak intensities almost remain constant in the device without an additive and with DIO additive along with time during operation. However, a slight decrease of Bragg peak intensity is recorded in the device with CBA additive, suggesting a decrease of the polymer crystallinity during the operation time and resulting in a loss of J_{sc}. Above all, the GIWAXS measurements suguest that the V_{oc} value has a closely

correlation with the polymer crystalline, and the decrease sizes of the polymer crystallites lead to the decay of the V_{oc}.
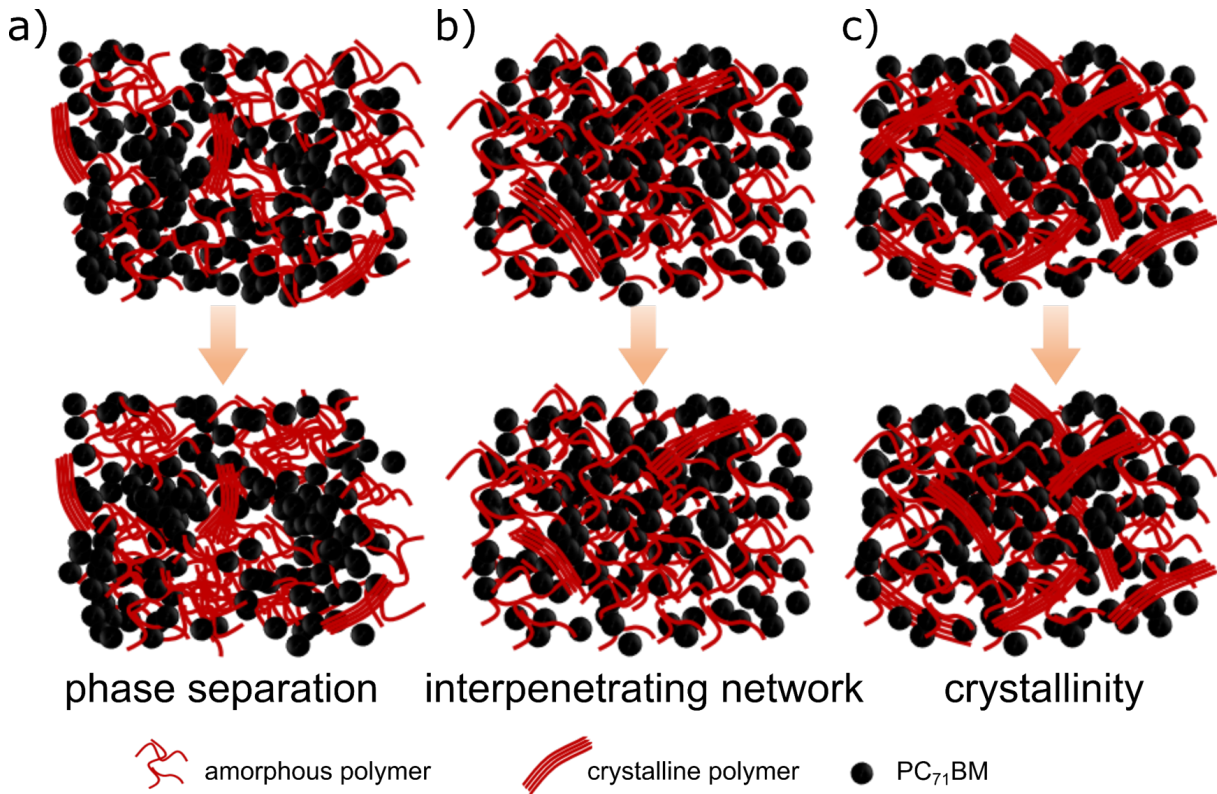
8.3 Discussions

Figure 8.14: *Schematic illustration of the morphology of PffBT4T-2OD:PC$_{71}$BM solar cells without solvent additive (a), with DIO (b) and with CBA (c).*

Notably, the intensity of the Bragg peak indicates the crystallinity degree. Figure 8.9 also tells us that the absolute peak intensities in the sample with CBA additive are significantly higher than that of the devices without an additive and with DIO additive. Therefore, we propose that a competition of polymer molecules between forming interpenetrating D/A networks and growing crystallites is triggered by an additive in the BHJ films. In conclusion, combining the results of GISAXS and GIWAXS measurements, we know that the polymer morphology experiences a phase separation during the device aging in the device without solvent additives, which may cause by a motion of polymer molecules. As shown in Figure 8.14a, the polymer domains become larger during the in-operando measurements. GIWAXS measurements we observe that, the polymer crystals are more stable in this device, which means that the growth of the domains is not caused

by growing polymer crystals but by the addition of amorphous polymers. In contrast, from the use of a high boiling point additive like DIO, an interpenetrating D/A network is promoted(8.14b), resulting in a better J_{sc} and FF (Table 8.1) [49,179]. A lower boiling point additive like CBA, is also beneficial for polymer molecule aggregation as well, but more favorable for polymer crystallite growth (8.14c) [223]. Moreover, the extended film drying time in the case of doping with solvent additives is also beneficial for forming face-on orientated crystallites [238]. The out-of-plane (010) and (100) Bragg peaks correspond to the face-on and edge-on crystallites of the polymer phase [176]. Figure 8.12 shows the initial vertical cake cuts of all devices. There are almost no face-on crystallites in the BHJ film prepared without solvent additives. However, for the devices fabricated with solvent additives, the (010) Bragg peak becomes obvious, and especially in the sample with DIO additive, it is more pronounced than that in the sample with CBA additive, as compared with the (100) Bragg peak.

8.4 Summary

In the present chapter, we focus on investigating the influences of solvent additives on the stability of PffBT4T-2OD:PC$_{71}$BM based solar cells via in-operando GISAXS/GIWAXS measurements. We still use DIO and CBA as solvent additives in the BHJ blend solution, and two corresponding devices are fabricated to compare them with the reference device. Thermal spin-coating and thermal annealing are involved in the device assembly process, hereby, no substantial residual solvents are released during the device operation. The photovoltaic performances show that the degradation of the device without a solvent additive is mainly caused by the decay of the J_{sc}. This is attributed to the increase of polymer domain sizes according to the results of in-operando GISAXS measurements, which makes the exciton dissociation harder. However, the polymer domains are quite stable during the measurements in the samples with solvent additives. We consider the stable morphology is due to the more interpenetrating network in the BHJ films, which is caused by doping solvent additives, resulting in a stable fill factor (FF).

Moreover, the decay of the devices with solvent additives is dominated by the degradation of the V_{oc}, which is closely related to the polymer crystallinity. Thus, in-operando GIWAXS measurements are carried out for these three devices individually. We find that the polymer crystallinity is stable in the device without solvent additives, and the stable V_{oc} values present in this device during the operation. However, the polymer crystallites undergo a decrease during the in-operando GIWAXS measurements in the devices with DIO additive, and the decay trend of crystallites is coincides well with the trend of the

V_{oc} changes along with time. Therefore, we conclude that the stability of polymer crystallinity has profound effects on the photovoltaic parameter of the V_{oc} during operation. Also, based on the peak intensity of (100) Bragg peak, we propose that solvent additives can cause competition between forming a D/A interpenetrating network and crystallite growth in donor polymer molecules. DIO enhances the polymer's ability to form interpenetrating networks in the BHJ film, but it lowers the polymer crystallinity, and results in a lower V_{oc}. Our work gives a further understanding of the degradation mechanism behind solvent additives. The findings can help to choose a suitable solvent additive, which can well balance the interpenetrating network character and the crystallinity in a BHJ film for next generation solar cells.

9 Conclusion and outlook

The main aim of this thesis is to optimize the morphology and compatibility of donor and acceptor materials in the BHJ film, and investigate the degradation mechanism of the active layer doped with solvent additives. Solar cells based on P3HT:PC_{71}BM, PTB7-Th:PC_{71}BM and PffBT4T-2OD:PC_{71}BM are studied. To address these issues, a model, based on the polymer composition at interfaces, is built to decide whether an interfacial layer can affect the polymer gradient in the BHJ layer. A third component (PBDTTPD-COOH) is introduced into the D/A blend to improve the compatibility of donor and acceptor molecules and the light absorption. Also, in-operando X-ray scattering measurements are applied to investigate the polymer morphology and crystallinity dynamics during the device aging.

Five interfacial modifiers, with a wide range of surface energy, are employed to provide a model based on the relative polymer accumulation at the interfacial layer/BHJ interface. The prediction is confirmed by the photovoltaic performance of the corresponding assembled devices and the polymer gradient changes, which are detected by ToF-SIMS. The approach described there provides a set of simple guidelines to rationally predict, in advance, the role of an interfacial modifier or interface before undergoing for laborious device assembly and testing.

A conjugated polymer, PBDTTPD-COOH, is doped into the D/A blend solution (PTB7-Th:PC_{71}BM and PffBT4T-2OD:PC_{71}BM) with different concentrations. The effects of the third component on the polymer crystalline size and order, film morphology, device performances and stability are studied. It has been found that the addition of PBDTTPD-COOH is beneficial since it optimizes the polymer crystallite size and orientation simultaneously in BHJ films. The size of the favorable domain is increased and more face-on oriented crystallites present in the BHJ films when the third component is added. Furthermore, the stability tests show that PBDTTPD-COOH significantly improves the device stability. The T80 lifetime values of the optimized devices (3.7 h and 4.3 h) is enhanced by the addition of PBDTTPD-COOH as compared to the corresponding references (0.35 h and 2.6 h). Therefore, our study presents a new and efficient strategy to optimize the crystallinity and compatibility of BHJ materials as well as device stability, and could thereby contribute to further development of OSCs.

To figure out the effects of solvent additives on the device stability, the investigation is firstly carried on the solar cells based on PTB7-Th:PC_{71}BM without and with solvent additives (DIO and CBA) by in-operando measurements. The solar cell performance is probed simultaneously to a structure characterization via GISAXS measurements. The morphological changes are found in the active layers in the solar cells without solvent additive, with DIO and with CBA during operation. The increase of polymer domain sizes is shown in the sample without a solvent additive and the device degradation is dominated by a decay of J_{sc}. Due to no post-treatments in the device fabrication process, DIO and CBA with high boiling points are likely to be residual in the device after the assembly. Therefore, the polymer domains become smaller and more isolated after the residual solvent additives are evaporated during the in-operando process, resulting in a decay of FF. Moreover, DIO has a higher boiling point, and therefore more of it is left in the film compared to CBA. The final film after the measurement still contains some DIO. The in-operando characterizations give us a better understanding of the complex degradation processes in organic solar cells. Two major types of morphological degradation processes, namely domain growth and domain shrinkage, are confirmed for the high efficiency system PTB7-Th:PC_{71}BM depending on the presence of solvent additives. Such general knowledge will be important to improve the stability of organic solar cells and thereby contribute to a successful real-world use of this class of next generation solar cells.

To avoid residual solvent additives in the solar cells, further investigations are performed on the PffBT4T-2OD:PC_{71}BM based solar cells without and with solvent additives (DIO and CBA) by in-operando GISAXS and GIWAXS measurements. As high temperature spin-coating and thermal annealing are carried out on the BHJ films, almost all solvent can be removed during the assembly process, which is confirmed by in-operando GISAXS measurements that no escaping solvent is detected during the in-operando measurements and FF is the most stable photovoltaic parameter. However, the decay of V_{oc} has a significant codependence with the polymer crystallinity obtaining from in-operando GI-WAXS measurements. Comparing the behaviors of these three devices, we conclude that doping with solvent additives helps to obtain more donor and acceptor interpenetration networks in a BHJ layer to form a stable morphology, which reflects on a stable fill factor (FF). However, solvent additives also can cause competition between forming a D/A interpenetrating network and crystallite growth in donor polymer molecules. DIO enhances the polymer's ability to form interpenetrating networks in BHJ film, but it interrupts the polymer crystallinity, and results in a lower V_{oc}. Thereby, our work gives an insight in the degradation mechanism of BHj processed with solvent additives. These findings can help choosing a suitable solvent additive, which can well balance formation of an interpenetrating network and crystallinity in a BHJ film for next generation solar cells.

Several aspects are feasible for further exploration based on this present thesis. Firstly, as mentioned before, the third component can improve the polymer crystallinity and D/A compatibility, which means doping the third component can improve the capability of forming polymer crystallites but competes with forming an interpenetrating network. Therefore, further investigations can have to carried out on the ternary solar cells with solvent additive. Solar cells with high efficiency and long-term stability can be expected from the optimal volumes of solvent additive and a third component. Secondly, non-fullerene based OSCs are emerging in the recent years. Solvent additives are still widely used in this system. To understand whether the observed degradation mechanisms are still present in non-fullerene system, more experiments have to be taken into consideration. At last, we cannot skip the large-scale fabrication process before the solar cells can develop as a real world application. To well control the film morphology, the understanding of film morphology development is essential, especially when processing with solvent additives.

Bibliography

[1] *Bp statistical review of world energy june 2017.* tech. rep., BP, London, 2017.

[2] A. C. Yeh and H. Bai, "Comparison of ammonia and monoethanolamine solvents to reduce CO2 greenhouse gas emissions," *Science of The Total Environment*, vol. 228, pp. 121–133, apr 1999.

[3] N. S. Lewis and D. G. Nocera, "Powering the planet: Chemical challenges in solar energy utilization," *Proceedings of the National Academy of Sciences*, vol. 103, pp. 15729–15735, oct 2006.

[4] A. Becquerel, "Recherches sur les effets de la radiation chimique de la lumiere solaire au moyen des courants electriques," *Comptes Rendus de L´Academie des Sciences*, vol. 9, pp. 145–149, 1839.

[5] D. M. Chapin, C. S. Fuller, and G. L. Pearson, "A new silicon p-n junction photocell for converting solar radiation into electrical power," *Journal of Applied Physics*, vol. 25, pp. 676–677, may 1954.

[6] M. A. Green, K. Emery, Y. Hishikawa, W. Warta, and E. D. Dunlop, "Solar cell efficiency tables (version 46)," *Progress in Photovoltaics: Research and Applications*, vol. 23, pp. 805–812, jun 2015.

[7] "Best research-cell efficiency chart — photovoltaic research — nrel, https://www.nrel.gov/pv/cell-efficiency.html, (accessed december 23, 2019).."

[8] A. Polman, M. Knight, E. C. Garnett, B. Ehrler, and W. C. Sinke, "Photovoltaic materials: Present efficiencies and future challenges," *Science*, vol. 352, pp. aad4424–aad4424, apr 2016.

[9] B. M. Kayes, H. Nie, R. Twist, S. G. Spruytte, F. Reinhardt, I. C. Kizilyalli, and G. S. Higashi, "27.6% conversion efficiency, a new record for single-junction solar cells under 1 sun illumination," in *2011 37th IEEE Photovoltaic Specialists Conference*, IEEE, jun 2011.

[10] C. K. Chiang, C. R. Fincher, Y. W. Park, A. J. Heeger, H. Shirakawa, E. J. Louis, S. C. Gau, and A. G. MacDiarmid, "Electrical conductivity in doped polyacetylene," *Physical Review Letters*, vol. 39, pp. 1098–1101, oct 1977.

[11] S. Gnes, H. Neugebauer, and N. S. Sariciftci, "Conjugated polymer-based organic solar cells," *Chemical Reviews*, vol. 107, pp. 1324–1338, apr 2007.

[12] M. Grel, "Dye-sensitized solar cells," *Journal of Photochemistry and Photobiology C: Photochemistry Reviews*, vol. 4, pp. 145–153, oct 2003.

[13] P. V. Kamat, "Quantum dot solar cells. semiconductor nanocrystals as light harvesters," *The Journal of Physical Chemistry C*, vol. 112, pp. 18737–18753, oct 2008.

[14] E. H. Jung, N. J. Jeon, E. Y. Park, C. S. Moon, T. J. Shin, T.-Y. Yang, J. H. Noh, and J. Seo, "Efficient, stable and scalable perovskite solar cells using poly(3-hexylthiophene)," *Nature*, vol. 567, pp. 511–515, mar 2019.

[15] M. A. Green, E. D. Dunlop, D. H. Levi, J. Hohl-Ebinger, M. Yoshita, and A. W. Ho-Baillie, "Solar cell efficiency tables (version 54)," *Progress in Photovoltaics: Research and Applications*, vol. 27, pp. 565–575, jun 2019.

[16] N. Espinosa, M. Hsel, D. Angmo, and F. C. Krebs, "Solar cells with one-day energy payback for the factories of the future," *Energy Environ. Sci.*, vol. 5, no. 1, pp. 5117–5132, 2012.

[17] N. Espinosa, R. García-Valverde, and F. C. Krebs, "Life-cycle analysis of product integrated polymer solar cells," *Energy & Environmental Science*, vol. 4, no. 5, p. 1547, 2011.

[18] E. A. A. Arbab, B. Gebremichael, A. Kumar, and G. T. Mola, "Morphology-dependent performance of thin film organic solar cells," *Journal of Modern Optics*, vol. 66, pp. 399–406, oct 2018.

[19] F. Zhao, C. Wang, and X. Zhan, "Morphology control in organic solar cells," *Advanced Energy Materials*, vol. 8, p. 1703147, mar 2018.

[20] T. L. Benanti and D. Venkataraman, "Organic solar cells: An overview focusing on active layer morphology," *Photosynthesis Research*, vol. 87, pp. 73–81, jan 2006.

[21] L. Meng, Y. Zhang, X. Wan, C. Li, X. Zhang, Y. Wang, X. Ke, Z. Xiao, L. Ding, R. Xia, H.-L. Yip, Y. Cao, and Y. Chen, "Organic and solution-processed tandem solar cells with 17.3% efficiency," *Science*, vol. 361, pp. 1094–1098, aug 2018.

[22] J. Yuan, Y. Zhang, L. Zhou, G. Zhang, H.-L. Yip, T.-K. Lau, X. Lu, C. Zhu, H. Peng, P. A. Johnson, M. Leclerc, Y. Cao, J. Ulanski, Y. Li, and Y. Zou, "Single-junction organic solar cell with over 15% efficiency using fused-ring acceptor with electron-deficient core," *Joule*, vol. 3, pp. 1140–1151, apr 2019.

[23] L. Song, W. Wang, E. Barabino, D. Yang, V. Krstgens, P. Zhang, S. V. Roth, and P. Müller-Buschbaum, "Composition–morphology correlation in PTB7-th/PC71bm blend films for organic solar cells," *ACS Applied Materials & Interfaces*, vol. 11, pp. 3125–3135, dec 2018.

[24] Z. He, B. Xiao, F. Liu, H. Wu, Y. Yang, S. Xiao, C. Wang, T. P. Russell, and Y. Cao, "Single-junction polymer solar cells with high efficiency and photovoltage," *Nature Photonics*, vol. 9, pp. 174–179, feb 2015.

[25] C. J. Schaffer, J. Schlipf, E. D. Indari, B. Su, S. Bernstorff, and P. Mller-Buschbaum, "Effect of blend composition and additives on the morphology of PCPDTBT:PC71bm thin films for organic photovoltaics," *ACS Applied Materials & Interfaces*, vol. 7, pp. 21347–21355, sep 2015.

[26] J. Miao, H. Chen, F. Liu, B. Zhao, L. Hu, Z. He, and H. Wu, "Efficiency enhancement in solution-processed organic small molecule: Fullerene solar cells via solvent vapor annealing," *Applied Physics Letters*, vol. 106, p. 183302, may 2015.

[27] D. Zomerman, J. Kong, S. M. McAfee, G. C. Welch, and T. L. Kelly, "Control and characterization of organic solar cell morphology through variable-pressure solvent vapor annealing," *ACS Applied Energy Materials*, sep 2018.

[28] W. Wang, S. Guo, E. M. Herzig, K. Sarkar, M. Schindler, D. Magerl, M. Philipp, J. Perlich, and P. Müller-Buschbaum, "Investigation of morphological degradation of p3ht:PCBM bulk heterojunction films exposed to long-term host solvent vapor," *Journal of Materials Chemistry A*, vol. 4, no. 10, pp. 3743–3753, 2016.

[29] W. Ma, G. Yang, K. Jiang, J. H. Carpenter, Y. Wu, X. Meng, T. McAfee, J. Zhao, C. Zhu, C. Wang, H. Ade, and H. Yan, "Influence of processing parameters and molecular weight on the morphology and properties of high-performance PffBT4t-2od:PC71bm organic solar cells," *Advanced Energy Materials*, vol. 5, p. 1501400, sep 2015.

[30] X. Song, N. Gasparini, and D. Baran, "The influence of solvent additive on polymer solar cells employing fullerene and non-fullerene acceptors," *Advanced Electronic Materials*, vol. 4, p. 1700358, nov 2017.

[31] F. Liu, W. Zhao, J. R. Tumbleston, C. Wang, Y. Gu, D. Wang, A. L. Briseno, H. Ade, and T. P. Russell, "Understanding the morphology of PTB7:PCBM blends in organic photovoltaics," *Advanced Energy Materials*, vol. 4, p. 1301377, oct 2013.

[32] W. Kim, J. K. Kim, E. Kim, T. K. Ahn, D. H. Wang, and J. H. Park, "Conflicted effects of a solvent additive on PTB7:PC71bm bulk heterojunction solar cells," *The Journal of Physical Chemistry C*, vol. 119, pp. 5954–5961, mar 2015.

[33] B. Cao, X. He, C. R. Fetterly, B. C. Olsen, E. J. Luber, and J. M. Buriak, "Role of interfacial layers in organic solar cells: Energy level pinning versus phase segregation," *ACS Applied Materials & Interfaces*, vol. 8, pp. 18238–18248, jun 2016.

[34] W. Wang, *Nanostructure performance relationship in polymer based solar cells.* PhD thesis, TECHNISCHE UNIVERSITÄT MÜNCHEN, 2016.

[35] W. Zhao, L. Ye, S. Zhang, B. Fan, M. Sun, and J. Hou, "Ultrathin polyaniline-based buffer layer for highly efficient polymer solar cells with wide applicability," *Scientific Reports*, vol. 4, oct 2014.

[36] J. W. Rumer and I. McCulloch, "Organic photovoltaics: Crosslinking for optimal morphology and stability," *Materials Today*, vol. 18, pp. 425–435, oct 2015.

[37] M. Jørgensen, K. Norrman, S. A. Gevorgyan, T. Tromholt, B. Andreasen, and F. C. Krebs, "Stability of polymer solar cells," *Advanced Materials*, vol. 24, pp. 580–612, dec 2011.

[38] M. Jørgensen, K. Norrman, and F. C. Krebs, "Stability/degradation of polymer solar cells," *Solar Energy Materials and Solar Cells*, vol. 92, pp. 686–714, jul 2008.

[39] C. J. Schaffer, C. M. Palumbiny, M. A. Niedermeier, C. Jendrzejewski, G. Santoro, S. V. Roth, and P. Müller-Buschbaum, "A direct evidence of morphological degradation on a nanometer scale in polymer solar cells," *Advanced Materials*, vol. 25, pp. 6760–6764, sep 2013.

[40] C. J. Schaffer, C. M. Palumbiny, M. A. Niedermeier, C. Burger, G. Santoro, S. V. Roth, and P. Müller-Buschbaum, "Morphological degradation in low bandgap polymer solar cells - an in operando study," *Advanced Energy Materials*, vol. 6, p. 1600712, jul 2016.

[41] D. M. González, C. J. Schaffer, S. Prller, J. Schlipf, L. Song, S. Bernstorff, E. M. Herzig, and P. Mller-Buschbaum, "Codependence between crystalline and photo-voltage evolutions in p3ht:PCBM solar cells probed with in-operando GIWAXS," *ACS Applied Materials & Interfaces*, vol. 9, pp. 3282–3287, jan 2017.

[42] G. Griffini, J. D. Douglas, C. Piliego, T. W. Holcombe, S. Turri, J. M. J. Fréchet, and J. L. Mynar, "Long-term thermal stability of high-efficiency polymer solar cells based on photocrosslinkable donor-acceptor conjugated polymers," *Advanced Materials*, vol. 23, pp. 1660–1664, feb 2011.

[43] J. Ahmad, K. Bazaka, L. J. Anderson, R. D. White, and M. V. Jacob, "Materials and methods for encapsulation of OPV: A review," *Renewable and Sustainable Energy Reviews*, vol. 27, pp. 104–117, nov 2013.

[44] Y.-J. Cheng, C.-H. Hsieh, P.-J. Li, and C.-S. Hsu, "Morphological stabilization by in situ polymerization of fullerene derivatives leading to efficient, thermally stable organic photovoltaics," *Advanced Functional Materials*, vol. 21, pp. 1723–1732, mar 2011.

[45] M. D. Clark, M. L. Jespersen, R. J. Patel, and B. J. Leever, "Predicting vertical phase segregation in polymer-fullerene bulk heterojunction solar cells by free energy analysis," *ACS Applied Materials & Interfaces*, vol. 5, pp. 4799–4807, may 2013.

[46] Z. Li, X. Xu, W. Zhang, X. Meng, Z. Genene, W. Ma, W. Mammo, A. Yartsev, M. R. Andersson, R. A. J. Janssen, and E. Wang, "9.0% power conversion efficiency from ternary all-polymer solar cells," *Energy & Environmental Science*, vol. 10, no. 10, pp. 2212–2221, 2017.

[47] J. Chen, L. Zhang, X. Jiang, K. Gao, F. Liu, X. Gong, J. Chen, and Y. Cao, "Usingo-chlorobenzaldehyde as a fast removable solvent additive during spin-coating PTB7-based active layers: High efficiency thick-film polymer solar cells," *Advanced Energy Materials*, vol. 7, p. 1601344, oct 2016.

[48] H.-C. Liao, C.-C. Ho, C.-Y. Chang, M.-H. Jao, S. B. Darling, and W.-F. Su, "Additives for morphology control in high-efficiency organic solar cells," *Materials Today*, vol. 16, pp. 326–336, sep 2013.

[49] J. K. Lee, W. L. Ma, C. J. Brabec, J. Yuen, J. S. Moon, J. Y. Kim, K. Lee, G. C. Bazan, and A. J. Heeger, "Processing additives for improved efficiency from bulk heterojunction solar cells," *Journal of the American Chemical Society*, vol. 130, pp. 3619–3623, mar 2008.

[50] A. D. Jenkins, P. Kratochvíl, R. F. T. Stepto, and U. W. Suter, "Glossary of basic terms in polymer science (IUPAC recommendations 1996)," *Pure and Applied Chemistry*, vol. 68, pp. 2287–2311, jan 1996.

[51] M. L. Huggins, "THERMODYNAMIC PROPERTIES OF SOLUTIONS OF LONG-CHAIN COMPOUNDS," *Annals of the New York Academy of Sciences*, vol. 43, pp. 1–32, mar 1942.

[52] P. J. Flory, "Thermodynamics of high polymer solutions," *The Journal of Chemical Physics*, vol. 10, pp. 51–61, jan 1942.

[53] T.-H. Le, Y. Kim, and H. Yoon, "Electrical and electrochemical properties of conducting polymers," *Polymers*, vol. 9, p. 150, apr 2017.

[54] G. Kaur, R. Adhikari, P. Cass, M. Bown, and P. Gunatillake, "Electrically conductive polymers and composites for biomedical applications," *RSC Advances*, vol. 5, no. 47, pp. 37553–37567, 2015.

[55] C. M. Palumbiny, *Polymeric PEDOT:PSS electrodes for organic electronics: Understanding the conductivity-structure relation.* PhD thesis, TECHNISCHE UNIVERSITÄT MÜNCHEN, 2015.

[56] L. Dai, *Intelligent Macromolecules for Smart Devices: From Materials Synthesis to Device Applications.* Springer-Verlag, 2004.

[57] Y. Tamai, H. Ohkita, H. Benten, and S. Ito, "Exciton diffusion in conjugated polymers: From fundamental understanding to improvement in photovoltaic conversion efficiency," *The Journal of Physical Chemistry Letters*, vol. 6, pp. 3417–3428, aug 2015.

[58] M. Pope and C. E. Swenberg, *Electronic Processes in Organic Crystals and Polymers.* Oxford University Press, 1999.

[59] L. Onsager, "Initial recombination of ions," *Physical Review*, vol. 54, pp. 554–557, oct 1938.

[60] C. L. Braun, "Electric field assisted dissociation of charge transfer states as a mechanism of photocarrier production," *The Journal of Chemical Physics*, vol. 80, pp. 4157–4161, may 1984.

[61] G. Dennler, M. C. Scharber, and C. J. Brabec, "Polymer-fullerene bulkheterojunction solar cells," *Advanced Materials*, vol. 21, pp. 1323–1338, apr 2009.

[62] A. Miller and E. Abrahams, "Impurity conduction at low concentrations," *Physical Review*, vol. 120, pp. 745–755, nov 1960.

[63] H. Bässler, "Charge transport in disordered organic photoconductors a monte carlo simulation study," *physica status solidi (b)*, vol. 175, pp. 15–56, jan 1993.

[64] A. K. Ghosh, D. L. Morel, T. Feng, R. F. Shaw, and C. A. Rowe, "Photovoltaic and rectification properties of al/mg phthalocyanine/ag schottky-barrier cells," *Journal of Applied Physics*, vol. 45, pp. 230–236, jan 1974.

[65] A. K. Ghosh and T. Feng, "Merocyanine organic solar cells," *Journal of Applied Physics*, vol. 49, pp. 5982–5989, dec 1978.

[66] H. Spanggaard and F. C. Krebs, "A brief history of the development of organic and polymeric photovoltaics," *Solar Energy Materials and Solar Cells*, vol. 83, pp. 125–146, jun 2004.

[67] C. W. Tang, "Two-layer organic photovoltaic cell," *Applied Physics Letters*, vol. 48, pp. 183–185, jan 1986.

[68] Y. Cui, H. Yao, J. Zhang, T. Zhang, Y. Wang, L. Hong, K. Xian, B. Xu, S. Zhang, J. Peng, Z. Wei, F. Gao, and J. Hou, "Over 16% efficiency organic photovoltaic cells enabled by a chlorinated acceptor with increased open-circuit voltages," *Nature Communications*, vol. 10, jun 2019.

[69] F. Padinger, R. Rittberger, and N. Sariciftci, "Effects of postproduction treatment on plastic solar cells," *Advanced Functional Materials*, vol. 13, pp. 85–88, jan 2003.

[70] S. Guo, B. Cao, W. Wang, J.-F. Moulin, and P. Müller-Buschbaum, "Effect of alcohol treatment on the performance of PTB7:PC71bm bulk heterojunction solar cells," *ACS Applied Materials & Interfaces*, vol. 7, pp. 4641–4649, feb 2015.

[71] D. Yang, F. C. Lhrer, V. Körstgens, A. Schreiber, S. Bernstorff, J. M. Buriak, and P. Müller-Buschbaum, "In-operando study of the effects of solvent additives on the stability of organic solar cells based on PTB7-th:PC71bm," *ACS Energy Letters*, vol. 4, pp. 464–470, jan 2019.

[72] Y. Li, Y. Chen, X. Liu, Z. Wang, X. Yang, Y. Tu, and X. Zhu, "Controlling blend film morphology by varying alkyl side chain in highly coplanar donor–acceptor copolymers for photovoltaic application," *Macromolecules*, vol. 44, pp. 6370–6381, aug 2011.

[73] F. Fungura, *Organic solar cells: Degradation processes and approaches to enhance performance.* PhD thesis, Iowa State University, 2016.

[74] K. Norrman, N. Larsen, and F. Krebs, "Lifetimes of organic photovoltaics: Combining chemical and physical characterisation techniques to study degradation mechanisms," *Solar Energy Materials and Solar Cells*, vol. 90, pp. 2793–2814, nov 2006.

[75] M. S. A. Abdou and S. Holdcroft, "Mechanisms of photodegradation of poly(3-alkylthiophenes) in solution," *Macromolecules*, vol. 26, pp. 2954–2962, may 1993.

[76] S. Chambon, A. Rivaton, J.-L. Gardette, and M. Firon, "Reactive intermediates in the initiation step of the photo-oxidation of MDMO-PPV," *Journal of Polymer Science Part A: Polymer Chemistry*, vol. 47, pp. 6044–6052, nov 2009.

[77] M. Manceau, A. Rivaton, and J.-L. Gardette, "Involvement of singlet oxygen in the solid-state photochemistry of p3ht," *Macromolecular Rapid Communications*, vol. 29, pp. 1823–1827, nov 2008.

[78] R. A. Street and D. M. Davies, "Kinetics of light induced defect creation in organic solar cells," *Applied Physics Letters*, vol. 102, p. 043305, jan 2013.

[79] R. A. Street, J. E. Northrup, and B. S. Krusor, "Radiation induced recombination centers in organic solar cells," *Physical Review B*, vol. 85, may 2012.

[80] S. Shah and R. Biswas, "Atomic pathways underlying light-induced changes in organic solar cell materials," *The Journal of Physical Chemistry C*, vol. 119, pp. 20265–20271, aug 2015.

[81] M. Gopal, W. J. M. CHAN, and L. C. D. JONGHE *Journal of Materials Science*, vol. 32, no. 22, pp. 6001–6008, 1997.

[82] R. Lazzari, "IsGISAXS: a program for grazing-incidence small-angle x-ray scattering analysis of supported islands," *Journal of Applied Crystallography*, vol. 35, pp. 406–421, jul 2002.

[83] V. Holý and T. Baumbach, "Nonspecular x-ray reflection from rough multilayers," *Physical Review B*, vol. 49, pp. 10668–10676, apr 1994.

[84] S. K. Sinha, E. B. Sirota, S. Garoff, and H. B. Stanley, "X-ray and neutron scattering from rough surfaces," *Physical Review B*, vol. 38, pp. 2297–2311, aug 1988.

[85] P. Müller-Buschbaum, "Grazing incidence small-angle x-ray scattering: an advanced scattering technique for the investigation of nanostructured polymer films," *Analytical and Bioanalytical Chemistry*, vol. 376, pp. 3–10, mar 2003.

[86] O. J. Guentert, "Study of the anomalous surface reflection of x rays," *Journal of Applied Physics*, vol. 36, pp. 1361–1366, apr 1965.

[87] R. Hosemann, W. Vogel, D. Weick, and F. J. Baltá-Calleja, "Novel aspects of the real paracrystal," *Acta Crystallographica Section A*, vol. 37, pp. 85–91, jan 1981.

[88] G. Renaud, R. Lazzari, and F. Leroy, "Probing surface and interface morphology with grazing incidence small angle x-ray scattering," *Surface Science Reports*, vol. 64, pp. 255–380, aug 2009.

[89] R. A. Marcus, "On the theory of oxidation-reduction reactions involving electron transfer. i," *The Journal of Chemical Physics*, vol. 24, pp. 966–978, may 1956.

[90] J. L. Baker, L. H. Jimison, S. Mannsfeld, S. Volkman, S. Yin, V. Subramanian, A. Salleo, A. P. Alivisatos, and M. F. Toney, "Quantification of thin film crystallographic orientation using x-ray diffraction with an area detector," *Langmuir*, vol. 26, pp. 9146–9151, jun 2010.

[91] F. T. L. Muniz, M. A. R. Miranda, C. M. dos Santos, and J. M. Sasaki, "The scherrer equation and the dynamical theory of x-ray diffraction," *Acta Crystallographica Section A Foundations and Advances*, vol. 72, pp. 385–390, apr 2016.

[92] M. D. Abrámo, P. J. Magalhães, and S. J. Ram, "Image processing with imagej," *Biophotonics International*, 2004.

[93] C. J. van Oss, *Interfacial Forces in Aqueous Media*. CRC Press: Boca Raton, 2006.

[94] J. M. Casper, "Physical chemistry of surfaces (3rd ed.), arthur w. adamson, wiley-interscience, new york, 1976, 698 pp. $24.95.," *Journal of Polymer Science: Polymer Letters Edition*, vol. 15, pp. 632–633, oct 1977.

[95] J. C. Berg, *An Introduction to Interfaces and Colloids*. WORLD SCIENTIFIC, nov 2009.

[96] B. Cappella and G. Dietler, "Force-distance curves by atomic force microscopy," *Surface Science Reports*, vol. 34, pp. 1–104, jan 1999.

[97] D. Nečas and P. Klapetek, "Gwyddion: an open-source software for SPM data analysis," *Open Physics*, vol. 10, jan 2012.

[98] A. Nelson, "Co-refinement of multiple-contrast neutron/x-ray reflectivity data usingMOTOFIT," *Journal of Applied Crystallography*, vol. 39, pp. 273–276, mar 2006.

[99] G. Benecke, W. Wagermaier, C. Li, M. Schwartzkopf, G. Flucke, R. Hoerth, I. Zizak, M. Burghammer, E. Metwalli, P. Mller-Buschbaum, M. Trebbin, S. Frster, O. Paris, S. V. Roth, and P. Fratzl, "A customizable software for fast reduction and analysis of large x-ray scattering data sets: applications of the newDPDAKpackage to small-angle x-ray scattering and grazing-incidence small-angle x-ray scattering," *Journal of Applied Crystallography*, vol. 47, pp. 1797–1803, sep 2014.

[100] R. Lazzari, "IsGISAXS: a program for grazing-incidence small-angle x-ray scattering analysis of supported islands," *Journal of Applied Crystallography*, vol. 35, pp. 406–421, jul 2002.

[101] Z. Jiang, "GIXSGUI: a MATLAB toolbox for grazing-incidence x-ray scattering data visualization and reduction, and indexing of buried three-dimensional periodic nanostructured films," *Journal of Applied Crystallography*, vol. 48, pp. 917–926, apr 2015.

[102] L. Ye, S. Zhang, W. Zhao, H. Yao, and J. Hou, "Highly efficient 2d-conjugated benzodithiophene-based photovoltaic polymer with linear alkylthio side chain," *Chemistry of Materials*, vol. 26, pp. 3603–3605, jun 2014.

[103] Y. Liu, J. Zhao, Z. Li, C. Mu, W. Ma, H. Hu, K. Jiang, H. Lin, H. Ade, and H. Yan, "Aggregation and morphology control enables multiple cases of high-efficiency polymer solar cells," *Nature Communications*, vol. 5, nov 2014.

[104] J. Zhao, Y. Li, H. Lin, Y. Liu, K. Jiang, C. Mu, T. Ma, J. Y. L. Lai, H. Hu, D. Yu, and H. Yan, "High-efficiency non-fullerene organic solar cells enabled by a difluorobenzothiadiazole-based donor polymer combined with a properly matched small molecule acceptor," *Energy & Environmental Science*, vol. 8, no. 2, pp. 520–525, 2015.

[105] F. Zhang, Z. Zhuo, J. Zhang, X. Wang, X. Xu, Z. Wang, Y. Xin, J. Wang, J. Wang, W. Tang, Z. Xu, and Y. Wang, "Influence of pc60bm or pc70bm as electron acceptor on the performance of polymer solar cells," *Solar Energy Materials and Solar Cells*, vol. 97, pp. 71–77, feb 2012.

[106] A. Nardes, M. Kemerink, M. de Kok, E. Vinken, K. Maturová, and R. Janssen, "Conductivity, work function, and environmental stability of PEDOT:PSS thin films treated with sorbitol," *Organic Electronics*, vol. 9, pp. 727–734, oct 2008.

[107] P. Ravirajan, A. M. Peiró, M. K. Nazeeruddin, M. Graetzel, D. D. C. Bradley, J. R. Durrant, and J. Nelson, "Hybrid polymer/zinc oxide photovoltaic devices with vertically oriented ZnO nanorods and an amphiphilic molecular interface layer," *The Journal of Physical Chemistry B*, vol. 110, pp. 7635–7639, apr 2006.

[108] P. Müller-Buschbaum, "Influence of surface cleaning on dewetting of thin polystyrene films," *The European Physical Journal E*, vol. 12, pp. 443–448, nov 2003.

[109] D. W. Schubert and T. Dunkel, "Spin coating from a molecular point of view: its concentration regimes, influence of molar mass and distribution," *Materials Research Innovations*, vol. 7, pp. 314–321, oct 2003.

[110] T. Zhang, H. Han, Y. Zou, Y.-C. Lee, H. Oshima, K.-T. Wong, and R. J. Holmes, "Impact of thermal annealing on organic photovoltaic cells using regioisomeric donor–acceptor–acceptor molecules," *ACS Applied Materials & Interfaces*, vol. 9, pp. 25418–25425, jul 2017.

[111] T. M. Clarke, A. M. Ballantyne, J. Nelson, D. D. C. Bradley, and J. R. Durrant, "Free energy control of charge photogeneration in polythiophene/fullerene solar cells: The influence of thermal annealing on p3ht/PCBM blends," *Advanced Functional Materials*, vol. 18, pp. 4029–4035, dec 2008.

[112] B. Friedel, P. E. Keivanidis, T. J. K. Brenner, A. Abrusci, C. R. McNeill, R. H. Friend, and N. C. Greenham, "Effects of layer thickness and annealing of PEDOT:PSS layers in organic photodetectors," *Macromolecules*, vol. 42, pp. 6741–6747, sep 2009.

[113] G. Yu, J. Gao, J. C. Hummelen, F. Wudl, and A. J. Heeger, "Polymer photovoltaic cells: Enhanced efficiencies via a network of internal donor-acceptor heterojunctions," *Science*, vol. 270, pp. 1789–1791, dec 1995.

[114] J. D. Servaites, M. A. Ratner, and T. J. Marks, "Organic solar cells: A new look at traditional models," *Energy & Environmental Science*, vol. 4, no. 11, p. 4410, 2011.

[115] A. J. Heeger, "25th anniversary article: Bulk heterojunction solar cells: Understanding the mechanism of operation," *Advanced Materials*, vol. 26, pp. 10–28, dec 2013.

[116] R. Steim, F. R. Kogler, and C. J. Brabec, "Interface materials for organic solar cells," *Journal of Materials Chemistry*, vol. 20, no. 13, p. 2499, 2010.

[117] C.-Z. Li, H.-L. Yip, and A. K.-Y. Jen, "Interfacial materials for efficient solution processable organic photovoltaic devices," in *Topics in Applied Physics*, pp. 273–297, Springer Berlin Heidelberg, 2015.

[118] K. Li, Y. Wu, Y. Tang, M.-A. Pan, W. Ma, H. Fu, C. Zhan, and J. Yao, "Ternary blended fullerene-free polymer solar cells with 16.5% efficiency enabled with a higher-LUMO-level acceptor to improve film morphology," *Advanced Energy Materials*, vol. 9, p. 1901728, jul 2019.

[119] M.-A. Pan, T.-K. Lau, Y. Tang, Y.-C. Wu, T. Liu, K. Li, M.-C. Chen, X. Lu, W. Ma, and C. Zhan, "16.7%-efficiency ternary blended organic photovoltaic cells with PCBM as the acceptor additive to increase the open-circuit voltage and phase purity," *Journal of Materials Chemistry A*, vol. 7, no. 36, pp. 20713–20722, 2019.

[120] T. Yan, W. Song, J. Huang, R. Peng, L. Huang, and Z. Ge, "16.67% rigid and 14.06% flexible organic solar cells enabled by ternary heterojunction strategy," *Advanced Materials*, vol. 31, p. 1902210, aug 2019.

[121] L. Ciammaruchi, R. Oliveira, A. Charas, Tulus, E. von Hauff, G. Polino, F. Brunetti, R. Hansson, E. Moons, M. Krassas, G. Kakavelakis, E. Kymakis, J. G. Sánchez, J. Ferre-Borrull, L. F. Marsal, S. Zfle, D. Fluhr, R. Roesch, T. Faber, U. S. Schubert, H. Hoppe, K. Bakker, S. Veenstra, G. Zanotti, E. A. Katz, P. Apilo, B. Romero, T. A. Tumay, E. Parlak, L. M. Stagno, V. Turkovic, H.-G. Rubahn, M. Madsen, V. Kažukauskas, D. M. Tanenbaum, S. Shanmugam, and Y. Galagan, "Stability of organic solar cells with PCDTBT donor polymer: An interlaboratory study," *Journal of Materials Research*, vol. 33, pp. 1909–1924, jun 2018.

[122] T. Kim, S. Kang, J. Heo, S. Cho, J. W. Kim, A. Choe, B. Walker, R. Shanker, H. Ko, and J. Y. Kim, "Nanoparticle-enhanced silver-nanowire plasmonic electrodes for high-performance organic optoelectronic devices," *Advanced Materials*, vol. 30, p. 1800659, may 2018.

[123] D. Wang, J. Wang, L. liang Li, Q. shi An, H. Huang, C. qun Jiao, Y. Liu, and F. jun Zhang, "Ultrathin anode buffer layer for enhancing performance of polymer solar cells," *International Journal of Photoenergy*, vol. 2014, pp. 1–6, 2014.

[124] B. Xu, S.-A. Gopalan, A.-I. Gopalan, N. Muthuchamy, K.-P. Lee, J.-S. Lee, Y. Jiang, S.-W. Lee, S.-W. Kim, J.-S. Kim, H.-M. Jeong, J.-B. Kwon, J.-H. Bae, and S.-W. Kang, "Functional solid additive modified PEDOT:PSS as an anode buffer layer for enhanced photovoltaic performance and stability in polymer solar cells," *Scientific Reports*, vol. 7, mar 2017.

[125] Y. Xia and J. Ouyang, "Significant conductivity enhancement of conductive poly(3,4-ethylenedioxythiophene): Poly(styrenesulfonate) films through a treatment with organic carboxylic acids and inorganic acids," *ACS Applied Materials & Interfaces*, vol. 2, pp. 474–483, feb 2010.

[126] B. Meng, Y. Fu, Z. Xie, J. Liu, and L. Wang, "Phosphonate-functionalized donor polymer as an underlying interlayer to improve active layer morphology in polymer solar cells," *Macromolecules*, vol. 47, pp. 6246–6251, sep 2014.

[127] W. Zhang, B. Zhao, Z. He, X. Zhao, H. Wang, S. Yang, H. Wu, and Y. Cao, "High-efficiency ITO-free polymer solar cells using highly conductive PEDOT:PSS/surfactant bilayer transparent anodes," *Energy & Environmental Science*, vol. 6, no. 6, p. 1956, 2013.

[128] L. Huang, G. Wang, W. Zhou, B. Fu, X. Cheng, L. Zhang, Z. Yuan, S. Xiong, L. Zhang, Y. Xie, A. Zhang, Y. Zhang, W. Ma, W. Li, Y. Zhou, E. Reichmanis, and Y. Chen, "Vertical stratification engineering for organic bulk-heterojunction devices," *ACS Nano*, vol. 12, pp. 4440–4452, apr 2018.

[129] J.-J. Chen, K. N. Struk, and A. B. Brennan, "Surface modification of silicate glass using 3-(mercaptopropyl)trimethoxysilane for thiol–ene polymerization," *Langmuir*, vol. 27, pp. 13754–13761, nov 2011.

[130] I. Ucar, M. Doganci, C. Cansoy, H. Erbil, I. Avramova, and S. Suzer, "Combined XPS and contact angle studies of ethylene vinyl acetate and polyvinyl acetate blends," *Applied Surface Science*, vol. 257, pp. 9587–9594, sep 2011.

[131] X. Ma, B. Wigington, and D. Bouchard, "Fullerene c60: Surface energy and interfacial interactions in aqueous systems," *Langmuir*, vol. 26, pp. 11886–11893, jul 2010.

[132] W. Li, B. J. Worfolk, P. Li, T. C. Hauger, K. D. Harris, and J. M. Buriak, "Self-assembly of carboxylated polythiophene nanowires for improved bulk heterojunction morphology in polymer solar cells," *Journal of Materials Chemistry*, vol. 22, no. 22, p. 11354, 2012.

[133] H.-L. Yip and A. K.-Y. Jen, "Recent advances in solution-processed interfacial materials for efficient and stable polymer solar cells," *Energy & Environmental Science*, vol. 5, no. 3, p. 5994, 2012.

[134] Z. Xu, L.-M. Chen, G. Yang, C.-H. Huang, J. Hou, Y. Wu, G. Li, C.-S. Hsu, and Y. Yang, "Vertical phase separation in poly(3-hexylthiophene): Fullerene derivative blends and its advantage for inverted structure solar cells," *Advanced Functional Materials*, vol. 19, pp. 1227–1234, apr 2009.

[135] R. Singh, S. R. Suranagi, J. Lee, H. Lee, M. Kim, and K. Cho, "Unraveling the efficiency-limiting morphological issues of the perylene diimide-based non-fullerene organic solar cells," *Scientific Reports*, vol. 8, feb 2018.

[136] S. L. Anderson, E. J. Luber, B. C. Olsen, and J. M. Buriak, "Substance over subjectivity: Moving beyond the histogram," *Chemistry of Materials*, vol. 28, pp. 5973–5975, sep 2016.

[137] E. J. Luber and J. M. Buriak, "Reporting performance in organic photovoltaic devices," *ACS Nano*, vol. 7, pp. 4708–4714, jun 2013.

[138] H.-S. Ko, J.-W. Lee, and N.-G. Park, "15.76% efficiency perovskite solar cells prepared under high relative humidity: importance of PbI2 morphology in two-step deposition of CH3nh3pbi3," *Journal of Materials Chemistry A*, vol. 3, no. 16, pp. 8808–8815, 2015.

[139] A. J. Taylor, D. J. Graham, and D. G. Castner, "Reconstructing accurate ToF-SIMS depth profiles for organic materials with differential sputter rates," *The Analyst*, vol. 140, no. 17, pp. 6005–6014, 2015.

[140] D.-M. Smilgies, "Scherrer grain-size analysis adapted to grazing-incidence scattering with area detectors," *Journal of Applied Crystallography*, vol. 42, pp. 1030–1034, oct 2009.

[141] J. Zhao, S. Zhao, Z. Xu, B. Qiao, D. Huang, L. Zhao, Y. Li, Y. Zhu, and P. Wang, "Revealing the effect of additives with different solubility on the morphology and the donor crystalline structures of organic solar cells," *ACS Applied Materials & Interfaces*, vol. 8, pp. 18231–18237, jul 2016.

[142] S. Bi, Z. Ouyang, S. Shaik, and D. Li, "Effect of donor-acceptor vertical composition profile on performance of organic bulk heterojunction solar cells," *Scientific Reports*, vol. 8, jun 2018.

[143] X. Li, X. Liu, P. Sun, Y. Feng, H. Shan, X. Wu, J. Xu, C. Huang, Z.-K. Chen, and Z.-X. Xu, "Effect of fluorination on n-type conjugated polymers for all-polymer solar cells," *RSC Advances*, vol. 7, no. 28, pp. 17076–17084, 2017.

[144] D. Yang, B. Cao, V. Krstgens, N. Saxena, N. Li, C. Bilko, S. Grott, W. Chen, X. Jiang, J. E. Heger, S. Bernstorff, and P. Mller-Buschbaum, "Tailoring morphology compatibility and device stability by adding PBDTTPD-COOH as third component to fullerene-based polymer solar cells," *ACS Applied Energy Materials*, vol. 3, pp. 2604–2613, feb 2020.

[145] R. Meier, M. A. Ruderer, A. Diethert, G. Kaune, V. Körstgens, S. V. Roth, and P. Müller-Buschbaum, "Influence of film thickness on the phase separation mechanism in ultrathin conducting polymer blend films," *The Journal of Physical Chemistry B*, vol. 115, pp. 2899–2909, mar 2011.

[146] T. Ameri, P. Khoram, J. Min, and C. J. Brabec, "Organic ternary solar cells: A review," *Advanced Materials*, vol. 25, pp. 4245–4266, may 2013.

[147] A. Mhamdi, W. Boukhili, M. Raissi, M. Mahdouani, L. Vignau, and R. Bourguiga, "Simulation and optimization of the performance of organic photovoltaic cells based on capped copolymers for bulk heterojunctions," *Superlattices and Microstructures*, vol. 96, pp. 241–252, aug 2016.

[148] K. Nakabayashi and H. Mori, "Donor-acceptor block copolymers: Synthesis and solar cell applications," *Materials*, vol. 7, pp. 3274–3290, apr 2014.

[149] C.-L. Chung, H.-C. Chen, Y.-S. Yang, W.-Y. Tung, J.-W. Chen, W.-C. Chen, C.-G. Wu, and K.-T. Wong, "S,n-heteroacene-based copolymers for highly efficient organic field effect transistors and organic solar cells: Critical impact of aromatic subunits in the ladder -system," *ACS Applied Materials & Interfaces*, vol. 10, pp. 6471–6483, feb 2018.

[150] Y. Zhang, S. K. Hau, H.-L. Yip, Y. Sun, O. Acton, and A. K.-Y. Jen, "Efficient polymer solar cells based on the copolymers of benzodithiophene and thienopyrroledione," *Chemistry of Materials*, vol. 22, pp. 2696–2698, may 2010.

[151] A. Hadipour, B. de Boer, J. Wildeman, F. Kooistra, J. Hummelen, M. Turbiez, M. Wienk, R. Janssen, and P. Blom, "Solution-processed organic tandem solar cells," *Advanced Functional Materials*, vol. 16, pp. 1897–1903, sep 2006.

[152] Q. An, F. Zhang, J. Zhang, W. Tang, Z. Deng, and B. Hu, "Versatile ternary organic solar cells: a critical review," *Energy & Environmental Science*, vol. 9, no. 2, pp. 281–322, 2016.

[153] Y. Huang, E. J. Kramer, A. J. Heeger, and G. C. Bazan, "Bulk heterojunction solar cells: Morphology and performance relationships," *Chemical Reviews*, vol. 114, pp. 7006–7043, may 2014.

[154] M. Makha, P. Schwaller, K. Strassel, S. B. Anantharaman, F. Nesch, R. Hany, and J. Heier, "Insights into photovoltaic properties of ternary organic solar cells from phase diagrams," *Science and Technology of Advanced Materials*, vol. 19, pp. 669–682, sep 2018.

[155] P. Bi and X. Hao, "Versatile ternary approach for novel organic solar cells: A review," *Solar RRL*, vol. 3, p. 1800263, nov 2018.

[156] R. R. Lunt, J. B. Benziger, and S. R. Forrest, "Relationship between crystalline order and exciton diffusion length in molecular organic semiconductors," *Advanced Materials*, vol. 22, pp. 1233–1236, mar 2010.

[157] H. Lee, J. Sohn, P. Tyagi, and C. Lee, "Crystallinity dependent thermal degradation in organic solar cell," *Applied Physics Letters*, vol. 110, p. 053301, jan 2017.

[158] J. R. Tumbleston, B. A. Collins, L. Yang, A. C. Stuart, E. Gann, W. Ma, W. You, and H. Ade, "The influence of molecular orientation on organic bulk heterojunction solar cells," *Nature Photonics*, vol. 8, pp. 385–391, apr 2014.

[159] J. Liu, S. Chen, D. Qian, B. Gautam, G. Yang, J. Zhao, J. Bergqvist, F. Zhang, W. Ma, H. Ade, O. Ingan K. Gundogdu, F. Gao, and H. Yan, "Fast charge separation in a non-fullerene organic solar cell with a small driving force," *Nature Energy*, vol. 1, jun 2016.

[160] D. Meng, D. Sun, C. Zhong, T. Liu, B. Fan, L. Huo, Y. Li, W. Jiang, H. Choi, T. Kim, J. Y. Kim, Y. Sun, Z. Wang, and A. J. Heeger, "High-performance solution-processed non-fullerene organic solar cells based on selenophene-containing perylene bisimide acceptor," *Journal of the American Chemical Society*, vol. 138, pp. 375–380, dec 2015.

[161] C. B. Nielsen, S. Holliday, H.-Y. Chen, S. J. Cryer, and I. McCulloch, "Non-fullerene electron acceptors for use in organic solar cells," *Accounts of Chemical Research*, vol. 48, pp. 2803–2812, oct 2015.

[162] J. Zhang, H. S. Tan, X. Guo, A. Facchetti, and H. Yan, "Material insights and challenges for non-fullerene organic solar cells based on small molecular acceptors," *Nature Energy*, vol. 3, pp. 720–731, jul 2018.

[163] J. Hou, O. Ingan R. H. Friend, and F. Gao, "Organic solar cells based on non-fullerene acceptors," *Nature Materials*, vol. 17, pp. 119–128, jan 2018.

[164] W. Li, Y. Yan, Y. Gong, J. Cai, F. Cai, R. S. Gurney, D. Liu, A. J. Pearson, D. G. Lidzey, and T. Wang, "Contrasting effects of energy transfer in determining efficiency improvements in ternary polymer solar cells," *Advanced Functional Materials*, vol. 28, p. 1704212, dec 2017.

[165] K. Nakano, K. Suzuki, Y. Chen, and K. Tajima, "Roles of energy/charge cascades and intermixed layers at donor/acceptor interfaces in organic solar cells," *Scientific Reports*, vol. 6, jul 2016.

[166] I. Lee, G. W. Kim, M. Yang, and T.-S. Kim, "Simultaneously enhancing the cohesion and electrical conductivity of PEDOT:PSS conductive polymer films using DMSO additives," *ACS Applied Materials & Interfaces*, vol. 8, pp. 302–310, dec 2015.

[167] P. P. Khlyabich, B. Burkhart, and B. C. Thompson, "Efficient ternary blend bulk heterojunction solar cells with tunable open-circuit voltage," *Journal of the American Chemical Society*, vol. 133, pp. 14534–14537, sep 2011.

[168] B. Fan, C. Sun, X.-F. Jiang, G. Zhang, Z. Chen, L. Ying, F. Huang, and Y. Cao, "Improved morphology and efficiency of polymer solar cells by processing donor-acceptor copolymer additives," *Advanced Functional Materials*, vol. 26, pp. 6479–6488, jul 2016.

[169] B. Francis, K. Watkins, and J. Kubelka, "Double hydrogen bonding between side chain carboxyl groups in aqueous solutions of poly (-l-malic acid): Implication for the evolutionary origin of nucleic acids," *Life*, vol. 7, p. 35, aug 2017.

[170] M. A. Ruderer and P. Mller-Buschbaum, "Morphology of polymer-based bulk heterojunction films for organic photovoltaics," *Soft Matter*, vol. 7, no. 12, p. 5482, 2011.

[171] S. Fischer, O. Marti, T. Diesner, and B. Rieger, "Small-angle x-ray scattering on melt-spun polypropylene fibers: Modeling and data reduction," *Macromolecules*, vol. 43, pp. 5009–5015, jun 2010.

[172] K. M. Coakley and M. D. McGehee, "Photovoltaic cells made from conjugated polymers infiltrated into mesoporous titania," *Applied Physics Letters*, vol. 83, pp. 3380–3382, oct 2003.

[173] Y. Gu, C. Wang, and T. P. Russell, "Multi-length-scale morphologies in PCPDTBT/PCBM bulk-heterojunction solar cells," *Advanced Energy Materials*, vol. 2, pp. 683–690, apr 2012.

[174] J. W. Lukas Schmidt-Mende, *Organic and Hybrid Solar Cells: An Introduction.* Walter de Gruyter GmbH & Co KG, 2016.

[175] V. Vohra, K. Kawashima, T. Kakara, T. Koganezawa, I. Osaka, K. Takimiya, and H. Murata, "Efficient inverted polymer solar cells employing favourable molecular orientation," *Nature Photonics*, vol. 9, pp. 403–408, may 2015.

[176] H. Sirringhaus, P. J. Brown, R. H. Friend, M. M. Nielsen, K. Bechgaard, B. M. W. Langeveld-Voss, A. J. H. Spiering, R. A. J. Janssen, E. W. Meijer, P. Herwig, and D. M. de Leeuw, "Two-dimensional charge transport in self-organized, high-mobility conjugated polymers," *Nature*, vol. 401, pp. 685–688, oct 1999.

[177] H. Kang, M. A. Uddin, C. Lee, K.-H. Kim, T. L. Nguyen, W. Lee, Y. Li, C. Wang, H. Y. Woo, and B. J. Kim, "Determining the role of polymer molecular weight for high-performance all-polymer solar cells: Its effect on polymer aggregation and phase separation," *Journal of the American Chemical Society*, vol. 137, pp. 2359–2365, feb 2015.

[178] L. Song, *Tailoring titania photoanodes for application in solid-state dye-sensitized solar cells and hybrid solar cells.* PhD thesis, TECHNISCHE UNIVERSITÄT MÜNCHEN, 2017.

[179] S. J. Lou, J. M. Szarko, T. Xu, L. Yu, T. J. Marks, and L. X. Chen, "Effects of additives on the morphology of solution phase aggregates formed by active layer components of high-efficiency organic solar cells," *Journal of the American Chemical Society*, vol. 133, pp. 20661–20663, dec 2011.

[180] L. Shi, T. L. Young, J. Kim, Y. Sheng, L. Wang, Y. Chen, Z. Feng, M. J. Keevers, X. Hao, P. J. Verlinden, M. A. Green, and A. W. Y. Ho-Baillie, "Accelerated lifetime testing of organic–inorganic perovskite solar cells encapsulated by polyisobutylene," *ACS Applied Materials & Interfaces*, vol. 9, pp. 25073–25081, jul 2017.

[181] M. Theelen, K. Bakker, H. Steijvers, S. Roest, P. Hielkema, N. Barreau, and E. Haverkamp, "emin situ/em monitoring of the accelerated performance degradation of solar cells and modules: A case study for cu(in,ga)sesub2/sub solar cells," *Journal of Visualized Experiments*, oct 2018.

[182] F. C. Krebs, "Degradation and stability of polymer and organic solar cells," *Solar Energy Materials and Solar Cells*, vol. 92, p. 685, jul 2008.

[183] Z. A. Page, Y. Liu, V. V. Duzhko, T. P. Russell, and T. Emrick, "Fulleropyrrolidine interlayers: Tailoring electrodes to raise organic solar cell efficiency," *Science*, vol. 346, pp. 441–444, sep 2014.

[184] D. Barreiro-Argüelles, G. Ramos-Ortiz, J.-L. Maldonado, E. Pérez-Gutiérrez, D. Romero-Borja, M.-A. Meneses-Nava, and J. C. Nolasco, "Stability study in organic solar cells based on PTB7:PC71bm and the scaling effect of the active layer," *Solar Energy*, vol. 163, pp. 510–518, mar 2018.

[185] H.-S. Lee, H. Ahn, J. W. Jo, B. Kim, and H. J. Son, "Synergistic effects of solvent and polymer additives on solar cell performance and stability of small molecule bulk heterojunction solar cells," *Journal of Materials Chemistry A*, vol. 4, no. 47, pp. 18383–18391, 2016.

[186] H. Unay, G. A. dos Reis Benatto, M. J. Beliatis, S. A. Gevorgyan, P. Kavak, S. Memiş, A. Cirpan, L. Toppare, E. A. Parlak, and F. C. Krebs, "High stability of benzotriazole and benzodithiophene containing medium band-gap polymer solar cell," *Solar Energy Materials and Solar Cells*, vol. 174, pp. 433–444, jan 2018.

[187] F. Fungura, *Organic solar cells: Degradation processes and approaches to enhance performance.* PhD thesis, Iowa State University, 2016.

[188] İ. V. Öner, "Operational stability and degradation of organic solar cells," *Periodicals of Engineering and Natural Sciences (PEN)*, vol. 5, jun 2017.

[189] C. V. Hoven, X.-D. Dang, R. C. Coffin, J. Peet, T.-Q. Nguyen, and G. C. Bazan, "Improved performance of polymer bulk heterojunction solar cells through the reduction of phase separation via solvent additives," *Advanced Materials*, vol. 22, pp. E63–E66, feb 2010.

[190] J. T. Rogers, K. Schmidt, M. F. Toney, G. C. Bazan, and E. J. Kramer, "Time-resolved structural evolution of additive-processed bulk heterojunction solar cells," *Journal of the American Chemical Society*, vol. 134, pp. 2884–2887, feb 2012.

[191] X. Guo, C. Cui, M. Zhang, L. Huo, Y. Huang, J. Hou, and Y. Li, "High efficiency polymer solar cells based on poly(3-hexylthiophene)/indene-c70 bisadduct with solvent additive," *Energy & Environmental Science*, vol. 5, no. 7, p. 7943, 2012.

[192] Y. Choi, G. Kim, H. Kim, S. H. Lee, S. Kwon, J. Kim, and K. Lee, "Optimized phase separation in low-bandgap polymer:fullerene bulk heterojunction solar cells with criteria of solvent additives," *Nano Energy*, vol. 30, pp. 200–207, dec 2016.

[193] Y. Sun, G. C. Welch, W. L. Leong, C. J. Takacs, G. C. Bazan, and A. J. Heeger, "Solution-processed small-molecule solar cells with 6.7% efficiency," *Nature Materials*, vol. 11, pp. 44–48, nov 2011.

[194] Z. He, C. Zhong, S. Su, M. Xu, H. Wu, and Y. Cao, "Enhanced power-conversion efficiency in polymer solar cells using an inverted device structure," *Nature Photonics*, vol. 6, pp. 591–595, aug 2012.

[195] Q. Wan, X. Guo, Z. Wang, W. Li, B. Guo, W. Ma, M. Zhang, and Y. Li, "10.8% efficiency polymer solar cells based on PTB7-th and PC71bm via binary solvent additives treatment," *Advanced Functional Materials*, vol. 26, pp. 6635–6640, jul 2016.

[196] Y. Yoneda, "Anomalous surface reflection of x rays," *Physical Review*, vol. 131, pp. 2010–2013, sep 1963.

[197] L. Salamandra, L. La Notte, G. Paronesso, G. Susanna, L. Cinà, G. Polino, L. Mattiello, A. Catini, C. Di Natale, E. Martinelli, A. Di Carlo, F. Brunetti, T. M. Brown, and A. Reale, "On the role of PTB7-th:[70]PCBM blend concentration in ortho -xylene on polymer solar-cell performance," *Energy Technology*, vol. 5, pp. 2168–2174, sep 2017.

[198] S. Guo, W. Wang, E. M. Herzig, A. Naumann, G. Tainter, J. Perlich, and P. Müller-Buschbaum, "Solvent–morphology–property relationship of PTB7:PC71bm polymer solar cells," *ACS Applied Materials & Interfaces*, vol. 9, pp. 3740–3748, jan 2017.

[199] L. Zhao, S. Zhao, Z. Xu, B. Qiao, D. Huang, and X. Xu, "Two effects of 1,8-diiodooctane on PTB7-th:PC71bm polymer solar cells," *Organic Electronics*, vol. 34, pp. 188–192, jul 2016.

[200] B. A. Collins, Z. Li, J. R. Tumbleston, E. Gann, C. R. McNeill, and H. Ade, "Absolute measurement of domain composition and nanoscale size distribution explains performance in PTB7:PC71bm solar cells," *Advanced Energy Materials*, vol. 3, pp. 65–74, oct 2012.

[201] Q. Sun, F. Zhang, J. Wang, Q. An, C. Zhao, L. Li, F. Teng, and B. Hu, "A two-step strategy to clarify the roles of a solution processed PFN interfacial layer in highly efficient polymer solar cells," *Journal of Materials Chemistry A*, vol. 3, no. 36, pp. 18432–18441, 2015.

[202] S.-H. Liao, H.-J. Jhuo, Y.-S. Cheng, and S.-A. Chen, "Fullerene derivative-doped zinc oxide nanofilm as the cathode of inverted polymer solar cells with low-bandgap polymer (PTB7-th) for high performance," *Advanced Materials*, vol. 25, pp. 4766–4771, aug 2013.

[203] J. Yu, Y. Zheng, and J. Huang, "Towards high performance organic photovoltaic cells: A review of recent development in organic photovoltaics," *Polymers*, vol. 6, pp. 2473–2509, sep 2014.

[204] R. Yu, H. Yao, L. Hong, Y. Qin, J. Zhu, Y. Cui, S. Li, and J. Hou, "Design and application of volatilizable solid additives in non-fullerene organic solar cells," *Nature Communications*, vol. 9, nov 2018.

[205] L. Ye, Y. Jing, X. Guo, H. Sun, S. Zhang, M. Zhang, L. Huo, and J. Hou, "Remove the residual additives toward enhanced efficiency with higher reproducibility in polymer solar cells," *The Journal of Physical Chemistry C*, vol. 117, pp. 14920–14928, jul 2013.

[206] E. A. L. Mol, G. C. L. Wong, J. M. Petit, F. Rieutord, and W. H. de Jeu, "Thermal fluctuations of freely suspended smectic-a films from mesoscopic to molecular length scales," *Physical Review Letters*, vol. 79, pp. 3439–3442, nov 1997.

[207] P. Müller-Buschbaum, J. S. Gutmann, C. Lorenz, T. Schmitt, and M. Stamm, "Decay of interface correlation in thin polymer films," *Macromolecules*, vol. 31, pp. 9265–9272, dec 1998.

[208] Y. Yao, E. Metwalli, B. Su, V. Körstgens, D. M. González, A. Miasnikova, A. Laschewsky, M. Opel, G. Santoro, S. V. Roth, and P. Müller-Buschbaum, "Arrangement of maghemite nanoparticles via wet chemical self-assembly in PS-b-PNIPAM diblock copolymer films," *ACS Applied Materials & Interfaces*, vol. 7, pp. 13080–13091, jun 2015.

[209] D. Babonneau, S. Camelio, D. Lantiat, L. Simonot, and A. Michel, "Waveguiding and correlated roughness effects in layered nanocomposite thin films studied by grazing-incidence small-angle x-ray scattering," *Physical Review B*, vol. 80, oct 2009.

[210] P. Müller-Buschbaum and M. Stamm, "Correlated roughness, long-range correlations, and dewetting of thin polymer films," *Macromolecules*, vol. 31, pp. 3686–3692, jun 1998.

[211] N. K. Elumalai and A. Uddin, "Open circuit voltage of organic solar cells: an in-depth review," *Energy & Environmental Science*, vol. 9, no. 2, pp. 391–410, 2016.

[212] W. Wang, L. Song, D. Magerl, D. M. González, V. Krstgens, M. Philipp, J.-F. Moulin, and P. Müller-Buschbaum, "Influence of solvent additive 1,8-octanedithiol on p3ht:PCBM solar cells," *Advanced Functional Materials*, vol. 28, p. 1800209, mar 2018.

[213] S. Guo, E. M. Herzig, A. Naumann, G. Tainter, J. Perlich, and P. Mller-Buschbaum, "Influence ofsolvent and solvent additive on the morphology of PTB7 films probed via x-ray scattering," *The Journal of Physical Chemistry B*, vol. 118, pp. 344–350, dec 2013.

[214] R. Sharma, V. Gupta, H. Lee, K. Borse, R. Datt, C. Sharma, M. Kumar, S. Yoo, and D. Gupta, "Charge carrier dynamics in PffBT4t-2od: PCBM organic solar cells," *Organic Electronics*, vol. 62, pp. 441–447, nov 2018.

[215] C.-W. Chu, H. Yang, W.-J. Hou, J. Huang, G. Li, and Y. Yang, "Control of the nanoscale crystallinity and phase separation in polymer solar cells," *Applied Physics Letters*, vol. 92, p. 103306, mar 2008.

[216] T. Erb, U. Zhokhavets, G. Gobsch, S. Raleva, B. Sthn, P. Schilinsky, C. Waldauf, and C. J. Brabec, "Correlation between structural and optical properties of composite polymer/fullerene films for organic solar cells," *Advanced Functional Materials*, vol. 15, pp. 1193–1196, jul 2005.

[217] J. Zhao, Y. Li, G. Yang, K. Jiang, H. Lin, H. Ade, W. Ma, and H. Yan, "Efficient organic solar cells processed from hydrocarbon solvents," *Nature Energy*, vol. 1, jan 2016.

[218] P. Mller-Buschbaum, "The active layer morphology of organic solar cells probed with grazing incidence scattering techniques," *Advanced Materials*, vol. 26, pp. 7692–7709, feb 2014.

[219] G. L. Frontini, F. Otero, M. G. Messineo, and G. E. Eliçabe, "Estimation of size distribution in concentrated particle systems from light scattering measurements," *Inverse Problems in Science and Engineering*, vol. 16, pp. 995–1004, dec 2008.

[220] D. Gazzillo, A. Giacometti, R. G. D. Valle, E. Venuti, and F. Carsughi, "A scaling approximation for structure factors in the integral equation theory of polydisperse nonionic colloidal fluids," *The Journal of Chemical Physics*, vol. 111, pp. 7636–7645, oct 1999.

[221] M. Gomez, A. Nogales, M. C. G. Gutierrez, and T. Ezquerra, *Applications of synchrotron light to scattering and diffraction in materials and life sciences*. Springer Berlin Heidelberg, 2009.

[222] Y. Zhang, A. J. Parnell, F. Pontecchiani, J. F. K. Cooper, R. L. Thompson, R. A. L. Jones, S. M. King, D. G. Lidzey, and G. Bernardo, "Understanding and controlling morphology evolution via DIO plasticization in PffBT4t-2od/PC71bm devices," *Scientific Reports*, vol. 7, mar 2017.

[223] S. Kouijzer, J. J. Michels, M. van den Berg, V. S. Gevaerts, M. Turbiez, M. M. Wienk, and R. A. J. Janssen, "Predicting morphologies of solution processed polymer:fullerene blends," *Journal of the American Chemical Society*, vol. 135, pp. 12057–12067, aug 2013.

[224] A. Pivrikas, N. S. Sariciftci, G. Juška, and R. terbacka, "A review of charge transport and recombination in polymer/fullerene organic solar cells," *Progress in Photovoltaics: Research and Applications*, vol. 15, no. 8, pp. 677–696, 2007.

[225] A. C. Mayer, S. R. Scully, B. E. Hardin, M. W. Rowell, and M. D. McGehee, "Polymer-based solar cells," *Materials Today*, vol. 10, pp. 28–33, nov 2007.

[226] C. J. Schaffer, C. M. Palumbiny, M. A. Niedermeier, C. Jendrzejewski, G. Santoro, S. V. Roth, and P. Müller-Buschbaum, "A direct evidence of morphological degradation on a nanometer scale in polymer solar cells," *Advanced Materials*, vol. 25, pp. 6760–6764, sep 2013.

[227] S. Mukherjee, C. M. Proctor, G. C. Bazan, T.-Q. Nguyen, and H. Ade, "Significance of average domain purity and mixed domains on the photovoltaic performance of high-efficiency solution-processed small-molecule BHJ solar cells," *Advanced Energy Materials*, vol. 5, p. 1500877, jul 2015.

[228] G. Garcia-Belmonte and J. Bisquert, "Open-circuit voltage limit caused by recombination through tail states in bulk heterojunction polymer-fullerene solar cells," *Applied Physics Letters*, vol. 96, p. 113301, mar 2010.

[229] J. D. Zimmerman, X. Xiao, C. K. Renshaw, S. Wang, V. V. Diev, M. E. Thompson, and S. R. Forrest, "Independent control of bulk and interfacial morphologies of small molecular weight organic heterojunction solar cells," *Nano Letters*, vol. 12, pp. 4366–4371, jul 2012.

[230] D. Credgington, R. Hamilton, P. Atienzar, J. Nelson, and J. R. Durrant, "Nongeminate recombination as the primary determinant of open-circuit voltage in polythiophene:fullerene blend solar cells: an analysis of the influence of device processing conditions," *Advanced Functional Materials*, vol. 21, pp. 2744–2753, jun 2011.

[231] N. Li, J. D. Perea, T. Kassar, M. Richter, T. Heumueller, G. J. Matt, Y. Hou, N. S. Gldal, H. Chen, S. Chen, S. Langner, M. Berlinghof, T. Unruh, and C. J. Brabec, "Abnormal strong burn-in degradation of highly efficient polymer solar cells caused by spinodal donor-acceptor demixing," *Nature Communications*, vol. 8, feb 2017.

[232] C. H. Peters, I. T. Sachs-Quintana, W. R. Mateker, T. Heumueller, J. Rivnay, R. Noriega, Z. M. Beiley, E. T. Hoke, A. Salleo, and M. D. McGehee, "The mechanism of burn-in loss in a high efficiency polymer solar cell," *Advanced Materials*, vol. 24, pp. 663–668, oct 2011.

[233] J. Kong, S. Song, M. Yoo, G. Y. Lee, O. Kwon, J. K. Park, H. Back, G. Kim, S. H. Lee, H. Suh, and K. Lee, "Long-term stable polymer solar cells with significantly reduced burn-in loss," *Nature Communications*, vol. 5, dec 2014.

[234] R. Roesch, M. Seeland, M. Bnklau, G. Gobsch, and H. Hoppe, "Stability of polymer solar cells: Dependence on working pressure," *Solar Energy Materials and Solar Cells*, vol. 111, pp. 212–215, apr 2013.

[235] S. M. Abdullah, S. Rafique, K. S. Hamdan, K. Sulaiman, D. Taguchi, and M. Iwamoto, "Mathematical modelling of degradation phenomena in organic solar cells under various fabrication conditions," *Organic Electronics*, vol. 58, pp. 46–52, jul 2018.

[236] M. D. Perez, C. Borek, S. R. Forrest, and M. E. Thompson, "Molecular and morphological influences on the open circuit voltages of organic photovoltaic devices," *Journal of the American Chemical Society*, vol. 131, pp. 9281–9286, jul 2009.

[237] H.-J. Jhuo, S.-H. Liao, Y.-L. Li, P.-N. Yeh, S.-A. Chen, W.-R. Wu, C.-J. Su, J.-J. Lee, N. L. Yamada, and U.-S. Jeng, "The novel additive 1-naphthalenethiol opens a new processing route to efficiency-enhanced polymer solar cells," *Advanced Functional Materials*, vol. 26, pp. 3094–3104, mar 2016.

[238] M.-S. Su, C.-Y. Kuo, M.-C. Yuan, U.-S. Jeng, C.-J. Su, and K.-H. Wei, "Improving device efficiency of polymer/fullerene bulk heterojunction solar cells through enhanced crystallinity and reduced grain boundaries induced by solvent additives," *Advanced Materials*, vol. 23, pp. 3315–3319, jun 2011.

List of publications

Publications related to the dissertation

- D. Yang, F. C. Löhrer, V. Körstgens, A. Schreiber, S. Bernstorff, J. M. Buriak, P. Müller-Buschbaum, "In-operando Study of the Effects of Solvent Additives on the Stability of Organic Solar Cells Based on PTB7-Th:PC$_{71}$BM", *ACS Energy Letters*, vol. 4, 464–470, 2019.

- D. Yang, B. Cao, V. Körstgens, N. Saxena, N. Li, C. Bilko, S. Grott, W. Chen, X. Jiang, J. E. Heger, S. Bernstorff, P. Müller-Buschbaum, "Tailoring morphology compatibility and device stability by adding PBDTTPD-COOH as third component to fullerene-based polymer solar cells", *ACS Appl. Energy. Mater.*, vol. 3, 2604–2613, 2020

- D. Yang, F. C. Löhrer, V. Körstgens, A. Schreiber, B. Cao S. Bernstorff, P. Müller-Buschbaum, "In-operando GISAXS and GIWAXS stability study of organic solar cells based on PffBT4T-2OD:PC$_{71}$BM with and without solvent additive", *Advanced science*, accepted, 2020. DOI: 10.1002/advs.202001117.

- D. Yang, T. Hauger, B. Olsen, E. J. Luber, B. Cao, P. Müller-Buschbaum, J. M. Buriak, "How to choose an interfacial modifier for organic photovoltaics using simple surface energy considerations",to be submitted, 2020.

- D. Yang, S. Grott, X. Jiang, K. S. Wienhold, M. Schwartzkopf, S. V. Roth, P. Müller-Buschbaum, "Comparison of the effects of solvent additives on the morphology development of printed PPDT2FBT:PC$_{71}$BM films", under review, 2020.

Further publications

- F. Nübling, D. Yang, P. Müller-Buschbaum, M. Brinkmann, and M. Sommer, "In situ synthesis of ternary block copolymer/homopolymer blends for organic photovoltaics", *ACS Appl. Mater. Interfaces.*, vol. 10, pp. 18149–18160, 2018.

- L. Song, W. Wang, E. Barabino, D. Yang, V. Krstgens, P. Zhang, S. V. Roth, and P. Müller-Buschbaum, "Composition–morphology correlation in PTB7-th/PC71bm blend films for organic solar cells", *ACS Appl. Mater. Interfaces.*, vol. 11, pp. 3125–3135, 2018.

- N. Saxena, B. Pretzl, X. Lamprecht, L. Bießmann, D. Yang, N. Li, C. Bilko, S. Bernstorff, and P. Müller-Buschbaum, "Ionic liquids as post-treatment agents for simultaneous improvement of seebeck coefficient and electrical conductivity in PE-DOT:PSS films", *ACS Appl. Mater. Interfaces.*, vol. 11, pp. 8060–8071, 2019.

- W. Chen, J. Zhong, J. Li, N. Saxena, L. P. Kreuzer, H. Liu, L. Song, B. Su, D. Yang, K. Wang, J. Schlipf, V. Krstgens, T. He, K. Wang, and P. Müller-Buschbaum, "Structure and charge carrier dynamics in colloidal PbS quantum dot solids", *J. Phys. Chem. Lett.*, vol. 10, pp. 2058–2065, 2019.

Scientific reports

- D. Yang, B. Cao, V. Körstgens, N. Saxena, N. Li, C. Bilko, S. Grott, W. Chen, X. Jiang, J. E. Heger, S. Bernstorff, P. Müller-Buschbaum, "Tailoring morphology compatibility and device stability by adding PBDTTPD-COOH as third component to fullerene-based polymer solar cells", *Lehrstuhl für Funktionelle Materialien, Annual Report*, 2019.

- D. Yang, F. C. Löhrer, V. Körstgens, A. Schreiber, S. Bernstorff, P. Müller-Buschbaum, "Improving compatibility of donor and acceptor materials in ternary organic solar cells by adding BPO", *Lehrstuhl für Funktionelle Materialien, Annual Report*, 2018.

- D. Yang, F. C. Löhrer, V. Körstgens, A. Schreiber, S. Bernstorff, J. M. Buriak, P. Müller-Buschbaum, "Investigating the degradation of PffBT4T-2OD: $PC_{71}BM$ solar cells by inoperando GIWAXS measurements", *Lehrstuhl für Funktionelle Materialien, Annual Report*, 2017.

- D. Yang, B. Su, W. Wang, S. V. Roth, P. Müller-Buschbaum, "Employing water/alcohol soluble conjugated polymer as cathode interlayer in organic solar cells", *Lehrstuhl für Funktionelle Materialien, Annual Report*, 2016.

- D. Yang, W. Wang, P. Müller-Buschbaum, "Printing high efficiency solar cells", *Lehrstuhl für Funktionelle Materialien, Annual Report*, 2015.

Conference talks

- D. Yang, F. C. Löhrer, V. Körstgens, A. Schreiber, S. Bernstorff, J. M. Buriak, P. Müller-Buschbaum, "Investigating the effects of solvent additives on the stability of organic solar cells", *ATUMs annual meeting*, Canmore (Canada), November 2019.

- D. Yang, F. C. Löhrer, V. Körstgens, A. Schreiber, S. Bernstorff, J. M. Buriak, P. Müller-Buschbaum, "In-operando Study of the Effects of Solvent Additives on the Stability of Organic Solar Cells Based on PTB7-Th:$PC_{71}BM$", *DPG-Frühjahrstagung*, Regensburg (Germany), March 2019.

- D. Yang, B. Cao, T. Hauger, E. J. Luber, P. Müller-Buschbaum, J. M. Buriak, "How to rationally select an interfacial modifier for high performance organic photovoltaics", *ATUMs annual meeting*, Garching (Germany), November 2018.

- D. Yang, N. Hohn, J. E. Heger, "GISAXS/GIWAXS and GISANS/GIWANS", *E13 Polymer Physics Summer School*, Obertauern (Austria), June 2018.

- D. Yang, F. C. Löhrer, V. Körstgens, A. Schreiber, S. Bernstorff, J. M. Buriak, P. Müller-Buschbaum, "In-operando Study of the Effects of Solvent Additives on the Stability of Organic Solar Cells Based on PTB7-Th:PC71BM", *DPG-Frühjahrstagung*, Berlin (Germany), March 2018.

- D. Yang, F. C. Löhrer, V. Körstgens, A. Schreiber, S. Bernstorff, J. M. Buriak, P. Müller-Buschbaum, "Investigating the degradation of organic solar cells by in-operando GISAXS/GIWAXS measurements", *ATUMs annual meeting*, Jasper (Canada), November 2017.

- D. Yang, S. Xia, "Block copolymers", *E13 Polymer Physics Summer School*, Obertauern (Austria), June 2016.

Conference poster presentations

- D. Yang, B. Cao, T. Hauger, E. J. Luber, P. Müller-Buschbaum, J. M. Buriak, "How to rationally select an interfacial modifier for high performance organic photovoltaics", *9th Colloquium of the Munich School of Engineering*, Garching (Germany), August 2019.

- D. Yang, B. Cao, T. Hauger, E. J. Luber, P. Müller-Buschbaum, J. M. Buriak, "How to rationally select an interfacial modifier for high performance organic photovoltaics", *E13 Polymer Physics Summer School*, Grainau (Germany), June 2019.

- D. Yang, B. Cao, T. Hauger, E. J. Luber, P. Müller-Buschbaum, J. M. Buriak, "How to rationally select an interfacial modifier for high performance organic photovoltaics", *101st Canadian Chemistry Conference and Exhibition*, Edmonton (Canada), May 2018.

- D. Yang, W. Wang, P. Müller-Buschbaum, "Employing water/alcohol soluble conjugated polymer as cathode interlayer in organic solar cells", *6th Colloquium of the Munich School of Engineering*, Munich (Germany), July 2016.

- D. Yang, W. Wang, P. Müller-Buschbaum, "Printing high efficiency solar cells", *5th International SolTech Conference in Munich*, Munich (Germany), April 2016.

- D. Yang, W. Wang, P. Müller-Buschbaum, "Printing high efficiency solar cells", *DPG-Frühjahrstagung*, Regensburg (Germany), April 2016.

Acknowledgments

First of all, I would like to thank my supervisor, Prof. Dr. Peter Müller-Buschbaum, for his patience and guidance throughout my Ph.D. training. He not only offered me the precious opportunity to work in E13 of the physics department in Technische Universität München, and also in the exciting fields such as organic solar cells, softmatter and X-ray scattering. He is always there and glad to share his experience and opinion, provide me his support and encouragement. I am extremely grateful that Peter gave me the great chance to join in the Alberta/Technical University of Munich International Graduate School (ATUMs) program, which enables me to have a precious experience staying abroad in an international institution (UofA, Edmonton, Canada).

Moreover, I also would like to thank my co-supervisor, Prof. Dr. Jillian M. Buriak, in Alberta, Canada. Many thanks to her for hosting me as a visiting research student to work in her research group. Jillian generously offers me a lot of support, encouragement, and guidance during my stay. Her passion for science and self-motivated attitude profile an outstanding female scientist, which definitely encourages me.

Again, Peter and Jillian are always there for scientific discussions and personal talks. Their encouragement, patience, and trust strengthen my self-confidence and positively influence my personality. The experience of staying with them is no doubt precious treasure in my whole life.

For those great experiments, I am also grateful for the great support from the beamline scientists in Elettra, Italy, and DESY, Hamberg. Specifically, thanks to Dr. Sigrid Bernstorff (Elettra), Prof. Dr. Stephan V. Roth (DESY) and Dr. Matthias Schwartzkopf (DESY) for their guidance, patience and discussion. Also, the help from E13 colleagues can not be ignored for achieving successful beamtime at beamlines. In no specific order, I want to thank Dr. Johannes Schlipf, Dr. Su Bo, Dr. Volker Körstgens, Franziska Löhrer Dr. Nuri Hohn, Dr. Kun Wang, Dr. Nitin Saxena, Nian Li, Xinyu Jiang, Sebastian Grott, Kerstin S. Wienhold. Thanks for their help and discussion, which makes our beamtimes super wonderful. Especially thanks to Dr. Johannes Schlipf and his student Bernhard Roland Kalis for building and improving the in-operando chamber.